THE UNIVERSITY OF CHICAGO

RECIPROCAL REGULATION OF CELL SIGNALING BY REACTIVE CENTRAL GLYCOLYTIC METABOLITES

A DISSERTATION SUBMITTED TO

THE FACULTY OF THE DIVISION OF THE BIOLOGICAL SCIENCES

AND THE PRITZKER SCHOOL OF MEDICINE

IN CANDIDACY FOR THE DEGREE OF

DOCTOR OF PHILOSOPHY

COMMITTEE ON CANCER BIOLOGY

BY

CHRISTOPHER WILLIAM LEE

CHICAGO, ILLINOIS

MARCH 2024

以近知遠，以一知萬，以微知明.
–荀子

Through the near and evident, we envision the far unseen,
Through singular instances, we arrive at myriad understandings,
Through small fragments, we piece together clarity of the whole.

-Xunzi

TABLE OF CONTENTS

LIST OF FIGURES

LIST OF TABLES

ACKNOWLEDGEMENTS

I would like to give my heartfelt thanks for the guidance, support, and inspiration provided by my mentor Dr. Raymond E. Moellering. I deeply appreciate Ray's mentorship style, defined by high standards for scientific rigorous scientific inquiry, personal responsibility, initiative, and giving in return, candid feedback paired with a constant stream of support and encouragement. Although some discussions weren't easy at the time, in hindsight, I consider each of them an essential and invaluable part of my personal growth.

From a scientific standpoint, I've had the privilege of immersing myself in an interdisciplinary environment full of diverse and interesting questions on the cutting-edge of scientific discovery; all of which are being tackled by incredibly smart and hard-working colleagues. As invaluable parts of this immersive experience, I want to thank all Moellering lab members, past and present, all of whom have invested their time and energy to help me learn a diverse array of skills and techniques that I'll be able to use going forward. In particular, I would like to thank Dr. John S. Coukos for his mentorship in the first half of my graduate student career and with whom I worked with on several projects mentioned in this thesis. I'd also like to thank Kavya S. Pillai, Anthony J. Carlos, Dr. Peter Dongbo Yang, and Dr. Zeyu Qiao; not just as colleagues but as friends who have enriched my experience with their valuable discussions, insights, and camaraderie, both within the lab and beyond its confines, adding both depth and enjoyment to my professional and personal life.

I would also like to extend many thanks to Dr. Gihoon Lee, Dr. Jae Won Chang, Dr. Jun X. Huang who helped set the foundation for the science that the projects in this thesis are based on, as well as Dr. Shaghayegh, Dr. Colin Swenson, and Debbie Thomas for their invaluable

chemistry expertise. I would also like to thank Xavier Rousseau, a talented UChicago undergraduate, for his dedication and hard work in helping me with various experiments. Last, but definitely not least, I would like to thank Dr. Somayeh Ahmadiantehrani for her help in improving my scientific communication and presentation skills.

I would like to also extend many thanks to collaborators namely Dr. Gopal Pattanayak in the lab of Mike Rust whom I collaborate with and UChicago Proteomics and Metabolomics Core personnel including Director Samuel (Shao-Huan) Weng, Director Hardik Shah, Allen Huff, and Dr. Roya Amini Tabrizi for their help and expertise.

Additionally, I would like to thank my CCB thesis committee members: Dr. Marsha R. Rosner, Dr. Kay F. Macleod, and Dr. Barbara L. Kee for their mentorship, guidance, encouragement, and patience as well as the UChicago Committee on Cancer Biology Program for allowing me to pursue my Ph.D. at UChicago and making today possible.

Stepping back, I would also like to thank the people at UCSD for their support, without whom I would not be here at UChicago. Namely my scientific mentors Dr. Robert 'Skip' Pomeroy, Dr. Yingxiao 'Peter' Wang and Dr. Molly Allen as well as my friends Dr. Brian Sutjiadi, Carlos Anaya, Edward Aminov, Dr. Laurence Chen, Omar Imami, Hoai-An 'Ryan' Nguyen, and Zulfar Ghulam-Jelani. I have fond memories of UCSD and the California sun.

Finally, I would like to dedicate my thesis to my parents Li-Lin Yang and Horng-Juing Lee, without whom, nothing would be possible. Thank you for all your love, guidance, and support every step of my life.

ABSTRACT

Metabolism, a fundamental aspect of all biological systems, encompasses the intricate network of chemical reactions that occur within a living organism to maintain life. Metabolism interconnects a broad range of crucial biological processes including energy production, cellular repair, growth, and response to environmental changes. The study of metabolism not only provides insights into basic biological functions but also aids in understanding and treating metabolic disorders and diseases like cancer, diabetes, aging, and obesity. As a reflection of the diverse aspects of metabolism, this thesis outlines a variety of studies centered around regulatory signaling pathways that arise from reactive metabolites of the central, highly conserved glycolytic pathway to understand both fundamental aspects of cellular metabolism and disease mechanisms. It delves into the dynamics of 3-phosphoglyceryl-lysine (pgK) modifications in cyanobacteria, highlighting their oscillation in response to environmental light/dark cycles and impact on glycolytic enzymes and central carbon metabolism flux. It confirms the role of DJ-1 in detoxifying methylglyoxal as a glyoxalase, to set the foundation for future pathophysiological studies of the metabolism of neurodegenerative disorders. Furthermore, it explores the potential of histone deacetylases, specifically HDAC3, in regulating pgK modifications, and suggests potential research directions to study the broader functional implications of this mechanism. Lastly, this thesis maps how cancer cells respond to glycolytic perturbations, focusing in particular on the relationship between different forms of central glycolytic perturbation and the resulting stress responses, highlighting especially the role of central glycolysis as a nexus for redox stress signaling. Overall, this thesis aims to present findings that offer new insights into metabolic regulation and disease pathology by reactive metabolite post-translational

modifications, with the goal of improving insight for next generation therapeutic approaches against metabolically aberrant diseases.

CHAPTER 1. BACKGROUND

1.1 Cancer Metabolism: Expanding our Understanding of a Classic Hallmark

Cancer metabolism, a complex and multifaceted phenomenon, represents a fundamental reprogramming of metabolic processes within malignant cells that profoundly influences their growth, survival, and proliferation. [1, 2] This aberrant metabolic landscape is characterized by a plethora of intricate alterations in cellular bioenergetics, nutrient utilization, and macromolecular biosynthesis, all orchestrated to support the insatiable demands of proliferating cancer cells.

At the core of cancer metabolism lies a pronounced shift in energy production strategies, where cancer cells display a predilection for glycolysis, a phenomenon commonly referred to as the Warburg effect.[3] This preference for glycolytic metabolism, even in the presence of ample oxygen, allows cancer cells to rapidly generate adenosine triphosphate (ATP) through the enzymatic conversion of glucose to pyruvate, which is subsequently reduced to lactate, a process that circumvents the comparatively more efficient oxidative phosphorylation conducted within the mitochondria.[4] This metabolic shift toward glycolysis serves a dual purpose: it provides cancer cells with the necessary energy reserves and also fosters the accumulation of glycolytic intermediates, which can be diverted into various anabolic pathways to support the synthesis of nucleotides, lipids, and amino acids, crucial for cell division and biomass expansion.

Furthermore, cancer cells exhibit an enhanced ability to harness alternative nutrient sources, such as glutamine, to fuel their metabolic machinery. Glutamine,[5] a non-essential amino acid, serves as a critical carbon and nitrogen source for the production of intermediates that feed into central metabolic pathways, facilitating the synthesis of macromolecules required for rapid

cellular proliferation. This metabolic flexibility underscores the adaptability of cancer cells to diverse microenvironmental conditions and nutrient availability, granting them a survival advantage in the hostile tumor milieu.

Beyond altered nutrient utilization, cancer metabolism encompasses dysregulated signaling pathways, including the activation of oncogenes and the loss of tumor suppressor function, which converge to further perpetuate the metabolic reprogramming observed in cancer cells. A prominent example of this is the oncogene MYC which is dysregulated in approximately 70% of cancers. Associated with uncontrolled cellular growth once dysregulated, MYC orchestrates the dysregulation of various hallmark biological processes including uncontrolled cell differentiation, upregulated protein biosynthesis, upregulated proliferation via uncontrolled cell cycle progression to name a few pathways. In the context of cancer metabolism, MYC upregulates the expression of enzymes of various metabolic pathways including glucose metabolism (for example: SLC2A1, HK2, ENO1, LDHA), glutamine metabolism (for example: SLC1A5, GLS, GOT2/GPT), serine metabolism (for example: PHGDH, PSAT1, PSPH), and amino acid metabolism (for example: SLC7A5, BCAT1, ACLY, ACC, FASN) to provide the energy and biosynthetic components for growth (Figure 1.1).[6-10] Other examples of oncogenes which alter metabolism include RAS and BRAF which are similarly linked to upregulation of glucose metabolism and biosynthesis in the pentose phosphate pathway. Collectively, these genetic and epigenetic alterations culminate in the activation of key metabolic enzymes and transporters, as well as the upregulation of nutrient receptors, collectively driving the metabolic shift towards anabolism and sustaining the energetic demands of uncontrolled cell growth.[11, 12]

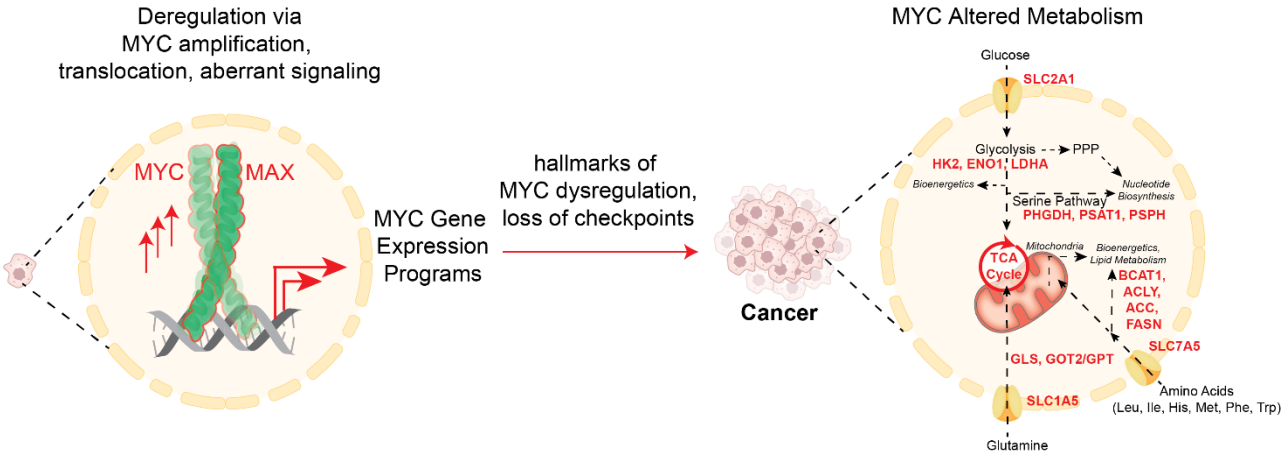

Figure 1.1 Simplified example schematic of oncogenic metabolic reprogramming by MYC: Dysregulation of central metabolic pathways in MYC dysregulated cancers supports increased growth and proliferation via upregulation of bioenergetics and biosynthesis. Highlighted in red are example enzymes that are upregulated by MYC. HK2 hexokinase, ENO enolase, LDHA lactate dehydrogenase A, PHGDH 3-phosphoglycerate dehydrogenase, PSAT1 phosphoserine aminotransferase, PSPH phosphoserine phosphatase, BCAT1 branched chain aminotransferase, ACLY ATP citrate lyase, ACC acetyl-CoA carboxylase, FASN fatty acid synthase, GLS glutaminase, GOT2/GPT glutamate oxaloacetate transaminase/glutamine pyruvate transaminase, TCA tricarboxylic acid, PPP pentose phosphate pathway, SLC solute carrier family

In conclusion, cancer metabolism represents a sophisticated and intricate reconfiguration of cellular metabolic networks that not only ensures the bioenergetic needs of proliferating cancer cells but also supports their biosynthetic demands. This profound metabolic reprogramming, underpinned by a spectrum of genetic and epigenetic alterations,[13] underscores the pivotal role of metabolism in the oncogenic process and provides a rich terrain for therapeutic exploration[14] aimed at targeting the metabolic vulnerabilities of cancer cells. Research mapping oncogenes to their respective alterations to cancer metabolism and then to specific types of cancer is a widespread ongoing area of research which goes far beyond the scope of this, or any one, thesis. This thesis will focus on the fundamental signaling mechanisms

formed by post translational modification of select reactive metabolites originating from glycolysis.

1.2 Glycolysis: An Overview, Disease Associations, and Key Features

Glycolysis holds a central and indispensable role in the metabolic processes of a diverse range of organisms, providing the necessary energy and biosynthetic components. This intricate metabolic pathway orchestrates the conversion of a single glucose molecule through a precise series of ten enzymatic reactions, ultimately yielding two pyruvate molecules and a net production of two ATP molecules. Pyruvate, the end product of glycolysis, exhibits the flexibility to either enter the tricarboxylic acid (TCA) cycle or undergo fermentation to transform into lactate.

In mammalian cells, numerous glycolytic intermediates contribute to various branching biosynthetic pathways, including the pentose phosphate pathway (PPP), serine synthesis pathway (SSP), and the glycerol-3-phosphate shuttle. Given its vital role in supplying energy and biosynthetic building blocks, glycolysis becomes a focal point for the development of various regulatory mechanisms. These mechanisms, crucial for governing a wide array of cellular functions dependent, either directly or indirectly, on glycolysis, manifest in diverse forms, including allosteric regulation.

The historical recognition of glycolysis[15] as a fundamental metabolic process dates back to Louis Pasteur's observations in live yeast cells in 1860, followed by Eduard Buchner's work with cell-free extracts in 1897. Glycolysis's significance in carbohydrate metabolism lies in its ability to convert one glucose molecule into two pyruvate molecules, generating two ATP and two NADH molecules in the process. Notably, glycolysis accomplishes this without the

involvement of molecular oxygen, classifying it as an anaerobic pathway, although it does not completely oxidize glucose. The final product, pyruvate, proceeds to the mitochondria, where it undergoes further catabolism into CO2, yielding approximately 36 ATP per glucose through the tricarboxylic acid (TCA) cycle. This sequential carbohydrate oxidation process, encompassing glycolysis and the TCA cycle, constitutes oxidative phosphorylation (OXPHOS), an exceedingly efficient method of ATP production in aerobic organisms.

On the contrary, anaerobic organisms or tissues with limited access to oxygen resort to converting pyruvate into lactate (as seen in human muscle) or ethanol (as observed in yeast), a process known as anaerobic glycolysis or fermentation. The multifaceted implications of glycolysis extend to its association with a multitude of human metabolic diseases, including cancer, diabetes, central obesity, neurodegenerative conditions, and aging. Despite these associations, the intricate mechanisms that integrate metabolic states with regulatory signaling pathways remain predominantly unexplored.[16]

The Warburg effect sheds light on the unique phenomenon of tumors producing lactate from glucose, even in the presence of ample oxygen.[17] Although early models suggested impaired mitochondrial metabolism, subsequent research revealed the independence of mitochondrial activity from aerobic glycolysis in cancer cells. This implies alternative mechanisms underlie the distinctive glucose metabolism in cancer cells, prompting investigations aided by metabolomic technologies such as positron-emission tomography (PET) and stable isotope-resolved metabolomics. These studies have given rise to alternative models explaining the Warburg effect, emphasizing heightened glycolysis in tumor cells and its correlation with aggressive phenotypes.

Another perspective suggests that cancer cells possess substantial metabolic demands for biosynthesis beyond energy production, with lactate serving as an energy source in certain cases. The intricate connections between altered glucose metabolism and tumor proliferation necessitate further exploration.

Beyond cancer disease metabolism, Type 2 diabetes (T2D) represents another disease intricately linked to impaired glucose metabolism.[18, 19] Insulin, originating from pancreatic β cells, plays a pivotal role in regulating plasma glucose levels by stimulating glucose uptake in muscle, fat, and brain cells while suppressing hepatic glucose production. T2D arises when hepatic cells, adipocytes, and muscles become resistant to insulin, resulting in elevated blood glucose levels. Insulin's mechanisms involve the translocation of glucose transporter GLUT4, impacting glucose uptake, and reprogramming hepatocyte glucose metabolism. Obesity, closely associated with insulin resistance and T2D, warrants deeper investigation into the mechanistic roles of glucose metabolism.

Aging, characterized by the chronic accumulation of damage and stress, exhibits a strong association with glycolysis.[20, 21] Age-related alterations in glucose metabolism have been identified in the brain, presenting as a reduction in aerobic glycolysis. Additionally, the formation of advanced glycation end products (AGEs) through non-enzymatic reactions between glycolytic intermediates and proteins contributes to many diseases, notably diabetes,[22, 23] but also cancer, inflammation, and aging.[24-26] Elderly individuals with altered glucose metabolism show an increased risk of glucose intolerance and insulin resistance. Moreover, neurodegenerative diseases such as Alzheimer's and Parkinson's diseases exhibit correlations with cerebral glucose

metabolism, potentially influenced by elevated glycolysis in astrocytes and disruptions in the pentose phosphate pathway.[27]

In summary, glucose metabolism plays a significant role in numerous human metabolic diseases. However, the precise regulatory functions of glucose metabolism and its specific regulatory feedback pathways remain incompletely understood. Understanding the nuances of how metabolic crosstalk intrinsically regulates itself may offer promising avenues for future research and therapeutic advancements targeting disease metabolism.

1.3. Reactive Metabolites and Non-Enzymatic Post-Translational Modifications (rmPTMs) Regulate Cellular Activity

One class of post-translational modifications known as reactive metabolite post translational modifications (rmPTMs) have recently been increasingly shown to play pivotal roles in signaling the regulation of various cellular functions, including metabolic and transcriptional processes. rmPTMs refer to the chemical alterations that occur on proteins after they have been synthesized within a cell. These modifications involve the covalent attachment or alteration of specific chemical groups to amino acid residues in proteins, mediated by highly reactive chemical metabolic species that can form covalent bonds with protein functional groups of amino acid residues such as cysteine, lysine, arginine, and histidine. Upon covalent alteration, the side chain of these residues is dramatically altered. For example, formerly positively charged residues (histidine, lysine, and arginine) can be modified to become negatively charged thereby repulsing negatively charged substrate molecules while nucleophilic residues (cysteine) which formerly served as catalytic nucleophiles for an enzymatic reaction mechanism are no longer available to be bound by the original substrate. (Figures 1.3 and 1.4) Moreover, in the case of

residues involved in active site enzyme-substrate complexes, the formation of rmPTMs sterically hinder enzymatic activity by blocking access of the substrate to the enzyme active site. Additionally, in some cases, modifications can also form protein adducts, resulting in misfolding, loss of protein stability, localization, and ability to functionally interface with other proteins[22, 28, 29] (Figure 1.2), which ultimately promote disease pathology in cancer, diabetes, neurodegeneration, and aging. In other cases, modifications can form inter-protein crosslinks, forming covalently bonded protein dimers resulting in altered/ loss of protein activity (Figure 1.2 and Chapter 1.4).[30-32]

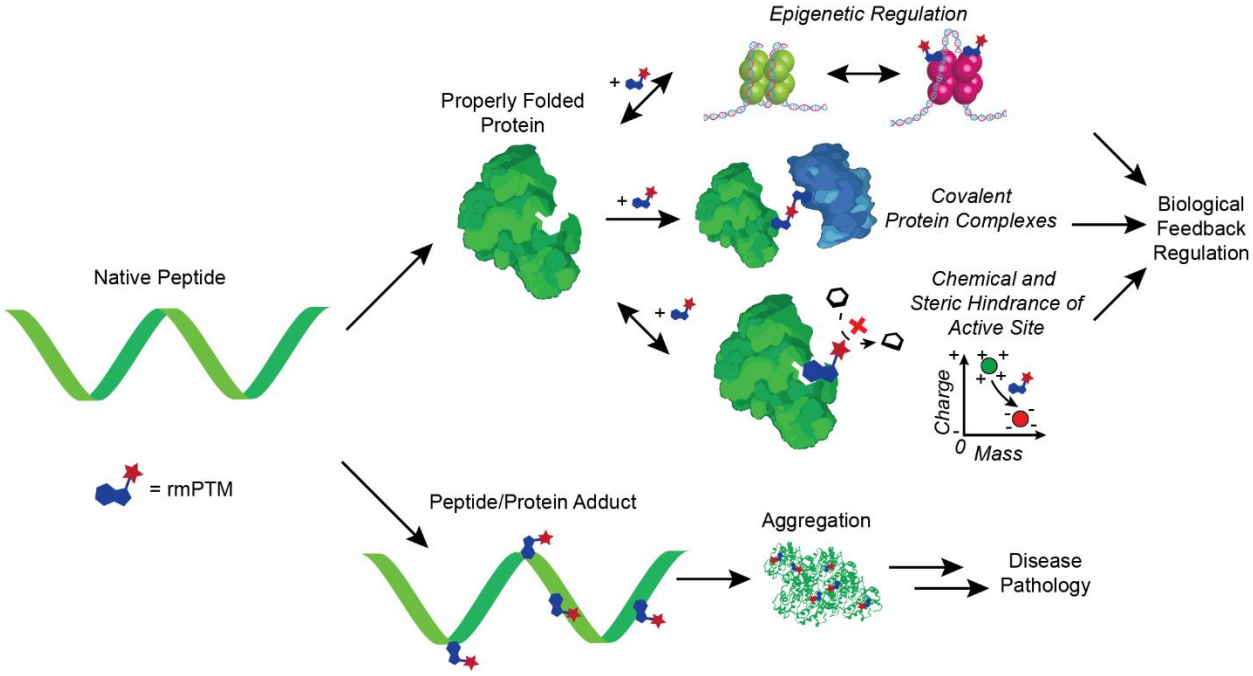

Figure 1.2 Simplified schematic of various effects of rmPTMs on protein state and activity

Among the earliest covalent PTMs originating from metabolism to be widely characterized were lysine acetylation, deriving from degeneration of fatty acids by Acyl-CoA synthetase. With mass spectrometry gaining more widespread use in the study of biology to profile the proteome, acetylation was found to be widespread across the proteome and important

for a variety of biological functions; in particular as enzymatically mediated reversible modification of lysines on histones for epigenetic regulation with numerous erasers and writers regulating epigenetic architecture. This 'acetyl-ome' was found to be widely conserved and found on proteins that regulated of a wide panel of cell functions including RNA splicing, DNA damage repair, cell cycle regulation, nuclear transport, cytoskeletal remodeling, translation, and protein folding despite acetylated proteo-forms making up a small fraction of the total proteome. Moreover, acetylation was found to be able to target central metabolic enzymes and directly modulate enzymatic activity of these metabolic proteins to globally redirect the flux direction of metabolic intermediates.[33] Collectively, acetylation was shown to be a means by which cells were able to dynamically feedback regulate metabolic processes using chemical intermediates sourced from metabolism; coupling cellular energy status with biosynthesis to regulate cellular processes in response to environmental nutrients. [34, 35]

Following acetylation, various other acyl-CoA metabolite PTMs targeting lysine residues were characterized including but not limited to propionylation, butyrylation, lactylation, malonylation, and succinylation[36, 37] (Figure 1.3) and found to functionally regulate epigenetic signatures [37, 38] as well as enzymatic activity on non-histone proteins as a function of metabolic flux[36, 39, 40] and linked to a variety of physiological and pathological phenotypes. As an example, perturbation of propionylation on histone H3 was found to impact cardiac function via epigenetic regulation of genes of the cGMP pathway, responsible for signal transduction of contractility.[41] On the other hand, butyrylation of the chaperone protein HSP90 at K754 was found to mediate chemoresistance by actively stabilizing a panel of proteins associated with cancer progression including HER2, EGFR, HIF-1, CDK4, and CDK6.[42, 43]

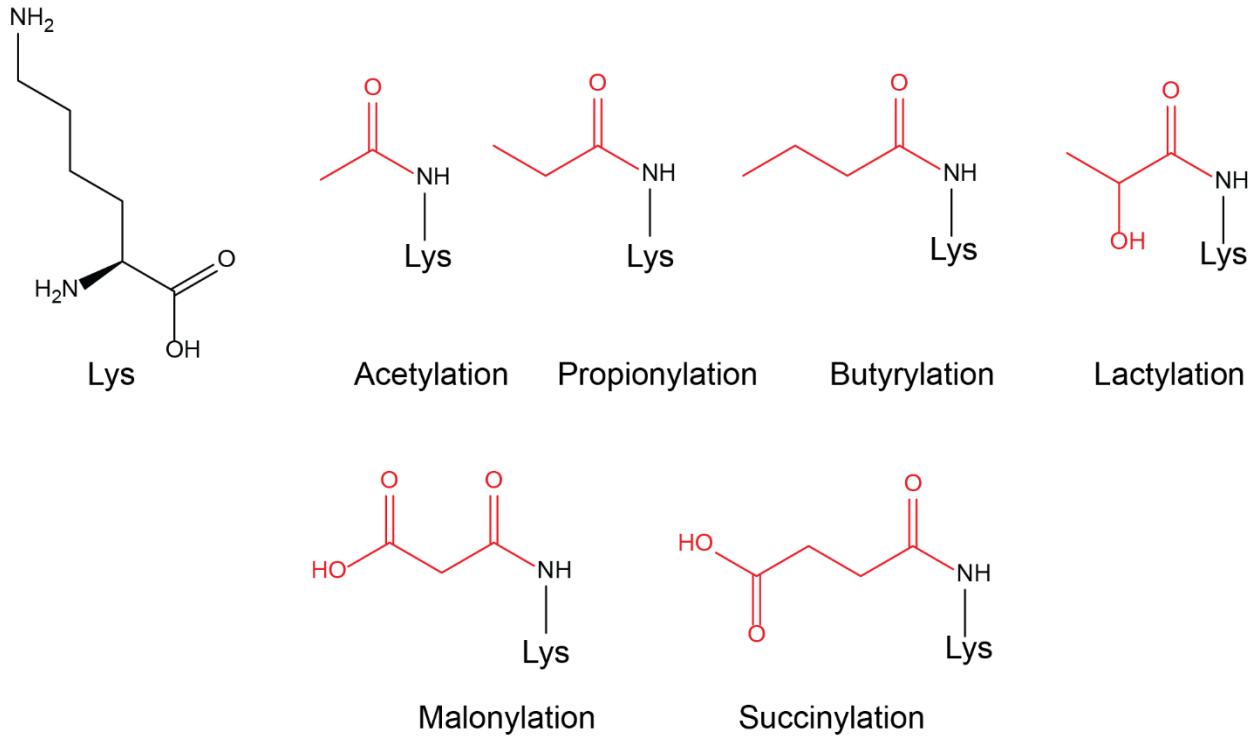

Figure 1.3 Representative CoA-metabolite PTMs (in red) of Lysine (Lys)

Importantly, malonylation, succinylation (Figure 1.3), and in particular phosphoglyceryl-lysine (Figure 1.4) [44-46] were first described in the early 2010s to be modifications that were removed off of proteins by eraser enzymes but installed onto proteins purely by intrinsic molecular electrophilicity without the need of a writer enzyme. In addition, extensive profiling of phosphoglyceryl-lysine rmPTMs were found to often occur within catalytic or regulatory residues of a variety of enzymes across various subcellular localizations and were able to respond in concert to changing glucose conditions to dynamically reroute metabolic flux. Furthermore, the conservation of these regulatory lysine residues across species implied that metabolic enzymes evolved to be responsive to the flux of reactive metabolic intermediates; making reactive metabolites and rmPTMs a highly conserved, intrinsic way in which metabolism regulates itself across all manners of life. These studies shifted the canonical

paradigm at the time that metabolite PTMs were installed and uninstalled via enzymatic activity.

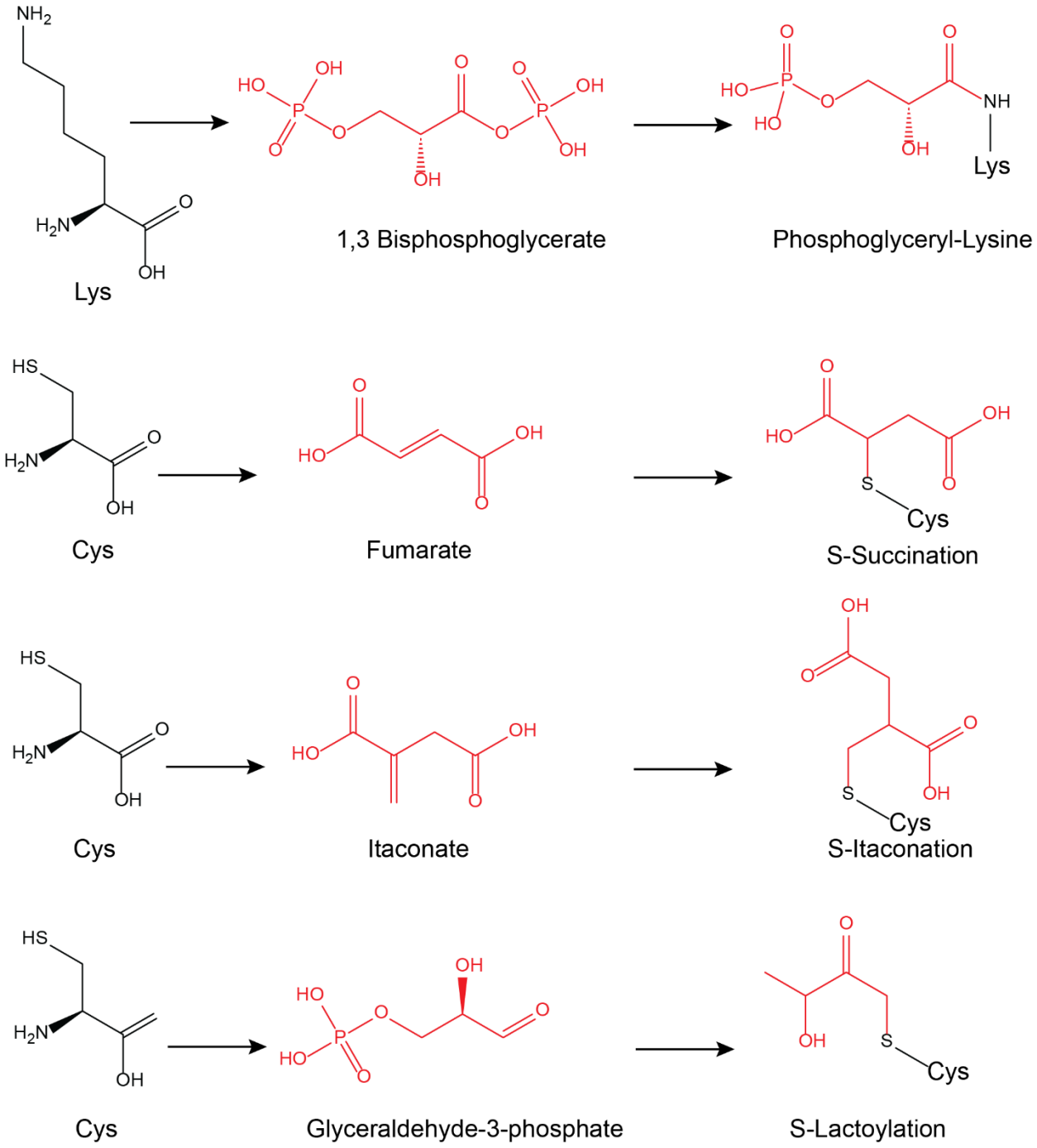

Figure 1.4 Representative PTMs derived from reactive metabolites (in red)

Subsequent studies increasingly found that many of the earlier described metabolite PTMs were able to be installed by both enzymatic and non-enzymatic mechanisms[40, 47, 48] while metabolite intermediates, such as the glycolytic metabolite PEP (phosphoenolpyruvate) could feedback regulate the flux of upstream glycolysis via competitive inhibition at the catalytic pocket of upstream glycolytic enzyme triose-phosphate isomerase (TPI).[49, 50] Additional glycolytic metabolites that regulate cellular processes beyond glycolysis include the primary metabolites dihydroxyacetone phosphate (DHAP) which has been identified to signal glucose availability towards growth pathway via mTORC1 in order to coordinate both glucose metabolism as well as lipogenesis.[51]

Furthermore, over the years, additional non-enzymatic rmPTMs (Figure 1.4) were discovered and functionally annotated in both fundamental biology as well as in disease contexts. An example of this is cysteine succination, which derives from fumarate, an intermediate in the tricarboxylic acid (TCA) cycle. Examples of functional protein sites of S-succination include C520 of SMARCC1, a component of the SWI-SNF chromatin remodeling complex. This modification disrupts the interaction between SMARCC1 and SNF5,[32] potentially leading to an altered transcriptional profile. Another example is C211 of PTEN,[52] preventing regulation of the central PI3K/AKT pathway, leading to widespread changes in growth, motility, cell survival, and metabolism.

Another instance of a TCA cycle-derived reactive metabolite is itaconate,[53] generated from the TCA cycle intermediate aconitate dehydrogenase 1 (ACOD1) which has found emerging importance within immunological contexts. Within macrophages, itaconate and its derivatives have demonstrated anti-inflammatory effects in various preclinical models of

inflammatory diseases.[54] These effects are attributed to a wide range of actions, including the inhibition of succinate dehydrogenase (which regulates succinate levels, a metabolite with multiple roles in inflammation), inhibition of glycolysis[55, 56] at multiple levels (resulting in reduced inflammation), activation of anti-inflammatory transcription factors NRF2 and ATF3, and inhibition of the NLRP3 inflammasome.

Finally, in recent studies, phosphoglyceryl-lysine modifications have been increasingly annotated onto more sites of interest while efforts in profiling the glycation rmPTMs formed by the reactive glycolytic byproduct methylglyoxal have given greater understanding in molecularly and mechanistically linking its role in glycation damage to disease pathology. The regulation of their endogenous concentrations and the target proteins with which they form functional rmPTMs documented to play pivotal roles in regulating various cellular functions are outlined in greater detail in subsequent sections (1.4 and 1.5).

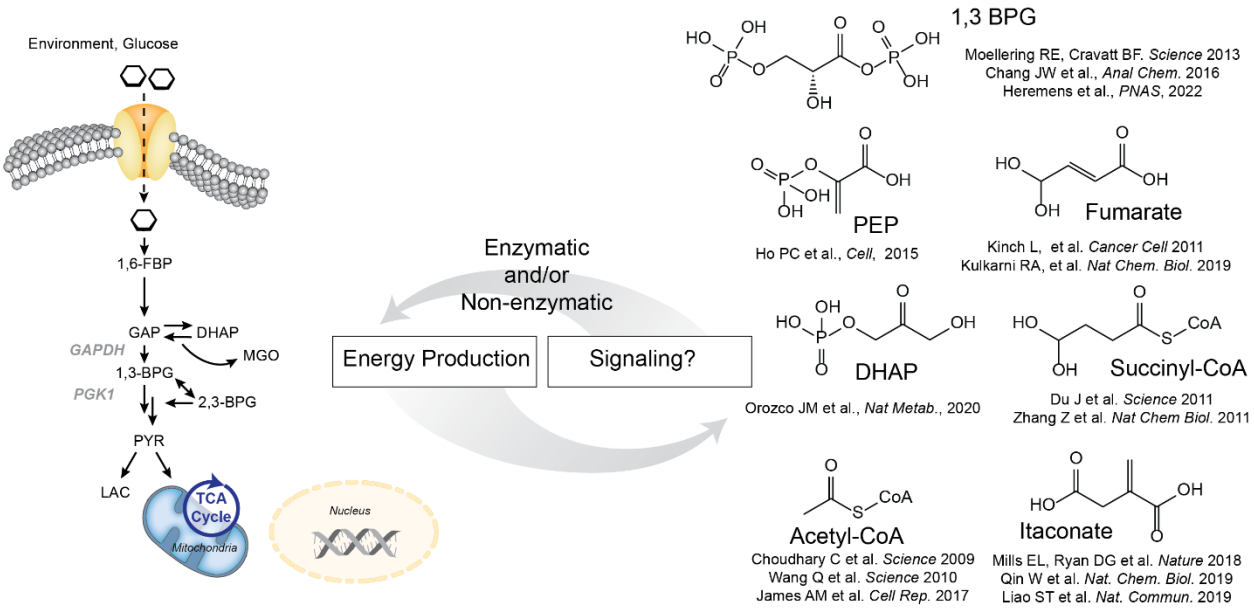

Figure 1.5 Representative studies of non-enzymatic rmPTMs formed from metabolites that were first mapped and molecularly described.

1.4. 1, 3 Bisphosphoglycerate (1,3 BPG)

The post-translational modification 3-Phosphoglyceryl-Lysine (pgK) is an intriguing and dynamic alteration found on numerous proteins within living organisms. It arises from the reaction between specific lysine residues in proteins and the primary glycolytic metabolite 1,3-bisphosphoglycerate (1,3-BPG)[46]. Despite being a primary metabolite of glycolysis, one of, if not the most, well studied biological pathways, it has remained understudied since its discovery nearly a century ago in part due to its inherently labile nature which made it difficult to measure prior to the recent metabolomic method of chemically trapping it for targeted mass spectrometry.[57]

Thus, much of 1,3 BPG's function comes from its formation into pgK modifications which have been identified across a diverse range of protein classes and are particularly enriched in or around the active sites of glycolytic enzymes. This modification acts as a covalent attachment that can affect protein structure, function, and cellular processes. One significant aspect of pgK modification is its ability to inhibit glycolytic enzyme activities in concert with respect to glucose input, thereby leading to a buildup of glycolytic intermediates and their redirection from bioenergetic metabolism into alternative biosynthetic pathways.

Importantly, as mentioned above, while this modification does not require enzyme catalysis to be installed as a PTM, it was demonstrated that the mechanism by which it is removed off proteins is enzymatic. Though it is not known which enzyme or enzymes are responsible for removal of pgK, among the likeliest enzymes responsible for this activity are Histone deacetylases (HDACs) and sirtuins (SIRTs), which are critical enzymes in the regulation of lysine acylation[58]. Though these deacetylases are predominantly studied in an epigenetic

context for their ability to selectively remove acetyl and other acyl groups from lysine residues on histones, they are also able to play this dynamic role on non-histone proteins, including those of transcriptional regulation, DNA damage repair, and metabolic pathways.[59] Whether they regulate the erasure of pgK modifications in the proteome, and whether this activity has functional consequences on cellular physiology and disease pathogenesis is an area of active study.

Intriguingly, the protein PARK7 (DJ-1), predominantly annotated to play a role in detoxification of MGO and redox stress response, has been observed to also be involved in mitigating damage caused by the reactive glycolytic intermediate 1,3-bisphosphoglycerate to amino groups on both proteins and metabolites through a tentative identification and characterization of 1,3 BPG undergoing an intramolecular attack to form a reactive cyclic 1,3 phosphoglycerate reactive intermediate that either undergoes spontaneous degradation into 3PG or cyclic 2,3 PG, forms phosphoglyceroyl adducts with proteins and metabolites, or is detoxified by PARK7[60]. PARK7's potentially pivotal role in counteracting the accumulation of 1,3-bisphosphoglycerate (1,3-BPG) on lysine residues may explain its high abundance across different cell types and species; underlying a universal need to for organisms to mediate the reactive byproducts of glycolysis. This tentatively identified mechanism may also imply a greater involvement of aberrant pgK signaling in the pathogenesis of neurodegenerative diseases like Parkinson's disease.

Another potentially relevant context for pgK modification lies in erythrocytes. As a key intermediate in the glycolytic pathway, 1,3-BPG facilitates the generation of ATP in erythrocytes, which are devoid of mitochondria and reliant on anaerobic glycolysis for energy. Crucially, the

product of 1,3-BPG and BPGM: 2,3 BPG is known to modulate oxygen delivery by allosterically binding to hemoglobin, reducing its affinity for oxygen, and thus promoting efficient oxygen release in tissues. Prior studies have further mapped glycerate modifications to lysine residues on hemoglobin[60], including pgK modifications within the hemoglobin tetramer. This data shows differential lifespan of pgK modifications dependent upon whether lysines are solvent exposed and accessible by phosphatases and hints at a potential role for relatively 'longer-lived' active site located pgK in regulating oxygen binding to hemoglobin in addition to the traditional allosteric regulation model.

Despite research showing that pgK modifications are dynamic and reversible, most sites in the proteome that are pgKylated remain yet to be functionally uncharacterized. However, the conserved intrinsic nature of pgK modifications in both fundamental biology underscore the need to discover the molecular identify of the enzyme(s) responsible for removing and regulating this rmPTM. Moreover, changes in glycolytic flux and intracellular glucose concentrations are common hallmarks of diseases beyond neurodegenerative diseases such as cancer and diabetes. The aberrant labeling of pgK modifications in these diseases are also of importance to study to determine whether pgK plays a role in the onset or progression of these diseases, and whether dietary or pharmacologic interventions to modulate reactive central metabolites such as 1,3 BPG should be explored as potential avenues of disease therapy or prevention.

1.5. Methylglyoxal (MGO)

Methylglyoxal (MGO), a reactive byproduct of glycolysis, is generated through non-enzymatic breakdown of triose phosphates glyceraldehyde phosphate (GAP), and dihydroxyacetone phosphate (DHAP). This alpha-dicarbonyl compound demonstrates remarkable reactivity, readily forming covalent bonds with diverse biomolecules, including lipids, nucleic acids, and proteins. Buildup of these modifications results in various stress responses including heat shock, unfolded protein, antioxidant, and DNA damage responses.[61] MGO induces various post-translational modifications (PTMs) on amino acids such as arginine, lysine, and cysteine. Initially, MGO forms hemiaminals and hemithioacetals with these residues, which gradually stabilize into advanced glycation end-products (AGEs), including prominent hydroimidazolone modifications on arginine (MG-H1, MG-H2, and the less stable MG-H3).[62, 63] Other arginine modifications by MGO encompass argpyrimidine, tetrahydropyrimidine (THP), and carboxyethyl-arginine (CEA).[64] Lysine residues are also susceptible to MGO-induced modifications, like carboxyethyl-lysine[65], and recent findings have shown MGO-derived lactoyl-glutathione reacting non-enzymatically with lysine to form D-lactoyl-lysine.[66]

Furthermore, MGO is capable of creating covalent crosslinks between amino acids (Figure 1.6), evidenced by MODIC (arginine to lysine) and MOLD (lysine to lysine) crosslinks.[67, 68] A novel MGO-derived crosslink named MICA (mercapto-methylimidazole crosslink of cysteine to arginine) which dimerizes two KEAP1 proteins between C151 and R135 has been identified by the Moellering lab,[31] which notably inhibits KEAP1 from degrading NRF2, thereby establishing a Glycolysis-NRF2 pathway feedback loop for regulating cellular MGO levels.

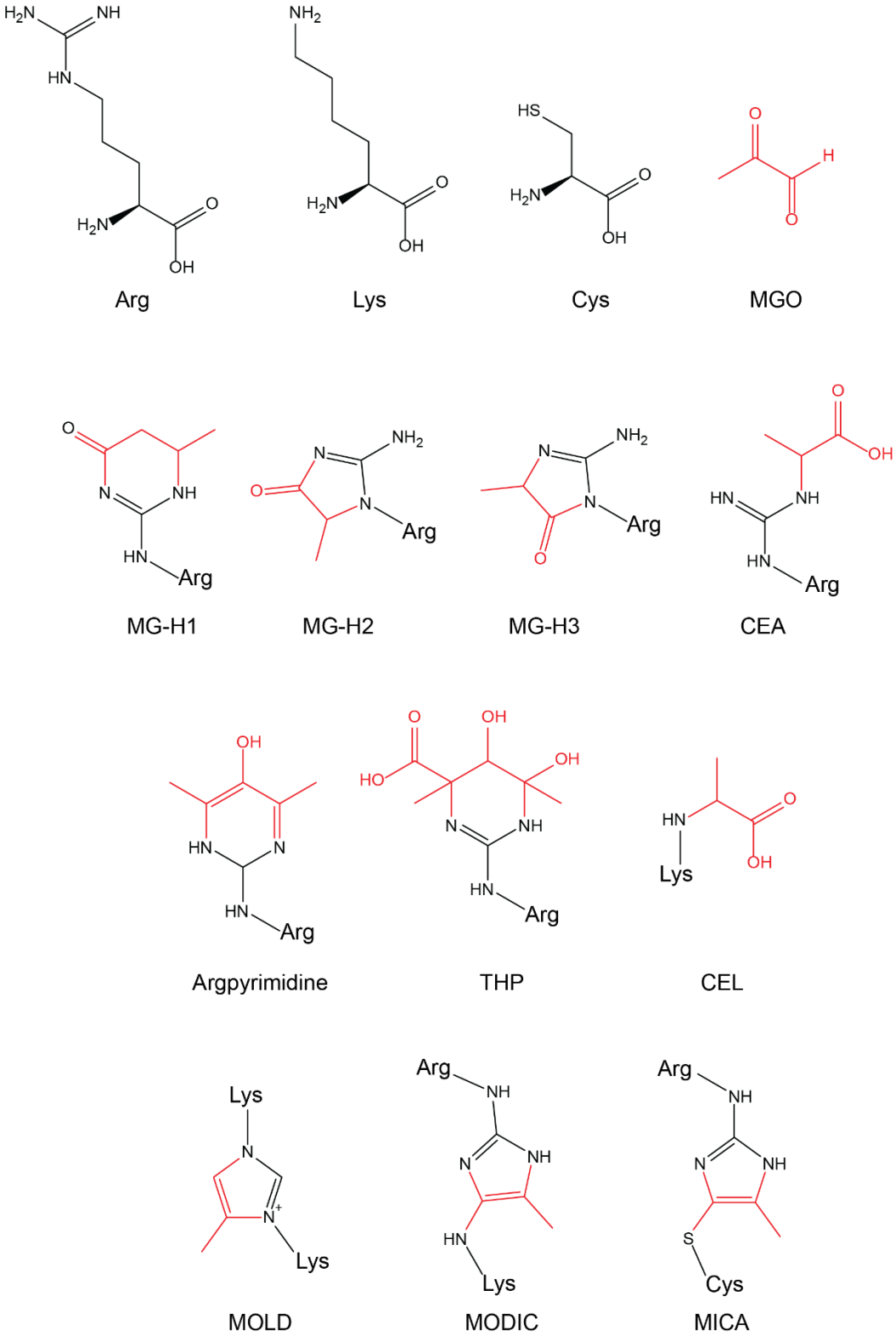

Figure 1.6 Representative MGO derived rmPTMs

KEAPl, a cysteine-rich sensor protein within cellular systems, plays a pivotal role in stress regulation by recognizing various reactive species.[69] Comprising 624 amino acids, human KEAPl is notable for its 27 cysteine residues, particularly those like C151, C273, and C288, which are uniquely responsive to electrophilic molecules in cells. These sensitive residues are instrumental in dictating KEAPl's conformations and actions. KEAPl typically exists as a non-covalent homodimer in the cytosol, with its KELCH repeats domain interacting with NRF2, a crucial transcription factor. Functioning as a BTB family protein, KEAPl forms an E3-ubiquitin ligase complex with Cullin3 and RBX1. Its primary function in the KEAPl-NRF2 signaling pathway involves regulating cellular NRF2 levels through NRF2 ubiquitination and subsequent proteolytic degradation under normal conditions. However, in response to increased levels of chemical stressors, covalent modifications of KEAPl's cysteine thiol sensor residues by reactive species trigger the activation of the KEAPl-NRF2 pathway. This activation leads to NRF2 accumulation, its translocation into the nucleus, and the formation of a heterodimer with small MAF proteins. Consequently, NRF2 activates genes responsible for expressing antioxidant-responsive elements (AREs), thus providing cyto-protection via mechanisms such as glutathione production, reduction of cellular ROS, detoxification of xenobiotics, and expression of drug transporters. The KEAPl-NRF2 pathway is therefore a critical regulator in maintaining cellular homeostasis, both under normal and deregulated metabolic states.

Specifically, the detoxification of MGO is predominantly mediated by the NRF2-ARE regulated glyoxalase system,[61] consisting of GLO1 and GLO2 enzymes. MGO initially reacts with reduced glutathione to form a reversible hemi-thioacetal, which GLO2 converts into lactoyl- glutathione. GLO2 further hydrolyzes this compound, producing D-lactate and recycling

glutathione. GLO1, evolutionarily conserved across species, has been associated to play important roles in various diseases including cancer,[70, 71] diabetes, cardiovascular diseases, and aging. Studies have shown that modulating GLO1 expression in organisms like C. elegans can significantly impact lifespan.[72, 73] Beyond the animal kingdom, plants possess a dozen or more genes corresponding to glyoxalase proteins (GLYI, GLYII, GLYIII).[74] While GLYI and GLYII operate in concert in a similar manner as GLO1 and 2 in animals, GLYIII[75] has been proposed to be an alternative single step, GSH independent means of MGO detoxification. Though the glyoxalases in plants have been thought to detoxify MGO accumulation over the course of light-based sugar metabolism and maintain homeostasis, there have been additional roles discovered for individual glyoxalases.[76, 77] For example, GLYI expression has been found to be critical in plant reproduction, where successful pollination and germination rely upon rapid formation of pollen tubes which in turn rely on an intense glycolytic burst and intense detoxification of MGO byproducts. Moreover, it has been speculated that the emergence of glyoxalases as a multi-membered family in plant families are a result of the loss of motility in plants over the course of evolution. Under high light or CO_2 conditions, plants undergoing high levels of light metabolism and consequently high levels of MGO dicarbonyl stress do not have the option of relocating themselves to lower stress environments. To prevent the emergence of 'plant diabetes', plants instead evolved multiple redundant means by which to detoxify excess levels of MGO.[74] At a global metabolic level, the utilization of triose-phosphates,[78-80] from which MGO is derived, is commonly used as a measure of theoretical maximal photosynthetic capacity for phototrophs and reflects the uptake and distribution of carbon between the Calvin-Benson cycle, glycolysis, respiration, and the production of sugars based on phosphate group exchange with respect to a

given plant species under measured environmental conditions (light, CO_2, temperature, nitrogen availability, soil composition, etc.). Despite a lack of consensus over how to best design a robust quantitative model for triose-phosphate utilization due to the sheer number of variables needed to account for diverse environmental factors, the need to understand and measure carbon metabolism in plants continues to be of critical importance in phytology. The unique position of triose-phosphates at the nexus of major metabolic processes[81] may help explain why the expression of GLY proteins have been linked to a wide variety of vital processes in plants including aging, cell death, seed germination and viability, cell division, and differentiation. These studies collectively suggest that there are tissue specific, diverse molecular mechanisms beyond MGO detoxification still yet to be discovered for glyoxalases.

In addition to the glyoxalase system, the PARK7 gene-encoded protein DJ-1 has emerged as a GSH independent means of MGO detoxification.[82, 83] The exact mechanism of DJ-1's action, whether as a glyoxalase or a deglycase complementary to the glyoxalase pathway, remains a topic of ongoing research and debate. [84-87] Its mutant genotype is linked to familial Parkinson's diseases, and it has been the focus of studies into its potential role as a critical regulator in other neurodegenerative diseases like Alzheimer's and Huntington's. Moreover, it has been noted to be upregulated in a variety of cancers, linking it to the induction or tumor progression as well as subsequent tumor initiation, proliferation, metastasis, recurrence, and chemotherapy resistance as well as immuno-modulation. [88] However, its proposed role in diseased phenotypes and the mechanism(s) by which it causes these disease phenotypes are myriad. For example, DJ-1 has been proposed as a regulator of MGO induced histone modifications/glycation damage, notably on canonical histone regulatory sites of H2B, H3, and H4 which overlap or are adjacent with

sites of acetylation and ubiquitylation resulting in the disruption of nucleosome stability itself (H2BK120, H3K56, H3R53, H3R8) or preventing the binding of writers and erasers such as DOT1L (H3K79), AF9, and KDM4A (H3R8, H3R26).[89, 90] In addition, DJ-1 has been proposed to act as a oxidative sensor in the cytosol and mitochondria similar to KEAP1, using its conserved solvent exposed C106 site to sense and detoxify radical oxygen species[91] by predominantly through promoting expression and stability of superoxide radical detoxification enzyme SOD1.[92, 93] Additional putative antioxidant and cell stress preventative mechanisms of DJ-1 include acting as a transcriptional activator of mitochondrial uncoupling proteins[94] and a regulator of the NRF2-KEAP1 pathway[95-97] as well as a variety of other diverse, often inconsistent, functions[98] that are difficult to uncouple from MGO induced cellular stress and the direct interaction of MGO with the NRF2-KEAP1 response. [31] As such, understanding the mechanism of DJ-1, the pathway(s) it regulates, and how they contribute to disease pathogenesis continues to be an area of major study.

Though the primary MGO detoxification pathway is primarily thought to be the glyoxalase pathway, other proteins linked to methylglyoxal detoxification and regulation include arginine deiminase 1, which has been observed to PAD4[99] may prevent or reverse MGO-induced modifications on arginine on histones. Additionally, members of the aldo-keto reductase family as well as aldehyde dehydrogenases have been observed to be able to detoxify MGO.[100]

MGO and AGE levels, elevated in conditions like diabetes, metabolic disorders, and cancer, are of significant concern. In cancer, high MGO levels, resulting from increased glucose metabolism and oxidative stress, lead to aberrant protein and DNA modifications, contributing to

cellular dysfunction, genomic instability, and resistance to therapy. In diabetes, elevated serum MGO levels cause widespread protein damage, contributing to various complications.

Beyond its damaging roles, specific MGO modifications can confer protective effects, such as activating the KEAP1-NRF2 pathway against oxidative stress. MGO's hormetic effects in diseases like cancer and aging are also notable,[101, 102] where low levels can induce protective cellular responses, while high levels exacerbate disease progression. Additionally, MGO's ability to modify histones, affecting gene expression, adds another layer to its biological significance. Ongoing research aims to unravel the detailed mechanisms of MGO's influence in cellular homeostasis, disease progression, and potential therapeutic strategies.

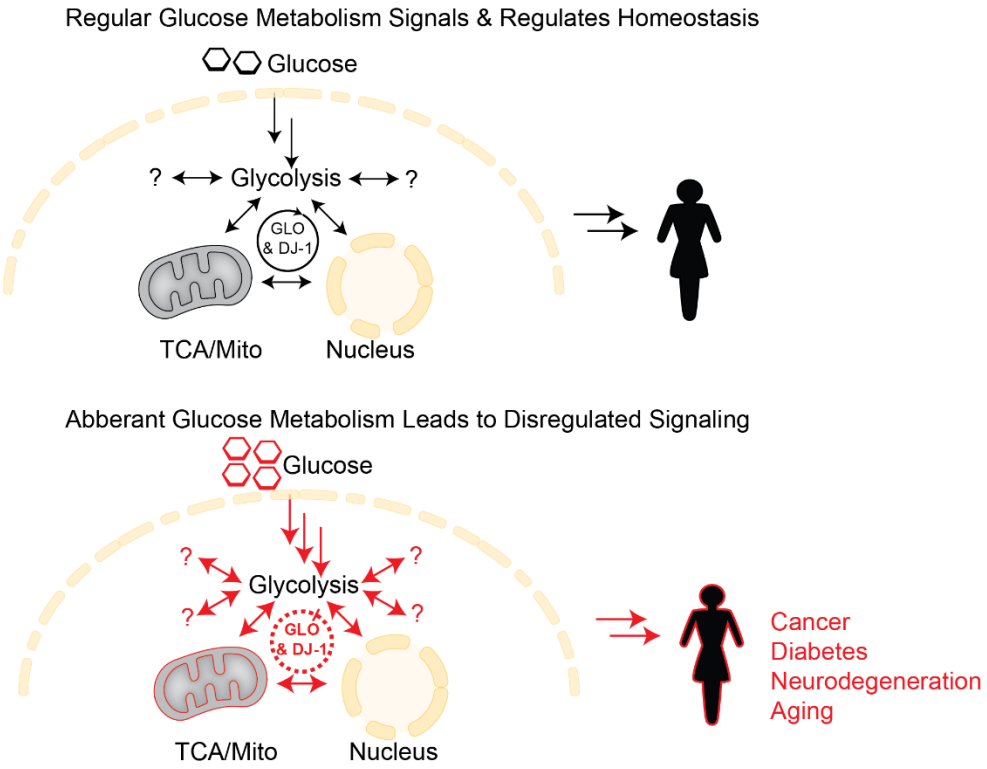

Figure 1.7 Regular versus Aberrant Metabolic Signaling
Glycolytic influx is utilized by cells for bioenergetics, biosynthesis, and rmPTM signaling. (top) Aberrant glycolysis (bottom) results in aberrant rmPTM signaling and is associated with disease initiation and progression.

1.6. Detoxification and Regulation of Redox Stress in Cancers

Glutathione, among the most well studied reactive metabolites, acts to detoxify other reactive metabolites. This serves as the most pivotal and intricate facet of cellular defense mechanisms, assuming paramount importance in orchestrating the neutralization and elimination of a diverse array of reactive organic species and reactive oxygen species, which can inflict extensive cellular damage to proteins, lipids, nucleic acids, and other metabolites, precipitate genomic mutations, and foster an environment conducive to pathogenesis.[103]

At the heart of glutathione detoxification lies the tripeptide thiol molecule glutathione (GSH), an indispensable intracellular redox buffer and antioxidant, revered for its versatile and potent properties in counteracting oxidative and chemical stressors. In cancer cells, this pathway assumes a pivotal role in averting the deleterious consequences of heightened oxidative stress, which often accompanies the rapid and aberrant proliferation of malignant cells.[104]

One of the primary functions of the glutathione detoxification system is the quenching of reactive oxygen species, which includes superoxide anions, hydroxyl radicals, and hydrogen peroxide. These highly reactive species can inflict oxidative damage upon cellular macromolecules, including lipids,[105] proteins,[106] and nucleic acids,[107] thereby driving genomic instability and mutagenesis. Glutathione, serving as a potent antioxidant, participates in a redox cycle orchestrated by glutathione peroxidases (GPXs), wherein it reduces hydrogen peroxide to water and lipid peroxides to their respective alcohols. This reaction not only shields critical cellular components from oxidative damage but also converts GSH into its oxidized form, glutathione disulfide (GSSG). Furthermore, glutathione (GSH) serves as a co-factor for enzymes, notably glutathione S-transferases (GSTs), which play a critical role in conjugating xenobiotics

and carcinogens with GSH. This conjugation process renders these harmful compounds less toxic and expedites their removal from the cell. The regulation of GSH/GSSG ratio is therefore pivotal to maintain redox homeostasis, as aberrations in this balance can trigger cellular dysfunction and drive pathogenic processes. Similarly, in oncological contexts, the same detoxification processes remain pivotal in maintaining redox homeostasis and survival of cells which are dysfunctional.[108]

Furthermore, glutathione detoxification plays a critical role in the elimination of electrophilic compounds and xenobiotics, as well as native reactive organic species such as methylglyoxal (MGO). These electrophilic species readily conjugate with GSH, forming stable GSH-conjugates that can be detoxified by various pathways or even excreted from the cell.[109] This detoxification process not only defends against exogenous carcinogens but also assists in the regulation of endogenously generated metabolites, allowing for complex feedback regulation of biochemical pathways based on metabolic flux whilst preventing cytotoxic damage.

These defenses are critically reliant on the biosynthesis of nicotinamide adenine dinucleotide phosphate (NADPH).[110] GSH reductase utilizes NADPH to convert oxidized glutathione (GSSG) back to its reduced form (GSH), which is a vital co-substrate for enzymes like glutathione peroxidase (GPX), responsible for reducing harmful compounds like hydrogen peroxide (H2O2) and other peroxides to non-toxic forms. Similarly, TRXR relies on NADPH as an electron donor to maintain the reduced form of thioredoxin (TRX), which helps in scavenging hydrogen peroxide and supports processes like DNA synthesis through the reduction of ribonucleotide reductase (RNR).

To support cellular levels of NADPH and/or in response to oxidative stress via the activation of the NRF2-ARE pathway, the Pentose Phosphate Pathway (PPP), branching off at the initial phase of glycolysis, stands as a primary contributor to cytosolic NADPH production through three irreversible steps in its oxidative branch. Research shows that enhanced glucose flux into this branch markedly elevates NADPH synthesis in various cancers. Key enzymes like Glucose-6-phosphate dehydrogenase (G6PD) and 6-phosphogluconate dehydrogenase (PGD) play pivotal roles in this process, with their activities notably upregulated in numerous cancer types, correlating with poor clinical outcomes and increased tumor growth and chemoresistance. G6PD, fluctuating between active and inactive states, initiates this pathway, while PGD's activity is crucial for NADPH production. Intriguingly, the homeostasis of NADPH is also maintained by posttranslational modifications of these enzymes, like glycosylation and deacetylation, enhancing G6PD activity, and phosphorylation enhancing PGD activity. Additionally, the regulation of G6PD is influenced by various signaling pathways in cancer, highlighting the complex interplay of metabolic and signaling networks in cancer pathophysiology.

Yet, other sources of NADPH production have been identified in cancer contexts.[111] Folate-mediated one-carbon metabolism, integral in the biosynthesis of nucleic acids and methionine, also plays a pivotal role in generating NADPH,[112] with serine and glycine as primary carbon sources. This pathway's activation, particularly through serine biosynthesis, is crucial for NADPH production in cancer cells. Key enzymes like Methylene tetrahydrofolate dehydrogenases (MTHFD1, MTHFD2, MTHFD2L) and 10-formyl-THF dehydrogenases (ALDH1L1, ALDH1L2) catalyze reactions essential for NADPH generation. MTHFD2, a central player in mitochondrial one-carbon unit production, is linked to cancer cell survival and

chemoresistance. Its expression correlates with poor prognosis in various cancers. Conversely, depleting these enzymes disrupts redox balance, sensitizing cells to oxidative stress and impeding cancer proliferation and metastasis.

Malic Enzymes (ME)[113, 114] serve as vital catalysts, bridging catabolic and anabolic pathways in cellular metabolism. These enzymes facilitate the oxidative decarboxylation of malate to pyruvate, thereby fostering NADPH production. The ME family encompasses three isoforms, each with distinct cellular localizations and cofactor requirements, contributing to NADPH production either directly or via the NNT-mediated transfer of hydride ions. Overexpression of ME1 is linked to poor cancer prognoses, regulating redox balance, and impacting cell survival mechanisms. ME2, similarly overexpressed in cancers, influences cell response to chemotherapy and cellular redox state. Intriguingly, ME2 and ME3 can compensate for each other's absence in certain cancer types, underscoring their potential as therapeutic targets in cancer treatment.

Isocitrate dehydrogenases (IDH)[115] play a pivotal role in cellular metabolism, particularly in the tricarboxylic acid (TCA) cycle, by catalyzing the oxidative decarboxylation of isocitrate to α-ketoglutarate, simultaneously generating NADPH. Among the IDH subtypes, IDH1 and IDH2, functioning within cytosolic, peroxisomal, and mitochondrial compartments, have garnered significant attention in cancer research due to their overexpression and correlation with poor prognoses in various malignancies. These enzymes not only contribute to the redox balance and macromolecular synthesis in tumor cells but also exhibit altered enzymatic activities and expression levels under stress conditions, impacting cancer cell survival and response to therapies. Furthermore, mutations in IDH1/2, leading to the abnormal production of the

oncometabolite 2-hydroxyglutarate, have opened new avenues for understanding carcinogenesis and therapeutic interventions.

Glutamine metabolism[116] also plays a crucial role in cancer cell physiology, acting as a key contributor to the TCA cycle and a nitrogen donor for various biosynthetic pathways including glutathione biosynthesis. In the context of rapid cancer cell proliferation, glutamine's role extends to NADPH production and ammonia generation. The process of glutaminolysis, primarily occurring in mitochondria, involves the conversion of glutamine to glutamate and subsequently to α-ketoglutarate, facilitating amino acid synthesis and replenishing TCA cycle intermediates. This metabolic pathway, especially the activity of glutamate dehydrogenases, is intricately linked to tumor progression, redox balance, and the adaptation of cancer cells to metabolic stress. The study of glutamine metabolism in cancer cells offers potential therapeutic targets, especially in tumors exhibiting distinct metabolic dependencies.

The fatty acid oxidation[117] (FAO) pathway plays a critical role in cancer metabolism, particularly under metabolic stress. It contributes to NADPH production, a key molecule in cancer cell survival and proliferation. FAO leads to the generation of NADH, FADH2, and acetyl-CoA, with the latter entering the TCA cycle to produce citrate. This citrate is then transported to the cytosol, where it aids in NADPH production via enzymes such as ME1 and IDH1. The pathway is regulated by key enzymes like carnitine palmitoyltransferases (CPTs) and is linked to cancer cell metastasis and chemoresistance. Additionally, the interplay between FAO and fatty acid synthesis (FAS) is crucial for tumor progression. The regulation of FAO by transcriptional coactivators and proteins like AMP-activated protein kinase (AMPK) underscores

its importance in maintaining redox balance and promoting cancer cell adaptation to oxidative and metabolic stress.

Furthermore, the importance of NADPH extends to being an essential electron donor and cofactor for numerous anabolic reactions though the concentration and distribution of NADP(H) within cells.[113] For example, NADPH provides reducing equivalents necessary for fatty acid synthase (FASN), a rate-limiting enzyme in fatty acid synthesis. It also plays a role in the assembly of iron-sulfur (Fe/S) proteins, contributing to non-essential amino acid biosynthesis, lipoic acid synthesis, tRNA modification, DNA replication and repair, and telomere maintenance. Moreover, NADPH is essential for dihydrofolate reductase (DHFR), which catalyzes the reduction of dihydrofolate to tetrahydrofolate (THF) in folate metabolism. THF is a critical precursor for the biosynthesis of thymidylate, purines, methionine, and certain amino acids. Additionally, NADPH acts as a reducing reagent for enzymes like 3-hydroxy-3-methylglutaryl-coenzyme A reductase (HMGCR), which is crucial for the synthesis of cholesterol and nonsterol isoprenoids. It also serves as a co-substrate for dihydropyrimidine dehydrogenase (DPYD), involved in the reduction of uracil and thymine. Furthermore, the activity of cytochrome P450 reductase (POR), an enzyme involved in the metabolism of drugs, xenobiotics, and steroid hormones, is dependent on NADPH. NADPH levels vary significantly among different tissues, reflecting its diverse roles in cellular physiology. As such, dysregulated maintenance, and regeneration of cellular NADP(H) itself is implicated in various pathologies, including cancer, where elevated NADPH levels are observed, supporting both redox defense and rapid cellular growth.

The intricate relationship between these enzymes and cancer progression underscores the importance of redox potential in cancer and their potential as therapeutic targets. To target and limit NADPH to modulate antioxidative and anabolic activities, a non-exhaustive list of current strategies to target this metabolic vulnerability include:

1. NADPH-synthesis Enzymes: Thionicotinamide (TN) derivatives like NADS and NADPS inhibit NADKs, impacting NADPH levels and potentially synergizing with chemotherapeutics in cancers like DLBCL and colon cancer.
2. PPP Enzymes: G6PD inhibitors include NADP+ analogs, 6-aminonicotinamide (6-AN), G6PD-i, and natural molecules like gallate-catechins. These compounds decrease NADPH availability and inhibit cancer cell growth.
3. Folate Metabolism Pathway: Inhibitors like DS18561882 and LY345899 target MTHFD2 and MTHFD2L, altering the cellular NADPH/NADP+ ratio and affecting tumor progression.
4. Glutamine Metabolism Pathway: Compounds like ebselen and epigallocatechin-3-gallate (EGCG) target GDH1, impacting cancer cell functions.
5. Anapleurotic Reactions: This includes targeting IDH1/2, ME1/2/3, and CPT1/2 with inhibitors like GSK864 (IDH1 inhibitor) and embonic acid (against ME2), which affect NADPH production and cancer cell viability.

Similarly, the targeting of GSH includes strategies such as:

1. Inhibitors of Glutathione Synthesis[118, 119]: Compounds like Buthionine sulfoximine (BSO) inhibit the enzyme glutathione synthetase, which is essential for glutathione

biosynthesis. Inhibiting this enzyme decreases the availability of glutathione within cancer cells, rendering them more susceptible to oxidative stress and DNA damage.

2. Depletion of Cysteine: Cysteine is a precursor required for glutathione synthesis. Limiting the availability of cysteine can hinder glutathione production, and this can be achieved through dietary restrictions or the use of drugs that target cysteine transporters such as erastin.
3. Stimulation of GSH efflux pumps: Cancer cells can develop resistance to chemotherapy drugs through various mechanisms, including the overexpression of drug efflux pumps that actively pump out drugs from the cell, reducing their effectiveness. Moreover, high levels of glutathione can help cancer cells defend themselves against oxidative stress and detoxify chemotherapy drugs, contributing to drug resistance. Lowering intracellular glutathione levels through the stimulation of efflux pumps can sensitize cancer cells to chemotherapy, making them more vulnerable to treatment.

On the other hand, strategies to reduce oxidative stress and ameliorate oxidative stress include:

1. Superoxide Dismutase (SOD) Mimics: These compounds are designed to mimic the action of SOD, an enzyme that catalyzes the dismutation of superoxide radicals ($O_2^{\bullet -}$) into less harmful molecules. They are especially effective in extracellular spaces where natural SOD levels are low. Examples include metalloporphyrins, Mn cyclic polyamines, and nitroxides.

2. Glutathione Peroxidase (GPX) Mimics: These mimic the function of GPX, an enzyme that reduces hydrogen peroxide and lipid hydroperoxides. Ebselen is a notable example, known for its broad substrate specificity.
3. NRF2 Activation: This strategy focuses on activating the NRF2 pathway to increase the production of antioxidant enzymes primarily either through blockage of KEAP1 or induction of NRF2 nuclear translocation and activation of the ARE. NRF2 activators are largely phytochemicals directly or synthetically derived from many fruits and vegetables and include sulforaphane, bardoxolone methyl, curcumin, and resveratrol.
4. Chelation Therapy: Used primarily for managing iron overload in certain medical conditions, this approach involves the use of chelating agents to bind excess metal ions that can contribute to oxidative damage.
5. NADPH Oxidase Inhibition: Targeting NADPH oxidase enzymes that contribute to oxidative stress, this approach aims to reduce the production of reactive oxygen species.
6. Dietary Antioxidants: Includes the use of vitamins and other dietary supplements to bolster the body's natural antioxidant defenses. Common examples are vitamins C and E or water-soluble analogues.
7. Mitochondrial Antioxidant Defense: Focusing on protecting the mitochondria from oxidative damage by targeting specific mitochondrial processes or using targeted antioxidants.

Yet, despite how integral a role oxidative stress plays in many diseases, it still presents a complex challenge to target for therapeutic antioxidant strategies. Although enhancing antioxidant defenses offers potential, its effectiveness is often curtailed when oxidative stress is secondary to other disease factors, such as driver mutations (oncogenes, tumor suppressors, genetic instability, chromosomal translocations, etc.). Moreover, the role of oxidative stress is highly context dependent. As an example, NRF2-dependent expression of antioxidant enzymes may simultaneously be cytoprotective and tumor suppressive in healthy cells, but also tumorigenic in cancerous cells by limiting oxidative damage. Thus, this intricate landscape underscores the need for greater understanding of the biological coverage and function of reactive species and redox balance within a cell to make rational, informed strategies when developing antioxidant therapies.

In summary, redox stress regulation emerges as an integral and multifaceted cellular mechanism, wherein it exerts its influence by quelling oxidative stress, neutralizing harmful electrophiles, coupling numerous anabolic reactions, and maintaining cellular metabolism, balancing detoxification processes with signaling feedback mechanisms. As such, understanding native communication networks facilitates a greater understanding of fundamental biology and how diverse pathways are coordinated together to maintain biological homeostasis whereas understanding how dysregulation of these vital mechanisms contributes to initiation and progression of diseases makes them attractive to study for development of therapeutic interventions.

1.7. Summary and Scope of the Dissertation

The focus of this dissertation is a series of vignettes centered around the study of glycolytic reactive metabolite post translational modifications (rmPTMs) signaling aimed at answering: To what extent does glycolytic rmPTM signaling regulate the biological kingdoms of life? Do they play distinct roles in different organisms? What are some pathways and mechanisms which are used to regulate central metabolic reactive metabolites and/or rmPTM signaling? What effects does perturbing the homeostasis of central rmPTM signaling have?

Chapter 2 outlines the materials and methods used for these studies.

Chapter 3 examines the question of how evolutionarily conserved is the rmPTM pgK in the evolutionary timeline of life and how central reactive glycolytic metabolite signaling is used within a cyanobacteria model.

Chapter 4 examines in-depth the mechanism used by the protein PARK7 to detoxify methylglyoxal under physiological conditions. In addition, it will outline unpublished preliminary data demonstrating how glyceryl-lysine is specifically deacylated by HDAC3 and discuss future directions.

Chapter 5 elucidates the differential response of cancer cells to central glycolytic perturbation under acute, intermediate, and chronic conditions.

Chapter 6 will provide future directions collectively for all the chapters of this dissertation.

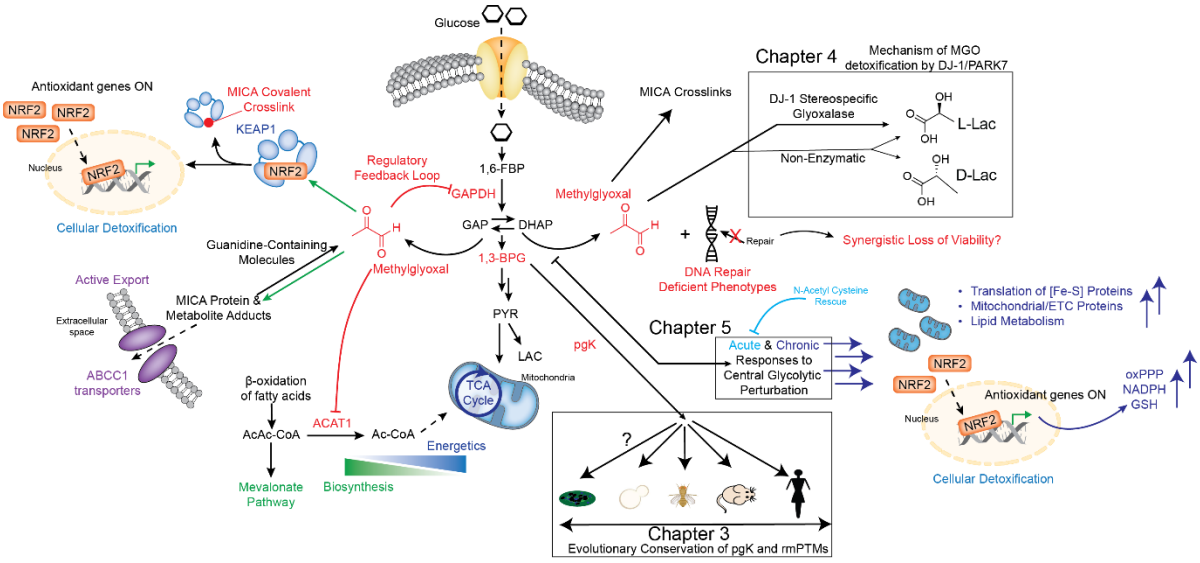

Figure 1.8 Simplified schematic of glycolytic reactive metabolite post translational modification (rmPTMs) signaling pathways.
Landscape of glycolytic rmPTM signaling and regulation network pathways covered within this dissertation with respect to each other.

CHAPTER 2. MATERIALS AND METHODS

Materials and Methods for Chapter 3: Ancient, circadian phosphoglyceryl-lysine modifications respond to and regulate metabolism in cyanobacteria.

2.3.1 Cyanobacterial Cell Culture

The S. elongatus PCC 7942 strain wild-type was grown in triplicate in BG-11M media [120] with shaking at 175 rpm in a Percival incubator under constant light (intensity of approximately ~100 µmol photons m−2 s −1 using cool white fluorescent bulbs), where each 250 mL flask contained 100 mL culture volume. When a high density (OD730 =1) was achieved, the culture was subjected to two 12:12 LD cycles. After synchronization, the sample was subsequently harvested every 6 hours across a 24 h period. Sample amounts were normalized via OD 730 nm. quantification.

2.3.2 Cyanobacterial Phosphopeptide Enrichment and TMT Labeling

The major fraction of lyophilized peptides (95%) was re-dissolved in 28.5% lactic acid (Sigma- Aldrich), 57% acetonitrile (LC-MS grade, Sigma-Aldrich), 0.28% TFA (Sigma-Aldrich), and applied to TiO2 spin tips (88303, Thermo Pierce) for phosphopeptide enrichment according to manufacturer's protocol. Eluted phosphopeptides were acidified with formic acid (pH 2-3), desalted using ZipTip C18 tips (100 µL, Millipore), and lyophilized. The two sets of peptides (phospho-enriched and unenriched) were separately labeled with 10-plex isobaric tandem mass tags (90406, Thermo Scientific) according to manufacturer's protocol with slight modification. TMT reagents were reconstituted to 8 mg/mL in anhydrous acetonitrile (Sigma-Aldrich) and added to lyophilized peptides dissolved in 100 µL of 200 mM HEPES buffer, pH 8.0 (~8:1

reagent/peptide ratio). Labeling reaction was carried out at room temperature for 1 hour with gentle shaking and quenched with 5 µL of 5% hydroxylamine (Thermo Scientific). Labeled peptides were combined into a single pool per experiment, acidified with formic acid (pH 2-3), desalted using ZipTip C18 tips (100 µL, Millipore), and lyophilized. The final processed peptides were dissolved in LC-MS/MS Buffer A (H2O with 0.1% formic acid, LC-MS grade, Sigma-Aldrich) for LC-MS/MS analysis.

2.3.3 Cyanobacterial Proteomic LC-MS/MS and Data Analysis

LC-MS/MS experiments were performed with an Easy-nLC 1000 ultra-high pressure LC system (ThermoFisher) using a PepMap RSLC C18 column (75 µm x 50 cm; 3 µm, 100 A, Thermo Scientific) heated to 40°C coupled to a Q Exactive HF orbitrap and Easy-Spray nanosource (ThermoFisher). TMT-labeled digested peptides in MS/MS Buffer A were injected onto the column and separated using the following gradient of buffer B (0.1% Formic acid acetonitrile) at 300 nL/min: 0-10% buffer B in 5 minutes, 10-40% buffer B in 240 minutes, 40-90% buffer B over 6 minutes, and hold at 90% for 20mins. MS/MS spectra were collected from 0 to 250 minutes using a data-dependent, top-10 ion setting with the following settings: full MS scans were acquired at a resolution of 120,000, scan range of 375-1500 m/z, maximum IT of 60 ms, AGC target of 1e6, and data collection in profile mode. MS2 scans was performed by HCD fragmentation with a resolution of 60,000, AGC target of 1e5, maximum IT of 60 ms, NCE of 30, and data type in centroid mode. Isolation window for precursor ions was set to 1.0 m/z with an underfill ratio of 0.5%. Peptides with charge state 1 and undefined were excluded and dynamic exclusion was set to 20 seconds. Furthermore, S-lens RF level was set to 60 with a spray voltage value of 2.60kV and ionization chamber temperature of 300°C.

MS2 files were generated and searched using the ProLuCID algorithm in the Integrated Proteomics Pipeline (IP2) software platform. Cyanobacteria *Synechococcus elongatus* (strain ATCC 33912 / PCC 7942 / FACHB-805) proteome data were searched using a concatenated target/decoy UniProt database (https://www.uniprot.org/taxonomy/1140). Basic searches were performed with the following search parameters: HCD fragmentation method; monoisotopic precursor ions; high resolution mode (3 isotopic peaks); precursor mass range 600-6,000 and initial fragment tolerance at 600 p.p.m.; enzyme cleavage specificity at C-terminal lysine and arginine residues with 3 missed cleavage sites permitted; static modification of +57.02146 on cysteine (carboxyamidomethylation), +229.1629 on N-terminal and lysine for TMT-10-plex tag; 4 total differential modification sites per peptide, including oxidized methionine (+15.9949), phosphorylation (+79.9663) on serine, threonine, and tyrosine (only for phospho-enriched samples), and phosphoglyceryl (+167.98238) on lysine (only for phospho-enriched samples); primary scoring type by XCorr and secondary by Zscore; minimum peptide length of six residues with a candidate peptide threshold of 500. A minimum of one peptide per protein and half-tryptic peptide specificity were required. Starting statistics were performed with a mass cutoff = 10 p.p.m. with modstat, and trypstat settings. False-discovery rates of peptide (sfp) were set to 1%. TMT quantification was peformed using the isobaric labeling 10-plex labeling algorithm, with a mass tolerance of 5.0 p.p.m. or less in cases where co-eluting peptide interfere. Reporter ions 126.127726, 127.124761, 127.131081, 128.128116, 128.134436, 129.131417, 129.13779, 130.134825, 130.141145, and 131.13838 were used for relative quantification. In general, all quantified peptides have mass error within 3 p.p.m.

2.3.4 Modification Site Localization Analysis

Phosphorylation site localization analysis was performed using the LuciPHOR algorithm available on the Integrated Proteomics Pipeline (IP2). A global FDR score was calculated for every detected phosphopeptide from each MS run. Phosphosites, and therefore phosphomodiforms, were included in the dataset only if they satisfied a global FDR localization score of < 0.01.

2.3.5 Cyanobacteria Full Scan Metabolomics Sample Preparation

Protocol input amount, filtration, and extraction were amalgamated from previously established workflows[121-123]. Bacterial cultures were filtered through a 0.45 µm nylon filter (Sigma Z290815) and the filters were immediately quenched in conical tubes with 2 mL ice cold 40/40/20 MetOH/ACN/Water, briefly vortexed, then rapidly snap frozen on dry ice. The following day, samples were vortexed (30 sec), sonicated in an ice bath (2 min), thermomixed at 4°C (5 min). Samples were then given a 20 min incubation on ice, before they were centrifuged at max rcf for 25 min, and then dried on speed-vac. For resuspension, dried samples were resuspended in 150 µL 60/40 ACN/Water, and then vortexed, sonicated, thermomixed, and incubated on ice as was done above. After another centrifugation at max rcf for 25 min, 50 µL of the sample was used for LC-MS/MS analysis, with the remainder pooled for protein quantification control.

2.3.6 Cyanobacteria Full Scan Metabolomics

Metabolite separation was performed in the UChicago Medicine Comprehensive Cancer Center Metabolomics Platform using a Thermo Scientific Vanquish Horizon UHPLC system and XBridge BEH amide 2.5 µm (2.1x150 mm Column XP, Waters Corporation, MA) under acidic

conditions. Mobile phase A (MPA) was 90/5/5 water/acetonitrile/methanol, 20 mM ammonium acetate, 0.2% acetic acid and mobile phase B (MPB) was 90/10 acetonitrile/water, 10 mM ammonium acetate, 0.2% acetic acid. The column temperature was 40°C, flow rate was 0.3 mL/min, and injection volume was 5 µL. The chromatographic gradient was: 0min: 95% B, 9min: 70% B, 9.75min: 40% B, 12min: 40% B, 13min: 30% B, 14min: 30%B, 14.1min: 10% B, 17min: 10% B, 17.5min: 95% B, 22min: 95% B. An Orbitrap IQ-X Tribrid mass spectrometer (Thermo Scientific) with a H-ESI probe operating in negative polarity was utilized for MS detection using the following parameters: Acquisition range of 70-1000 m/z at 60K resolution, spray voltage: 2800V, sheath gas flow: 40, aux gas flow: 7, sweep gas flow: 1, AGC target: 100, maximum injection time: 118 ms, capillary temperature: 250°C, RF level: 60 and aux gas heater temperature: 350°C. Data acquisition was done using the Xcalibur software (Thermo Scientific) and data analysis was performed using Tracefinder 5.1 software (ThermoScientific). Specific metabolite information is found in Supplementary Table 3.1 in the addendum.

2.3.7 Cyanobacteria Targeted Metabolomics

For targeted metabolite profiling experiments, cells were grown and collected using the same protocol as above in Section 2.3.5. Dried metabolites were dried metabolites resuspended in 50 µl of 60/40 MeOH/H2O for analysis on an Agilent triple quadrupole LC-MS/MS (Agilent Technologies 6460 QQQ). For negative mode operation, metabolites were separated by hydrophilic interaction chromatography with a Luna-NH2 column (Phenomenex) running mobile phase A (CH3CN supplemented with 0.2% NH4OH) and B (95:5 v/v H2O:CH3CN supplemented with 50 mM NH4OAc and 0.2% NH4OH) and the following gradient: 0% B for 3 min; linear increase to l00% B for 27 min at a flow rate of 0.4 ml/min, followed by an isocratic flow of l00% B for 3 min.

The spectrometer settings were: capillary voltage = 4.0 kV, drying gas temperature = 350oC at l0 L/min, and the nebulizer pressure was 45 psi. Metabolite peak transitions and specific MRM settings can be found on Supplementary Table 3.2 in the addendum.

2.3.8 Cyanobacteria Active Site Analysis

The UniProt PTM/ database was used to identify validated functional active sites. For putative sites of interest, cyanobacteria proteins from the UniProt database were input by accession number into the NCBI Conserved Domains Tool[124-126] found at: (https://www.ncbi.nlm.nih.gov/Structure/cdd/wrpsb.cgi), and searched under default settings to annotate putative active sites and protein domains conserved across species. To identify and predict whether PTM sites were proximal to any active or regulatory site and potentially regulatory for a given protein, the PDB crystal structure or AlphaFold predicted structure available in the UniProt database was visualized using the UCSF ChimeraXv1.1 molecular visualization software.

2.3.9 Gene Ontology Analysis

Gene Ontology analysis was performed by uploading lists of proteins containing the high-quality filtered peptide sites in each data set to the DAVID bioinformatics tool[127] (https://david.ncifcrf.gov/) and performing functional annotation analyses using the default settings.

Materials and Methods for Chapter 4: PARK7 Catalyzes Stereospecific Detoxification of Methylglyoxal Consistent with Glyoxalase not Deglycase Function

2.4.1 Chemicals

All reagents were from Sigma-Aldrich, and all bulk solvents were from Thermo Fisher Scientific unless otherwise stated.

2.4.2MG-alkyne synthesis

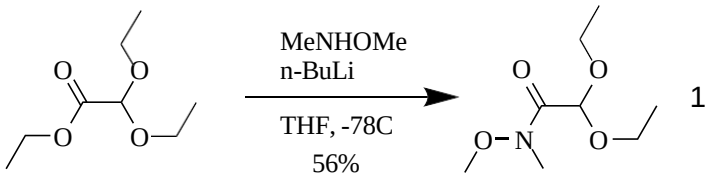

1

N,O-dimethylhydroxylamine (535 mg, 8.82 mmol) was dissolved in anhydrous THF (30 mL) under nitrogen and cooled to -78°C. n-Butyllithium (1.6 M in hexanes, 10.5 mL, 16.8 mmol) was added dropwise, then the solution was allowed to warm to r.t. and stir for 30 minutes. The reaction was again cooled to -78□C. Ethyl diethoxy-acetate (1.0 mL, 5.6 mmol) was added dropwise, and the reaction was warmed to r.t. and allowed to run for 3 hours. The reaction was quenched by the addition of saturated NH_4Cl solution (40 mL), extracted 3 times with ethyl ether, dried over $MgSO_4$, and concentrated in vacuo. The crude product **1** was purified by silica column (10% Et_2O in DCM), yielding a clear oil (600 mg, 56%): ^{1}H NMR ($CDCl_3$, 400 MHz) δ 5.30 (s, 1H), 3.75 (s, 3H), 3.72 (q, 4H, *J* = 5.0 Hz), 3.22 (s, 3H), 1.26 (t, 6H, *J* = 8.0 Hz).

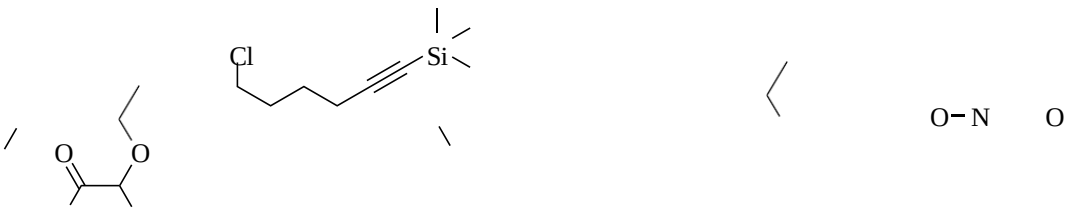

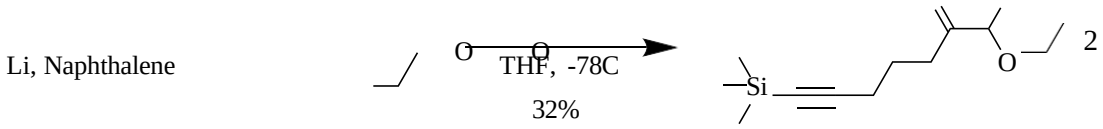

Napthalene (1.153 g, 9 mmol) and lithium metal (62.5 mg, 9 mmol) were added to anhydrous THF (30 mL) and sonicated at r.t. for 1 hour. The mixture was cooled to -78□C. (5-chloro-1- pentynyl)trimethylsilane (1.61 mL, 9 mmol) was added to anhydrous THF (15 mL) and then added to the reaction dropwise over the course of 30 minutes. The reaction was allowed to run for an additional 30 minutes and then the Weinreb amide starting material (575 mg, 3 mmol) was added dropwise and the reaction allowed to run for one hour. The reaction was quenched by the addition of saturated NH_4Cl solution (40 mL), extracted 3 times with ethyl ether, dried over $MgSO_4$, and concentrated in vacuo. The crude product **2** was purified by silica column (5% ethyl acetate in petroleum ether) yielding a clear oil (260 mg, 32%): ^{1}H NMR ($CDCl_3$, 400 MHz) δ 4.57 (s, 1H), 3.72-3.66 (m, 2H), 3.60-3.52 (m, 2H), 2.72 (t, 2H, *J* = 6.0), 2.27 (t, 2H, *J* = 8.0), 1.79 (tt, 2H, *J* = 8.0, 8.0), 1.26 (t, 6H, *J* = 8.0 Hz), 0.11 (s, 9H).

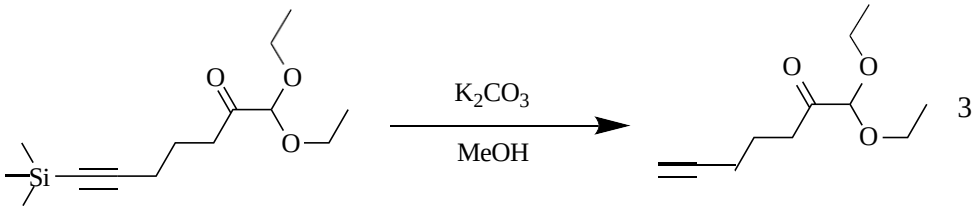

The starting material (125 mg, 0.46 mmol) and K_2CO_3 (380 mg, 2.76 mmol) were added to methanol (20 mL) and the reaction stirred at r.t. for 5 hours. The reaction was diluted with H_2O, extracted three times with DCM, washed once with H_2O, dried over $MgSO_4$, and concentrated in vacuo. The crude product **3** was purified by silica column (5% acetone in pentane) yielding a clear oil (90 mg, 98%): ^{1}H NMR ($CDCl_3$, 400 MHz) δ 4.57 (s, 1H), 3.74-3.66 (m, 2H), 3.60-3.53 (m, 2H), 2.74 (t, 2H, *J* = 6.0), 2.24 (dt, 2H, *J* = 4.0,6.0), 1.81 (tt, 2H, *J* = 8.0, 8.0), 1.25 (t, 6H, *J* = 8.0 Hz).

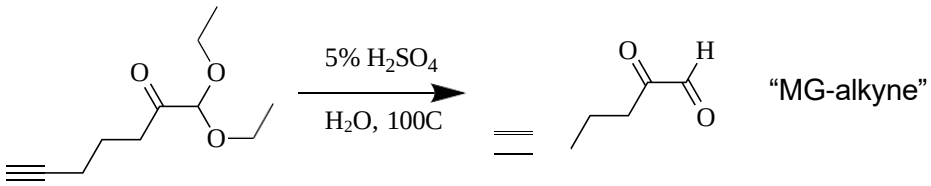

The starting material (34 mg, 0.17 mmol) was added to 1 mL of 5% H_2SO_4 solution and heated to a reflux for 1 hour. 10% NaOH solution (0.5 mL) was added to partially neutralize the reaction, then the reaction mixture was diluted with 50 mM sodium phosphate buffer pH 7.4. The probe solution was used as crude mixture without purification. Complete deprotection was confirmed by GC-MS (Supplementary Figure 4.2, theoretical m/z 125.05, observed 125.0). The deprotected product MG-alkyne was quantified as described below.

2.4.3 Methylglyoxal synthesis and distillation.

High purity MGO was prepared by acidic hydrolysis of MG-1,1-dimethylacetal followed by fractional distillation. Briefly, 6 mL of MG-1,1- dimethylacetal was added to 100 mL of 2.5%

(v/v) sulfuric acid and refluxed for 1 hour. The product was purified by fractional distillation under reduced pressure. The first fraction collected was discarded due to methanol impurity.

2.4.4 MGO and MG-alkyne quantification

MGO and MG-alkyne concentrations were quantified by colorimetric assay.[128, 129] Briefly, samples were diluted to below 2 mM concentration as needed and reacted with equal volume of 40 mM aminoguanidine in phosphate buffer for 5-6 hours at 37°C. Absorbance was measured at 320 nm and compared to a calibration curve generated by serial dilutions of 3-amino-1,2,4-triazine in phosphate buffer. MGO fractions were then diluted to 50 mM stock solutions using phosphate buffer and pH was confirmed to be 7.4. MGO stocks were stored at -80°C until use. Deprotected MG-alkyne was diluted 25 mM stock solutions using phosphate buffer and pH was confirmed to be 7.4. MG-alkyne stocks were stored at -80°C until use.

2.4.5 Cell culture

HEK293T cells were purchased from ATCC and were propagated in RPMI 1640 with 2 mM glutamine supplemented with 10% fetal bovine serum and 1% penicillin/streptomycin (Gibco).

2.4.6 Plasmids and cloning

The pDONR221-DJ-1 was generated by cloning a gene block purchased from Integrated DNA Technologies (IDT) containing the human *PARK7* (UniProt: Q99497) open reading frame into the pDONR221 plasmid. The pHAGE-CMV-C-Flag-HA-DJ-1 plasmid was generated via Gateway LR clonase (Thermo Fisher Scientific) reaction with the pDONR221-DJ-1 and pHAGE-CMV-C-Flag-HA-Puro plasmids.

2.4.7 Generation of stable cell lines

HEK-Flag-DJ-1 cells were generated by transducing HEK293T cells with the pHAGE-CMV-C-Flag-HA-DJ-1 plasmid. Briefly, lentiviruses were generated in HEK293T cells by transient transfection of pHAGE-CMV-C-Flag-HA-DJ-1 plasmid with pSPAX2 and pMD2.G packaging vectors (Addgene plasmids #11260 and #12259) using lipofectamine 2000 (Thermo Fisher Scientific). Viral supernatants were collected after 48 hours of expression, passed through a 45-µm syringe filter, and supplemented with 8 µg/mL of polybrene (hexadimethrine bromide) before exposure to target cells. Selection was performed with 2µg/mL puromycin.

2.4.8 Western blotting

Cells were washed with PBS buffer, collected by scraping in PBS buffer, resuspended in PBS buffer containing EDTA-free complete protease inhibitors (Roche), and sonicated (Fisher Scientific FB-505) for 15 seconds (30% amplitude, 1 second on, 1 second off). Insoluble debris was cleared by a 15-minute centrifugation at 16,000g and 4°C. Protein concentrations were normalized via BCA assay. The supernatant was diluted into 4x Laemmli buffer containing 100 mM βME. Samples were prepared for SDS-PAGE by heating to 95°C for 5 min, cooled to room temperature, resolved on a 10% or 15% SDS-PAGE gel depending on the proteins of interest, and transferred onto nitrocellulose membrane by standard western blotting methods. Membranes were blocked in 2% BSA in TBS containing 0.1% Tween-20 (TBST) and probed with primary and secondary antibodies. Antibodies used in this study include: anti-Flag- M2 (1:3000, F1804, Sigma Aldrich) and secondary donkey anti-mouse 680 (Licor,1:10,000). Blots were imaged on a Licor infrared scanner.

2.4.9 Rhodamine labeling and imaging

For in-gel fluorescence readout, 50 μL of MG-alkyne- treated sample was reacted with 1 μL of 50 mM CuSO4, 1 μL of 50 mM TCEP-HCl, 3 μL of 1.67 mM TBTA in 4:1 t-butanol/DMSO, and 1 μL of rhodamine-azide (1 mM stock in DMSO) at RT for 1 hour. The samples were diluted into 4x Laemmli buffer containing 100 mM βME. Samples were prepared for SDS-PAGE by heating to 95°C for 5 min, cooled to RT, resolved on a 10% SDS-PAGE gel, and imaged on a BioRad ChemiDoc MP Imager.

2.4.10 MG-alkyne in vitro dose response and competition samples

HEK293T cells were washed with PBS buffer, collected by scraping in PBS buffer, resuspended in PBS buffer containing EDTA-free complete protease inhibitors (Roche), and sonicated (Fisher Scientific FB-505) for 15 seconds (30% amplitude, 1 second on, 1 second off). Insoluble debris was cleared by a 15- minute centrifugation at 16,000g and 4°C. Protein concentrations were determined by Bradford assay, and samples were diluted to 2 mg/mL with PBS buffer containing EDTA-free complete protease inhibitors. Samples were treated for 2 hours with indicated concentrations of MGO at 37°C followed by 2-hour treatment with indicated concentrations of MG-alkyne at 37°C. Samples were subsequently rhodamine labeled for in gel-fluorescence imaging.

2.4.11 DJ-1 Flag purification.

HEK-Flag-DJ-1 cells were grown to confluence in a 10 cm dish then washed with PBS buffer, collected by scraping in PBS buffer, resuspended in PBS buffer containing EDTA-free complete protease inhibitors (Roche), and sonicated (Fisher Scientific FB- 505) for 15 seconds (30% amplitude, 1 second on, 1 second off). Insoluble debris was cleared by a 15-minute centrifugation

at 16,000g and 4°C. Lysates were incubated overnight at 4°C with pre-washed M2 anti-Flag affinity resin (Sigma Aldrich). The Flag resin was washed 5 times with 1 mL of PBS and then the Flag-DJ-1 protein was eluted from the resin by incubating it in 300 μL of PBS with 100 μg/mL 3xFlag peptide at r.t. for 1 hour. The resin was pelleted by centrifugation at 4000g for 2 minutes, and the supernatant containing the Flag-DJ-1 was kept for further experiments. Protein concentration was determined via Coomassie stain using a calibration curve with serial dilutions of BSA.

2.4.12 DJ-1 enzymatic assay

1 μg of recombinant DJ-1, BSA, or vehicle were added to 50 μL of 1 mM MGO or MG-alkyne in PBS and incubated for 24 hours at 37°C. Final MGO and MG-alkyne concentrations were determined as described above. For LC-MS/MS analysis of MG-alkyne enzymatic product, samples were acidified with 0.2% TFA, centrifuged at 16,000g for 3 minutes, and the supernatant kept. Data presented are representative of three independent experiments.

2.4.13 L- and D-Lactate enantiomer quantification

1 μg of recombinant DJ-1, BSA, or vehicle were added to 50 μL of 1 mM MGO in PBS and incubated at 37°C for 24 hours or for the indicated time points in the kinetic assay. For non-enzymatic conversion assays, 1 mM MGO was added to 50 μL of commercial cell culture grade PBS (Corning, 21-031-CV) or Milli-Q Ultra-pure water (Sigma) that was either used directly or first boiled at 100°C for 30 mins, de-gassed for 15 mins, and then cooled to room temp. Samples were then incubated at 37°C or kept on ice for 8 hours.

Following incubations, samples were then derivatized with (+)-*O,O'*-Diacetyl-L-tartaric anhydride (DATAN) and then analyzed by LC-MS/MS as previously described.[130] Briefly, samples

and L- and D- lactate standards were dried under N2 stream and then resuspended in 100 µL of 50 mg/mL DATAN in 4:1 vol/vol DCM/acetic acid solution and heated at 75°C for 30 min. Samples were then again dried under N2 stream and then resuspended in H2O for LC-MS/MS analysis.

Targeted MS/MS analyses were performed on an Agilent triple quadrupole LC-MS/MS instrument (Agilent Technologies 6460 QQQ) with 1290 UHPLC and 1260 nanoLC-Chip set to negative ion mode with a mass window of 50 to 1000 m/z. The capillary voltage was set to 4.0 kV. The drying gas temperature was 300°C, flow rate = 5 L/min, and nebulizer pressure = 45 psi. The mass spectrometer was run in MRM mode with precursor ion of 305, product ion of 89.1, MS1 resolution set to wide, MS2 resolution set to unit, dwell time of 100 ms, a fragmentor voltage of 100V, and collision energy of 14V. Chromatography was performed with an Acquity UPLC HSS T3 analytical column (2.1x100 mm, 1.8 µm, Waters) held to 40°C. Mobile phase A was composed of 125 mg/L ammonium formate in H2O adjusted to pH 3.5 with formic acid, and mobile phase B was composed of methanol. The instrument was run at 0.3 mL/min with the following gradient: 3% Buffer B (0-5 min); 3-80% Buffer B (5-5.5 min); 80% Buffer B (5.5-8 min); 80-5% Buffer B (8-8.5 min); 5% Buffer B (8.5-18.5 min). Relative abundance was quantified by integrated peak area.

2.4.14 Non-enzymatically produced lactate quantification by LC-MS/MS without DATAN derivatization.

50 µL of 1 mM MGO in PBS was incubated for 0-8 hours at 37°C. The reaction was then quenched in 80/20 methanol/water before being dried under N2 stream. The dried down samples were re-suspended in 60 µL of 60/40 acetonitrile/water, sonicated for 3 minutes, vortexed for 5 minutes at 4°C using an Eppendorf ThermoMixer, centrifuged at 20,000g for 15 minutes and the supernatant was transferred in LC-MS vial for analysis.

Metabolite separation was performed using a Thermo Scientific Vanquish Horizon UHPLC system and XBridge BEH amide 2.5 µm (2.1x150 mm Column XP, Waters Corporation, MA) under acidic conditions. Mobile phase A (MPA) was 90/5/5 water/acetonitrile/methanol, 20 mM ammonium acetate, 0.2% acetic acid and mobile phase B (MPB) was 90/10 acetonitrile/water, 10 mM ammonium acetate, 0.2% acetic acid. The column temperature was 40°C, flow rate was 0.3 mL/min, and injection volume was 5 µL. The chromatographic gradient was: 0min: 95% B, 9min: 70% B, 9.75min: 40% B, 12min: 40% B, 13min: 30% B, 14min: 30%B, 14.1min: 10% B, 17min: 10% B, 17.5min: 95% B, 22min: 95% B. An Orbitrap IQ-X Tribrid mass spectrometer (Thermo Scientific) with a H-ESI probe operating in negative polarity was utilized for MS detection using the following parameters: Acquisition range of 70-1000 m/z at 60K resolution, spray voltage: 2800V, sheath gas flow: 40, aux gas flow: 7, sweep gas flow: 1, AGC target: 100, maximum injection time: 118 ms, capillary temperature: 250°C, RF level: 60 and aux gas heater temperature: 350°C. Additionally, Selected Ion Monitoring (SIM) was utilized to collect high resolution fragmentation for lactate (m/z 89.0244) using the following parameters: isolation mode: quadrupole, isolation window (m/z): 0.8, normalized HCD collision energy: 30%, and detector type: orbitrap at 30K resolution. Data acquisition was done using the Xcalibur software (Thermo Scientific) and data analysis was performed using Tracefinder 5.1 software (Thermo Scientific). Lactate peak was confirmed by matching the retention time and MS/MS fragmentation (m/z 43.0185 fragment ion) to an in-house database generated using a reference standard.

2.4.15 LC-MS/MS analysis of DJ-1 MG-alkyne product

Samples were analyzed on an Agilent 6540 Q-TOF MS-MS with 1290 UHPLC and 1260 nanoLC-Chip set to positive ion mode with a mass window of 50 to 1000 m/z. The capillary voltage was set to 3.5 kV. The drying gas temperature was 300°C, the drying gas flow rate was 8

L/min, and the nebulizer pressure was 35 psi. The fragmentor voltage was set to 150 V. Chromatography was performed with a Phenomenex Gemini C18 column (50 x 4.6 mm, 5 μM) at a flow rate of 0.4 mL/min. Mobile phase A was composed of H2O supplemented with 0.1% TFA, and mobile phase B was composed CH3CN supplemented with 0.1% TFA. The instrument was run at 0.4 mL/min with the following gradient: 0% Buffer B (0-2 min); 0-60% Buffer B (2-7 min); 60-100% Buffer B (7-8 min); 100% Buffer B (8-10 min); 100-0% Buffer B (10-11 min); 0% Buffer B (11-13 min). Injection volume was 5 μL for all samples. Data presented are representative of three independent experiments.

2.4.16 DJ-1 glycation assay with BSA

1 μg of DJ-1 or vehicle were added to 100 μL of 1 mg/mL BSA and either 100 or 300 μM MG-alkyne. The reactions were incubated for 24 hours at 37°C and then labeled with rhodamine azide for gel-based analysis as described above. Densitometry measurements were performed with ImageJ software.

2.4.17 Membrane assay

1.1 mL of 1.36 mg/mL BSA in PBS was added to 1.7 mL microcentrifuge tubes. For the membrane containing conditions, a 0.5 mL Slide-A-Lyzer MINI dialysis device with 3.5 KDa cutoff (Thermo Fisher Scientific) was pre-wet and then added to the tube and rotated tight to ensure there were no air bubbles present between the solution and the dialysis membrane. 0.4 mL of PBS with or without 15 μg recombinant DJ-1 was added to each reaction followed by 6 μL of 25 mM MG-alkyne. The reactions were incubated for 24 hours at 37°C, samples containing 50 μg of BSA from each reaction were taken, and volumes were equalized across samples to 50 μL via the

addition of PBS as needed. Samples were labeled with rhodamine azide for gel-based analysis as described above. Densitometry measurements were performed with ImageJ software.

2.4.18 GC-MS analysis of MG-alkyne deprotection

Diethyl acetal-protected MG-alkyne and hydrolyzed MG-alkyne product were analyzed using an Agilent 5977A MSD with installed EI/CI ion source connected to an Agilent 7890B GC system with an Agilent 7693 autosampler. Samples were run using a 13-minute temperature gradient where temperature was held at 50^{o}C for 1 minute, followed by a linear increase to 250^{o}C over 5 minutes, and then held at 250^{o}C for 7 minutes an acquisition delay of 3.20 minutes was used to avoid the solvent front. Samples were analyzed in PCI mode with a scan range of 100 to 500 Da with a 0.1 m/z step size and 3.6 scans/second collected.

Materials and Methods for Follow Up Research Project: HDAC3 Contributes to Protein Quality Control as a Glyceryl-Lysine Eraser (Preliminary Results, Unpublished)

2.4.19 shRNA Knockdown and CRISPR-Knockout of HDAC3

The LentiCRISPR V2 plasmid (Addgene plasmid #52961) was a gift from Lucy Godley. HDAC3 KO gRNA were generated using CRISPR gRNA design tool CHOPCHOP (https://chopchop.cbu.uib.no/). Control and HDAC3 KO gRNA were generated by cloning forward and reverse primers (see Supplementary Table 4.1 in addendum) purchased from Integrated DNA Technologies (IDT) into the LentiCRISPR V2 plasmid backbone. Generation of HDAC3 KO stable cell lines HEK293T and HCT116 cells were generated by transducing HEK293T cells with HDAC3-KO1, HDAC3-KO2, and control-KO plasmids, respectively. Briefly, lentiviruses were generated in HEK293T cells by transient transfection of the above vectors with pSPAX2 and pMD2.G packaging vectors (Addgene plasmids #11260 and #12259) using lipofectamine 2000 (Thermo Fisher Scientific). Viral supernatants were collected after 48 hours of expression, passed through a 45-μm syringe filter, and supplemented with 8 μg/mL of polybrene (hexadimethrine bromide) before exposure to target cells. Selection was performed with 10 μg/mL blasticidin for all plasmids in all cell lines. Single clones were grown up and knock out confirmed via western blot. Each knock out cell line above was produced by pooling at least two clones together.

2.4.20 HDAC3 Western blotting

Western blotting protocol was done as per the protocol in section 2.4.8, using the HDAC3 antibody: Cell Signaling HDAC3 (D2O1K) Rabbit mAb #85057 as the primary antibody.

2.4.21 Generation of stable HDAC3 shRNA knockdown cells

The pLKO.1 puro plasmid (Addgene plasmid #8453) was a gift from Bryan Dickinson. The shHDAC3 shRNA sequences were purchased from Integrated DNA Technologies (IDT) and added into the pLKO.1 puro plasmid backbone (see Table 4.1 in addendum). Scramble plasmid refers to SHC002 (Sigma). Lentiviruses were generated in HEK293T cells by transient transfection of vectors with pSPAX2 and pMD2.G packaging vectors (Addgene plasmids #11260 and #12259) using lipofectamine 2000 (Thermo Fisher Scientific). Viral supernatants were collected after 48 hours of expression, passed through a 45-µm syringe filter, and supplemented with 8 µg/mL of polybrene (hexadimethrine bromide) before exposure to target cells. Selection was performed with 2 µg/mL puromycin.

2.4.22 Recombinant protein peptide assay

Purified recombinant human SIRT 1, 2, 3, 4, 5, 6, 7 and HDAC 3, 6, 8, 11 (Sigma-Aldrich) was incubated with 10 µL of 1 mM peptides AAKAAV, AAgKAAV, and AApgKAAV previously synthesized by Dr. John S. Coukos. (K = lysine, gK = glyceryl lysine, pgK = phosphoglyceryl-lysine, pictured below). in Tris assay buffer[131] for a total of 100 µL and incubated at 37°C for 4 hr. on a tabletop shaker.

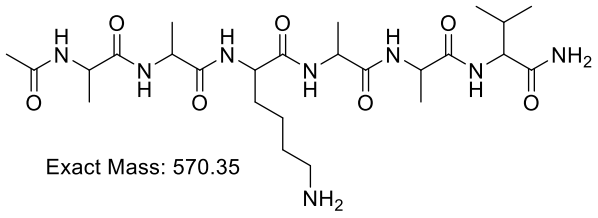

2.4.22 Recombinant protein peptide assay continued

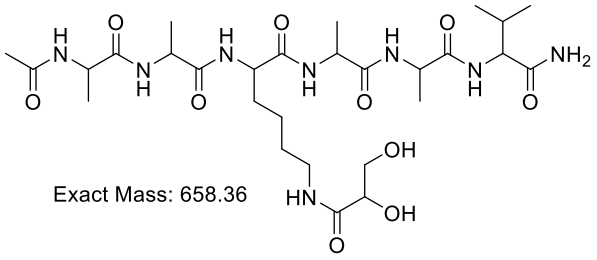

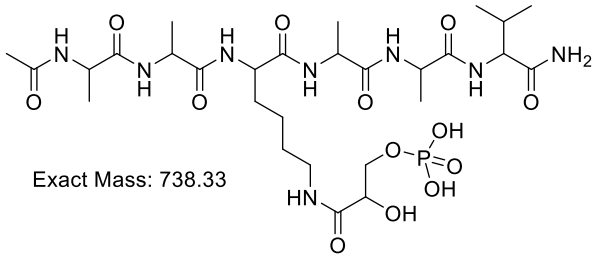

The reaction was then quenched, and protein precipitated by addition of acetonitrile (50 µL) on ice, followed by centrifugation at 13,000 g for 10 minutes. The supernatant was removed, dried by speedvac, resuspended in 50 µL of 50:50 H2O:ACN and injected onto an Agilent 1100 series LC-MS with a Phenomenex Gemini C18 column (50 x 4.6 mm, 5 µM). Chromatography was performed at a flow rate of 0.5 mL/min. Mobile phase A was composed of H2O supplemented with 0.1% TFA, and mobile phase B was composed CH3CN supplemented with 0.1% TFA with the following gradient: 5% Buffer B (0-1 min); 5-15% Buffer B (1-5 min); 15-50% Buffer B (5-7 min); 50-95% Buffer B (7-7.5 min) 95-5% Buffer B (7.5-10 min); 5% Buffer B (10-13 min). Injection volume was 5 µL for all samples. Data presented are representative of three independent experiments.

2.4.23 HDAC3 KO cell lysate peptide assay

HEK293T HDAC3 Scr and HDAC3 KO1 cells were lysed on ice via sonication (Fisher Scientific FB-505) for 15 seconds (1 second on, 1 second off) and diluted to 0.5 mg/mL in PBS

plus EDTA-free complete protease inhibitors (Roche) via BCA protein assay (Fisher Scientific) After lysis and sonication, light centrifugation (5000 g for 3 min at 4°C) was done to clear insoluble debris. Peptides AAKAAV and AAgKAAV (10μL of 1 mM) were added to cell lysates or PBS (50 μL) and incubated at 37°C for 0, 15, or 30 min, shaking at 400 rpm on tabletop shaker. Heat-inactivated lysate control samples were heated at 95°C for 30 min. prior to peptide + lysate incubation. In total, conditions consisted of: AAgKAAV peptide control, AAKAAV peptide control, Scr lysate + AAgKAAV peptide, KO lysate + AAgKAAV peptide, Scr heat inactivated (HI) lysate + AAgKAAV peptide, KO heat inactivated (HI) lysate + AAgKAAV peptide.

At the end of each timepoint, the reaction was then quenched, and protein precipitated by addition of acetonitrile (50 μL) on ice, followed by centrifugation at 13,000 g for 10 minutes. The supernatant was removed, dried by speedvac, resuspended in 50 μL of 50:50 H2O:ACN and injected onto an Agilent 1100 series LC-MS with a Phenomenex Gemini C18 column (50 x 4.6 mm, 5 μM). Chromatography was performed at a flow rate of 0.5 mL/min. Mobile phase A was composed of H2O supplemented with 0.1% TFA, and mobile phase B was composed CH3CN supplemented with 0.1% TFA with the following gradient: 5% Buffer B (0-1 min); 5-15% Buffer B (1-5 min); 15-50% Buffer B (5-7 min); 50-95% Buffer B (7-7.5 min) 95-5% Buffer B (7.5-10 min); 5% Buffer B (10-13 min). Injection volume was 7.5 μL for all samples. Data presented are representative of three independent experiments. Peak integration was performed on extracted ion chromatograms of the expected exact mass ± 0.05 Da.

Materials and Methods for Chapter 5: Differential response of cancer cells to central glycolytic perturbation under acute, intermediate, and chronic conditions

2.5.1 Chemicals

All compounds and reagents used were from Sigma-Aldrich, and all bulk solvents were from Thermo Fisher Scientific unless otherwise stated. CBR-470-l (initially from ChemDiv as D470-2l72) was synthesized and purified in house according to previously published methods[31] by Dr Shaghayegh Fathi. All commercially obtained chemicals were dissolved in DMSO and used without further purification unless otherwise stated.

2.5.2 Mammalian Cell Lines and Cell Culture

The human cell lines A549, A375, U87-MG, LNCaP, MDA-MB-231, MCF7, SW480, PC3, HT29, CAOV3, H1299, Raji, Ramos, Hela, HEK 293T, SKOV3, OVCAR3, K562, HCT116, and IMR32 were used in our studies. All cells were purchased from American Type Culture Collection (ATCC). Cells were propagated in RPMI 1640 (Corning) supplemented with 10% fetal bovine serum (Gemini Bio) and 1% penicillin/streptomycin (Gibco). Cells were grown in 5% CO2 incubators at 37 °C. All cell lines were authenticated by mycoplasma detection (Lonza, LT07-218). SILAC labeling was performed by growing cells for at least five passages in lysine- and arginine free RPMI 1640 Media for SILAC with 2 mM glutamine supplemented with 10% dialyzed fetal bovine serum and 1% penicillin/streptomycin (Gibco). “Light” and “Heavy” media were supplemented with natural lysine and arginine (0.1 mg/mL) and 13C,15N-labeled lysine and arginine (0.1 mg/mL), respectively.

2.5.3 Generation of stable GAPDH shRNA knockdown cells

The pLKO.1 puro plasmid (Addgene plasmid #8453) was a gift from Bryan Dickinson. The shGAPDH shRNA sequence corresponding to Sigma Mission shRNA lentiviral clone NM_002046.2-1002s1c2 and its reverse complement was purchased from Integrated DNA Technologies (IDT) and added into the pLKO.1 puro plasmid backbone by Dr. John S. Coukos to form the GAPDH-targeting shRNA plasmid.

2.5.4 shRNA knockdown studies

PGKl-targeting shRNA refers to Sigma Mission shRNA lentiviral clone NM_00029l.2-935slcl. The non-targeting scrambled (Scr) control vector refers to SHC002 (Sigma). Lentiviruses were generated in HEK293T cells by transient expression of the above vectors with pSPAX2 and pMD2.G packaging vectors (Addgene plasmids ll260 and l2259). Viral supernatants were collected after 48 hours of expression in DMEM media and passed through a 45 μm filter before exposure to target cells.

2.5.5 Metabolomics

The night prior, cells grown in RPMI 1640 (Corning) supplemented with 10% dialyzed fetal bovine serum (Gemini Bio) and 1% penicillin/streptomycin (Gibco) for 2 passages were plated at 1 million cells per 10 cm plate using a cell counter. 8 hr. later, cells were harvested for metabolomics. To quantify metabolic redox intermediates such as NAD, NADH, NADP, NADPH, GSH, GSSG and nucleotide phosphates such as ATP, ADP, AMP, GTP, GDP, GMP, CTP, CDP, CMP, UTP, UDP, and UMP, media was aspirated and 1 mL of lysis buffer (0.1 M Formic acid in 9:1 (75% acetonitrile: 25% methanol): water)) was added. After 2 minutes on ice, 87.5 μl of 15% NH_4HCO_3 was added, and the mixture was incubated for another 20 min on ice. Cells were scraped and lysate

was transferred into a pre-chilled 1.5 ml centrifuge tube, vortexed briefly, and spun at 14000 rpm for 20 min at 4 °C. 200 µl of supernatant was then transferred into an LCMS vial. For other metabolites, media was aspirated, and cells washed with 2 mL of room temperature PBS. Then, 1 mL of dry ice-cold 80% methanol was added to cell monolayer to quench metabolism. Cells were incubated at −80 °C for 30 min, harvested with cell scraper, and centrifuged at 21,000 × *g* for 5 mins to precipitate proteins. The supernatant was collected in pre-chilled tubes and stored at −80 °C. On the day of analysis, the supernatant was incubated on ice for 20 min and centrifuged at 21,000 × *g* at 4 °C to clarify. The supernatant was dried down in a speed vacuum concentrator and resuspended in 100 µL of 60/40 acetonitrile/water. The samples were then vortexed, sonicated in ice-cold water for 1 min, and incubated on ice for 20 mins. Supernatant was collected after centrifugation at 21,000 × *g* for 20 min at 4 °C.

Metabolite separation was performed in the UChicago Medicine Comprehensive Cancer Center Metabolomics Platform using a Thermo Scientific Vanquish Horizon UHPLC system and XBridge BEH amide 2.5 µm (2.1x150 mm Column XP, Waters Corporation, MA) under acidic conditions. Mobile phase A (MPA) was 90/5/5 water/acetonitrile/methanol, 20 mM ammonium acetate, 0.2% acetic acid and mobile phase B (MPB) was 90/10 acetonitrile/water, 10 mM ammonium acetate, 0.2% acetic acid. The column temperature was 40°C, flow rate was 0.3 mL/min, and injection volume was 5 µL. The chromatographic gradient was: 0min: 95% B, 9min: 70% B, 9.75min: 40% B, 12min: 40% B, 13min: 30% B, 14min: 30%B, 14.1min: 10% B, 17min: 10% B, 17.5min: 95% B, 22min: 95% B. An Orbitrap IQ-X Tribrid mass spectrometer (Thermo Scientific) with a H-ESI probe operating in negative polarity was utilized for MS detection using the following parameters: Acquisition range of 70-1000 m/z at 60K resolution, spray voltage: 2800V, sheath gas flow: 40, aux gas flow: 7, sweep gas flow: 1, AGC target: 100, maximum injection time: 118 ms, capillary temperature: 250°C, RF level: 60 and aux gas heater temperature:

350°C. Data acquisition was done using the Xcalibur software (Thermo Scientific) and data analysis was performed using Tracefinder 5.1 software (ThermoScientific). Specific metabolite information is found in Supplementary Table 5.1 in the addendum.

2.5.6 Cell viability and growth measurements

For Cell Titer Glo (CTG), 2500 cells were plated in 50 µL of RPMI growth medium in white 96-well plates. After 24 hours of growing, 50 µL of media was added to the wells for the final concentration of compound to be as indicated in each figure for a total volume of l00 µL. After incubation for the indicated time in figure descriptions, l00 µL of a Cell Titer Glo solution (Promega, diluted l:4 in PBS) was added, the plate was shaken gently at room temperature for 5 min and then imaged using a Synergy Neo HST plate reader (BioTek). Cell viability at the indicated timepoints was measured via luminescence using the CTG assay.

For crystal violet growth measurements, 2500 cells were plated in clear bottom 96 well plates in 50 µL RPMI. After 24 hours of growing, 50 µL of media was added to the wells for the final concentration of compound to be as indicated in each figure for a total volume of l00 µL. After incubation for the indicated time in figure descriptions, media was aspirated, and cells were gently washed twice with PBS. Then, ice-cold methanol was gently added to cells to fix the cells. The plates were then incubated 10 min on ice before being gently aspirated. 100 µL 0.5% crystal violet solution (250 mg in 12.5 mL methanol, 37.5 mL water for a 50 mL solution) was then added per well and cells were incubated for 20 minutes at room temperature. Following this, crystal violet was gently aspirated off the cells. Cells were washed gently in water 3 times and then allowed to dry at room temperature overnight. (At this point, dried plates can be stored for a long time at room temperature). To de-stain and quantify, 100 µL methanol was added to the wells and the plate were

gently shaken for 15 mins. Absorbance of each well at 590 nm was read by a plate reader, the absorbance of blank control wells was subtracted in order to quantify cell number per well.

For Incucyte cell proliferation assays, two thousand cells were seeded per well in a 96-well tissue culture plate in 50 µL RPMI. The tissue culture plate was incubated for 24 hours, and then the indicated compound conditions and concentrations were added to the wells, for a total of 200 µL per well before transferring into an IncuCyte S3 (Sartorius). Cells were monitored over time by scanning the plate with a 10X phase contrast objective for up to 7 days. Four images were acquired per well every 4 hours and analyzed by the IncuCyte 2020B software (Sartorius) to determine cell confluence. The mean and standard deviation of percent cell confluence across ten wells were calculated for each cell type at each time point. Proliferation curves were plotted by the IncuCyte software, and error bars represent standard deviations.

2.5.7 Seahorse Assay

Extracellular acidification rate (ECAR) and oxygen consumption rate (OCR) were analyzed with a Seahorse 95XF Analyzer (Seahorse Bioscience) using the XF Glycolysis Stress Test Kit 88 (Seahorse Bioscience) according to the manufacturer's protocol with slight modification. Briefly, 20,000 cells per well were plated on a 96-well Seahorse microplate in RPMI 24 hrs. prior to the experiment. The medium was replaced 4 hrs. before the experiment with Seahorse XF Base Medium. Cells were then incubated at 37 °C (low CO_2) for 4 hrs. The Seahorse cartridge was hydrated with water overnight at 37 °C (low CO_2) and then hydrated in calibrating solution (Seahorse Bioscience) for 2 hrs. prior to the experiment, followed by loading with glucose—PORT A (10 mM), oligomycin (3 µM)—PORT B and 2-deoxyglucose (50 mM)—PORT C. All 3 additives were dissolved in Seahorse XF Base Medium supplemented with compound at the indicated concentrations.

2.5.8 Proteomics sample preparation

Stable isotope labeling by amino acids in cell culture (SILAC) was performed by growing cells for at least five passages in lysine-free and arginine-free RPMI-1640 media for SILAC with 2 mM glutamine supplemented with 10% dialyzed FBS and 1% penicillin–streptomycin. 'Light' and 'Heavy' media were supplemented with natural lysine and arginine (0.1 mg ml^{-1}) and equimolar ^{13}C,^{15}N-labeled lysine and arginine, respectively. Confluent 10 cm plates (~10 million cells per plate) were washed twice with 1 ml of 1× PBS buffer, resuspended in lysis buffer (8 M urea, 25 mM NH_4HCO_3 and complete EDTA-free protease inhibitors) and sonicated using a Thermo Fisher Scientific FB-505 for 15 seconds (30% amplitude, 1 second on, 1 second off). Insoluble debris was cleared by a 15-minute centrifugation at 16,000*g* at 4 °C. Protein concentrations were determined by BCA assay (Thermo Fisher Scientific, 23255); samples were diluted to 1 mg ml^{-1} in lysis buffer; and 100 µl of each sample was prepared. Paired samples were combined followed by the addition of 2 µl of 1 M DTT, and the samples were heated at 65 °C for 15 minutes and then allowed to cool to room temperature. To the samples was then added 16 µl of 0.5 M iodoacetamide, and the samples were incubated for 30 minutes at room temperature in the dark. Samples were diluted with 25 mM NH_4HCO_3 to give a final concentration of 2 M urea, supplemented with 1 mM $MgCl_2$ using a 100 mM stock solution in water and then subjected to trypsin-mediated proteolysis with 4 µg of MS-grade trypsin for 16 hours at 37 °C. The peptides were desalted with tC18 Sep-Pak cartridges (Waters) and then dried via speedvac. Samples were then resuspended in 0.1% formic acid in H_2O for LC–MS/MS analysis.

2.5.9 Analysis of proteomics samples by LC–MS/MS

LC–MS/MS analysis for proteomics samples was performed with an UltiMate 3000 RSLCnano System (Thermo Fisher Scientific) using an Acclaim PepMap RSLC C18 column (75

μm × 15 cm, 2 μm, 100 Å, Thermo Fisher Scientific) with an in-line Acclaim PepMap 100 C18 trap column (75 μm × 2 cm, 3 μm, 100 Å, Thermo Fisher Scientific) heated to 45 °C. The LC system was coupled to an Orbitrap Exploris 480 and Nanospray Flex Ion Source with stainless steel emitter tip (Thermo Fisher Scientific). Mobile phase A was composed of H_2O supplemented with 0.1% formic acid, and mobile phase B was composed of CH_3CN supplemented with 0.1% formic acid. The instrument was run at 0.3 μl min^{-1} with 2-hour gradients tailored to fraction number. MS/MS spectra were collected for the entirety of the gradient using a data-dependent, 2-second cycle time setting with the following details: full MS scans were acquired at a resolution of 120,000, scan range of 380 *m*/*z* to 1,500 *m*/*z*, maximum IT of 25 ms, normalized AGC target of 300% and data collection in profile mode. MS2 scans were performed by high-energy collision dissociation (HCD) fragmentation with a resolution of 15,000, normalized AGC target of 50%, maximum IT of 50 ms, HCD collision energy of 30% and data collection in centroid mode. The isolation window for precursor ions was set to 1.6 *m*/*z*. Peptides with a charge state of 1, 7+ and unassigned were excluded, and dynamic exclusion was set to 40 seconds. The RF lens % was set to 40 with a spray voltage value of 2.0 kV and an ionization chamber temperature of 300 °C. Data were processed using the SEQUEST HT search engine node within the Proteome Discoverer 2.5 software package. Data were searched using a concatenated target/decoy UniProt database of the human proteome. Enzyme specificity was set to trypsin with up to two missed cleavages allowed, and peptide length was set to between six and 144 residues. Precursor mass range was set to 350–6,000. Precursor mass tolerance was set to 15 ppm, and fragment mass tolerance was set to 0.02 Da. Up to three dynamic modifications were allowed, including heavy lysine (+8.0142), heavy arginine (+10.0083), oxidized methionine (+15.9949), N-terminal acetylation (+42.0106), N-terminal Met-loss (−131.0405) and N-terminal Met-loss + acetylation (−89.0299). Cysteine carboxyamidomethylation (+57.0215) was set as a static modification. A minimum of two peptides

was required for protein identification, and false discovery rate (FDR) was determined using Percolator with FDR rate set at 1%. Before quantification, chromatographic alignment was performed, with a maximum retention time difference of 10 minutes allowed and a minimum signal/noise threshold of 5 required for feature mapping. SILAC ratios were determined using precursor-based quantification in a pairwise manner based on peak area without normalization or scaling using a maximum ratio of 20. Unless otherwise indicated, data presented are representative of $n = 4$ independent biological experiments.

2.5.10 Western blotting

Western blotting protocol was done as per the protocols in previous section 2.4.8, using the PGK1 antibody: Santa Cruz Biotechnology (sc-130335) mouse mAb, GAPDH antibody: Cell Signaling (14C10) rabbit mAb #2118, and the β-actin antibody: Cell Signaling (13E5) rabbit mAb #4970 as primary antibodies.

Additional statistical analyses and software

GraphPad Prism version 10 (GraphPad Software) was used for statistical tests as indicated in the figure legends. Figures were created with Prism and Adobe Illustrator.

CHAPTER 3. ANCIENT, CIRCADIAN PHOSPHOGLYCERYL-LYSINE MODIFICATIONS RESPOND TO AND REGULATE METABOLISM IN CYANOBACTERIA

The work of this chapter is in preparation for submission: Lee, C. W., Pattanayak, G., Huang, J.X., Shah, H., Huff, A.R., Rust, M.J. & Moellering, R. E. (2024). Ancient, oscillatory phosphoglyceryl-lysine modifications response to and regulate metabolism in cyanobacteria.

Author Contributions: C.W.L. performed cellular assays and mass spectrometry analysis. G.P. performed cellular assays and assisted with mass spectrometry. J.X.H. performed proteomic mass spectrometry analysis. H.S. assisted with metabolomic mass spectrometry analysis. A.R.H. assisted with proteomic mass spectrometry analysis. R.E.M. supervised research. R.E.M. conceived the study. R.E.M. and C.W.L. analyzed data and wrote the article.

Abstract

In this study, we perform a quantitative global analysis of the post-translational modification 3-phosphoglyceryl-lysine (pgK) in cyanobacteria *Synechococcus elongatus*, an evolutionarily ancient simple organism possessing robust circadian machinery. Through manipulating its metabolic processes via exposure to light/dark cycles, we find that levels of pgK modifications are particularly prevalent in glycolytic enzymes and oscillate in a coordinated manner across light/dark cycles. We further find that light/dark oscillations in pgK modified active sites of glycolytic enzymes correlate strongly with light/dark changes in central carbon metabolites flux, notably shifting away from energy production towards nucleotide metabolism over the course of the dark cycle. This buildup and shift from bioenergetics towards biosynthesis is consistent with studies done in heterotrophs by manipulating glucose availability, demonstrating evolutionary conservation across kingdoms. However, as a metabolite intermediate shunted between glycolysis, respiration, pentose phosphate pathway, and photosynthesis, 1,3 BPG modifications of lysine in phototrophs may instead be a feedback

mechanism that dynamically coordinates buildup and redirection of metabolites in response to environmental light/dark conditions.

Introduction

Glycolysis is a central source of energy production and biosynthesis across all forms of life. Therefore, homeostatic regulatory mechanisms to sense and respond to altered metabolic conditions must have emerged early in evolution; before the appearance of many of the complex posttranslational regulatory enzymes that are the focus of most studies in humans and higher organisms.[58, 132, 133]

Among post-translational modifications (PTMs), there is a distinct class of PTMs are formed from reactive metabolites that are installed onto proteins by intrinsic reactivity rather than enzymatic processes. These evolutionarily ancient reactive metabolite PTMs (rmPTMs) have emerged as a significant contributor to the regulation of biochemical processes, forging a direct link between the chemical reactivity of metabolites to connection between bioenergetics and intricate feedback signaling responses within cellular systems. A striking example of this phenomenon is the recent discovery of phosphoglyceryl lysine (pgK) as a PTM regulator of lysines, stemming from the central glycolytic metabolite 1,3-bisphosphoglycerate (1,3 BPG). In published studies, pgK modifications accumulate in response to elevated glycolysis and can inhibit central glycolytic enzymes to redirect flow from energy production to biosynthesis.[46] Beyond metabolism, pgK modifications have been mapped[46, 60] to proteins and metabolites involved in energy sensing, protein folding, ion channels, transcriptional regulation, and others.

Through modification of active site lysines, pgK has been found to exert profound control over the activity of glycolytic enzymes and finely modulate the distribution of carbon resources between the glycolysis pathway and the pentose phosphate pathway based on glucose flux.

Moreover, the presence and functional importance of pgK modifications extend beyond a specific organism, as they have been widely observed in various organisms, including humans, mice, and drosophila, underscoring the evolutionary conservation and physiological relevance of this intriguing PTM mechanism. However, as pgK has yet to be mapped in non-eukaryotes, we asked whether the feedback mechanism ascribed to pgK in eukaryotes is as universally conserved as glycolysis.

To answer this question, we utilized *Synechococcus elongatus* PCC 7942, a cyanobacteria that represents a fundamental cornerstone in the evolutionary development of life on Earth. These ancient, prokaryotic, phototrophic microorganisms are among the simplest biological systems in existence. Under tight regulation by a robust suite of circadian rhythm clock proteins known as the Kai proteins,[134, 135] cyanobacterial gene expression, translation, replication, and metabolism are all strictly coordinated in response to diurnal oscillations of light and dark cycles. This characteristic, which makes them ideal models for the study of biological clocks, also made them an ideal model to study pgK dynamics.

In the presence of light, the Calvin-Benson cycle steers metabolic flux towards carbon assimilation and energy production. While during the dark phase, cyanobacteria upregulate glycolysis and oxidative respiration, driven by the utilization of glycogen reserves to sustain cellular viability.

Thus, the glycolytic intermediates such as 1,3 BPG are exchanged between light associated carbon fixation and dark associated glycogen utilization in cyanobacteria[136, 137] and are ideally located to dynamically encode pgK modifications at the nexus of these processes. (Figure 3.1A).[138] Here, we embarked on a comprehensive proteomic study to ascertain the

presence, dynamics, and functional significance of pgK modifications within the context of cyanobacterial metabolism and circadian rhythm. Using quantitative (phospho)proteomics and metabolomics we mapped and confirmed the oscillation of pgK modifications in response to day/night cycles and identified a novel regulatory role in controlling carbon flow to control oxidative stress and nucleotide biosynthesis.

These data confirm that the chemistry and regulatory potential of non-enzymatic pgK modifications are an ancient, hard-wired signaling mechanism spanning single-celled autotrophs to higher mammals; likely representing some of the first posttranslational modifications and regulatory mechanisms to have appeared during the evolution of life on earth.

Results

Fig 3.1 Quantitative (phospho)proteomic profiling of cyanobacteria across the day/night cycle

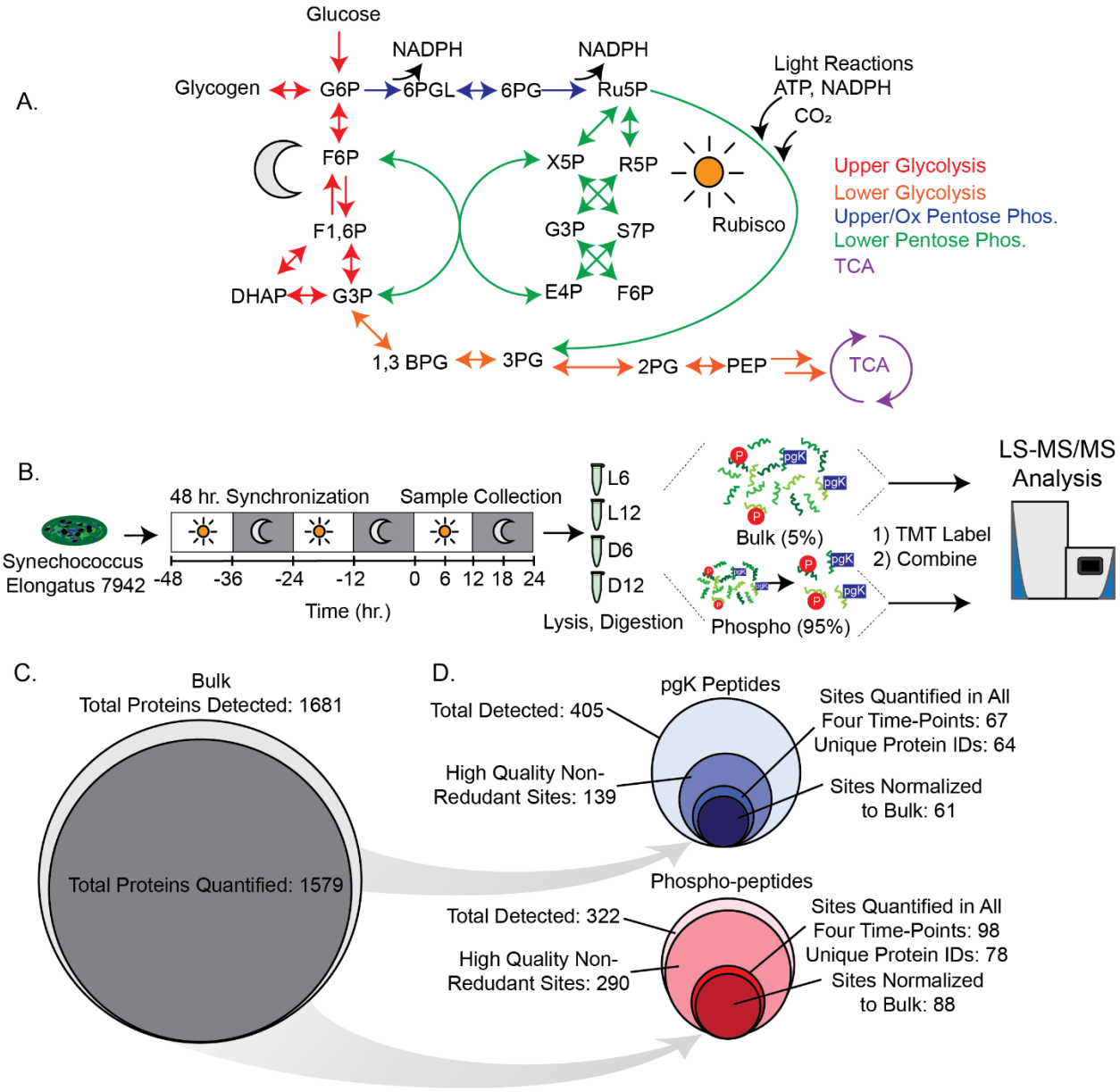

Figure 3.1 Continued
Figure 3.1: Quantitative (Phospho)Proteomics of Cyanobacteria A. Schematic of central metabolism. Upper glycolysis (red), Oxidative Pentose Phosphate Pathway (blue), Calvin-Benson
cycle (green), lower glycolysis (orange), TCA (purple) **B.** Workflow of sample preparation. Cultures of Synechococcus Elongatus 7942 was grown and exposed to 12-hour cycles of light and
darkness over the course of 48 hours prior to being collected for proteomic analysis. Briefly, samples were digested, TMT-labeled, pooled, separated for bulk or phospho-peptide enrichment workflows, fractionated, and then analyzed by LC-MS/MS. **C-D.** The output of each MS run was searched using an integrated platform for peptide identification and quantification for bulk protein **(C)**, or site level phospho/pgK modification **(D)** using the filters above. Each timepoint represents n = 4 biological replicates.

To comprehensively characterize global changes to protein abundance and modification state in a model cyanobacterium, we first synchronized Synechococcus elongatus (strain PCC 7942) to alternating 12-hour cycles of light and darkness over a 48-hour period. Subsequently, we collected samples at 6-hour intervals throughout a 24-hour period, which were prepared for whole proteome and phospho-peptide enrichment (Figure 3.1B). We utilized a column-based, TiO2 phosphopeptide enrichment strategy,[139] able to enrich both pgK-modified and phospho-serine, threonine and tyrosine-containing peptides. These separate peptide pools from each timepoint were barcoded using tandem mass tags (TMT) reagents and analyzed by Liquid Chromatography-Tandem Mass Spectrometry (LC-MS/MS; Figure 3.1C).

Approximately 95% of the 1,681 detected proteins were quantified across the four timepoints, encompassing over 80% of the S. elongatus proteome[140] (Figure 3.1C). In parallel, phosphoproteomic analyses identified more than 300 phosphorylation sites at serine, threonine and tyrosines, which confirms the significantly lower preponderance of this modification in cyanobacteria (Figure 3.1D). By contrast, more 300 pgK modification sites were observed throughout the day/night cycle. The roughly equivalent number of phospho- and pgK-modified

sites in this organism stands in stark contrast to the ~100:1 ratio observed in similar studies in human and mouse cells, underlining the distant place cyanobacteria occupy in the evolutionary and regulatory landscape.

In conclusion, our proteomics workflow demonstrated its capacity to quantitatively map pgK and phospho sites over the course of a 24-hour time frame. Importantly, our findings substantiate the conservation of the pgK modification even in evolutionarily ancient organisms, providing a foundational basis for further extrapolation and in-depth discussions regarding the dynamics and potential regulatory roles of post-translational modifications in cyanobacteria.

Fig 3.2 Qualitative Comparison of phospho and pgK Modified Proteins

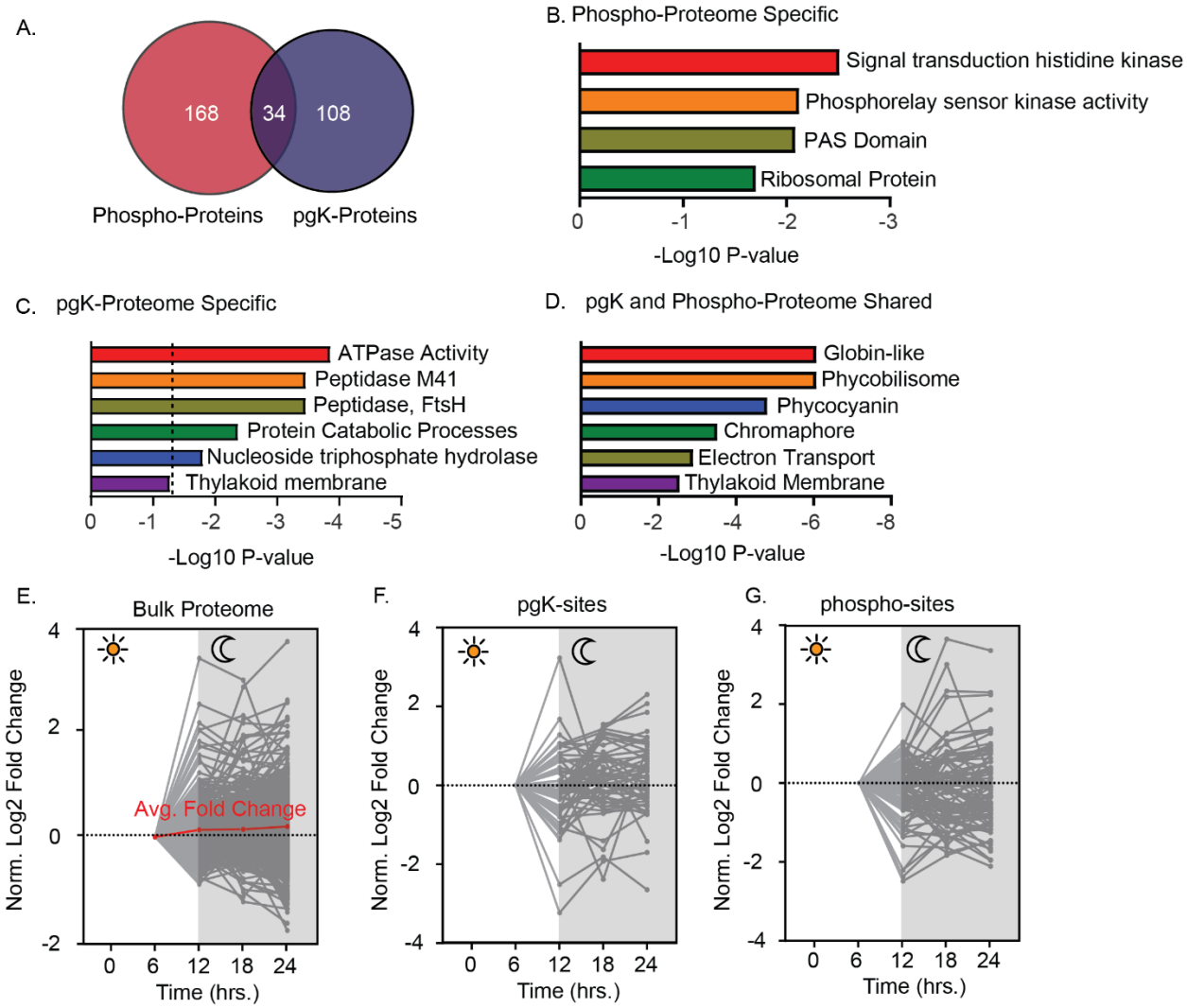

Figure 3.2: Functional Comparison of pgK and Phosphorylated PTM Sites A. Venn diagram comparison of the phospho- and pgKylated modified sites show relatively little overlap between the two proteomes **B-D.** DAVID-GO gene ontology functional pathway annotation of the modified proteome unique to **(B)** phosphorylated proteins, unique to **(C)** pgKylated proteome, or **(D)** shared between the two proteomes. **E-G.** Quantified fold change of **(E)** the bulk proteome, **(F)** pgKylated sites, or **(G)** phospho-sites across a 24-hour light-dark cycle.

After we observed that the prevalence of phospho-proteins and pgK-proteins in cyanobacteria was comparable, each modifying approximately 30% of the total detected proteome (Figure 3.1D), we sought to elucidate the specific subsets of the phosphorylation and

pgKylation modified proteome. To accomplish this, we compared the proteins modified by phosphorylation and pgKylation, followed by functional annotation of each subset protein list. Additionally, for proteins for which we possessed both site-level and bulk-level quantitative data at all four sampled time points, we normalized the levels of pgKylation and phosphorylation in our quantitative data to the bulk protein expression levels. This normalization process was achieved by internally normalizing the bulk, pgKylation, and phosphorylation data to the expression level of their respective proteins at the first time point (6 hours of light) to obtain fold changes over time.

Upon conducting our analysis, we made several significant observations. Despite their similar prevalence within the proteome, proteins modified by phosphorylation and pgKylation represented distinct subsets of the proteome (Figure 3.2A-D). Phosphorylated proteins exhibited functional diversity, encompassing processes such as signal sensing, phospho-signal transduction, and translation. Conversely, pgKylation primarily involved proteins associated with bioenergetic processes, including respiratory chain complexes and triphosphate molecule hydrolysis. Furthermore, proteins that could undergo either phosphorylation or pgKylation were predominantly linked to cellular energetics, particularly within the phycobilisome and electron transport pathways.

Examining quantitative changes revealed that post-translational modifications oscillated to a greater extent than protein expression levels throughout the light/dark cycles (Figure 3.2E-G). In stark contrast, the protein expression levels of the vast majority of proteins remained relatively stable[140] across the 24-hour light/dark cycle, with less than 2 dozen proteins

quantitatively labeled across all 4 timepoints exhibiting greater than a >2-fold or <0.5 fold change in expression.

In conclusion, our findings underscore the divergence in the proteome subsets modified by phosphorylation and pgKylation, with phosphorylation impacting a broader array of pathways compared to pgKylation, which predominantly influences bioenergetic processes. Additionally, the oscillation of post-translational modifications at similar amplitudes, albeit within distinct proteome subsets, highlights the significance of post-translational regulation in the context of light/dark cycles. This not only extends our understanding of pathway regulation at the post-translational level but also underscores the importance of pgKylation in bioenergetic pathway control, complementing the well-documented role of phosphorylation in Kai protein-mediated circadian regulation[134, 135].

Fig 3.3 pgKylation Patterns of Central Metabolic Proteins over the Light/Dark Cycle

We further analyzed the pgKylated proteome subset, aiming to ascertain whether it exhibited correlations to the well-documented bioenergetic to biosynthetic pgK regulatory mechanism observed in higher-order species. To achieve this, we searched enzymes of central metabolism (glycolysis, the pentose phosphate pathway, the Calvin-Benson Cycle, and the TCA cycle) for quantitative pgKylation site-level alterations in relation to bulk protein expression throughout the light/dark cycle.

A. **Glycolysis & Tricarboxylic Acid Cycle**

Enzyme	Lysine	Functional Annotation	Peptide (High Quality Non-Redundant Sites)
Enolase (Eno)	339	Active Site Binding Pocket	K.LQSGIEQGVGNAVLI**K(167.98238)**LNQIGTLTETLR.T
Phosphoglycerate Kinase (Pgk)	257,261	Proximal to hinge region	R.SLMA**K(167.98238)**AQE**K(167.98238)**GVQLLLPVDVVVADK.F
Triosphosphate Isomerase (tpiA)	59		R.**K(167.98238)**VVLCAPFTTLSSLSK.T
Pyruvate Kinase	492		R.GIGVGQGSVSG**K(167.98238)**AR.V
Fructose-1,6-bisphosphate aldolase (Fba)	206		K.FTR**K(167.98238)**PTGEILAISRIEEIHR.R
	313*		K.YM**K(167.98238)**QVCVDR.Y
	343*		K.IKQEGLDEFAA**K(167.98238)**YAKGELR.A
Glyceraldehyde-3-phosphate dehydrogenase (Gap2)	75		
	126		K.VLITAPG**K(167.98238)**GEGVGTYVIGVNDSEYR.H
	229		K.G**K(167.98238)**LNGIALR.V
Pyruvate Dehydrogenase	38		R.EEGLRIYEDMVLGRTFED**K(167.98238)**CAEMYYR.G

Pentose Phosphate Pathway, Calvin Cycle, Other Biosynthetic Pathways

Enzyme	Lysine	Functional Annotation	Peptide (High Quality Non-Redundant Sites)
Ribulose bisphosphate carboxylase large chain	172	Active Site	K.YGRPMLGCTI**K(167.98238)**PK.L
(RuBisCO)	180*	Proximal to hetero-dimer interface	K.LGLSA**K(167.98238)**NYGR.A
Fructose-1,6-bisphosphatase class 1 (Fbp)	282	Active Site	K.NPTG**K(167.98238)**LR.L
Phosphoribulokinase*	53		R.**K(167.98238)**EAGVTALDPR.A
	232		R.**K(167.98238)**LTCSYPGIR.L
Carboxysome assembly protein CcmM	480		R.ISAEVAD**K(167.98238)**R.R
Bifunctional protein GlmU	347	Active Site	R.IGNFVEV**K(167.98238)**K.S
Chorismate Synthase (AroC)	301	Active Site	R.VAF**K(167.98238)**PTATIRKEQETVTNSGEATTLAAR.G

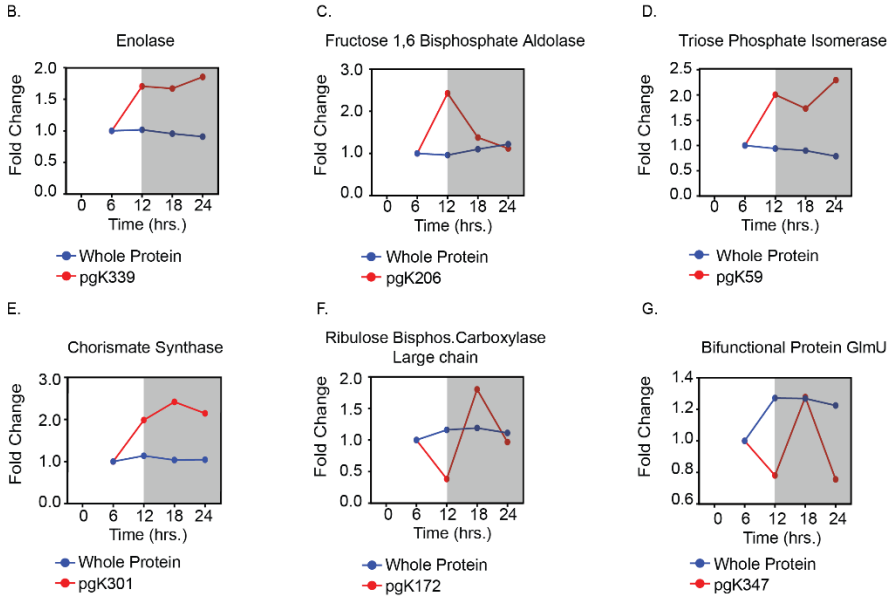

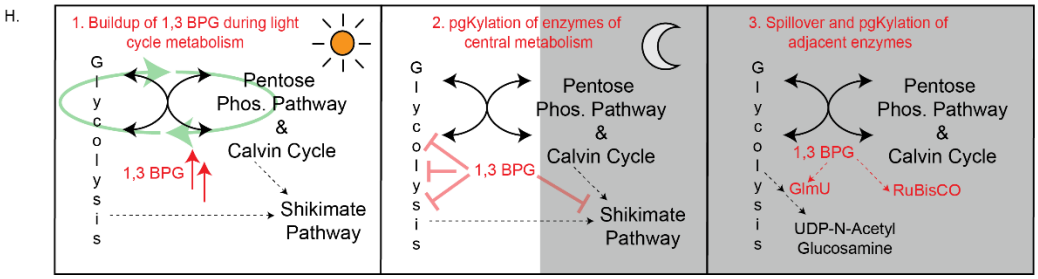

Figure 3.3: Quantitative Analysis of pgK Sites in Central Metabolic Enzymes over Light/Dark Cycles A. List of pgKylated peptides of interest in Central Metabolism **B-G.**

Figure. 3.3 continued
Quantitative changes in pgK site modification with respect to total protein expression of select enzymes of central metabolism **H.** Schematic of buildup in pgK modifications and subsequent pgKylation of cyanobacterial proteome across light/dark cycles.

Our results revealed active site pgKylation occurring on multiple enzymes central to metabolism (Figure 3.3A), notably those enzymes facilitating the flow of metabolites between the central glycolytic pathway and the pentose phosphate pathway, such as enolase, phosphoglycerate kinase, and fructose 1,6-bisphosphatase. For instance, pgK modification of the active site Lysine 339 in enolase (Figure 3.3B) is well-documented[141, 142] to down-regulate of enolase activity. Additionally, we observed pgK modifications on non-active site, solvent-exposed lysines in central glycolytic enzymes like aldolase and triose phosphate isomerase (Figure 3.3C&D). Intriguingly, enzymes utilizing intermediate glycolytic and pentose phosphate metabolites,[143] such as chorismate synthase, as substrates also exhibited a similar pgKylation profile at an active site[144, 145] (Figure 3.3E). Furthermore, we noted a temporal sequence in which the accumulation of pgKylation in central glycolytic enzymes between 6-12 hours in light was followed by increased pgKylation at 18 hours in dark for enzymes of pathways adjacent to central metabolism, such as RuBisCO or GlmU, an enzyme involved in lipopolysaccharide and peptidoglycan biosynthesis.

From these observations, we draw several conclusions. The pgKylation patterns in central metabolism enzymes appear to align with a signal propagation event that initiates with the accumulation of pgKylation in central glycolytic enzymes over the course of the light cycle. This accumulation is subsequently followed by increased pgKylation in enzymes associated with adjacent pathways at the initial stages of the dark cycle.

Concurrently, it appears that more distant pathways which utilize glycolytic, or pentose phosphate pathway metabolite intermediates are also subjected to pgKylation in an inhibitory manner. For instance, the final enzyme in the shikimate pathway which synthesizes aromatic amino acids vital for photosynthetic organisms, chorismate synthase,[143] contains a pgKylation site in its active site. Notably, the substrates for this enzyme originate from central glycolysis and the pentose phosphate pathway, implying that this putative inhibition may also be playing a role in the accumulation of central metabolites pgKylation over the course of the light cycle.

Collectively, our findings indicate that pgKylation of enzymes in central metabolism synchronizes with the accumulation and redirection of central glycolytic flux toward biosynthetic pathways as the light cycle transitions to the dark cycle. As intermediates are exchanged between glycolysis, the pentose phosphate pathway, and the Calvin-Benson cycle, there is a gradual buildup of central glycolytic metabolites, including 1,3-BPG. Sites of central glycolytic enzymes become pgKylated by 1,3 BPG over the course of the light cycle into the dark cycle, which subsequently then also begins to pgKylated enzymes of central metabolism adjacent pathways in the dark. These insights showed that the cyanobacteria pgKylated proteome appeared to exhibit correlations to the bioenergetic to biosynthetic pgK regulatory transition observed in higher-order species, further underscoring the conserved nature of these glycolytic reactive metabolite modifications.

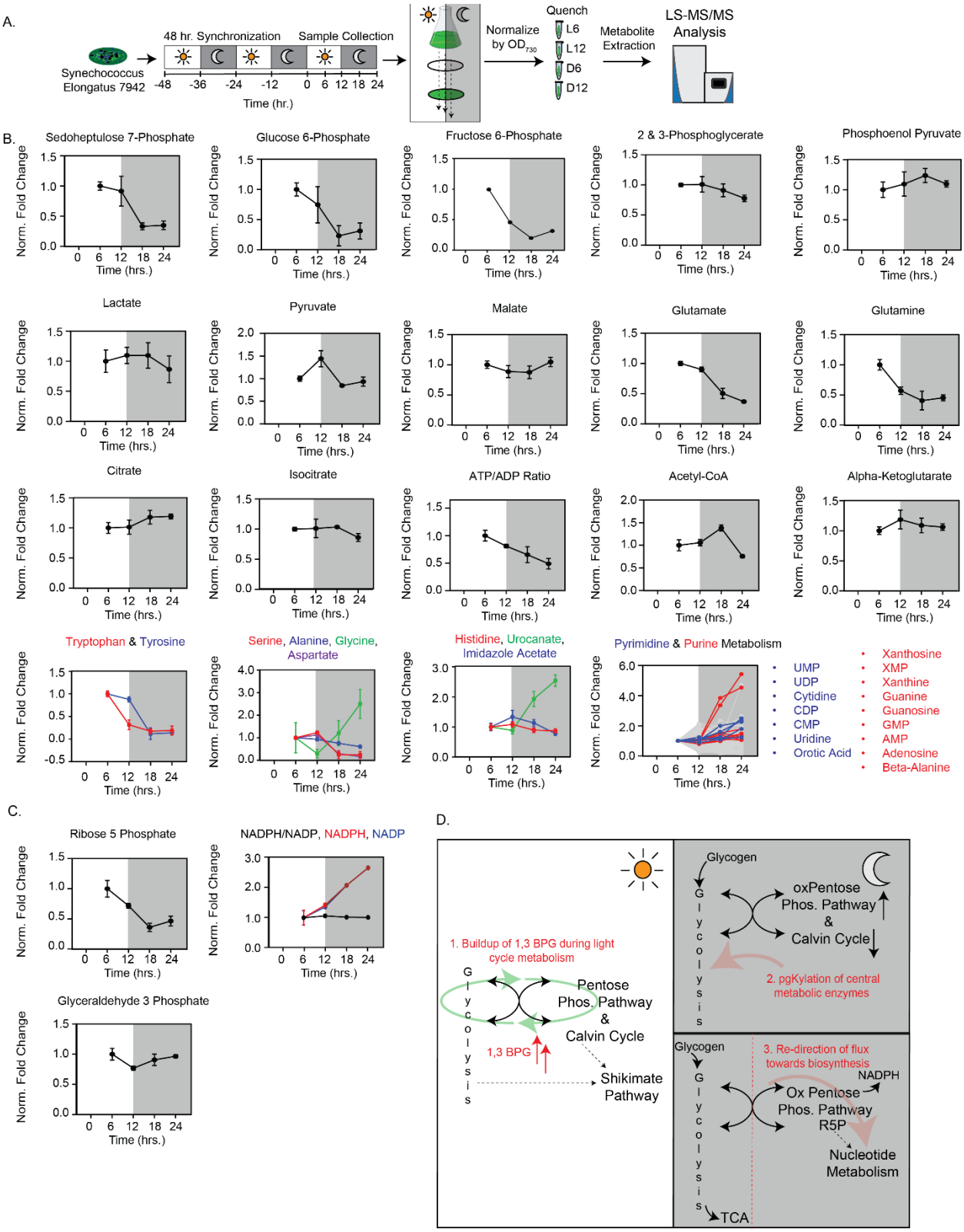

Figure 3.4: Quantitative Analysis of Central Metabolism over Light/Dark Cycles

Figure 3.4 Continued
A. Simplified workflow schematic of metabolite sample collection, normalization, and preparation **B.** Quantitative changes in metabolites using full MS scan mode with respect over light/dark cycle **C.** Quantitative changes in select metabolites using MRM **D.** Schematic of buildup in pgK modifications and subsequent redistribution of metabolic flux across light/dark cycles.

Fig 3.4 Quantitative Metabolomics Analysis of Metabolites across the Light/Dark Cycle

Finally, we conducted quantitative metabolomics to examine whether the observed changes in the pgKylated proteome trending toward biosynthetic metabolic pathways during the light-to-dark transition had corresponding metabolic implications. Our experimental design (Figure 3.4A) closely mirrored the setup employed in our quantitative proteomics experiments, involving the synchronization of Synechococcus elongatus (strain PCC 7942) to alternating 12-hour cycles of light and darkness over a 48-hour period, with samples collected every 6 hours across a 24-hour timeframe. To ensure consistent input across time points and minimal perturbation to cyanobacterial metabolome, we utilized vacuum filtration with a nitrocellulose membrane, normalized using OD730 measurements. Subsequently, the cyanobacterial samples were rapidly quenched in ice-cold organic solvent prior to LC-MS/MS-based quantitative metabolomics analysis.

Our results encompassed the measurement of fold changes for 150 metabolites, including amino acids and central metabolism metabolites found within glycolysis, the TCA cycle, the pentose phosphate pathway, and nucleotide metabolism (Figure 3.4B-C). Notably, we observed a significant increase in many metabolites associated with nucleotide metabolism as the transition from light to dark occurred. Furthermore, during the light-to-dark transition, the levels of upper glycolytic and pentose phosphate pathway intermediates including ribose 5 phosphate all exhibited a marked decrease in the dark cycle that was not reflected in central, lower glycolytic

and TCA intermediates, which remained steady. This potentially reflects a redirection of metabolite flux towards nucleotide metabolism, facilitated by a decrease in pgKylated enzyme activity in central and lower glycolysis. In addition, the simultaneous abrogation of carbon fixation in the dark[146] paired with the necessity for cyanobacteria to maintain NADPH redox via oxPPP[136, 147] implies that nucleotide metabolism is the only direction in which metabolites can exit upper glycolysis/oxPPP. This trend was also observed in pathways branching from central glycolysis that are associated with nucleotide metabolism such as the serine pathway, which can feed into purine metabolism via serine into glycine.

Moreover, the histidine pathway, which also originates from R5P, displayed an accumulation of urocanate, a metabolite that can contribute to the formation of glutamate and glutamine. Intriguingly, while glutamate and glutamine depleted over the course of the dark phase, TCA intermediates such as citrate, isocitrate, alpha-ketoglutarate, and malate levels remained relatively stable throughout the experiment. This observation suggests that glutamine/glutamate may be preferentially directed towards pyrimidine metabolism rather than the TCA cycle. Additionally, though TCA metabolite levels remained largely steady, we observe a consistent decrease in the ATP/ADP ratio over the light-to-dark transition consistent with prior research on dark oxidative respiration. Finally, the biosynthesis of aromatic amino acids such as tryptophan and tyrosine by the shikimate pathway, which depends on substrates from lower glycolysis and the lower pentose phosphate pathway, exhibited a substantial decrease during the light-to-dark transition, aligning with the general trend that metabolic flux is being reallocated towards nucleotide metabolism via pgKylation of central and lower glycolysis.

In conclusion, our findings provide evidence that the buildup of pgKylation sites on central glycolytic enzymes corresponds to a concurrent transition of intermediate glycolytic and pentose phosphate pathway metabolites, ultimately resulting in a substantial shift in metabolic flux towards accumulation of nucleotide metabolism intermediates (Figure 3.4D). This correlation highlights the role of pgKylation in orchestrating a metabolic shift from bioenergetic pathways to nucleotide biosynthesis as the metabolic cycle transitions from light to dark.

Discussion

In this study, we provide evidence for the functional significance of 3-phosphoglyceryl-lysine (pgK) modifications in cyanobacteria, shedding light on their conservation and role in central metabolism. Our findings underscore several key points of significance. Firstly, our investigation reveals that pgK modifications are highly conserved throughout evolution, suggesting their fundamental importance in cellular regulation of carbon flux across species. Notably, within the relatively simple model organism of cyanobacteria, using quantitative proteomics techniques to map the pgK, phospho, and bulk proteome dynamics of cyanobacteria throughout the light/dark cycle, we unveiled that pgK modifications are prevalent across hundreds of sites within the proteome, far beyond the ratio of pgK modifications to total proteome found in more complex organisms.[46, 60] Conversely, the ratio of phosphorylation sites to proteome in cyanobacteria[148] was far lesser than the ratio found in more complex organisms;[149, 150] all while overall protein expression stayed relatively static. Together, this evidence underscores the important participation of pgK in dynamic regulation of cellular processes and indicates that simple evolutionarily ancient organisms such as cyanobacteria utilize reactive metabolite post translational modifications deriving from biochemical flux for

regulation and signaling with respect to environmental conditions. Furthermore, given their reactive nature, rmPTMs may represent some of the first types of post translational modifications utilized by primitive life.[151]

Additionally, our quantitative metabolomics analyses unveiled a remarkable correlation between the levels of pgK modifications in central metabolic proteins and the fluctuations in light/dark metabolic pathways. Specifically, we observed a shift from central metabolic intermediates towards nucleotide metabolism via the pentose phosphate pathway during the dark cycle. This aligns with previous observations in other studies[152, 153] entrained to respond to light/dark cycles, where the accumulation of nucleotide metabolism intermediates over the course of the dark cycle has been hypothesized to be in preparation for light cycle growth and replication. This shift indicates that pgK plays a pivotal role in the regulation of carbon distribution between bioenergetic and biosynthetic pathways, in cyanobacteria just like in heterotrophs.

Moreover, triose-phosphates act as one of the most important central metabolic intermediates, shared between glycolysis, respiration, photosynthesis, and the pentose phosphate pathway in phototrophs. This implies that triose-phosphates and reactive molecules that stem from them such as 1,3 BPG are able to have dynamic metabolic regulatory roles highly conserved across a wide range of phototropic organisms including plants, fungi, other prokaryotes, and archaea, further emphasizing the universality of ancient glycolytic rmPTMs across life. This data further joins the growing consensus that triose-phosphate derived reactive metabolites like 1,3 BPG and methylglyoxal have potential to affect and regulate diverse and critical biological processes. It can be speculated that while both heterotrophs and phototrophs

rely on central metabolites to dynamically allocate carbon resources between bioenergetic and biosynthetic pathways—central metabolites like 1,3 BPG are used by heterotrophs as a proxy to determine the metabolic fate of carbon based on quantity of glucose acquired per day whereas phototrophs utilize the same metabolites to determine metabolic carbon fate based on quantity of light acquired per day.

Overall, our study provides valuable insights into the role of pgK modifications in central metabolism regulation and opens doors for further investigations into the molecular intricacies of reactive metabolite modification signaling processes in biology.

Future Directions

An immediate and direct future experiment stemming from this study includes validating whether the location of the pgK or phosphorylation site modifications found within the phospho-proteomic profiles have functional effects on the enzymatic activity of the protein. With respect to phosphorylation, some sites identified by our assay such as Y235 KaiC and T291, T305, and S314 on SasA are located on fundamental circadian rhythm proteins that regulate global transcriptional and translational activity of cyanobacteria and are phosphorylated in a manner that strongly correspond with the shift from light to dark conditions (see Fig. 3.7). These sites have yet to be identified within literature; and finding whether they affect the activity of the clock proteins would in turn imply that they have regulatory implications over the activity of the entire organism itself with respect to environmental conditions. To study whether these sites are functionally relevant, we could first develop mutant strains of cyanobacteria with the residues changed to either non-phosphorylatable residue alanine, or phospho-mimetic residue aspartic

acid. Then, the side-by-side growth comparisons of the relative biomass, Kai clock proteins phosphorylation pattern, and metabolomic steady state of these cyanobacteria strains versus wild type under light/dark cycling conditions would be relevant to determine whether environmental cues become de-synchronized in phospho-site mutant strains versus wild-type. If so, then the uncharacterized phospho-sites annotated above would be proven to be relevant in circadian clock regulation of biological activity.

With respect to pgK, some proteins within the cyanobacteria proteome, such as the glycolytic enzymes or the enzymes utilized for carbon fixation are well characterized with crystal structures and conserved across species. [141, 154] The effect of installation a pgK modification on these lysine residues, changing the positive nature of the lysine residue and sterically hindering substrates from entering the binding pocket, may be predicted to stop enzymatic activity via the effect of pgKylation on analogous lysine sites in the same conserved proteins of higher order organisms. However, for other enzymes which have putative active sites lysines[155] and predicted AlphaFold protein structure, validation that pgKylation has functional effect is of great importance. For validation of these sites, in vitro substrate turnover experiments utilizing recombinant proteins with K to E mutations to mimic pgKylation on the active site lysine(s) in question would serve as validation as to whether pgKylation induces loss of enzymatic activity.

Beyond protein level enzymatic measurements, systemic profiling of the downstream effects of pgKylation of a given enzyme could be accomplished by utilizing an engineered glucose consuming strain of cyanobacteria such as the GalP strain[156] and measuring the metabolomic profiles of the cyanobacteria with respect to incrementally increasing

concentrations of glucose fed under dark conditions. This would enable us to identify whether increasing glucose metabolism (and therefore increasing pgKylation) of a given enzyme changes the steady state amounts of its substrates and products. Utilizing isotopically labeled glucose in pulse-chase experiments would in turn capture altered flux or directionality of metabolism. Finally, it would be of great interest to investigate the lipidomic profiles of cyanobacteria between light/dark phases to determine whether pgKylation couples and regulates cyanobacteria bioenergetics with lipid metabolism. The presence of pgK on active site lysine K347 of bifunctional protein GlmU used to build membrane and cell wall polyliposaccharides within the proteomics dataset hints at the possibility that pgKylation regulates not only the distribution of carbon between bioenergetics versus biosynthesis but may also control which specific biosynthetic pathway that carbon is directed towards. Moreover, GlmU's use of acetyl-CoA as a substrate may indicate that other highly conserved rmPTMs, such as CoA species deriving from fatty acid metabolism, should also be searched within the cyanobacterial proteome to determine whether they also play roles in feedback regulating cyanobacterial metabolism. Collectively, these experiments would prove that rmPTMs, including but not limited to pgK, are of intrinsic importance in feedback regulating metabolism across life and underscore the importance of analyzing future metabolism studies additionally at the rmPTM level. Specifically, within the context of cyanobacteria, the greater understanding in metabolic regulation will pave efforts in engineering artificial strains optimized to produce products needed for a wide range of fields including bioenergy, natural products, medicine, agriculture, and environmental engineering. [157]

Additional Figures

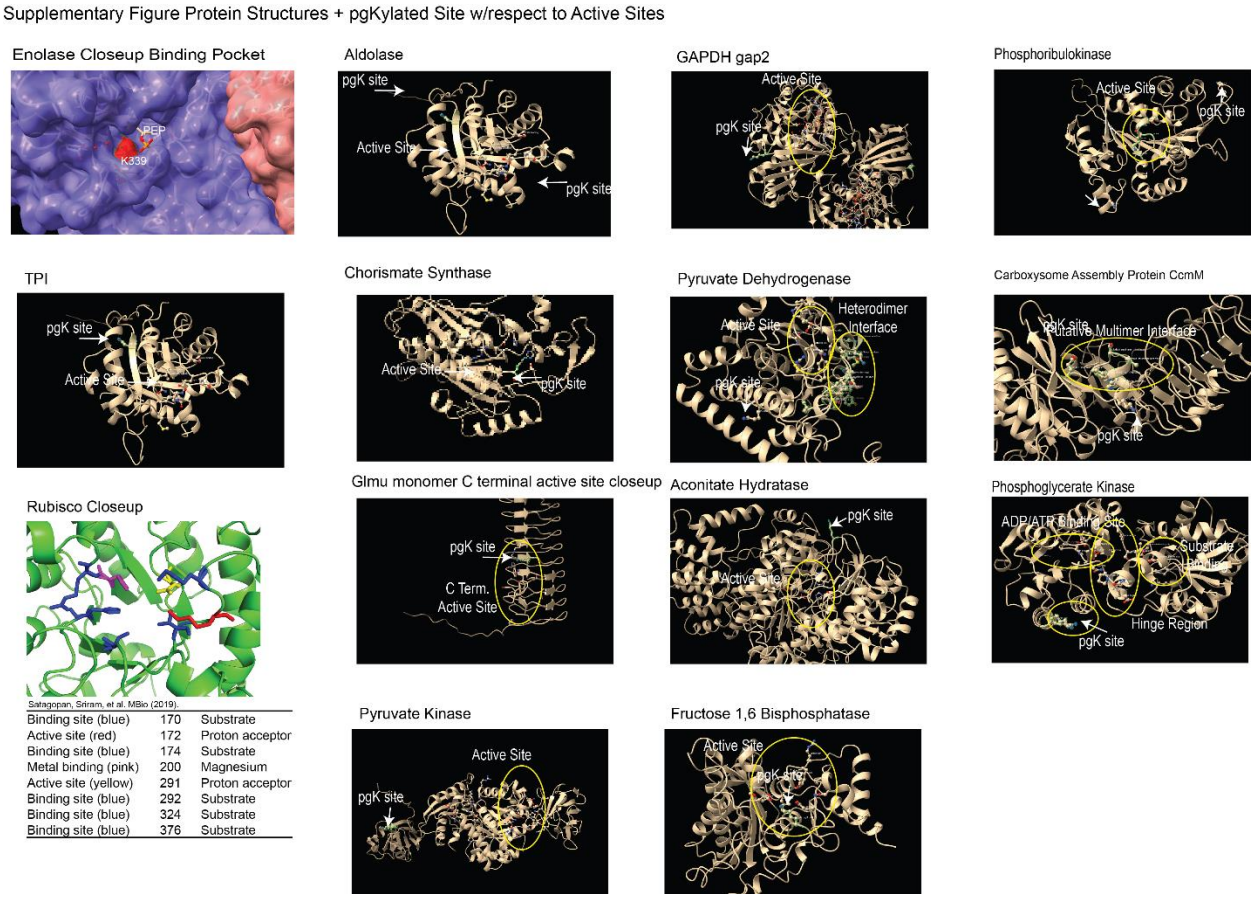

Figure 3.5: Site of pgK on Structures of Central Metabolic Enzymes: Validated or putative active sites from UniProt compared against pgK phosphoproteomics sites found in Figure 3.1D.

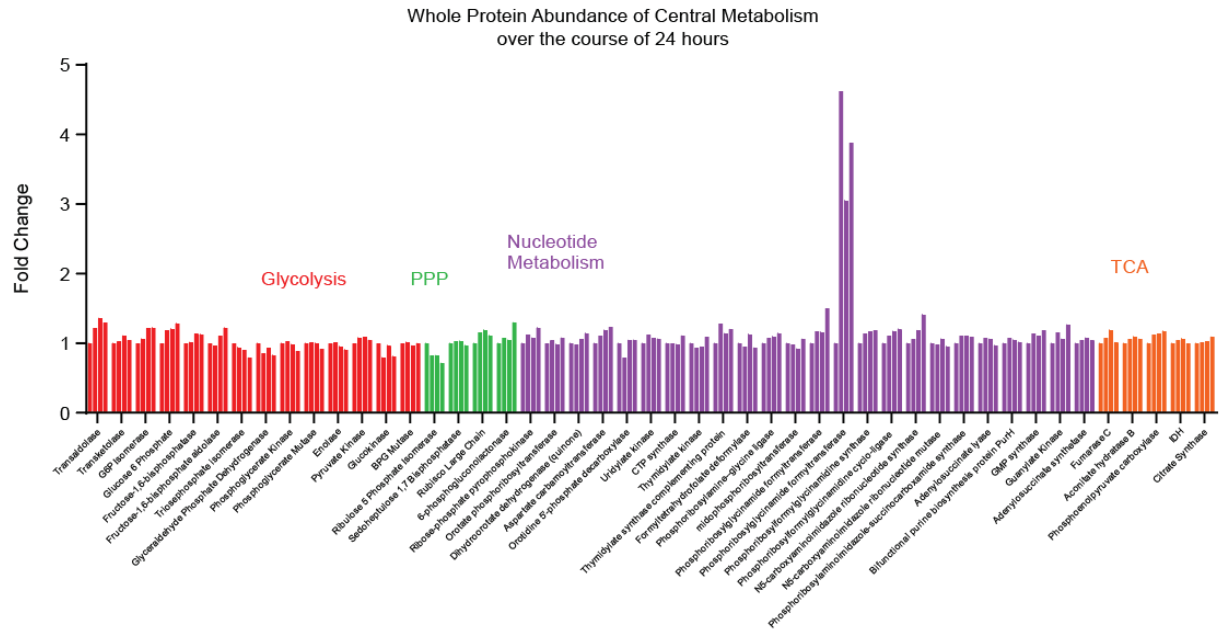

Figure 3.6: Whole Protein Abundance Changes Across 24 hrs. of Central Metabolic Enzymes: Fold change of central metabolite proteins across a 12-hr. light, 12 hr. dark cycle from protein expression data quantified in Figure 3.1C. using average TMT intensity values across 4 bioreplicates normalized to the 6-hr. light timepoint.

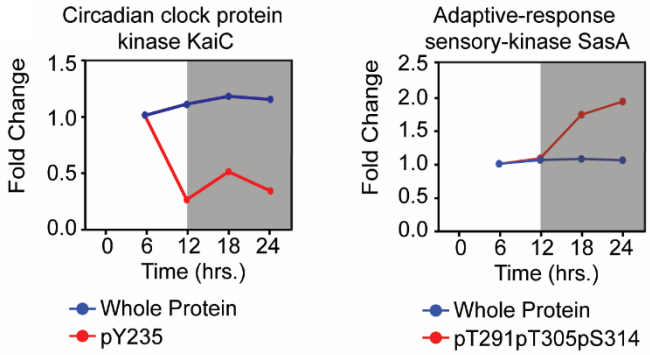

Figure 3.7: Novel clock-protein phospho-sites oscillate with respect to light/dark exposure: Total protein abundance (blue) and phospho-protein abundance (red) of clock proteins KaiC and SasA from Figures 3.1C and 3.1D. using average TMT intensity values across 4 bioreplicates normalized to the 6-hr. light timepoint.

Tables

Table 3.1: High Quality pgK sites quantified in Figure 3.1D normalized to whole protein abundance:

ACCESSION	SEQUENCE	norm_average 12hr light/6hr light ratio	norm_average 6hr dark/6hr light ratio	norm_average 12hr dark/6hr light ratio
Q31RH2	K.LK(229.1629)TWLQVEIAVCEAQAELGYIPADAVETIK(167.98238)AK(229.1629)ANFDPAR.V	0.457416	2.752254	4.936565
Q31RH2	K.LK(229.1629)TWLQVEIAVCEAQAELGYIPADAVETIK(229.1629)AK(167.98238)ANFDPAR.V	0.874732	2.715723	4.197145
Q31LU5	R.EEGLRIYEDMVLGRTFEDK(167.98238)CAEMYYR.G	0.664553	2.918014	3.610589
Q31QV9	R.LGTFQPSADLADYLAHK(167.98238)YSR.D	2.086188	2.027603	2.580814
Q31MT6	K.TGDIAMVVGDVGLIDMPSGK(167.98238)R.Y	2.054067	2.706838	2.331174
Q31NS8	R.K(167.98238)VVLCAPFTTLSSLSK(229.1629).T	2.00443	1.732203	2.29578
Q31PU8	R.IACADLIVGK(167.98238)ELNEPEVMNSR.G	1.955056	2.561942	2.140859
Q55108	K.ITQISGGMK(167.98238)QR.V	0.825059	2.482728	2.10902
Q31RS5	R.VAFK(167.98238)PTATIRK(229.1629)EQETVTNSGEATTLAAR.G	1.749207	2.334309	2.05788
Q31LG9	R.ALSAK(167.98238)VPEFNDLGLPQVVREM(15.9949)SEK(229.1629)PR.G	1.247029	0.191523	1.980891
Q31QJ8	R.LQSGIEQGVGNAVLIK(167.98238)LNQIGTLTETLR.T	1.706492	1.671627	1.853852
Q31KK8	K.VTEAQAVK(167.98238)LEGGYPRLLETVQR.L	1.081042	2.370702	1.85128
Q31MT0	R.QGLLRFWGETQAEMAEK(167.98238)ALALGK(229.1629).V	1.013884	1.678617	1.833898
Q31L83	K.IPSTPGSLK(167.98238)DALK(229.1629).A	1.010515	1.308586	1.762914
Q31NF6	R.SYK(167.98238)NLEK(229.1629).K	1.284354	1.306563	1.749455
P0A3F4	R.TGEIGDGK(167.98238)IFVSPVDQTIR.I	1.513216	1.546168	1.653037
Q31NG1	R.DAM(15.9949)K(229.1629)AWDGLPGLLVK(167.98238)VPLLGNAIASLINTLALR.K	1.010737	1.200339	1.576766
Q31L88	K.PFKVTPK(167.98238)GDTNSDGITINWSLITPLLTVM(15.9949)ILTIIGIVMR.S	0.814463	2.29826	1.574141
Q31L17	R.YAGVGDVIIAVVK(229.1629)DALPNM(15.9949)PVK(167.98238)KSDVVR.A	0.588912	0.323239	1.522485
Q31QR1	K.EGFAVLPYINADPLLAK(167.98238)RLEEVGCATVMPLGSPIGSGQGIR.N	1.000629	1.089566	1.460474
Q31MQ5	-.MNRVAIFGNAGGGK(167.98238)SALSR.R	0.891294	1.528951	1.382571
Q31LM6	-.M(15.9949)K(167.98238)QRSPWLLR.G	1.01593	1.535788	1.355813
Q31Q80	K.IPYQFGYQFTEVDNK(167.98238)K(229.1629).R	0.437156	0.791713	1.353892
Q31PD8	R.YPVRQSGTVQFK(167.98238)VPYAR.M	1.254177	1.181446	1.327234
Q31NF6	K.LLCVPAK(167.98238)DPR.Y	1.521357	1.686808	1.317757
Q31LU2	R.EGPVSLDLAPDGLAVIFDQPIAPDK(167.98238)TAVNR.S	0.610869	1.57968	1.287424
Q31KU8	R.ADAEAFANATQLIANCSGK(167.98238)VVLSGVGK(229.1629)SGIIAR.K	0.930768	1.077389	1.278822
Q31KL3	K.VWAADFETAK(167.98238)YDVRAVLGVR.G	1.364061	1.172557	1.182901
Q31KM0	K.DAFQK(167.98238)ANFQRFGNGLVGLAR.E	0.689312	1.000934	1.175129
Q31S06	R.K(167.98238)QLEK(229.1629)LQLNVSQFLEGR.T	0.977035	1.019502	1.156659
Q8VW88	K.FTRK(167.98238)PTGEILAISRIEEIHR.R	2.428471	1.377549	1.118624
Q31RG0	R.IVK(167.98238)QAGNQLFQK(229.1629).R	0.878472	1.164609	1.070186
P50021	R.AK(167.98238)FEELASDLIDR.C	0.893853	0.880121	1.049096
Q8GIS1	K.K(229.1629)NPDVPELVRGK(167.98238)TGR.V	0.920379	0.903093	1.003999

Table 3.1 continued

ACCESSION	SEQUENCE	norm_average 12hr light/6hr light ratio	norm_average 6hr dark/6hr light ratio	norm_average 12hr dark/6hr light ratio
Q31LK4	K.NYWYPVALAQK(167.98238)VGDRPLSVTLCGEAIALYRDSAGQIHALSDR.C	0.396589	1.012243	0.968029
Q31M79	K.LQDSETEATAQAVGRILGSLCVLTTQK(167.98238)EDVR.S	1.087502	1.026481	0.940457
Q31S87	R.EYEFPFTHRAGLIFMEDTYITPSGK(167.98238)ER.A	1.30678	1.02561	0.939473
Q31KM4	R.TLAAADNAVM(15.9949)LEDAAK(167.98238)GLEPQTR.K	1.669907	1.065761	0.904935
Q31P58	K.DAEGEIAAILTEWNGK(229.1629)PISANFPYLVSFSNK(167.98238)FRAHLR.D	1.571572	0.722885	0.877323
Q31QC1	R.MPLGLDATPLGVK(229.1629)QAEAK(167.98238)AHQVGLELQMDRFR.W	3.193393	0.870653	0.855555
Q54769	K.VVGLSK(167.98238)LAR.I	0.634247	0.992398	0.81443
Q31KK9	R.VQK(167.98238)LVDDLVAR.G	0.803595	0.683814	0.813234
Q31PI7	K.EQVFELPTGGAAVMHEGDNLLYFARK(167.98238)EQALALGTQLR.T	0.656006	1.035218	0.804565
Q31QC4	R.NLVISM(15.9949)K(167.98238)ASR.A	0.852111	1.704865	0.803813
Q31RJ9	R.IGNFVEVK(167.98238)K(229.1629).S	0.780907	1.276896	0.756185
P54207	K.YIEAVPMPVLEVLPLIEDIRISRVK(167.98238)GK(229.1629).T	0.848533	1.088072	0.753769
Q31S91	K.LK(167.98238)LRERFSLAR.A	1.001848	0.733708	0.752084
P06539	R.LVAEGNK(167.98238)RIDTVNR.I	1.258169	0.651712	0.718725
Q31Q29	R.YLRK(229.1629)ELLWPHLYTFADAILQYLAQQK(167.98238)R.T	0.574264	0.610589	0.716732
Q31RY1	R.ASTLVDK(229.1629)LRSQLPSLTGQK(167.98238)LGAYTVAYADDFR.Y	1.585039	0.688349	0.713325
Q31M24	K.LWMDGVLATSIWPGQRVDIRM(15.9949)AEK(167.98238)PAQFLVLDSDR.S	9.366382	0.821001	0.686246
Q31RG0	R.IK(167.98238)TFVVGGDRR.L	0.697632	0.639501	0.642287
Q31K05	R.ASK(167.98238)SALNMLTRTLALEWQRR.H	0.787865	0.808015	0.635145
Q31L88	K.PFK(167.98238)VTPK(229.1629)GDTNSDGITINWSLITPLLTVM(15.9949)ILTIIGIVMR.S	0.475801	0.377895	0.616005
Q31S41	R.VYAK(229.1629)DARILQTNLSFADEENLK(167.98238)AALEK(229.1629).A	0.87186	1.052107	0.610679
Q31LX8	R.VDATGAVQDYELQPSLVQLDQVLSPAEATDLLADSK(167.98238)AKGEGIK(229.1629)ALK(229.1629).E	0.974891	0.76477	0.598776
Q31RU6	R.VLCCENGK(167.98238)FGER.W	0.515849	1.636681	0.373679
Q31N57	R.LQSDGK(167.98238)VYVANVALYAPRDEQGNER.A	0.106649	0.263675	0.307784
Q31NL4	R.DIYRAAVQLHSQGQPTDLTSLTTSLQDAGQLDK(167.98238)VGGQSR.L	0.175258	0.284311	0.160046
Q31M72	-.M(15.9949)TK(167.98238)ILLVEDNEDNWDM(15.9949)LSRRLTR.K	0.484606	0.895062	0.984503
Q31NB3	K.YGRPMLGCTIK(167.98238)PK(229.1629).L	0.384351	1.802523	0.969653

Table 3.2: High Quality phospho sites quantified in Figure 3.1D normalized to whole protein abundance:

ACCESSION	SEQUENCE	norm_average 12hr light/6hr light ratio	norm_average 6hr dark/6hr light ratio	norm_average 12hr dark/6hr light ratio
Q31Q47	R.S(79.9663)GGGGNDNRR.S	1.862427	12.52604	10.25734
Q31L10	R.S(79.9663)GPVTPWGKPALGRK.T	1.680895	5.04664	4.90934
P0A3F4	R.Y(79.9663)RGSEYTVEFLQK.L	1.187757	4.533247	4.706637
P29686	R.S(79.9663)VPAYRDEEGADPQSFTPTYVAMK.L	0.96017	2.362337	3.622366
Q31L11	R.S(79.9663)LKKGPFVADHLLR.K	0.77288	2.088401	2.58809
P0A3F4	R.YRGS(79.9663)EYTVEFLQK.L	1.151095	2.404716	2.548414
Q8GJL0	R.SLTET(79.9663)ADPAITVVQGNPALWVSQLK.Q	3.959162	2.070603	2.500967
P29686	R.SVPAY(79.9663)RDEEGADPQSFTPTYVAMK.L	0.432746	1.633444	2.396783
Q06904	K.YT(79.9663)PPGGTITIAALHRT(79.9663)SQKVQISIS(79.9663)DTGSGIPRDQLSVIFK.N	1.030026	1.737861	2.004176
Q31NB2	R.RFETFSYLPPLS(79.9663)DR.Q	1.394263	1.47233	1.939969
Q31MB7	R.IVATNS(79.9663)TSRRDGLPLEELGFYNPR.T	1.134702	1.166018	1.936173
Q31Q58	R.YTVNEQDFRY(79.9663)PGPIPQSRETGIVMLADSCEAALRSLENAT(79.9663)M(15.9949)EDALR.M	2.064414	1.40966	1.918606
P0A3F4	R.GSEY(79.9663)TVEFLQK.L	1.115965	1.451301	1.846893
Q31Q44	R.QLT(79.9663)QQTEHIATLNRSLVDAERQVATAR.A	0.910447	1.664154	1.794557
Q31LB8	K.SLEDGPKHAILDLSKIDFIDSS(79.9663)GLGALVQLAK.Q	0.874274	1.605686	1.772751
Q8KUV6	R.KLAT(79.9663)Y(79.9663)QADLLIETVYGFGYRLRPS.-	1.357465	1.444222	1.713299
P38046	R.PT(79.9663)VLMITHDIDEALFLADR.V	1.677914	1.444832	1.671802
Q31PD9	R.QVLGNDYIM(15.9949)KSERLT(79.9663)AAES(79.9663)LLVNGSISVRDFVR.A	1.376474	0.631319	1.668377
Q31QZ7	K.YTEQELSRQAKT(79.9663)DELTGLINR.R	1.076153	1.493438	1.544254
Q31LB8	K.IDFIDS(79.9663)SGLGALVQLAK.Q	1.090779	1.1857	1.461048
Q31QS2	R.SLTGLQDPT(79.9663)VSLSPDSTTEFEA.-	1.535864	1.111702	1.453677
Q31PY2	R.LNPSDIQS(79.9663)PVGSVDASLVPFLR.G	1.795567	1.099737	1.447583
Q31LE3	R.LAQS(79.9663)DGLT(79.9663)GLANRR.H	1.28768	1.020094	1.318043
Q31L18	R.VAY(79.9663)TFTEDGRKVR.K	0.656734	1.548159	1.303233
Q31QS2	R.SLTGLQDPTVSLSPDS(79.9663)TTEFEA.-	1.921868	0.927563	1.261109
Q44115	R.RS(79.9663)ALMDLGAIGYLPAAPQIAQTLAENSLKLIS(79.9663)LKGLLDT(79.9663)HLR.Q	0.985189	0.906057	1.251153
P27134	R.CVVPLT(79.9663)EEVAVAPPEPEPVIAAVAAPPANYSS(79.9663)RGWLAPEQQQRIY(79.9663)R.G	1.737835	1.108617	1.246074
Q31NW3	K.QSLAYEVSAVFPTRLGPAPFVAY(79.9663)LGT(79.9663)AIENGPQALAALRSELDR.L	1.066717	1.199556	1.20383
Q31ME2	K.VPPS(79.9663)EDPAEFLET(79.9663)FDRSMSLLQTDY(79.9663)VDLLSIHGVNNAELLDWALR.K	0.987446	0.958307	1.178145
Q31MQ5	K.GWPEDSPLFKS(79.9663)SMSSYR.V	0.435988	0.388515	1.102003
Q31QK4	R.T(79.9663)T(79.9663)VALPKGTGQTIR.V	1.375107	1.026872	1.091208
Q31LJ4	R.IVTLDGELLETS(79.9663)GAMTGGS(79.9663)IARRSGGLSFGSPDSGESAEVRAIR.D	1.471549	8.035151	1.075919
Q31QS2	R.SLTGLQDPTVS(79.9663)LSPDSTTEFEA.-	1.397513	0.855491	1.010011
Q31NM0	R.TLNRLASQIVES(79.9663)ARQVDR.L	0.619899	1.166997	1.008768
Q31NB3	R.FSPQPGVPADEAGAAIAAESSTGTWTTVWTDLLT(79.9663)DMDRYK.G	0.913803	1.112214	1.003527
Q31PW3	R.LAEQIHPTEFVGY(79.9663)GDAVAT(79.9663)AK.V	1.631017	1.10793	0.953905
Q31QS2	R.SLTGLQDPTVSLSPDST(79.9663)TEFEA.-	1.442302	0.738818	0.953081
Q31NZ1	R.GRLAGS(79.9663)QRVTVTAADGT(79.9663)EK.T	1.484537	0.954256	0.952757
Q31QN7	R.KRPGLEALLQGS(79.9663)T(79.9663)GSIRPQ.-	0.886991	1.504437	0.937624
Q54755	K.LLEEAPSPALS(79.9663)ADLRQK.M	0.844968	0.592148	0.924591
Q6BBK3	-.MSDIQEKIEQARQEAHAISEEKGAT(79.9663)SPDAAAAWDAVEELQAEAAHQR.Q	1.426361	1.970422	0.923656
Q6BBK3	-.MS(79.9663)DIQEKIEQARQEAHAISEEKGATSPDAAAAWDAVEELQAEAAHQR.Q	0.885369	1.100729	0.891148
Q6BBK3	-.MSDIQEKIEQARQEAHAISEEKGATS(79.9663)PDAAAAWDAVEELQAEAAHQR.Q	0.9036	1.134488	0.879197

Q31QN7	R.KRPGLEALLQGS(79.9663)TGSIRPQ.-	0.917318	0.568434	0.8428
Q31N52	K.LRFNY(79.9663)GLSER.Q	0.66763	0.841428	0.803649
Q31RY1	R.QNGAFGGIILSAS(79.9663)HNPGGPEGDFGIK.Y	0.822897	0.623374	0.791716

Table 3.2 Continued

ACCESSION	SEQUENCE	norm_average 12hr light/6hr light ratio	norm_average 6hr dark/6hr light ratio	norm_average 12hr dark/6hr light ratio
Q31PW3	R.DY(79.9663)ASESESVKVSLK.V	0.886016	0.682113	0.702738
P31160	R.S(79.9663)GRPTRPGFEGGQMPLYR.R	0.975879	1.518579	0.697888
Q31RE0	K.ALRNEAY(79.9663)AR.K	0.722086	0.923997	0.692421
Q31RN5	R.NYCDEFPNADECRM(15.9949)Y(79.9663)DV.-	0.883899	0.335969	0.688357
Q31QS2	R.SLTGLQDPT(79.9663)VS(79.9663)LSPDSTTEFEA.-	1.337221	1.117319	0.661958
Q31QS2	R.SLTGLQDPTVS(79.9663)LSPDSTT(79.9663)EFEA.-	1.298172	0.949365	0.65576
Q79AV0	R.GY(79.9663)YRDFGLCR.N	0.756717	0.687578	0.652575
Q31QS2	R.SLTGLQDPTVSLSPDSTT(79.9663)EFEA.-	1.743691	0.601878	0.6525
P50590	R.ELAEQHY(79.9663)AVHR.E	0.430145	1.410693	0.646932
Q31NH0	R.EY(79.9663)KGLYHVLGGLISPMDGIGPEQLTVQALVR.R	0.216408	0.582657	0.626793
Q31LW9	R.LVQTASQVEAT(79.9663)TAADDKAEKDLRR.A	0.919599	0.652545	0.625946
P42452	-.MAEQPLIGKTILTTRAAGQS(79.9663)S(79.9663)PFAAQLR.A	0.530086	0.901137	0.624999
Q31QC1	R.YLSS(79.9663)KR.G	0.945318	0.509837	0.622954
Q79AV0	R.GYY(79.9663)RDFGLCR.N	0.691098	0.970126	0.620903
Q31MJ5	R.DRLIALLPAPS(79.9663)QGLAIFAS(79.9663)DQRLWQR.S	0.500462	0.722518	0.612552
P06539	R.IDTVNRITGNASS(79.9663)IVANAAR.A	1.239894	0.900402	0.589721
P06539	R.GEFLSDAQLDALS(79.9663)R.L	1.361222	0.53808	0.584513
Q31NS8	R.KVVLCAPFTT(79.9663)LSSLSKTLHGS(79.9663)RVR.V	0.623999	0.554138	0.569893
Q8RQ68	R.WWADFT(79.9663)LQTKLMAIATLVVSLIMSGLTFWAVNS(79.9663)IQEDARLNDTR.F	1.795241	0.533801	0.54663
Q31NE2	K.FGNFAEAHKDDLGQLLT(79.9663)SAQGK.A	0.825235	0.491233	0.544744
Q31KT2	K.S(79.9663)S(79.9663)RS(79.9663)DLATKIDNILVVK.E	0.396587	0.61336	0.540418
Q31MW5	K.EYYFYVDNT(79.9663)PTHS(79.9663)Y(79.9663)MR.W	0.945335	0.713134	0.532129
Q31LS4	R.GATQIVAVATS(79.9663)AVR.E	0.752795	0.37421	0.51062
P06539	R.ITGNAS(79.9663)SIVANAAR.A	0.818328	0.367362	0.497762
Q31NI4	R.YEEELSFSASHDVLT(79.9663)GLPNRAVLEDRLR.Q	1.237818	0.864052	0.485333
Q31QN3	K.AMTQKS(79.9663)VVIAPS(79.9663)ILSADFSR.L	0.815198	0.420746	0.472898
Q31LS4	R.GATQIVAVAT(79.9663)SAVR.E	0.957666	0.714059	0.471822
Q31K48	R.VQPYEGVVIANS(79.9663)GGGINES(79.9663)ITVR.R	0.38793	0.423252	0.445693
Q31MA2	R.QRGHNPS(79.9663)CGDT(79.9663)IELTLS(79.9663)LDEAGDR.I	0.462803	0.518854	0.440803
Q31K49	R.QS(79.9663)IS(79.9663)IDLGNAAGELRFFPSQLRLK.A	0.814128	0.531649	0.439264
Q31P68	K.AAAAEAVS(79.9663)QFAQR.R	0.682735	0.508885	0.419644
Q31MC8	R.DQVTQAELDLEAALEDLQLTVSEAYY(79.9663)R.L	1.173378	0.683027	0.415789
Q31NM6	R.T(79.9663)HYCGELRAEQVGTS(79.9663)VTLY(79.9663)GWVDR.R	0.178819	0.281396	0.365246
Q8GIR7	K.AEPPS(79.9663)DQMLSELLLAAT(79.9663)RT(79.9663)LAAEARDHLEAASAELK.Q	0.468292	0.295536	0.357514
P13530	-.MS(79.9663)KTPLTEAVAAADSQGR.F	0.714466	0.466005	0.339397
Q31L59	K.TKFS(79.9663)LPFPLVADPDR.S	0.218962	0.397657	0.317
Q31RJ1	R.GSGEPLQAIS(79.9663)LAR.R	0.647652	0.607328	0.302659
P13530	-.MSKT(79.9663)PLTEAVAAADSQGR.F	0.857711	0.473394	0.26027
Q79PF4	R.GTSHMKGEY(79.9663)PFTITDHGINIFPLGAM(15.9949)R.L	0.193143	0.403696	0.257237
Q31LM6	R.S(79.9663)QQLRNLT(79.9663)ADLEAIVRNPSLSR.D	0.33135	0.321221	0.23179
Q31RG0	K.S(79.9663)LGTPIEAVAEGVR.E	0.665192	0.407401	0.778697
P50590	R.KLIGAT(79.9663)NPLTAEPGTIR.G	0.703846	0.647231	0.711307

Table 3.3: Changes in metabolic intermediates measured by full scan metabolomics:

Metabolite	norm_average 12hr light/6hr light ratio	norm_average 6hr dark/6hr light ratio	norm_average 12hr dark/6hr light ratio
1-Methyladenosine	1.232519716	1.355031073	1.429821533
2'-Deoxyadenosine	0.969574346	0.950699441	1.448489322
2-hydroxyglutarate	1.055545046	1.140315917	1.336938951
2-Keto-3-Deoxy-D-Gluconic Acid/Gluconolactone	1.012378023	1.414076787	1.325823905
2-Methylmaleate	1.010760528	1.501662318	1.092274551
2-phosphoglycerate/3-phosphoglycerate	1.009469376	0.910734163	0.777955306
3-(2-Hydroxyphenyl)Propanoate	1.116415392	1.381137735	1.200597148
4-Imidazoleacetate	1.335831992	1.133267626	0.783828015
5'-Deoxyadenosine	1.26720184	0.21621917	0.093425379
Acetyl-CoA	1.05959898	1.383270644	0.756888343
Aconitate	1.009743957	1.335525385	1.074374311
Adenine	1.019251309	1.157773007	1.190932677
Adenosine	0.792827288	0.977003005	1.487709383
Adenosine 5'-Diphosphate	0.958259117	1.113905455	1.083305269
Adenosine monophosphate/Deoxyguanosine monophosphate	1.001217898	1.519153423	1.786604874
Adenosine Triphosphate	0.810221121	0.785797007	0.559583272
ADP-Glucose	1.337545833	0.231056703	0.124938543
Alanine	0.934512429	0.759749775	0.60820488
Allothreonine/Threonine	1.084274153	0.339004622	0.365746052
Anserine	0.780674075	1.123150394	2.416629376
Arachidate	1.120251611	1.213051018	1.408746784
Arginine	0.731828035	0.917173657	0.755609155
Aspartate	1.121987749	0.302915072	0.166129566
Azelate	0.872261954	1.240277023	2.67462822
Beta-Alanine	1.073366813	1.108479252	1.056273354
Betaine	1.005580315	2.370570292	1.965181687
Carnitine	1.806235597	1.70136653	0.96703744
Cellobiose/Maltose/Lactose/Trehalose_02	0.920761365	0.891626144	0.715648771
Choline	1.281469986	1.336355069	1.617677948
Citramalate	0.689335971	0.875547955	1.201428508
Citrate	1.013828086	1.177936647	1.191496471
Citrulline	0.886731707	0.515818715	0.586596667
Creatine	1.608588092	2.063250378	1.046767959
Cysteate	1.247733482	1.465338539	0.97899255
Cytidine	1.245998009	1.072884486	1.791801424
Cytidine 5' monophosphate(5'-CMP)	1.161363542	1.69525425	2.388019192
Cytidine Diphosphate	0.875804517	1.112288159	1.250476581
Cytidine monophosphate(CMP)	1.06531064	1.600283229	2.323934963
Decanoate	1.103701019	1.382968387	1.272636865
Deoxyguanosine	0.806403031	1.097680149	1.563238322
D-Sedoheptulose 7-phosphate	0.91546883	0.331182413	0.34715862
Ethyl 3-Ureidopropionate	1.461119358	0.985663211	4.73649368
FAD	0.736107964	0.795253101	0.867999359
Fumarate	0.859866504	0.870555365	1.042704418
Gluconate	0.9704101	1.1925533	1.071719542
Glucose 1-Phosphate/Fructose 6-phosphate	0.746352787	0.230877024	0.312371655
Glucose 6-Phosphate	0.812886237	0.160802753	0.186083206
Glutamate	0.997556214	1.019360318	0.850847606
Glutamine	0.569906349	0.405508928	0.451448354
Glutathione oxidized	1.134708171	1.256567287	1.240023817
Glycerate	1.101202226	1.164294052	0.949271284
Glycero-3-Phosphocholine	0.927137751	1.629005861	1.090033729
Glycerol 3-Phosphate/Glycerol 1-Phosphate	1.071797421	0.831822213	0.647697562
Glycine	0.299961107	1.202241265	2.500753505
Glycolaldehyde Dimer	0.939944385	1.069704629	0.872830535
Glyoxylate	0.664415725	0.165534578	0.467149772
Guanine	0.991817264	1.391341316	1.071068092
Guanosine	0.890281063	0.992225806	1.347289453
Guanosine Monophosphate	1.003276428	1.1983238	1.464171741
Heptadecanoate	1.065119545	1.000890151	0.9601861

Table 3.3 Continued

Metabolite	norm_average 12hr light/6hr light ratio	norm_average 6hr dark/6hr light ratio	norm_average 12hr dark/6hr light ratio
Histidine	1.085613441	0.896368674	0.873091911
Homocitrulline	0.997552517	1.000912161	0.998739753
Homoserine	0.764490524	0.545391804	0.788279058
Hydroxybenzaldehyde/Benzoate	0.985762374	1.160667895	1.363426939
Hydroxyproline	1.006580112	1.523818566	1.397459973
Indole-3-carboxaldehyde (Indole-3-carbaldehyde)	0.867486646	0.656599348	0.946823883
Isobutyrate/Butyrate/Acetoin	1.017976397	1.138429177	1.421338628
Isocitrate	1.011940719	1.035218732	0.86236072
Isoleucine	1.151037795	1.303310545	1.101792755
Lactate/Glyceraldehyde	0.817972579	1.775920457	1.475437917
Laurate	0.948337233	1.699291333	1.566737313
L-Cysteine-glutathione disulfide	1.133122029	0.722912516	0.569570102
Leucine	0.776867625	0.550105746	0.356948525
Lumichrome	0.524731373	0.741129986	0.828174004
Malate	0.886407654	0.875734596	1.047351094
Mannitol/Galactitol/Hexitol	2.140944293	1.939323691	2.23229029
Methionine	0.371212856	0.198359681	0.455208307
Methionine Sulfoxide	0.771530737	0.692863344	0.543471248
Methylthioadenosine	1.031437082	0.581826133	0.598078822
Myristate	1.079650438	1.159621426	1.375844926
N,N,N-Trimethyllysine	0.965882827	1.02668926	1.140650638
N,N-Dimethylarginine	0.887890667	1.001015358	1.075066819
N6-(Delta2-Isopentenyl)-Adenine	0.886493092	1.110373675	1.099998638
N-Acetylasparagine	0.477126042	0.24637223	0.287285785
N-Acetylaspartate	1.101402807	0.893698542	0.683615951
N-Acetylglucosamine -phosphate	2.02659431	0.656757866	0.379199948
N-Acetylglutamate	1.015134041	0.598620591	0.361875896
N-Acetylleucine	0.998513484	1.129881632	1.148598485
N-Acetylproline	1.059155032	1.120403703	1.110825488
NAD+	0.719996571	0.479853703	0.304167237
NADP	1.037554068	1.232207844	1.261285939
N-Formylglycine	0.236131996	0.264140344	0.491774129
Nicotinamide	1.041582784	1.058625827	0.769850693
Nicotinamide Mononucleotide	0.661188502	0.365730135	0.409592702
Nonanoate	1.126723355	1.174030813	1.322392346
Norvaline/Valine	0.534460408	0.329660089	0.277165692
O-Acetylcarnitine	1.917412789	1.62351371	0.656392079
Ophthalmate	1.051003437	0.662831693	0.571534694
Orotate	1.067067601	1.195354565	1.214050851
Oxoglutarate (alpha-Ketoglutarate)	1.186245703	1.089228479	1.062227074
Palmitate	1.016459434	0.946244222	1.032158743
Palmitoleate	0.95699072	1.064269689	1.250594441
Petroselinate/Elaidate/Oleate	1.124414075	1.115380873	1.473358814
Phosphoenolpyruvate (PEP)	1.793085094	1.140642466	0.699510692
Phosphorylcholine	2.109908053	1.454963504	0.406441077
Proline	0.832767287	0.847302352	0.920275256
Pterin	0.90730097	1.113498264	0.88903774
Pyridoxal	1.331491795	1.596646662	1.251136017
Pyruvate	1.442465644	0.846348883	0.934728331
Quinate	1.101285412	0.9864948	0.859817057
Raffinose	0.906813556	1.110746053	1.075839053
S-Adenosylhomocysteine	0.973259079	0.700509307	0.617486712
S-Adenosylmethionine	1.022903825	0.682993056	0.88377386
Salicylamide	1.340480683	1.046105232	1.176041354
S-Carboxymethylcysteine	1.029989829	1.066037724	0.965010619
Serine	1.232879535	0.257653615	0.24474998
Sorbate	1.739183632	1.522189226	1.883598603
Stachyose	0.858115073	0.833182948	0.926906043
Stearate	1.091644167	0.998399733	0.950188463

Table 3.3 Continued

Metabolite	norm_average 12hr light/6hr light ratio	norm_average 6hr dark/6hr light ratio	norm_average 12hr dark/6hr light ratio
Suberate	0.802942505	1.286899513	1.691761547
Succinate	1.135972751	1.288031574	1.283718027
Threitol/Erythritol	1.199315522	1.266146937	1.190539839
Thymidine	1.164384878	1.241947517	1.364467366
Thymidine-Monophosphate	0.853997298	1.233935266	1.362159015
Trans-1,2-Cyclohexanediol/Hexanoate	1.442728432	1.43431443	1.23216332
Treahalose/Maltose/Cellobiose/Lactose_01	1.524147291	1.46222184	0.869003077
Trigonelline	1.096142018	1.351484767	1.345796148
Tryptophan	0.315271326	0.174934	0.188617582
Tyrosine	0.878275956	0.115844529	0.138949477
Ureidosuccinic acid(Carbamoyl aspartate)	0.926583238	0.530738749	0.813822742
Uridine	1.046658056	1.264285355	2.499521382
uridine 5′-diphosphate	0.995453428	1.885936857	2.023291716
Uridine 5'-diphosphate (UDP)	1.016389175	1.998703129	2.261633628
Uridine Diphosphate Glucose/Uridine Diphosphategalactose	0.82199581	0.795907896	0.78346391
Uridine Diphosphate-N-Acetylglucosamine/Uridine Diphosphate-N-Acetylgalactosamine	0.913317979	0.441960924	0.257711585
Uridine Monophosphate	1.108138327	1.581971531	2.35082596
Urocanate	0.885611657	1.930166512	2.537908096
Xanthine	1.134501339	1.514156369	1.277145798
Xanthosine	0.979875785	3.359800218	5.42780103
Xanthosine-Monophosphate	1.047057677	3.847747903	4.536900435
Xylitol/Ribitol/Arabitol	1.14555883	1.449112996	1.190332034
ATP/ADP	0.809931896	0.652742927	0.489711454
Hexonate	0.749561153	1.474660161	1.489437878
Hexose phosphate	0.966133539	0.709976203	0.658590889

Table 3.4: Changes in central metabolic intermediates measured by MRM:

Metabolite	norm_average 12hr light/6hr light ratio	norm_average 6hr dark/6hr light ratio	norm_average 12hr dark/6hr light ratio
Glyceraldehyde 3 Phosphate	0.767975	0.034302	0.907285
Ribose 5 Phosphate	0.718475073	0.041069185	0.359006019

CHAPTER 4. PARK7 CATALYZES STEREOSPECIFIC DETOXIFICATION OF METHYLGLYOXAL CONSISTENT WITH GLYOXALASE NOT DEGLYCASE FUNCTION

The work of this chapter is based on the published work: Coukos, J. S., Lee, C. W., Pillai, K. S., Shah, H., & Moellering, R. E. (2023). PARK7 Catalyzes Stereospecific Detoxification of Methylglyoxal Consistent with Glyoxalase and Not Deglycase Function. Biochemistry, 62(21), 3126-3133.

Author Contributions: J.S.C. performed chemical synthesis, biochemical assays, and mass spectrometry analysis. C.W.L performed biochemical assays and mass spectrometry analysis of lactate production. K.S.P. performed chemical synthesis and biochemical assays. H.S. assisted with lactate derivatization and mass spectrometry analysis. R.E.M. supervised research. J.S.C. and R.E.M. conceived the study, analyzed data, and wrote the article.

Abstract

The protein PARK7 (also known as DJ-1) has been associated with several diseases, the most notable being neurodegenerative diseases such as Parkinson's Disease. While a myriad of molecular and cellular roles has been attributed to DJ-1, there is no real consensus on its true cellular functions and how loss of DJ-1 function contributes to pathogenesis. Recent studies have implicated DJ-1 in the detoxification of several glycolytic reactive metabolites, the most notable being the α-oxoaldehyde species methylglyoxal. While it is generally agreed that DJ-1 metabolizes methylglyoxal to lactate, its mechanism is hotly debated, with potential implications towards its function. In this work, we provide definitive evidence that recombinant DJ-1 produced in human cells prevents stable glycation of proteins via the conversion of methylglyoxal or a methylglyoxal derived alkynyl-dicarbonyl probe to their corresponding α-hydroxy carboxylic acid products. This protective mechanism of DJ-1 does not require physical interaction with a target protein, supporting a glutathione-free glyoxalase mechanism of action, not a deglycase mechanism. Stereospecific LC-MS measurements further confirm that DJ-1

almost exclusively produces L-lactate from methylglyoxal and that previously reported D-lactate production is caused by parallel non-enzymatic conversion of methylglyoxal to lactate in the presence or absence of DJ-1. Collectively, these studies provide direct support for the stereospecific conversion of MGO to L-lactate by DJ-1 in solution, with negligible or no contribution of direct protein deglycation.

Introduction

Protein DJ-1, produced by the *PARK7* gene, is implicated in familial Parkinson's Disease, where homozygous or compound heterozygous mutations were found to lead to early-onset of the disease.[158-161] DJ-1 is a 189 amino acid protein that is ubiquitously expressed and is primarily cytosolic,[162] though observed in the mitochondria and nucleus.[163, 164] In addition to its causative role in Parkinson's Disease, DJ-1 appears to have relevance in a variety of disease and other physiological contexts, such as being implicated as a potential oncogene in breast and other cancers,[90, 165, 166] or protecting mouse models from glucose intolerance and reduction in β-cell area as a function of age,[167] suggesting that DJ-1 might provide a protective function in the context of diabetes. This is further supported by experiments that show DJ-1 is highly upregulated by islet cells in response to glucose challenge.[168] Additionally, DJ-1 may preserve proper cellular function with aging as demonstrated by studies showing DJ-1 as an integral part of regulatory T cell function in aged mice.[169] In addition to the complex roles that DJ-1 plays in pathophysiology, pleiotropic molecular and cellular functions have been ascribed to DJ-1 including as a chaperone, a transcriptional regulator, protective antioxidant enzyme, and mitochondrial maintenance protein[170-173]. More recently, reports have highlighted the role that DJ-1 plays in the detoxification of reactive metabolites produced during glycolysis such as α-oxoaldehyde methylglyoxal[84-87] and 1,3-biphosphosphoglycerate (1,3-BPG), a highly reactive metabolites that can modify a variety of nucleophilic amines in cellular proteins and metabolites.[57, 60, 174]

Methylglyoxal (MGO) is a highly reactive metabolite produced by the degradation of the triose phosphates glyceraldehyde phosphate (GAP) and dihydroxyacetone phosphate (DHAP),

which interconvert within glycolysis through the enzyme triosephosphate isomerase. Like 1,3 BPG, MGO can chemically modify a variety of nucleophilic biomolecules including proteins, nucleic acids, and even metabolites.[31, 109, 175-179] The abundance of MGO-modified proteins has been associated with a number of diseases with dysregulated metabolism including diabetes, cancer, neurodegeneration, and aging,[101, 180-182] with Parkinson's Disease-specific connections putatively explained by a role for DJ-1 in protecting against accumulation of glycated alpha synuclein.[183, 184] MGO is principally detoxified by the glyoxalase system, which consists of enzymes GLO1 and GLO2[185-187]; reacting with reduced glutathione (GSH) to form a reversible hemithioacetal which is then converted to lactoyl-glutathione (Lac-GSH) by Zn^{2+} metalloenzyme GLO1.[188].GLO2 then hydrolyzes Lac-GSH to recycle the GSH and produce D-lactate.[189] D-lactate can then be further metabolized to pyruvate by lactate dehydrogenase D (LDHD).[190]

DJ-1 was first reported to detoxify MGO and related compounds in a GSH-independent manner in 2012.[85] Subsequent reports highlighted C106 and H126 as critical active site residues mediating this function as a catalytic dyad akin to those found in cysteine proteases such as the peptidase C56 family with which DJ-1 shares sequence homology.[85, 191] As with the glyoxalase system, detoxification of MGO by DJ-1 produces lactate. Despite a number of studies having examined the role of DJ-1 in MGO detoxification, the exact mechanism by which this occurs continues to lack consensus. While initial studies seemed to indicate that DJ-1 directly catalyzes the conversion of MGO to lactate in solution,[85] several recent studies have advanced the idea that DJ-1 acts as a so-called deglycase, i.e., an enzyme that removes reversible MGO modifications directly off of proteins or nucleic acids to produce lactate,[82, 90, 183, 192, 193] prompting a debate in the literature.[83, 194-198] The specific mechanism by which DJ-1 detoxifies MGO could have

significant implications for DJ-1's scope of protection against glycative stress and, by extension, its cellular function and role in disease. Thus, we sought to investigate the precise mechanism by which DJ-1 detoxifies MGO and protects proteins from glycation.

Results

Fig 4.1 Purified DJ-1 actively detoxifies methylglyoxal.

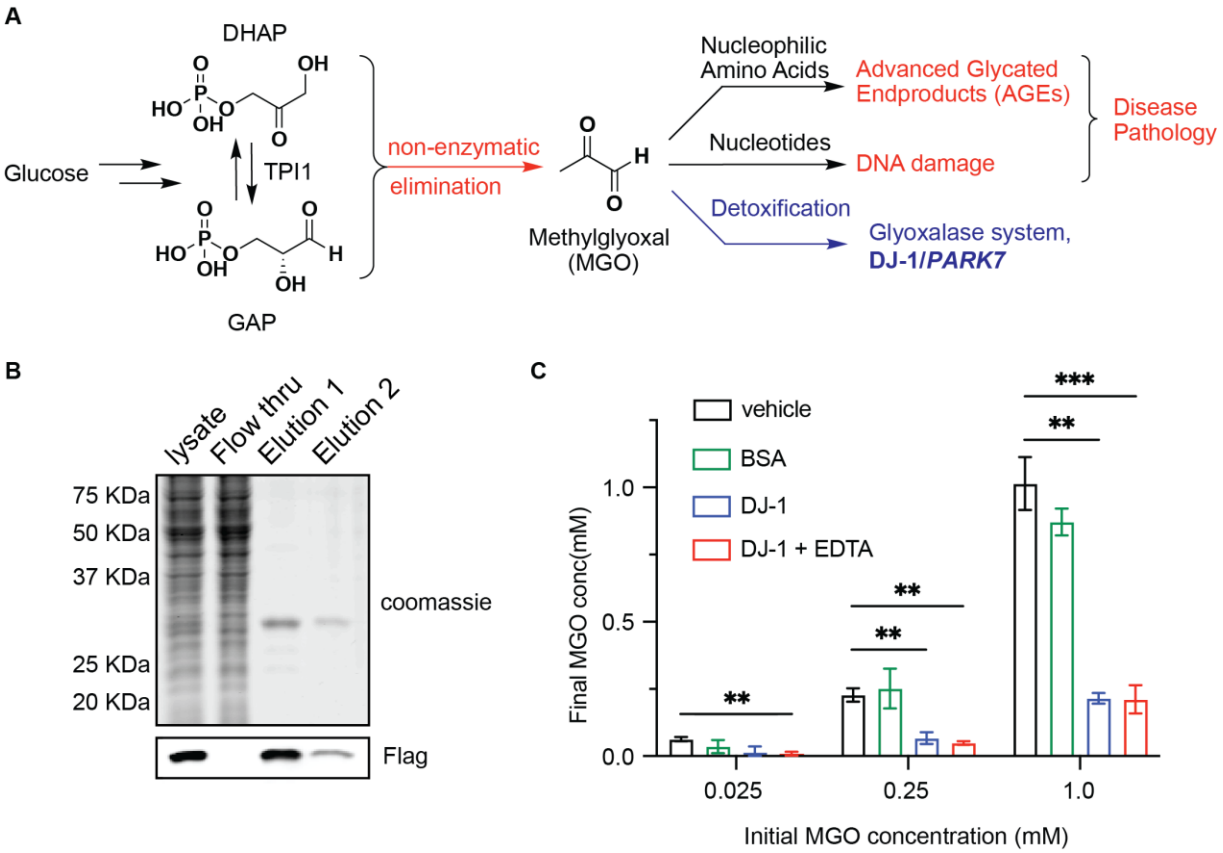

Figure 4.1 Purified DJ-1 actively detoxifies methylglyoxal: (A) Schematic depicting the formation and cellular fates of methylglyoxal. **(B)** Representative Coomassie gel and anti-FLAG western blot of purified FLAG-DJ-1 isolated from HEK293T cells stably overexpressing Flag-DJ-1. **(C)** MGO quantification in recombinant assays containing the indicated MGO concentration and protein condition following incubation for 24 hours at 37°C. Data plotted in (C) are mean ± S.E.M. from *n* = 6 independent biological replicates. Statistical analyses are by

ordinary one-way analysis of variance (ANOVA). *p< 0.05; **p< 0.01; ***p< 0.001; ****p< 0.0001.

Accumulation of MGO-derived adducts on proteins, collectively known as advanced glycation end-products (AGEs), have been correlated and causal in many diseases (Figure 4.1A). Multiple routes of detoxification of MGO have been identified, most notably the glutathione-dependent conversion to D-Lactate by the combined action of GLO1 and GLO2 (collectively referred to as the glyoxalase pathway in mammals). More recently, Parkinson's Disease associated protein DJ-1 has also been ascribed to detoxify MGO, though the mechanism by which it does so remains a matter of debate.[194] To enable study of this mechanism, we first stably expressed recombinant DJ-1 with a C-terminal FLAG-HA tag in HEK293T cells, which were used for anti-FLAG purification of active enzyme (Figure 4.1B). The structure of the recombinant DJ-1 was confirmed by proteomic analysis and quantification of protein concentration performed using gel-based measurements (Figure 4.6A-C, Table 4.1). We confirmed the activity of purified DJ-1 in MGO metabolism assays across several conditions and dose ranges (Figure 4.1C). Incubation of purified DJ-1 with MGO showed significant decrease in MGO levels across a range of concentrations (Figure 4.1C), which contrasted sharply with the negligible MGO depletion observed when incubated with control BSA protein alone to account for the potential removal of free MGO by adduct formation. Furthermore, addition of metal chelator EDTA to the reaction did not significantly affect the observed depletion of MGO by DJ-1, confirming the activity detected was not from low-level GLO1 or alternative metalloenzyme contamination.

While previous work has established the role of DJ-1 in detoxifying MGO and protecting proteins from glycation, significant debate still remains about its mechanism.[194] Studies have suggested that DJ-1 might behave as a glutathione-independent glyoxalase,[85, 196, 197] a glutathione-dependent glyoxalase,[199] or even an adduct-directed deglycase enzyme that removes MGO-derived modifications from proteins and nucleotides directly.[86, 87] While several recent studies have bolstered support for a glutathione-free glyoxalase model over a deglycase model, these papers either addressed proposed substrates that were not the early glycation hemiaminals and hemithioacetals[83, 197] proposed in the deglycase model, or relied on mechanistic inference from kinetic assays that were indirect and potentially open to interpretation.[198] Additionally, there remains conflicting reports regarding the stereochemistry of the lactate product of DJ-1 without satisfactory rationale to resolve these disparate results.[86, 197, 199] To conclusively rule out a deglycase model, it was necessary to determine whether direct interaction of DJ-1 with target proteins is required to protect them from MGO glycation. To do so, we utilized an analog of MGO with an alkyne handle for click chemistry derivatization to detect and quantify MGO-derived protein modifications on purified proteins, cell lysates and/or live cell proteomes. We devised a modified synthetic route for this α-oxoaldehyde, terminal alkyne containing probe (MG-alkyne) based on previously reported synthetic routes.[200, 201] Our route consisted of three steps to generate a stable acetal-protected precursor, which could undergo facile deprotection (Figure 4.7A) and direct use in biological experiments; this is necessary due to the reactive and unstable nature of the α-oxoaldehyde moiety. Once neutralized, the concentration of probe was determined by derivatization with amino guanidine and quantification based on a calibration

curve generated by serial dilutions of 3-amino-1,2,4-triazine (Figure 4.7B), a protocol originally developed to similarly quantify MGO concentration.[202]

Fig 4.2 DJ-1 detoxifies an alkynylated analog of MGO and protects proteins from modification.

We first confirmed that treatment of cell lysate with MG-alkyne followed by click chemistry derivatization with rhodamine-azide and in-gel fluorescence scanning revealed dose-dependent labeling of native HeLa proteome by the MG-alkyne probe; created from the formation of various stable adducts on target proteins (Figure 4.7C). Since the MG-alkyne probe is a reactive proxy for MGO, we sought to determine whether DJ-1 could enzymatically detoxify this larger pseudo-substrate and whether this activity could similarly prevent, or rescue MGO-mediated protein adduct formation. We treated MG-alkyne with purified DJ-1 or with BSA carrier protein and then performed targeted LC-MS analysis on the resultant reactions. Because MGO is metabolized to lactate by DJ-1, we hypothesized that the solution glyoxalase activity of DJ-1 could likewise convert MG-alkyne into the corresponding lactoyl-alkyne product (Figure 4.2A). As we expected, MG-alkyne levels were reduced and the corresponding lactoyl-alkyne product was generated in DJ-1 containing reactions, but not BSA control (Figure 4.2B).

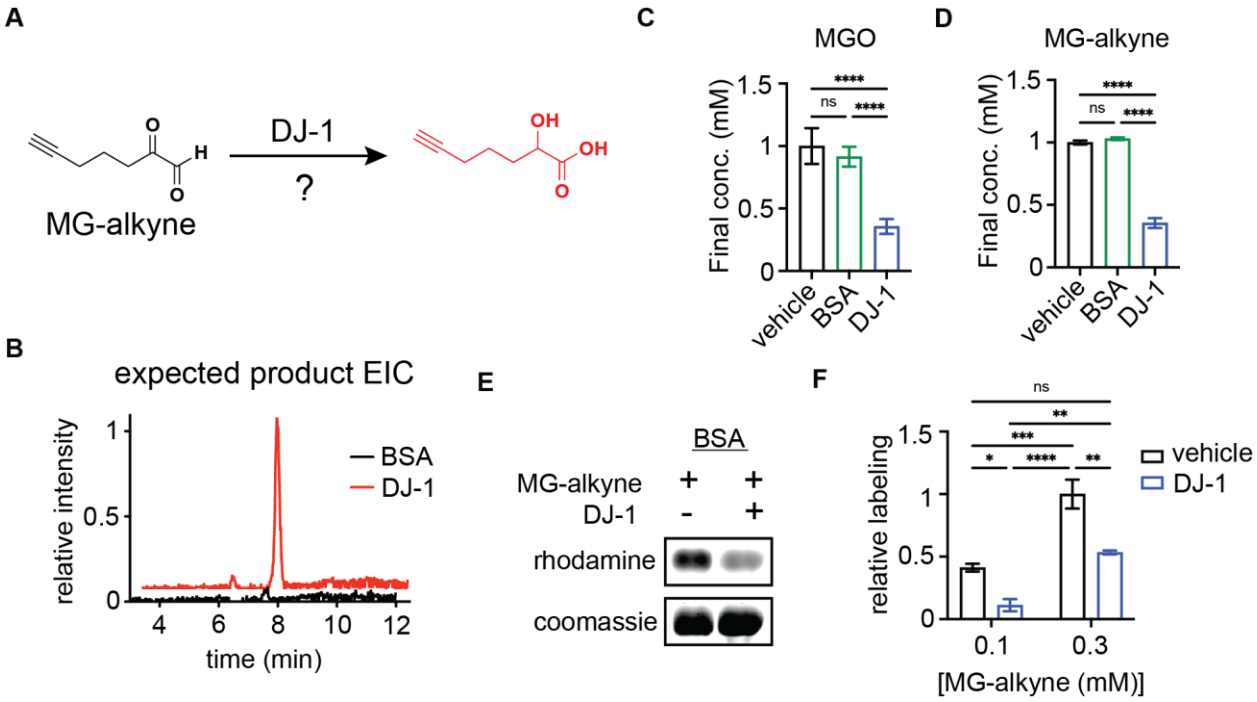

Figure 4.2 DJ-1 detoxifies an alkynylated analog of MGO and protects proteins from modification: (A-B) Structure **(A)** and extracted ion chromatogram **(B)** of predicted lactoyl-alkyne metabolic product of MG-alkyne treated with equal amounts of DJ-1 or BSA for 24 hours at 37°C. **(C)** Quantification of remaining MGO from reaction where 1 mM MGO was treated with equal amounts of recombinant DJ-1 or BSA, or with vehicle for 24 hours at 37°C. **(D)** Quantification of remaining MG-alkyne from reaction where 1 mM MG-alkyne was treated with equal amounts of DJ-1 or BSA, or with vehicle for 24 hours at 37°C. **(E)** Representative rhodamine gel of 2 mg/mL BSA treated with 300 μM MG-alkyne as well as recombinant DJ-1 or vehicle for 24 hours at 37°C. **(F)** Quantification of labeling of 2 mg/mL BSA treated with 100 or 300 μM MG-alkyne as well as recombinant DJ-1 or vehicle for 24 hours at 37°C. Data plotted in (C-F) are mean ± S.E.M. from *n* = 6 (C), 4, (D), or 3 (F) independent biological replicates. Statistical analyses are by ordinary one-way analysis of variance (ANOVA). *p< 0.05; **p< 0.01; ***p< 0.001; ****p< 0.0001.

Treatment of equal concentration of MGO or MG-alkyne with either DJ-1 or BSA control showed comparable degrees of turnover with both substrates by DJ-1, suggesting that despite the presence of an alkynyl tail, DJ-1 is able to catalyze the conversion of the dicarbonyl reactive head group into the corresponding α-hydroxyl carboxylate (Figure 4.2C-D) – an activity that would be less likely to occur if DJ-1 were acting on diverse protein adducts with the tail

group facing outward toward solvent. Finally, we incubated BSA, which is readily modified by MG-alkyne (Supplementary Figure 4.7C), with different concentrations of MG-alkyne probe for 24 hours in the presence or absence of DJ-1. BSA reactions containing DJ-1 showed significantly less labeling by MG-alkyne relative to control reactions even at this extended incubation period, confirming that the MG-alkyne glyoxalase activity by DJ-1 functionally protects proteins from stable modification (Figure 4.2E, F).

Fig 4.3 DJ-1 protects against proteins from glycation with or without physical interaction with target proteins.

While our experiments here cumulatively support an in-solution glyoxalase activity for DJ-1, the DJ-1-mediated detoxification of MGO and MG-alkyne could in theory be explained by the direct removal of transient dicarbonyl modifications (e.g., hemiaminals or similar) on target proteins (BSA) or DJ-1 in trans, as argued in some previous studies.[86] To directly uncouple these competing mechanisms, we sought to detect and quantify MG-alkyne modifications on a target protein when DJ-1 is physically separated from said target protein population. Specifically, we developed an assay where BSA was incubated with MG-alkyne and either co-incubated with DJ-1 in the same compartment or physically separated from DJ-1 by a dialysis membrane (Figure 4.3A). This barrier would prevent DJ-1 proteins from being able to physically interact with the BSA proteins – as would be necessary to mediate direct removal of dicarbonyl adducts via a deglycase mechanism – but would allow the free diffusion of MG-alkyne between compartments.

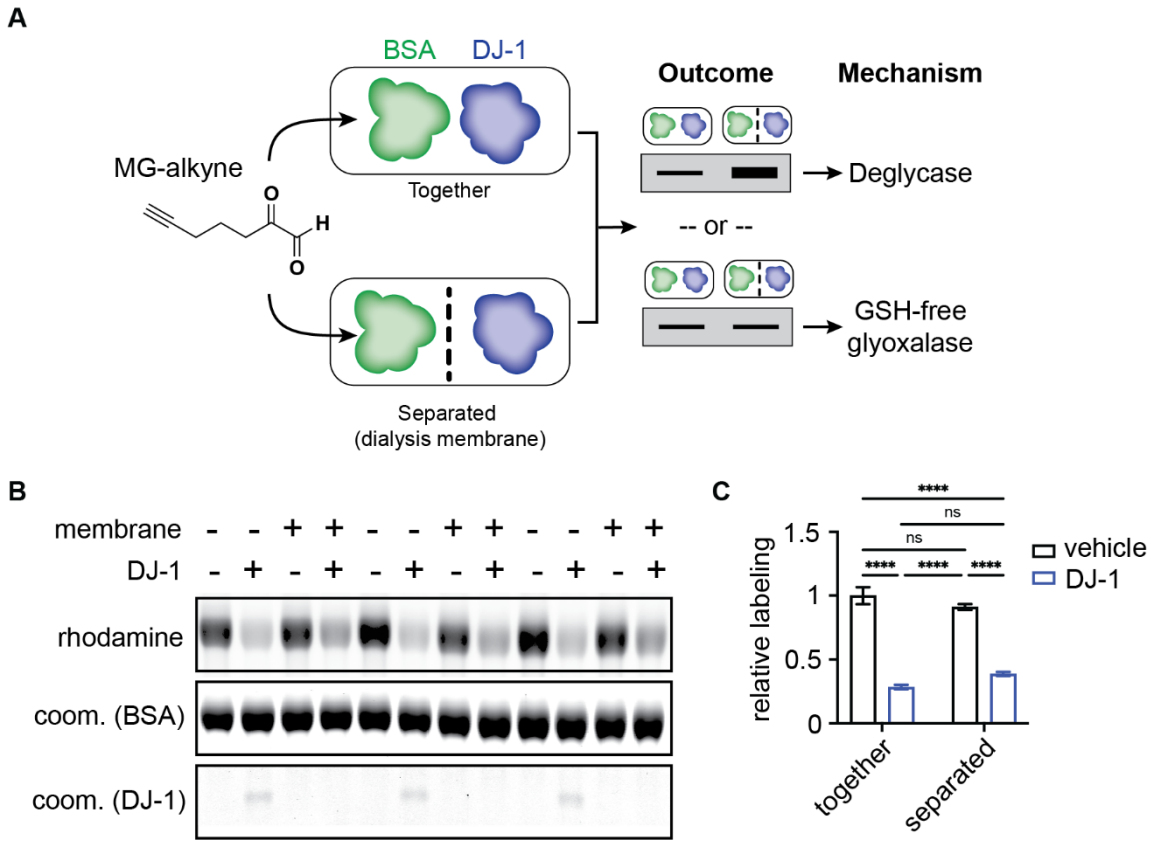

Figure 4.3 DJ-1 protects against proteins from glycation with or without physical interaction with target proteins: (A) Schematic depicting experiments where BSA and recombinant DJ-1 are incubated with MG-alkyne together or separated by dialysis membrane alongside predicted interpretations. **(B-C)** Rhodamine gel **(B)** and quantification of labeling **(C)** of BSA incubated with 100 μM MG-alkyne in the presence or absence of recombinant DJ-1 with and without separation by dialysis membrane. Data plotted in (C) are mean ± S.E.M from *n* = 3 independent biological replicates. Statistical analyses are by ordinary one-way analysis of variance (ANOVA). ****p< 0.0001.

As in previous experiments we observed significant MG-alkyne modification of BSA in this assay. Importantly, we found that the samples where BSA and DJ-1 were separated by a dialysis membrane and the samples where they were co-incubated showed no significant difference in degree of modification by the MG-alkyne probe (Figure 4.3B, C). These data confirm that physical interaction between DJ-1 and dicarbonyl modified protein targets is not necessary for

the observed detoxification and provides direct evidence for the in-solution glyoxalase activity of DJ-1 in converting MGO to lactate and protecting proteins against glycation.

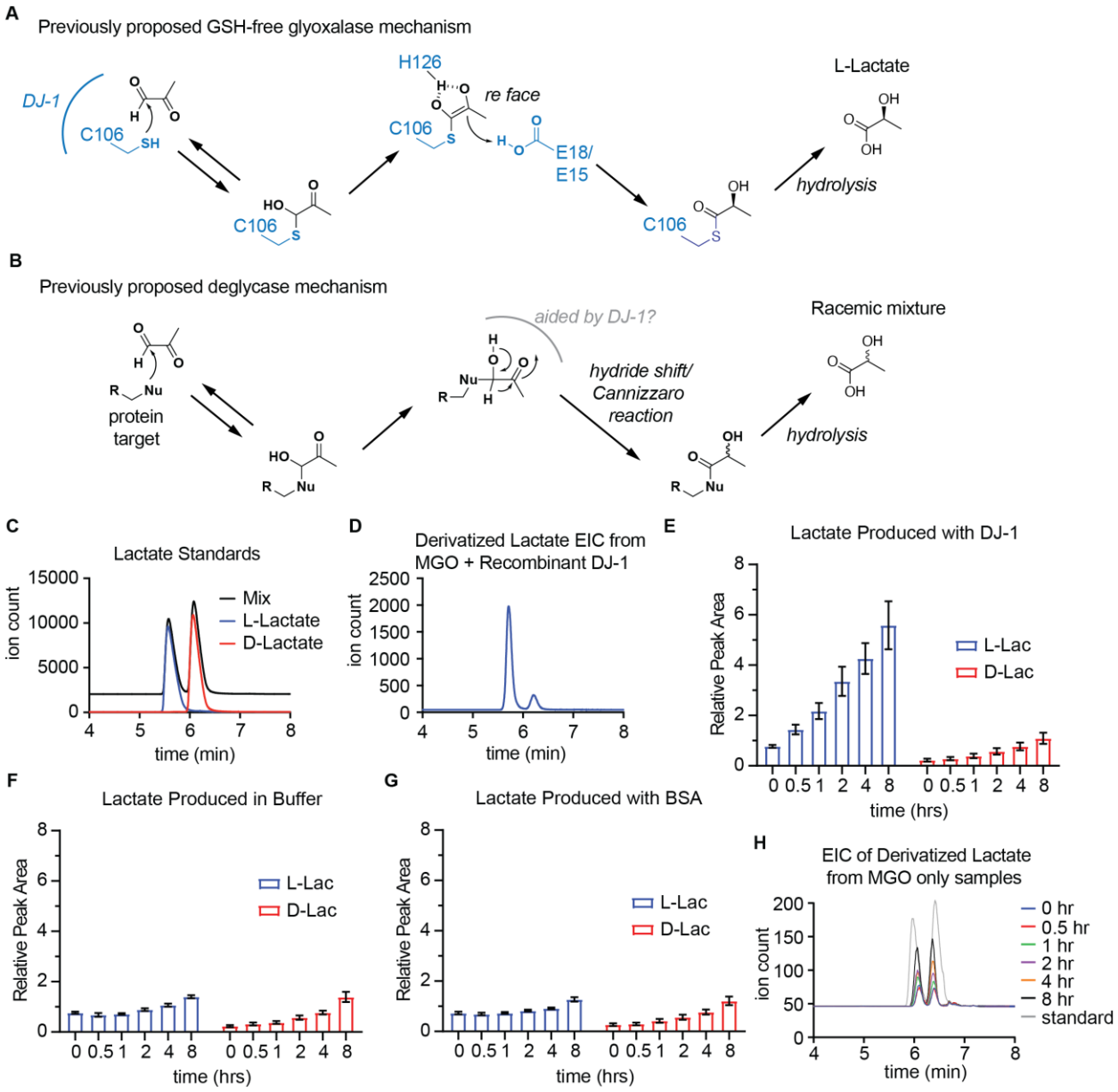

Figure 4.4 Lactate product stereochemistry is consistent with a GSH-free glyoxalase mechanism: **(A-B)** Previously proposed DJ-1 glyoxalase **(A)** and deglycase **(B)** mechanisms and predicted product lactate stereochemistry. **(C-D)** LC-MS separation of DATAN-derivatized lactate standards **(C)** and DJ-1 catalyzed products **(D)**. Both chromatograms show extracted ion chromatogram (EIC) for DATAN-derivatized product. **(E-G)** Quantification of integrated peak area of L- and D- lactate formed by DJ-1, BSA, or PBS treated with MGO for 0-8 hrs. at 37°C.

Figure 4.4 Continued
(H) Representative chromatograms of derivatized L- and D- Lactate formed from PBS treated with 1 mM MGO for 0-8 hrs. at 37°C along with L- and D- lactate synthetic standards. Data plotted in (E-G) are mean ± S.E.M from $n = 4$ independent biological replicates normalized across all conditions.

Fig 4.4 Lactate product stereochemistry is consistent with a GSH-free glyoxalase mechanism.

The proposed mechanism for a glutathione-free glyoxalase mechanism predicts that DJ-1 would catalyze the enantioselective formation of L-lactate (Figure 4.4A), while putative deglycase activity is expected to produce a racemic mixture of L- and D- lactate (Figure 4.4B).[86, 194] The fact that direct deglycation of protein-adducts would also infer a heterogeneous substrate pool mediated by diverse protein surfaces also strongly supports a mixture of lactate stereoisomers being produced by the deglycase mechanism. Despite these theoretical mechanisms, some previous studies have observed mixtures of D- and L-lactate generated by DJ-1,[86, 199] while others show significant preference for the L-lactate isomer,[197, 203] suggesting that both glyoxalase and deglycase mechanisms may be operating in parallel. To help separate these two potential mechanisms and clarify the disparity in prior findings of various studies in regards to lactate product stereochemistry, we utilized a chemical derivatization method to allow unambiguous separation and quantification of the L- and D-lactate enantiomers.[130] Using synthetic standards, we validated the ability to achieve baseline separation for accurate quantification of the diastereomeric derivatives of the lactate enantiomers (Figure 4.4C). Applying this method, we performed kinetic LC-MS quantification of the L- and D- lactate produced by incubating recombinant DJ-1 with MGO over time, which revealed that the vast majority, ~83%, of the lactate product was in the form of the L-enantiomer (Figure 4.4D). This

was inconsistent with either of the two proposed mechanisms operating exclusively and left open the possibility that both activities could be present.

To gain further insight into the production of L- and D- lactate by DJ-1, diastereomeric derivatization was again utilized to look at the kinetics of lactate production in an enantiospecific manner. Time series incubations over an 8-hour time period were performed where MGO was incubated with either DJ-1, equal concentration of BSA carrier protein, or PBS buffer alone and the relative rates of L- and D- lactate production were again quantified (Figure 4.4E). Unexpectedly, though the samples incubated with DJ-1 showed a much higher rate of overall lactate production, all three conditions showed some time-dependent production of lactate (Figure 4.4E-G). DJ-1 catalyzed reactions produced markedly more L-lactate than BSA or PBS control reactions. By contrast, the production of D-lactate was identical across DJ-1, BSA and PBS samples. This is consistent with a model where L-lactate is produced enzymatically by DJ-1, but a racemic mixture of L-lactate and D-lactate is arising from non-enzymatic, spontaneous conversion of MGO to lactate in buffer alone. Indeed, the amount of L- and D-lactate produced in reactions without DJ-1 was identical (Figure 4.4H). To confirm that the observed non-enzymatic production of lactate from MGO was not caused by our derivatization procedure, we incubated MGO alone in PBS and directly quantified total lactate over 8 hrs. via targeted LC-MS/MS. These experiments again confirmed time-dependent production of lactate from MGO without the presence of an enzymatic catalyst and in the absence of derivatization (Supplementary Figure 4.8A, B). To rule out lactate production from biological contaminants, we compared production of lactate from MGO in PBS that had been autoclaved immediately prior to the experiment, which showed no difference in lactate production (Supplementary Figure

4.8). To assess factors that regulate the non-enzymatic conversion, we incubated MGO in PBS or deionized water at either 4°C or 37°C. There was markedly reduced production in conditions where the MGO was incubated in water or at 4°C, suggesting that temperature and buffer composition play a role in rate of non-enzymatic conversion of MGO to lactate.

Fig 4.5 Stereospecific glyoxalase activity of DJ-1 supported by this study.

Altogether, these experiments support the exclusive enzymatic production of L-lactate by DJ-1, which is confounded by the simultaneous background production of equimolar D- and L-lactate in solution by mechanisms yet to be discovered. This observation, which has not been previously reported to the best of our knowledge, provides a parsimonious explanation for the previously observed production of D- and L- isomers in enzymatic reactions across studies, and combined with our biochemical studies here, strongly supports stereospecific glyoxalase activity of DJ-1 to form L-lactate (Figure 4.5). It additionally suggests that the variable ratios of L- and D- lactate observed in previous work with DJ-1 could be caused, at least in part, by variable ratios of enzymatic versus non-enzymatic production of lactate, likely dependent on the amount and degree of activity of DJ-1 used, as well as particular reaction conditions.

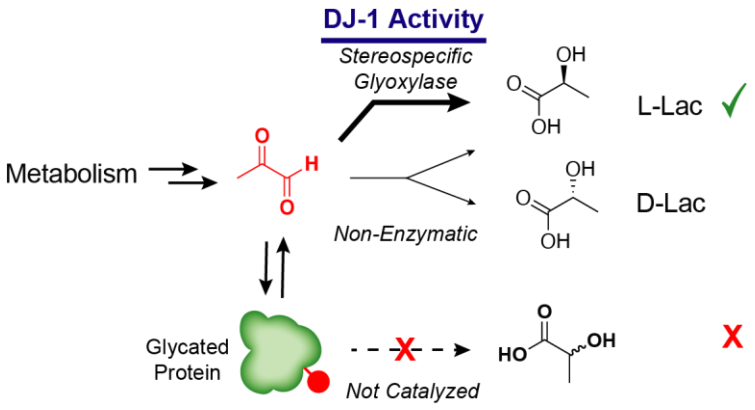

Figure 4.5: Schematic depicting the stereospecific glyoxalase activity of DJ-1 supported by this study.

Discussion

This study sought to determine the mechanism by which DJ-1 detoxifies the reactive metabolite methylglyoxal (MGO) and confirmed the role that DJ-1 plays in the detoxification of MGO as well as the enantioselective production of L-lactate by DJ-1 that points towards a glutathione-free glyoxalase mechanism. We demonstrated that DJ-1 protects proteins from glycation by MGO or an alkyne-containing analog without the need to physically interact with target proteins, suggesting that the protection stems from direct detoxification of dicarbonyl species in solution rather than removal of MGO from modified proteins. Additionally, this study demonstrates for the first time that MGO can non-enzymatically convert to lactate under physiologically relevant conditions and time courses. This unavoidable production of racemic lactate by MGO is likely both physiologically and experimentally important must be accounted for in any assays that seek to study enzymatic activity and parameters of proteins such as DJ-1 and GLO1, which are involved in MGO detoxification. Additionally, the finding may help explain the variable reports of the nature of lactate enantiomers products arising from DJ-1, which have primarily been characterized by inference from enzymatic assays rather than direct measurement.[194] From a biological perspective, non-enzymatic detoxification of MGO may help explain how cells can tolerate the loss of methylglyoxal detoxifying enzymes under unstressed conditions[89]. Most importantly, our enzymatic assays conclude that DJ-1 activity results in almost exclusive production of L-lactate, which is consistent with a stereospecific glyoxalase mechanism, not a deglycase mechanism for DJ-1 catalyzed lactate production (Figure 4.5).

Collectively, we posit that these experiments offer the most direct evidence in support of this mechanism and adds to recent studies[197, 203] and the overall body of evidence clarifying the role of DJ-1 in MGO detoxification.

Beyond activity on MGO, DJ-1 has recently been shown to act on other reactive metabolites such as 1,3-BPG.[60] Connecting the role of DJ-1 in the detoxification of such metabolites with its various reported cellular functions may give insight into why mutation of DJ-1 is causative in familial Parkinson's Disease. Moreover, future studies should focus on identifying important cellular targets of these metabolites and understanding how DJ-1 may modulate the function of these proteins through regulation of glycative stress as a glyoxalase.

Future Directions

Clarifying the detoxification mechanism of DJ-1/PARK7 is the first step in elucidating its role in disease pathology. While prior studies assigned a myriad of functions to PARK7, [92, 94, 97, 158, 161] much of those functions were made prior to the discovery that MGO was able to directly signal the activation of the NRF2-ARE pathway[31] through the use of DJ-1 knockdown or knockout models. Uncoupling whether the activation of many of these functions are the direct result of DJ-1 regulated functions or as an indirect result of MGO mediated NRF2-ARE pathway activation due to loss of MGO detoxification by DJ-1 will be important in helping to determine how loss of DJ-1 results in development of diseases such as Parkinson's. As an example, the loss of function mutations in PRKN, PINK1, and PARK7/DJ-1 cause autosomal recessive forms of Parkinson's disease and are associated with selective autophagy of damaged mitochondria (mitophagy). Previous studies concluded DJ-1 as being essential for mitophagy due to loss of DJ-1 affecting recruitment of selective autophagy receptors. However, more recent studies

attributed this PRKN, PINK1 signaling axis to NRF2 mediated regulation [161] (which in turn is dependent upon cellular concentrations of MGO, DJ-1's capacity to regulate MGO, and the MGO derived rmPTM MICA). While there is ample evidence linking dysregulated mitophagy to neurodegenerative disease phenotypes, questions remain as to whether regulating the proteome-wide MGO modification landscape by regulating MGO levels with DJ-1 are sufficient to prevent this mitophagy or whether dysregulated NRF2-ARE activation are the cause. In this case, re-visiting this study and measuring signs of mitophagy, mitochondrial aggregation, and neurodegeneration in cellular models where NRF2 is knocked out with either the glyoxalase pathway protein (GLO1), DJ-1/PARK7, or both the DJ-1 and GLO1 are knocked out would help uncouple DJ-1's role as either a regulator of mitophagy or a regulator of MGO, which can signal mitophagy via the NRF2-ARE pathway.

Beyond re-examining the pleiotropic roles of DJ-1, tracking crosstalk between the glyoxalase DJ-1 and the GLO glyoxalase pathway in regulating MGO is another area of critical importance. Prior studies in MGO damage to neurons mapped the effects of losing either the GLO pathway or PARK7 individually; resulting in MGO-induced aggregates of alpha synuclein and other critical proteins correlated with neurodegenerative diseases. Though both DJ-1/PARK7 and the GLO pathway process and detoxify MGO as glyoxalases rather than as a complementary pair of a glyoxalase and a deglycase, it remains unclear whether the redundancy of both detoxification enzymes is necessary to preventing accumulation of AGE damage or why the loss of PARK7 renders GLO1 unable to rescue from neurodegenerative phenotypes.[158] To investigate this, cellular models with either the glyoxalase pathway protein (GLO1), DJ-1/PARK7, or both the DJ-1 and GLO1 knocked out could be used to study why the loss of one glyoxalase system is

sufficient to induce disease pathology. One possible explanation may be related to the subcellular localization in which AGEs form, with the GLO pathway annotated to be solely cytosolic whereas the DJ-1/PARK7 proteins have been annotated to be cytosolic, nuclear, and mitochondrial. To determine whether glycation damage and aggregation of mitochondrial and/or nuclear proteins, unreachable by GLO detoxification, are important to neurodegenerative disease, subcellular compartment specific proteomic profiling of MGO-derived rmPTMs are of paramount importance. Doing so may help to explain why loss or mutation of DJ-1 is causative in a subset of familial Parkinson's patients.

Finally, another explanation of why DJ-1/PARK7 shows redundant glyoxalase activity to the GLO pathway may relate to its putative ability to detoxify more than one reactive metabolite. Though the intermediate was not characterized due to predicted spontaneous degradation, DJ-1/PARK7 was recently putatively annotated to detoxify a reactive, labile, cyclic form of 1,3 BPG into 3PG.[60] Developing methods to trap that cyclic reactive intermediate for quantitative measurements and mapping whether DJ-1/PARK7 is indeed able to perform detoxification of the 1,3 BPG cyclic reactive species in addition to MGO will be of importance in determining whether rmPTMs deriving from 1,3 BPG are linked to neurodegenerative diseases.

Additional Figures

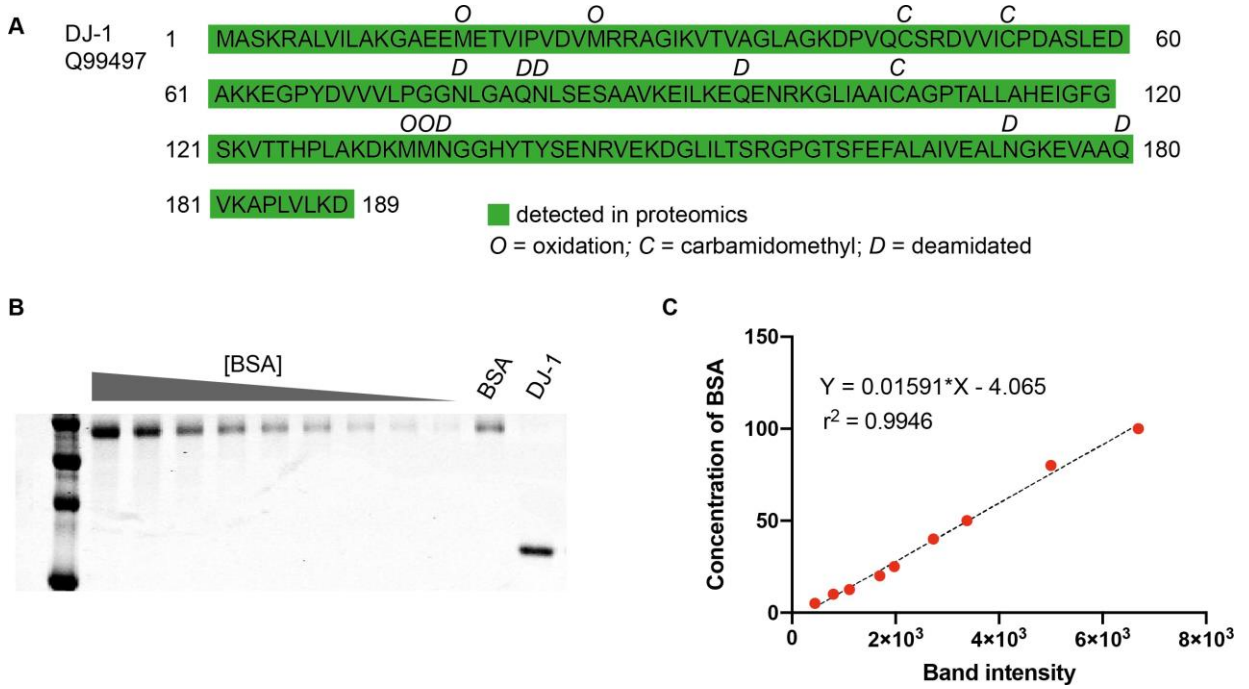

Supplementary Figure 4.6. Quantification of DJ-1 for enzymatic assays: (A) Sequence map of peptides detected by LC- MS/MS proteomic analysis of purified human DJ-1, which was used for experiments in this study. **(B-C)** Coomassie gel **(B)** of serial dilutions of BSA and quantification of the gel **(C)** used to estimate recombinant DJ-1 protein concentration.

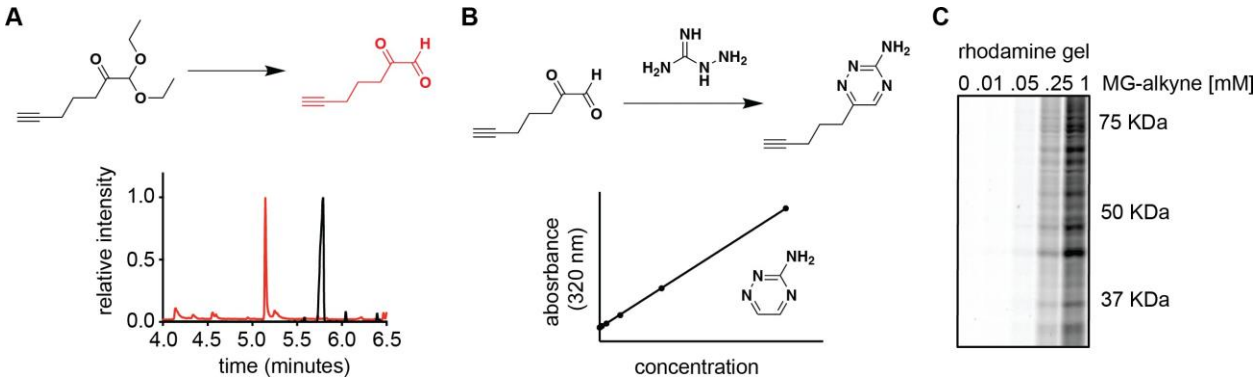

Supplementary Figure 4.7 Activation and evaluation of MG-alkyne probe: (A) GC-MS traces of protected and deprotected MG-alkyne. **(B)** Schematic of the quantification method for MG- alkyne after deprotection. **(C)** Rhodamine gel of 2 mg/mL HEK293T lysate treated with the indicated concentrations of MG-alkyne for 2 hours at 37°C.

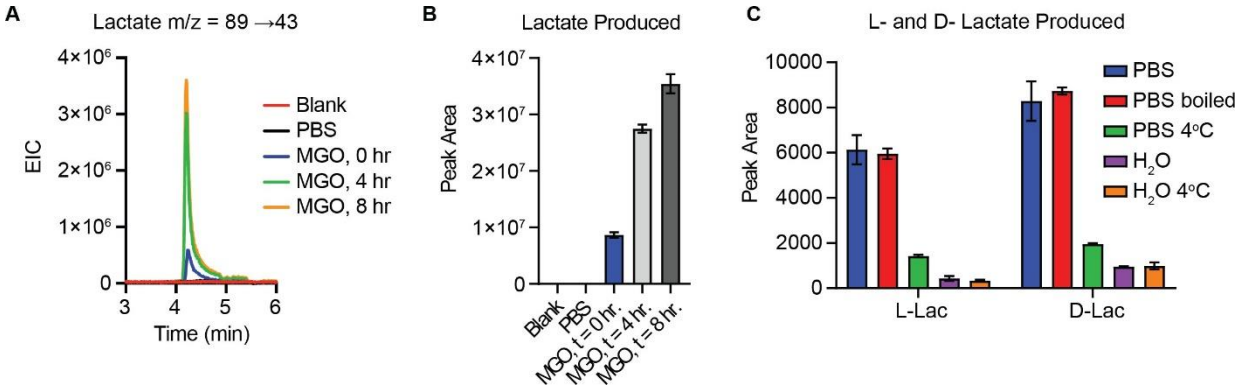

Supplementary Figure 4.8 Non-enzymatic production of lactate from methylglyoxal: **(A)** Representative chromatograms of lactate formed from PBS treated with 1 mM MGO for 0, 4, and 8 hrs. at 37°C alongside vehicle and blank injection controls. Lactate is measured by MS/MS directly, without derivatization. **(B)** Relative quantification of lactate formed in (A). **(C)** Quantification of integrated peak area of L- and D- lactate formed from 1 mM MGO incubated in from PBS, freshly autoclaved PBS, or deionized water at either 4°C or 37°C. Data plotted in (B, C) are mean ± S.E.M from $n = 4$ independent biological replicates normalized across all conditions.

Tables

Table 4.1 Specific DJ-1 tryptic peptides detected by LC-MS/MS analysis of purified DJ-1 used in this study. The observed peptides cover 100% of DJ-1.

Confidence	Sequence	# PSMs	# Missed Cleavages	Percolator q-Value (by Search Engine): Sequest HT	Percolator PEP (by Search Engine): Sequest HT	XCorr (by Search Engine): Sequest HT	Top Apex RT [min]
High	DVVICPDASLEDAKK	39	1	0.0001685	2.236E-06	3.39	58.35
High	EGPYDVVVLPGGNLGAQNLSESAAVK	35	0	0.0001685	5.449E-13	3.68	100.58
High	VTVAGLAGKDPVQCSR	30	1	0.0001685	4.282E-10	4.61	53.98
High	ALVILAK	28	0	0.0007979	0.01752	1.49	51.13
High	MMNGGHYTYSENRVEK	27	1	0.0001685	2.136E-06	2.39	32.94
High	GAEEMETVIPVDVMR	26	0	0.0001685	1.101E-07	4.23	81.36
High	MMNGGHYTYSENR	20	0	0.0001685	0.00021	2.92	27.73
High	DGLILTSR	19	0	0.000441	0.008749	2.31	48.01
High	KGLIAAICAGPTALLAHEIGFGSK	18	1	0.00016849	2.0111E-24	9.83	119.07
High	GAEEMETVIPVDVMR	16	0	0.0001685	3.807E-08	2.57	65.61
High	MMNGGHYTYSENR	14	0	0.0001685	4.219E-06	2.76	29.84
High	VTVAGLAGK	13	0	0.0001685	0.001286	1.85	39.31
High	GLIAAICAGPTALLAHEIGFGSK	11	0	0.0001685	2.878E-13	7.23	123.2
High	MMNGGHYTYSENRVEK	10	1	0.0001685	5.088E-06	2.82	30.49
High	DVVICPDASLEDAK	9	0	0.0001685	5.306E-07	3.1	68.03
High	GPGTSFEFALAIVEALNGK	9	0	0.0001685	1.16E-14	5.25	134.18
High	GPGTSFEFALAIVEALNGKEVAAQVK	8	1	0.0001685	1.007E-21	9.38	130.34
High	VEKDGLILTSR	8	1	0.0001685	0.000546	3.32	42.73
High	EGPYDVVVLPGGNLGAQNLSESAAVK	7	0	0.0001685	3.656E-08	2.77	102.68
High	GAEEMETVIPVDVMR	6	0	0.0001685	2.893E-06	1.67	95.24
High	GPGTSFEFALAIVEALNGK	6	0	0.0001685	2.221E-13	5.34	131.74
High	AGIKVTVAGLAGKDPVQCSR	5	2	0.0001685	2.146E-14	4.9	67.53
High	KEGPYDVVVLPGGNLGAQNLSESAAVK	5	1	0.0001685	4.924E-11	6.26	92.57
High	KGLIAAICAGPTALLAHEIGFGSKVTTHPLAK	5	2	0.0001685	1.704E-09	6.28	114.35
High	DKMMNGGHYTYSENRVEK	4	2	0.0001685	0.00003444	2.42	31.01
High	DVVICPDASLEDAKKEGPYDVVVLPGGNLGAQNLSESAAVK	4	2	0.0001685	2.142E-07	6.61	106.68

Table 4.1 Continued

Confidence	Sequence	# PSMs	# Missed Cleavages	Percolator q-Value (by Search Engine): Sequest HT	Percolator PEP (by Search Engine): Sequest HT	XCorr (by Search Engine): Sequest HT	Top Apex RT [min]
High	MMNGGHYTYSENR	4	0	0.0001685	1.159E-06	2.84	35.79
High	DKMMNGGHYTYSENRVEK	3	2	0.0001685	8.044E-09	4.31	37.25
High	EGPYDVVVLPGGNLGAQNLSESAAVKEILK	3	1	0.0001685	1.158E-12	5.5	118.92
High	EGPYDVVVLPGGNLGAQNLSESAAVKEILK	3	1	0.0001685	1.87E-07	2.98	
High	EILKEQENRKGLIAAICAGPTALLAHEIGFGSK	3	3	0.0001685	1.584E-06	5.51	117.07
High	GAEEMETVIPVDVMRR	3	1	0.0001685	0.0007268	1.7	57.61
High	GPGTSFEFALAIVEALNGKEVAAQVK	3	1	0.0001685	7.338E-14	6.12	130.75
High	KEGPYDVVVLPGGNLGAQNLSESAAVK	3	1	0.0001685	1.131E-11	4.27	92.57
High	MMNGGHYTYSENR	3	0	0.0001685	0.0000852	3.18	33.23
High	MMNGGHYTYSENRVEK	3	1	0.0001685	0.0003396	2.37	27.3
High	DGLILTSRGPGTSFEFALAIVEALNGKEVAAQVK	2	2	0.0001685	4.895E-09	6.53	
High	DKMMNGGHYTYSENR	2	1	0.0001685	0.0005949	2.54	34.76
High	DKMMNGGHYTYSENR	2	1	0.005884	0.09665	0.79	25.31
High	DKMMNGGHYTYSENRVEK	2	2	0.001147	0.02415	2.1	28.25
High	EQENRKGLIAAICAGPTALLAHEIGFGSKVTTHPLAK	2	3	0.0001685	7.645E-10	5.08	112.99
High	GPGTSFEFALAIVEALNGKEVAAQVK	2	1	0.0001685	0.0000486 1	1.59	
High	GPGTSFEFALAIVEALNGKEVAAQVKAPLVLK	2	2	0.0001685	3.124E-07	4.64	131.16
High	MMNGGHYTYSENR	2	0	0.0005542	0.01161	0.88	33.22
High	MMNGGHYTYSENR	2	0	0.0005542	0.01461	1.19	23.91
High	MMNGGHYTYSENRVEK	2	1	0.0001685	0.0000806 5	2.91	37.97
High	AGIKVTVAGLAGK	1	1	0.0001685	0.001393	2.03	59.21
High	ALVILAKGAEEMETVIPVDVMRR	1	2	0.0001685	0.0002015	3.01	96.43
High	ALVILAKGAEEMETVIPVDVMRR	1	2	0.0001685	5.144E-08	4.55	86.84
High	APLVLKD	1	1	0.001631	0.03907	1.21	38.72
High	DGLILTSRGPGTSFEFALAIVEALNGK	1	1	0.0001685	3.341E-14	6.27	134.74
High	DGLILTSRGPGTSFEFALAIVEALNGK	1	1	0.0001685	1.209E-06	2.75	
High	DGLILTSRGPGTSFEFALAIVEALNGKEVAAQVK	1	2	0.0001685	0.0006615	2.21	132.97

Table 4.1 Continued

Confidence	Sequence	# PSMs	# Missed Cleavages	Percolator q-Value (by Search Engine): Sequest HT	Percolator PEP (by Search Engine): Sequest HT	XCorr (by Search Engine): Sequest HT	Top Apex RT [min]
High	DGLILTSRGPGTSFEFALAIVEALNGKEVAAQVKAPLVLK	1	3	0.0001685	1.553E-06	4.8	131.54
High	DKMMNGGHYTYSENR	1	1	0.001631	0.03839	0.86	32.63
High	DVVICPDASLEDAKKEGPYDVVVLPGGNLGAQNLSESAAVK	1	2	0.0001685	2.494E-10	4.28	106.68
High	DVVICPDASLEDAKKEGPYDVVVLPGGNLGAQNLSESAAVK	1	2	0.001631	0.0388	2.7	
High	DVVICPDASLEDAKKEGPYDVVVLPGGNLGAQNLSESAAVKEILK	1	3	0.0001685	8.439E-07	5.31	118.69
High	EGPYDVVVLPGGNLGAQNLSESAAVK	1	0	0.000441	0.01078	1.67	
High	EGPYDVVVLPGGNLGAQNLSESAAVKEILK	1	1	0.0001685	0.0003102	2.71	
High	EGPYDVVVLPGGNLGAQNLSESAAVKEILKEQENR	1	2	0.0001685	1.923E-10	5.98	117.72
High	EGPYDVVVLPGGNLGAQNLSESAAVKEILKEQENRK	1	3	0.0001685	5.371E-06	7.34	112.98
High	EILKEQENR	1	1	0.00598	0.09772	1.94	
High	EQENRKGLIAAICAGPTALLAHEIGFGSK	1	2	0.0001685	0.0003395	3.63	117.91
High	EQENRKGLIAAICAGPTALLAHEIGFGSK	1	2	0.0001685	0.00003374	2.53	
High	GAEEMETVIPVDVMRR	1	1	0.0001685	0.000235	4.08	87.22
High	GPGTSFEFALAIVEALNGKEVAAQVKAPLVLK	1	2	0.0001685	2.27E-19	8.35	130.58
High	MASKRALVILAK	1	2	0.001377	0.02673	2.25	55.41
High	MASKRALVILAKGAEEMETVIPVDVMR	1	3	0.0001685	0.0001919	2.31	
High	MMNGGHYTYSENRVEK	1	1	0.0001685	1.404E-11	4.58	35.28
High	MMNGGHYTYSENRVEKDGLILTSR	1	2	0.002053	0.05016	1.68	62.43
High	MMNGGHYTYSENRVEKDGLILTSR	1	2	0.001377	0.0282	1.4	65.7
High	RAGIKVTVAGLAGK	1	2	0.0001685	0.002815	2.34	49.26
High	RAGIKVTVAGLAGKDPVQCSR	1	3	0.0001685	5.683E-08	4.11	59.62
High	VEKDGLILTSRGPGTSFEFALAIVEALNGK	1	2	0.0001685	1.712E-07	3.08	130.96
High	VEKDGLILTSRGPGTSFEFALAIVEALNGKEVAAQVK	1	3	0.0001685	2.453E-09	4.85	128.81
High	VTTHPLAK	1	0	0.002453	0.05661	1.57	30.58

CHAPTER 4.A APPENDIX: HDAC3 CONTRIBUTES TO PROTEIN QUALITY CONTROL AS A GLYCERYL-LYSINE ERASER (PRELIMINARY UNPUBLISHED RESULTS)

The work of this chapter is unpublished data by: Coukos, J.S.[#], Lee, C. W.[#], Rousseau, X., Moellering, R. E. (2024). HDAC3 Contributes to Protein Quality Control as a Glyceryl-Lysine Eraser

Author Contributions: J.S.C. and C.W.L. performed cellular and biochemical assays and proteomic mass spectrometry analysis. X.R. assisted with cellular and biochemical assays. R.E.M. supervised research. R.E.M. and J.S.C. conceived the study.

Background

Phosphoglyceryl-lysine (pgK) modifications are dynamic and reversible, capable of changing enzymatic activity as well as altering global metabolic flux via concerted modification of central metabolic enzymes. Given the potential importance of pgK modifications in both fundamental and disease biology, the yet unknown mechanisms in which pgK modifications are removed are of great interest. Prior studies testing (phospho)glycerate modified peptide standards in cell lysate under vehicle, heat denatured, and phosphatase inhibitor conditions have demonstrated that the mechanism to remove pgK modifications from proteins proceeds in an enzyme dependent manner, either as a single step removal of the entire phosphoglyceryl modification, or as a two-step removal of phosphoglyceryl to glyceryl, and then glyceryl to unmodified lysine.[46] Furthermore, the mapping of glycerate and phospho-glycerate modifications in the proteome has shown both overlapping and unique proteins and metabolites within each dataset, indicating that wild-type, pgKylated, and gKylated proteoforms (and metabolites) simultaneously exist within the proteome. Understanding whether the gKylated proteoform has any functional regulation of enzyme activity, whether the distribution and ratio of these three proteoforms in the proteome signals/regulates any pathway response, and whether the same

proteins have differential activity with respect to its pgK, gK, and wild-type proteoforms are all questions of active interest.

At the moment, it is unclear why some lysines are modified as pgK modifications and others are modified as gK modifications. However, solvent accessibility is considered a determining factor. Using an exemplar hemoglobin protein, it was found that pgK modifications, located within the oxygen binding sites are better shielded from being accessed by 'erasers' like phosphatases in the solvent, whereas many lysines that are solvent exposed are more readily modified by glyceryl modifications. Whether this dichotomy indicates that pgK modifications are rarer but more permanent modifications which can modify protein activity and biochemical pathway flux while gK modifications are potential markers of protein/metabolite adduct damage that are more abundant and more easily cleared, except in disease contexts like Parkinsons's is yet unknown.

However, determining the identity of the enzyme(s) that are able to regulate pgK to gK to lysine turnover is the first step in understanding the functional consequences of rmPTM regulation by erasers. Among the potential eraser candidates, it has been previously demonstrated that histone deacetylases such as sirtuin SIRT2 and class 1 histone deacetylases HDAC1-3 can remove K(D-Lac), along with L-lactate-derived K(L-Lac); lysine modifications that are structurally similar to pgK. Among these, HDAC3 appears to have greatest enzymatic activity at deacylating these modifications, making it the most likely enzyme to have phospho-glyceryl eraser activity.[204, 205]

The purposes of this study are to assess whether any of these histone deacetylase proteins can deacylate the pgK modification, to assess the relative coverage of phosphoglyceryl-lysine to

glyceryl-lysine to lysine in the proteome, and to determine whether this relative lysine coverage functionally regulates the activity of any protein(s) in terms of catalytic turnover, stability, structure, localization, etc. Furthermore, as different histone deacetylases cover different subcellular localizations, this study seeks to map the extent of the proteome by which histone deacetylases are able to regulate pgK modification levels. Finally, if histone deacetylases are able to regulate the turnover of pgK, gK, and lysine modifications on proteins in a functional manner, we would be interested in assessing whether current compounds specifically or broadly targeting histone deacetylases are able to also regulate the (p)gK dependent function of proteins. More broadly, with (p)gK adducts on proteins and metabolites implicated in Parkinson's models[60], if pgK modifications are able to be regulated by histone deacetylases, it may lend greater insight into the role of HDACs in neurodegenerative disorders, beyond epigenetic regulation.[58, 206]

Preliminary Results and Future Directions

We find that among the panel of HDAC family proteins we screened, purified recombinant HDAC3-NCOR1 complex uniquely shows activity removing the glyceryl modification off lysines under physiological conditions. (Figure 4A.1). No HDAC family protein tested showed any activity in removing the phospho group off phosphoglyceryl-lysine. implying that the removal of the pgK modification is a two-step process first mediated by unknown phosphatase(s) yet to be discovered followed by HDAC3 mediated removal of glyceryl-lysine. HDAC3's observed in-vitro activity was preserved in cell-lysate environments (Figure 4A.2), demonstrating that endogenous HDAC3 may play a role in dynamic erasure of pgK modifications in cell. Moreover, as HDAC3 is present both in cytoplasm and the nucleus, and is

among the highest expressed HDACs in the brain,[207] it implies that it may have critical importance regulating pgK across a diverse set of proteins in both fundamental and disease biology contexts.[46, 60]

The limitation of these in vitro assays is that they do not answer whether HDAC3 is able to remove gK modifications outside of the nucleus in native cells with cell compartments intact. It is well known that HDAC3 operates in complex with transcriptional regulator NCOR1 (nuclear receptor corepressor 1).[208] While both HDAC3 and NCOR1 have been annotated to exist in both the nucleus and the cytosol, it is unknown whether deacetylase activities take please outside the nucleus. Thus, whether HDAC3 removes gK off lysines in the cytosol and nucleus or whether its activities are specific to nuclear and nuclear trafficked proteins is yet unknown.

To map the dynamics of HDAC3 eraser activity in native cell contexts, the next step would be to perform quantitative proteomics on HDAC3-Ctrl and HDAC3-KO stable lines, utilizing standard phosphoproteomics protocols to enrich the pgK-ome in parallel with a 'glyceryl-enrichment' proteomic pipeline to enrich the gK-ome using Boronic Acid Resin (Pierce) and cross comparing these two enriched datasets with respect to HDAC3 status (a survey of annotated functional/regulatory sites, subcellular localization, overlap with other modifications known in literature, etc.). This would enable us to map whether pgK, gK, and lysine proteoforms exist for the same protein, what the distribution of these proteoforms is, whether proteins across various cellular compartments are dynamically (p)gK regulated or whether HDAC3's activity is specific to the nucleus, and whether the modified lysine site can putatively effect protein activity. From there, we could assess the effects of gK modification versus pgK modification and unmodified lysines in vitro using purified recombinant protein that

is co-incubated with substrate, 1,3 BPG, an exemplar phosphatase, and phosphatase inhibitor or substrate, 1,3 BPG, and an exemplar phosphatase. This would enable us to directly compare the effects of pgK-modification to gK-modification to wild-type unmodified protein.

Finally, we would validate whether these findings have implications to current studies utilizing HDAC3 targeting compounds by comparing against changes to the (p)gK modified proteome from HDAC3 specific or pan-HDAC inhibitor treatment. Collectively, while the functional regulation of histone deacetylases in the pathophysiology of Parkinson's disease and other neurodegenerative diseases is only beginning to be unraveled, this study has potential to unveil regulatory mechanisms performed by HDAC3 that are independent of epigenetic targets.

Preliminary Figures

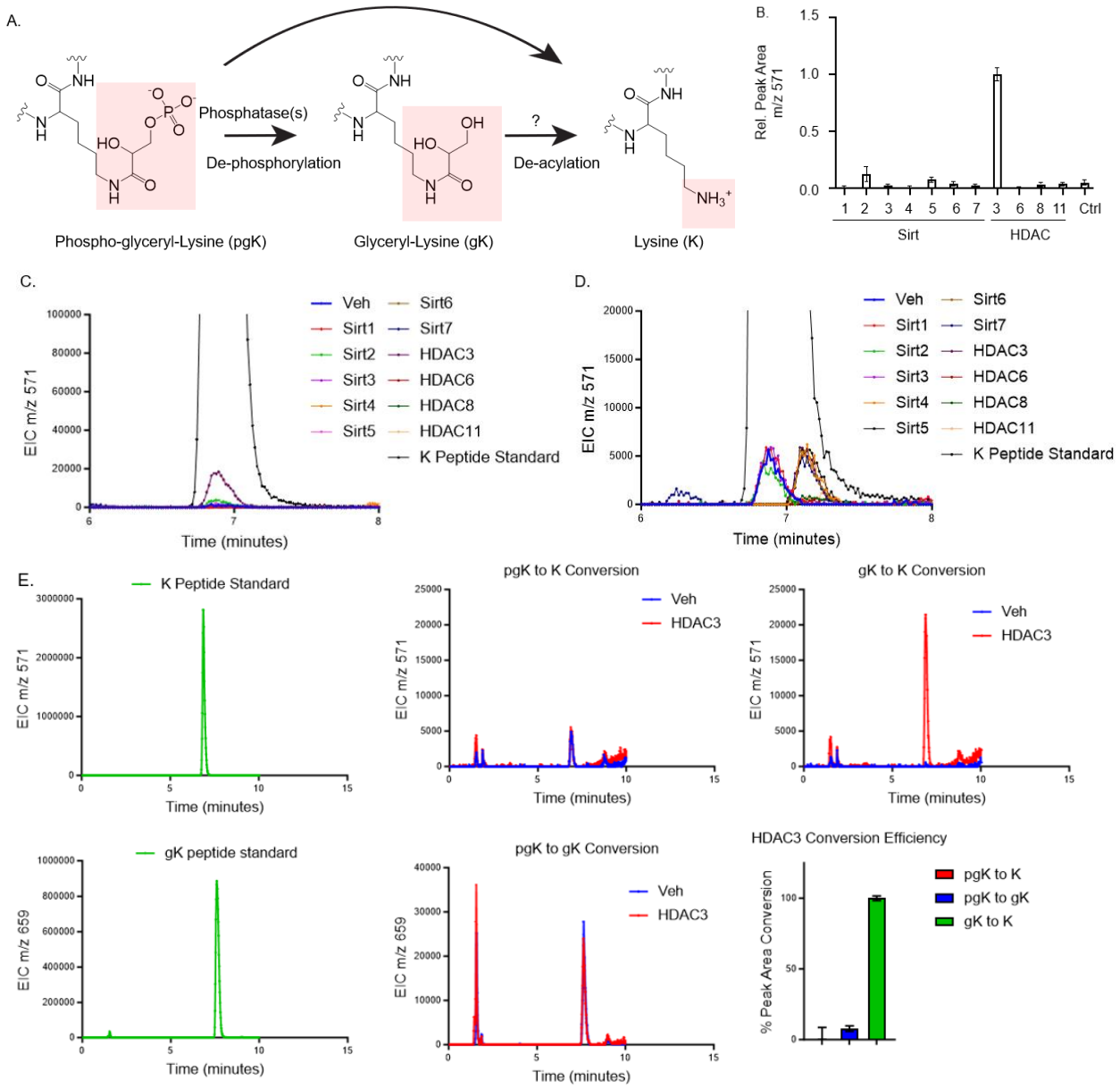

Figure 4.A1 pgK modifications do not appear to be directly removed by any HDACs tested, gK, however, appears to be removed selectively by HDAC3: (A.) Basic schematic of pgK, gK, and K flow based on model (**B)** Relative peak area of product K peptide generated in vitro when gK peptide is incubated with recombinant HDAC family proteins with (**C)** corresponding chromatogram **(D)** Representative chromatograms of negligible K peptide generated by HDAC3 family proteins versus vehicle when incubated with pgK peptide. **(E)** Representative chromatograms of selective HDAC3 activity to remove gK but not pgK modification

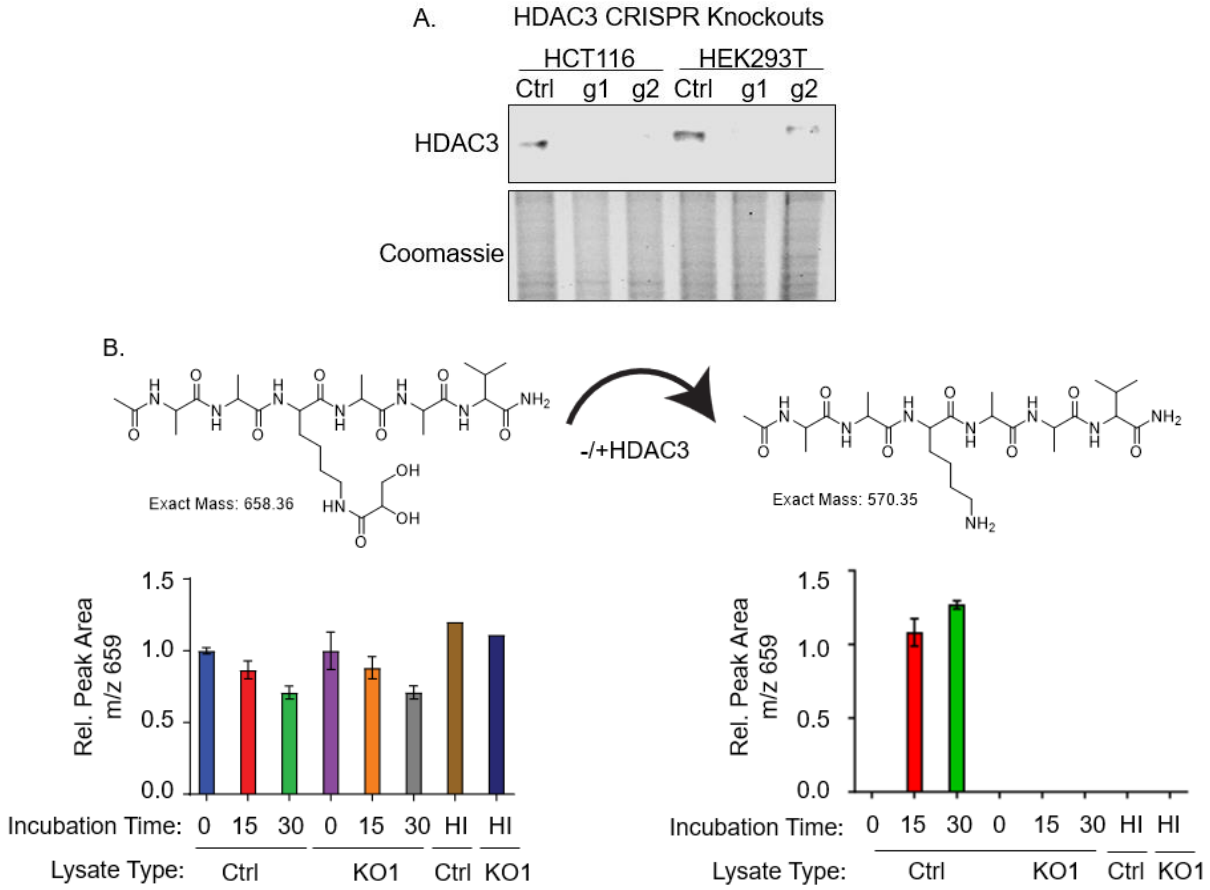

Figure 4.A2 Endogenous HDAC3 contributes to deglycation in cells: (A) Representative Western Blot of HDAC3 Knockout Stable Cell Lines (**B)** HEK293T HDAC3 KO1 or Ctrl lysates were incubated with input gK peptide for 0-30 mins. Quantification of relative peak area of gK input peptide (left) and resulting K product peptide (right) over time. HI = heat inactivated lysate. N = 3 Bioreplicates. Error bars are S.E.M.

Figure 4.A3 Representative chromatograms corresponding to Fig 4.A2

CHAPTER 5. DIFFERENTIAL RESPONSE OF CANCER CELLS TO ACUTE, INTERMEDIATE, AND CHRONIC CENTRAL GLYCOLYTIC PERTURBATION

The work of this chapter is unpublished work in preparation for submission: Lee, C. W.[#], Coukos, J.S.[#], Shah, H., Huff, A.R., & Moellering, R. E. (2024). Differential Response of Cancer Cells to Acute, Intermediate, and Chronic Central Glycolytic Perturbation.

Author Contributions: C.W.L. and J.S.C. performed cellular and biochemical assays and proteomic mass spectrometry analysis. C.W.L. performed metabolomic mass spectrometry analysis. H.S. assisted with metabolomic mass spectrometry analysis. A.R.H. assisted with proteomic mass spectrometry analysis. R.E.M. supervised research. R.E.M. conceived the study. R.E.M. and C.W.L. analyzed data and wrote the article.

Abstract

Glycolysis serves as a central metabolic pathway for bioenergetics and biosynthesis. Beyond supplying energy and glucose-derived carbon, reactive metabolites of glycolysis modify proteins, metabolites, and nucleic acids to regulate diverse processes such as energy homeostasis, biosynthesis, and dynamic redox stress. Although the Warburg Effect and upregulated glycolysis has long been a hallmark in cancers, the role of upregulated levels of reactive glycolytic metabolites and the upregulated signaling pathways that result from the Warburg Effect have yet to be fully characterized. In this work, we perturb central glycolysis in cancers and upregulate levels of reactive signaling metabolites such as methylglyoxal and 1,3-bisphosphate-glycerate via acute compound treatment, inducible knockdown, or a stable knock down. We find that acute and inducible induction of the Glycolysis-NRF2 pathway in cancers results in a differential response heavily correlated with redox stress and specific rescue by glutathione and glutathione associated processes. We further find that these redox liabilities remain under inducible but not stable knockdown models of central glycolysis and catalogue both the proteomic and metabolomic rewiring that arises from prolonged knockdown of PGK1 versus GAPDH, focusing

in particular on the similarities and differences that arise in the pentose phosphate pathway and TCA cycle.

Introduction

Glycolysis acts as a central metabolic pathway which supplies energy and biosynthetic precursors. Consequently, many of its intermediates are also linked to adjacent metabolic pathways such as the pentose phosphate pathway, citric acid cycle, and triglyceride and phospholipid biosynthesis pathways.[4] Flux in and out of glycolysis to and from these pathways are balanced between immediate and future bioenergetic, biosynthetic, and redox equilibrium needs and are regulated in the cell by a combination of surface receptor to nuclear signals, internal energy sensing/signaling proteins, and metabolite feedback signals acting in concert.[2, 3] Of these, mechanisms of metabolite feedback signaling to alter metabolic enzyme activity and metabolic flux include both allosteric binding as well as post translational modifications by reactive metabolites (rmPTM).[31, 36, 46, 66, 209]

One such reactive metabolite is methylglyoxal (MGO), which is produced as a by-product of central glycolysis via the non-enzymatic degradation of the triose phosphates glyceraldehyde phosphate (GAP) and dihydroxyacetone phosphate (DHAP). Due to its reactive nature, it can non-enzymatically modify a wide variety of biomolecules including proteins, nucleic acids, and metabolites and has been found to act as a signaling molecule between glycolysis and a diverse variety of cellular pathways ranging from antioxidant response[31] to cholesterol biosynthesis.[179] Another such metabolite is the central glycolytic metabolite 1,3 bis-phosphoglycerate (1,3 BPG), which arises from the subsequent step of glycolysis and has been found to non-enzymatically acylate active site lysines of adjacent glycolytic enzymes and

regulate flux distribution between bioenergetic requirements versus redox equilibrium and biosynthetic requirements in a glucose dependent manner. Proteome wide detection of rmPTM sites arising from both MGO and 1,3 BPG have revealed several dozens of sites across wide varieties of protein families for both metabolites. Yet, the sites are a small subset of the total proteome, suggesting that the center of glycolysis serves as a dynamic signaling hub which non-enzymatically targets a specific subset of proteins which function as sensors to coordinate diverse cellular pathways with metabolic state.

The upregulation of glycolysis has long been a hallmark of cancer.[1] The consequent upregulation of reactive central metabolites such as MGO have been associated with hormetic effects in cancer[102] in which lower doses of MGO potentiates cancer progression while excess doses of MGO results in formation of advanced glycation end products and subsequent cytotoxicity. Moreover, MGO derived rmPTMs have been identified in various contexts to act as a signaling metabolite between glycolysis and the antioxidant response pathway via the methylimidazole crosslink between proximal cysteine and arginine residues (MICA)[31] or the lactoylation of KEAP1 inducing NRF2 antioxidant response.[209] Finally, the amplification of the glyoxalase pathway across a wide variety of cancers[71] may correlate with the need for those cancers to regulate levels of MGO at levels sufficient to maintain beneficial rmPTM signaling axes.

Given these observations, we hypothesized that perturbing central glycolysis and its rmPTM signaling axes will disrupt the hormetic equilibrium and elicit antioxidant associated adaptive stress responses. To assess this possibility, we profiled the adaptive responses of these rmPTM signaling axes across a wide range of cancer cell lines by perturbing the central

glycolytic axis acutely with inhibitor, intermediately with inducible genetic knockdown, and chronically with stable genetic knockdown. In general, we found that perturbing the Glycolysis-NRF2 pathway in cancers results in an adaptive redox stress response specifically correlated to glutathione metabolism. We further find that this redox liability is replaced by upregulation in the pentose phosphate pathway and TCA under prolonged knockdown of PGK1 or GAPDH. By perturbing central glycolysis and profiling the adaptive responses of these rmPTM signaling axes, we determine metabolic rewiring adaptations to overcome central glycolytic stress and highlight potential target enzymes and pathways for the further development of more effective synthetic lethal strategies targeting cancer metabolism.

Results

Fig 5.1 Acute Inhibition of Central Glycolysis Enriches for Redox Stress Response Genes

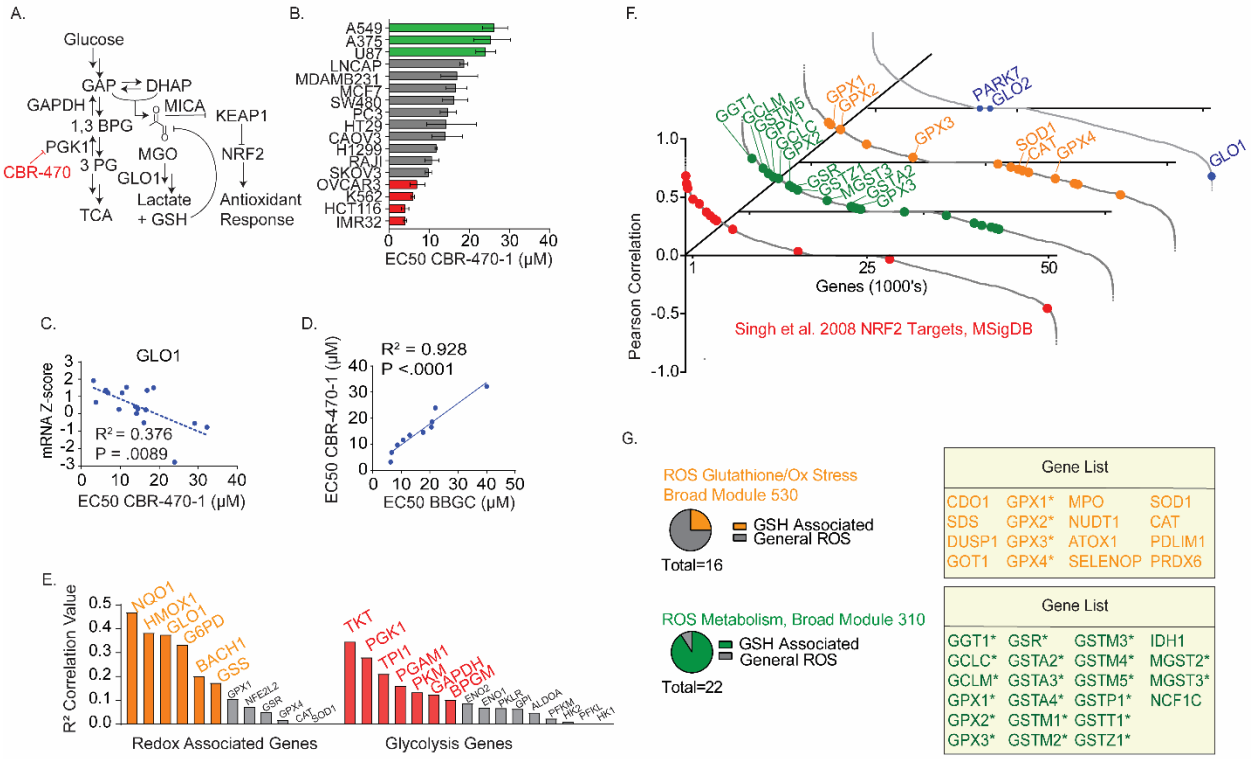

Figure 5.1 Continued
Figure 5.1: Acute Inhibition of Central Glycolysis Enriches for Redox Stress Response Genes: (A) Simplified schematic of Glycolysis-NRF2 pathway. Acute Perturbation of PGK1 by CBR-470-1 upregulates MGO levels in glycolysis and activates the antioxidant response via inhibition of KEAP1 and activation of NRF2 (shown). **(B)** Cellular viability in response to CBR-470-1 treatment across cell lines. Cells were treated with CBR-470-1 across a range of doses (0-40 μM), and viability was measured using the CTG assay 48 hours later. Graph depicts the cell lines tested, ranked according to their respective CBR-470-1 EC50. Data is the normalized viability ± S.E.M. from n = 1 biological replicate. **(C-D)** Linear correlation between sensitivity to CBR-470-1 and **(C)** GLO1 mRNA expression and **(D)** resistance to BBGC, an inhibitor of the MGO detoxification glyoxalase pathway. R^2 p-values are noted in the graph. **(E)** Canonical redox (orange) and glycolysis (red) associated genes ranked according to their respective correlation to CBR-470-1 sensitivity **(F)** Pearson correlations between sensitivity to CBR-470-1 and mRNA expression of all genes in the Cancer Cell Line Encyclopedia ranked largest to smallest. Genes associated with the NRF2-ARE pathway are colored red while redox stress metabolism genes are shown in orange and green. MGO detoxifying glyoxalases are highlighted in blue. **(G)** Gene lists of redox stress metabolism with glutathione metabolism dependent genes indicated by an asterisk. Quantified proportion of glutathione specific genes found within redox metabolism gene signatures.

We first conducted an acute screen of the relative response of a diverse panel of cancer cell lines to CBR-470-1, a specific inhibitor of the central glycolytic enzyme phosphoglycerate kinase (PGK1) shown to be able to consistently activate the NRF2 cascade at micromolar concentrations within 48 hours across a variety of cellular contexts. We sought to assess whether disruption of the rmPTM induced glycolysis-NRF2 (Figure 5.1A) signaling pathway would reduce viability across all cancer cell lines. We found that cancer cell lines were differentially susceptible to central glycolytic perturbation (Figure 5.1B) in terms of survival and viability. Among the most sensitive cell lines were the neuroblastoma cell lines IMR32 and the colorectal carcinoma cell lines HCT116 while the KEAP1 mutant NSCLC cell line A549 was among the most resistant cell lines. Because acute CBR-470 treatment has previously been demonstrated to upregulate levels of methylglyoxal (MGO) and induce the Glycolysis-NRF2 pathway (Figure 5.1A), we hypothesized that this differential cellular viability response was the related to the

differential expression of the rate limiting enzyme of the MGO detoxifying glyoxalase pathway GLO1[61] or the expression of enzymes related to glutathione biosynthesis and turnover. Using mRNA expression data from the Cancer Cell Line Encyclopedia (CCLE),[210] we correlated the expression of GLO1 of each cancer cell line against its respective EC50 (Figure 5.1C). We observed a strong negative r-squared correlation in cancer cell lines where cells more sensitive to CBR-470 displayed greater GLO1 expression, indicating that cell lines more sensitive to CBR-470 may be basally close to their maximum glyoxalase detoxifying limit and less able to acutely respond to and detoxify additional MGO. Comparing acute response of select cell lines from our cancer cell line panel to BBGC, an inhibitor of GLO1, demonstrated that cell lines sensitive or resistant to BBGC were strongly correlated to cell lines sensitive or resistant to CBR-470 (Figure 5.1D). Further CBR-470 EC50 vs. mRNA expression r-squared correlations of select genes of redox stress and glycolysis (Figure 5.1E) demonstrated 'positive' correlations wherein higher expression of NRF2 antioxidant stress response genes and central glycolytic enzymes proximal to PGK1 and the Glycolysis-NRF2 pathway correlated to acute resistance to CBR-470. Ranking the r-squared correlations of mRNA expression of all genes in the CCLE database (Figure 5.1F) versus CBR-470 EC50 of the cell lines in our panel showed that genes in curated molecular signatures of NRF2-antioxidant response, reactive oxygen species response, and redox stress response had among the highest positive or negative correlation scores. Of particular interest was that resistance to CBR-470 seemed especially associated with not only the NRF2-ARE response (Figure 5.1G, red), but also the expression of glutathione metabolism or glutathione mediated redox stress detoxification genes (Figure 5.1G, green and orange). More general redox stress response genes such as SOD1 and CAT and glutathione independent MGO glyoxalases such as

PARK7 had little to no correlation with CBR-470 acute response. Overall, cancer cell lines showed a differential acute response to CBR-470 correlated to the expression of glutathione associated genes and centrally located glycolytic enzymes.

Fig 5.2 Perturbation of Central Glycolysis Specifically Rescued by Glutathione Mediated Detoxification Processes

The correlations above indicated that determinants of sensitivity to acute perturbation of central glycolysis could be attributed to factors such as the turnover of MGO mediated redox stress, or the ability to turnover glycolytic intermediates and prevent bioenergetic stress from blockade of central glycolysis could be factors determining differential response to central glycolytic perturbation. To test which of these factors were determinants of central glycolytic stress response, we assessed the 48-hour relative viability of cells acutely challenged with CBR-470-1 alone or co-treated with a series of additives. If co-treatment with antioxidant additives resulted in rescue, it would indicate that acute loss in viability from central glycolytic perturbation was due to redox stress. If co-treatment with additives targeting bioenergetics resulted in rescue, it would indicate that acute loss in viability from central glycolytic perturbation was due to acute bioenergetic shortage.

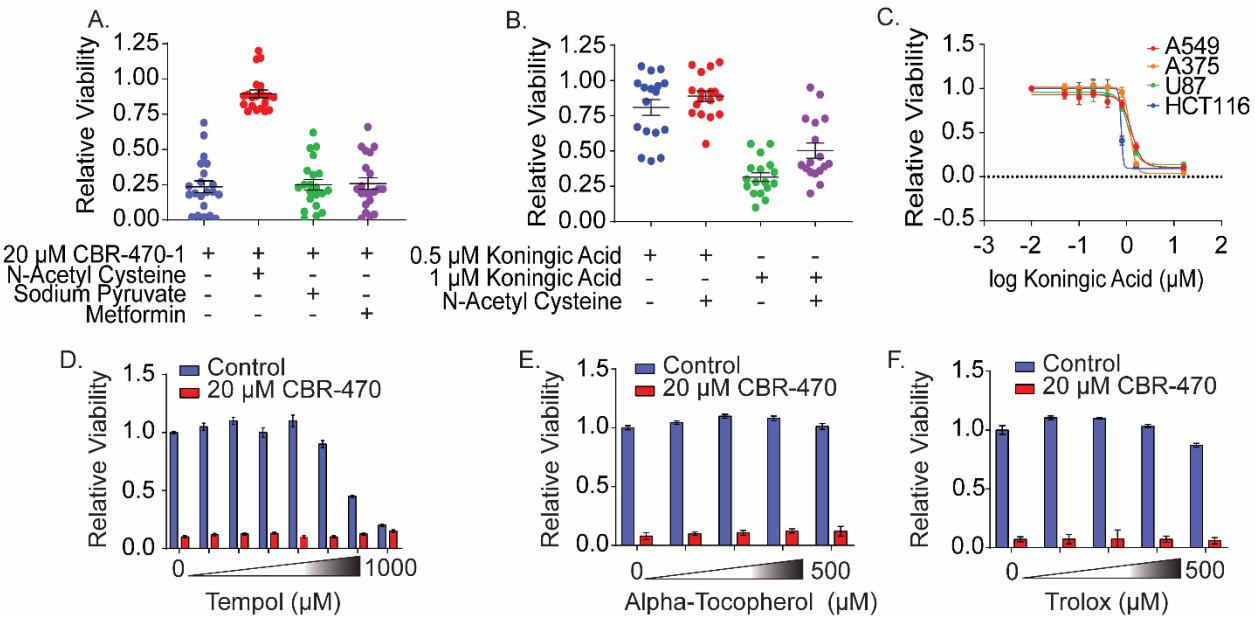

Figure 5.2: Perturbation of Central Glycolysis Specifically Rescued by Glutathione Mediated Detoxification Processes: (A-B) Cellular viability of cancer cell lines treated with **(A)** 20 μM CBR-470-1 alone or in combination with antioxidant additive 3 mM N-Acetyl Cysteine or bioenergetic additives 3 mM sodium pyruvate, or 1 mM metformin for 48 hours **(B)** 0.5 μM or 1 μM Koningic Acid alone or in combination with antioxidant 3 mM N-Acetyl Cysteine **(C)** Cellular viability of select cancer cell lines in response to Koningic Acid treatment. Cells were treated with Koningic Acid across a range of doses (0-2 μM), and viability was measured using the CTG assay 48 hours later. Graph depicts the EC50 Curves of the cell lines tested. Data is plotted with mean normalized viability plus S.E.M. from n = 1 biological replicates with triplicate wells per plate **(D)** Acute viability response of IMR32 cells treated with ROS scavenger Tempol alone or co-treated with CBR-470-1 **(E)** Acute viability of IMR32 cells treated with ROS scavenger Alpha-Tocopherol alone or co-treated with CBR-470-1 **(F)** Acute viability of IMR32 cells treated with ROS scavenger Trolox alone or co-treated with CBR-470-1. Data is plotted with mean normalized viability plus S.E.M. from n = 1 biological replicates with triplicate wells per plate

When we challenged the viability of our cancer cell line panel with a high dose of CBR-470-1 alone or in combination with additives N-acetyl cysteine, sodium pyruvate, or metformin, we observed global rescue from supplementation with the glutathione precursor N-acetyl cysteine (NAC). Additives targeting cellular bioenergetics such as the metabolic intermediate sodium pyruvate or metformin failed to rescue or synergistically decrease viability respectively (Figure 5.2A). This indicated that acute challenge with CBR-470-1 caused viability loss

correlated to redox stress pathways rather than acute bioenergetic stress caused by blockade of glycolysis. To determine whether central glycolytic blockade induced redox stress was a general response or specific to PGK1 inhibition, we used a potent irreversible inhibitor of GAPDH, Koningic acid[211, 212] (KA) alone or in combination with NAC and found that supplementation of NAC was able to rescue cell lines, though not as efficiently as when rescuing against CBR-470-1 (Figure 5.2B). The limited rescue from KA in combination with NAC in comparison to CBR-470-1 plus NAC could be attributed to the mechanistic difference between a reversible and an irreversible inhibitor, which in turn, also results in a limited differential response between cell lines (Figure 5.2C). Further development of a reversible and specific inhibitor of GAPDH would better answer whether targeting central glycolysis to induce a redox stress response is generalizable outside of PGK1. To assess whether the redox stress induced by CBR-470-1 and rescued by NAC supplementation was specific to glutathione or a general ROS response, we supplemented cell lines with superoxide dismutase mimetic tempol (Figure 5.2D), and vitamin E analogues alpha-tocopherol (Figure 5.2E), and Trolox (Figure 5.2F) and challenged cell lines to CBR-470-1 treatment. Although all three antioxidants are known to scavenge radicals and protect against oxidative stress and damage, they were unable to rescue cells against CBR-470-1 challenge. These results, together with the mRNA expression vs. CBR-470-1 sensitivity R^2 correlations for the genes SOD1, CAT, and GPX4 in Figure 5.1E, led us to conclude that cellular response to acute central glycolytic perturbation is specific and heavily correlated to glutathione redox metabolism but unrelated to oxygen or lipid peroxyl radical detoxification.

Fig 5.3 Acute Co-Perturbation of Central Glycolysis and Glutathione Metabolic Pathways Increases Sensitivity to Redox Stress

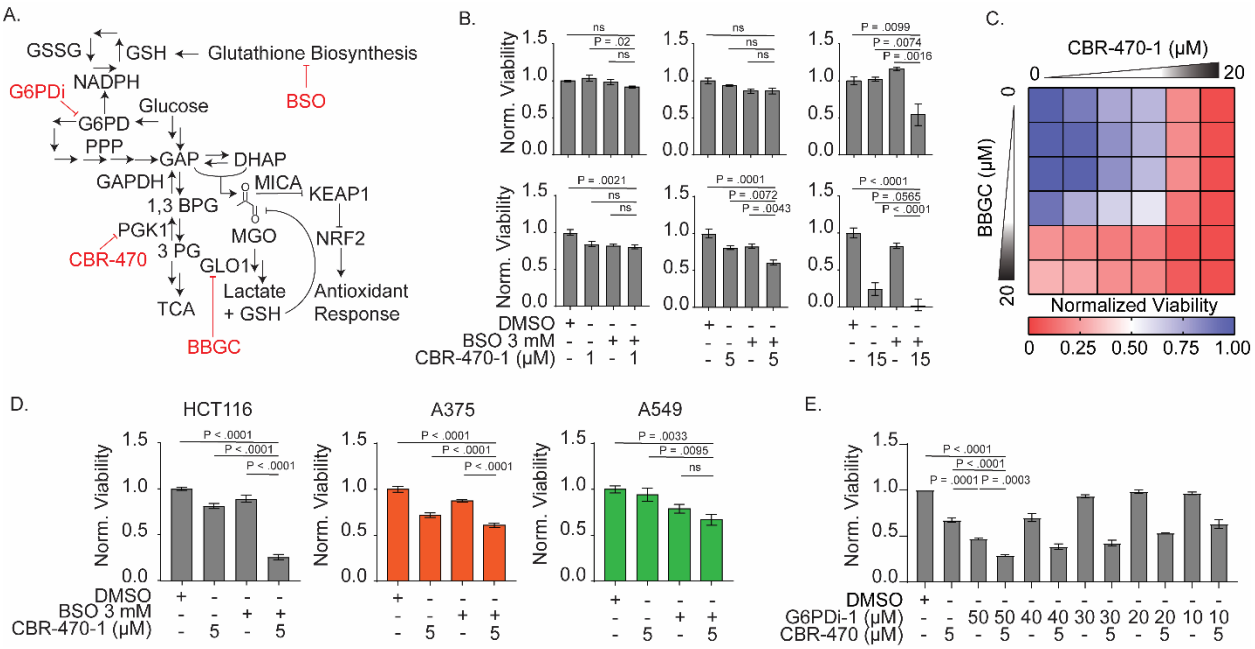

Figure 5.3: Acute Co-Perturbation of Central Glycolysis and Glutathione Metabolic Pathways Increases Sensitivity to Redox Stress: (A) Simplified schematic of Glycolysis-NRF2 pathway and adjacent glutathione metabolic pathways. Acute Perturbation of PGK1 by CBR-470-1 combined with perturbation of glutathione metabolism induces redox stress in the subset of cell lines sensitive to central glycolytic perturbation (shown). **(B)** Relative viability of HCT116 cells responding to acute perturbation of central glycolysis and glutathione biosynthesis treated with vehicle, BSO, and CBR-470-1 in the indicated concentrations and combinations for 24 hrs. (top) or 48 hrs. (bottom) **(C)** Relative viability of HCT116 cells responding to acute perturbation of central glycolysis and glyoxalase pathway inhibition treated for 48 hr. with 0, 1.25, 2.5, 5, 10, & 20 μM CBR-470-1 in combination with 0, 1.25, 2.5, 5, 10, & 20 μM BBGC **(D)** Relative viability of HCT116, A375, and A549 cells responding to acute perturbation of central glycolysis and glutathione biosynthesis treated with DMSO, BSO, or CBR-470-1 at indicated doses for 48 hours **(E)** Relative viability of HCT116 responding to acute perturbation of central glycolysis and pentose phosphate pathway inhibition treated with DMSO, CBR-470-1, and G6PDi at indicated doses. All data is plotted with mean normalized viability plus S.E.M. from n = 3 biological replicates with triplicate wells per plate, with exception of 3E which is n = 2 biological replicates. All statistical analysis is by ordinary one-way analysis of variance (ANOVA).

Upon finding this correlation between acute central glycolytic perturbation and glutathione specific redox stress response, we next sought to determine whether cellular viability

response was determined by a particular glutathione mediated pathway or general glutathione availability. To do so, we acutely challenge one of the most acutely sensitive cancer cell line HCT116 with CBR-470-1 in combination with BSO (buthionine sulphoximine) a potent and specific inhibitor of the glutathione biosynthesis enzyme gamma-glutamylcysteine synthetase, BBGC (S-p-bromobenzylglutathione cyclopentyl diester) a specific inhibitor of MGO detoxification enzyme Glyoxalase 1, or G6PDi, a specific inhibitor of the key rate limiting enzyme of the oxidative pentose phosphate pathway glucose-6 phosphate dehydrogenase. Acute perturbation of any of the aforementioned pathways would limit cellular ability to generate or regenerate reduced glutathione (Figure 5.3A).

We found that depleting cellular capacity to generate glutathione with BSO treatment strongly improved the effect of central glycolytic perturbation (Figure 5.3B) in a dose and time dependent manner. Using the same compound combination on cell lines previously found to be most resistant to acute CBR-470-1 treatment resulted in a similar result albeit with a lesser decrease in viability (Figure 5.3D) that strongly correlated with expression levels of glutathione metabolism genes. Likewise, co-targeting the glyoxalase pathway and limiting cellular ability to detoxify MGO and replenish reduced glutathione from hemithioacetal resulted in an additive effect at intermediate dosages of CBR-470-1 and BBGC (Figure 5.3C). Finally, co-treatment of CBR-470-1 and G6PDi to induce acute redox stress and simultaneously target generation of cytosolic NADPH and regeneration of reduced glutathione in the upper oxidative pentose phosphate pathway also demonstrated dose dependent loss of cellular viability upon co-treatment (Figure 5.3E). Altogether, these experiments demonstrate that general availability of reduced

glutathione is a key determining factor needed in cells to overcome the effects of acute central glycolytic perturbation.

Fig 5.4 Redox Stress Remains Present in Inducible but not Stable Central Glycolytic Knockdown

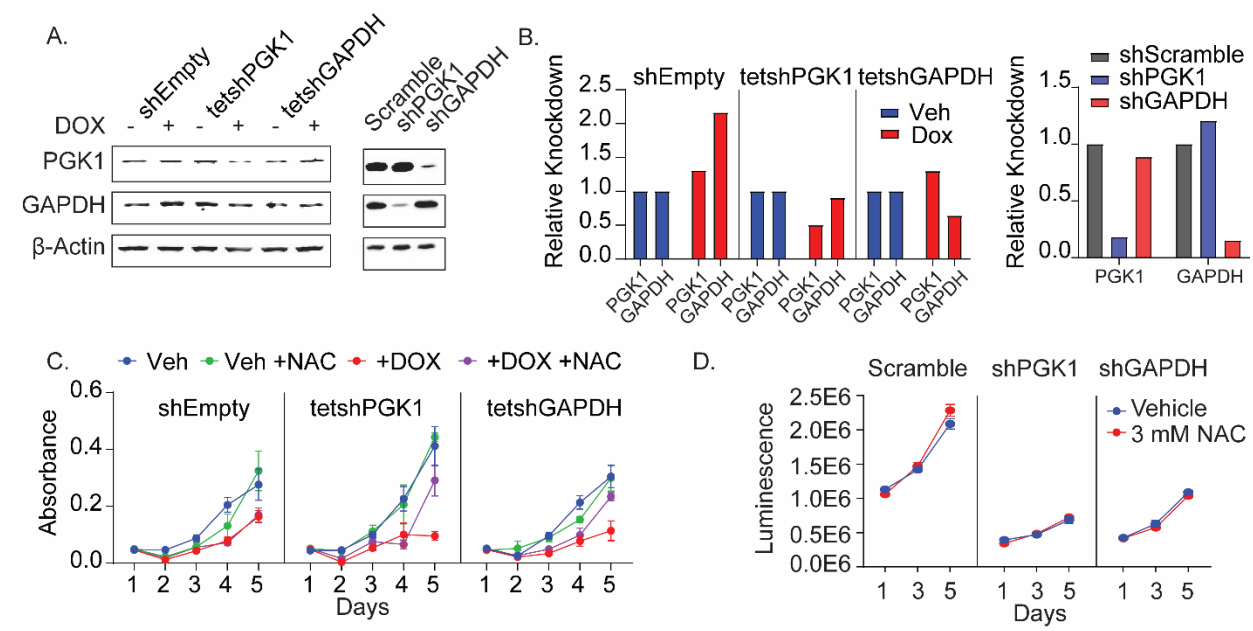

Figure 5.4: Redox Stress Remains Present in Inducible but not Stable Central Glycolytic Knockdown: (A) Representative western blots showing knocked down expression levels of PGK1, GAPDH, β-Actin in inducible tet-shRNA knockdown after 4 days treatment with/without doxycycline (DOX) and stable shRNA knockdown HCT116 cell lines. **(B)** Densitometry quantification of knockdown, normalized with respect to Veh condition for inducible knockdowns (left) and shScramble for stable knockdowns (right). **(C)** Crystal violet growth assay of inducible cell lines treated with Veh, 3 mM NAC, 1 µg/mL Doxycycline, or combination of NAC and Doxycycline over 5 days at 590 nm absorbance. Inducible knockdowns were treated daily with 1 µg/mL doxycycline for 4 days prior to being treated to the conditions stated above. **(D)** Representative growth curve of stable knockdown HCT116 cell lines treated with Veh or 3 mM over 5 days.

While acute perturbation of central glycolysis via inhibitor treatment induced redox stress in HCT116 cells, we sought to test whether this redox stress could be recapitulated in genetic knockdown models of central glycolytic perturbation or whether the prolonged depletion of

glycolytic enzymes would induce metabolic reprogramming that would adapt against central glycolytic redox stress.

We engineered stable and inducible HCT116 cell lines aimed at knocking down the central glycolytic enzymes PGK1 or GAPDH using shRNA, with knockdown controls expressing a scrambled shRNA (Figure 5.4A-B). The inducible knockdown lines were engineered to use the same shRNA sequences as the stable knockdown lines, coupled to a tet-ON expression system to induce knockdown of PGK1 or GAPDH upon doxycycline (Dox) treatment over the course of a week. These two genetic knockdown models served to represent different forms of perturbation. The inducible knockdown lines simulate the cellular response to a gradual buildup of glycolytic perturbation whereas the stable knockdown lines would simulate cells rewired against central glycolytic stress perturbation.

Despite differential knockdown efficiencies, cell lines representing both inducible and stable knockdown of both PGK1 and GAPDH exhibited attenuated growth rate when compared to controls. However, only the inducible PGK1 or GAPDH knockdown exhibited growth rate rescue from NAC supplementation, consistent with what was observed in acute rescue from redox stress (Figure 5.4C). In contrast, the PGK1 and GAPDH stable knockdown cell lines demonstrated no discernible differences in growth rate between vehicle or NAC supplementation (Figure 5.4D). We observe that, despite lesser knockdown efficiency relative to the stable knockdowns, inducible knockdowns remain responsive to antioxidant supplementation when challenged with central glycolytic perturbation on an ‘intermediate’ timescale, similar to results seen in acute compound treatment. In contrast, despite high knockdown efficiency, the stable

knockdown lines are metabolically rewired against redox stress from central glycolytic perturbation.

Figs 5.5 and 5.6 Stable Knockdown of Central Glycolysis Upregulates Pentose Phosphate Pathway Metabolism but Differentially Upregulates Mitochondrial Metabolism

We wished to understand what metabolic rewiring occurs to resist redox stress elicited by knockdown of central glycolysis; whether pathways identified under acute conditions such as the NRF2-antioxidant response and/or glutathione metabolism had been upregulated to compensate for chronic central glycolytic stress or whether the commonly observed upregulation of mitochondrial metabolism as an adaptation has de-prioritized glycolytic flux and central glycolytic rmPTM signaling. We therefore proceeded to use quantitative mass spectrometry to profile the relative protein expression changes in SILAC labeled PGK1 and GAPDH stable knockdown lines using light SILAC to label PGK1 and GAPDH knockdown cells and control Scramble cell lines using heavy SILAC. This was done to avoid the possibility of losing knockdown efficiency in the shPGK1 and shGAPDH cell lines over the 4-6 passages required for heavy SILAC labeling. In addition, we utilized quantitative metabolomics to measure the amounts of select metabolites which arise from glycolysis, the TCA, and the pentose phosphate pathway.

Using bulk proteomics protocols, we profiled and compared the relative expression of ~4000+ proteins in the PGK1 or GAPDH knockdown lines versus the Scramble control. Unlike in the correlations observed from the acute challenge of central glycolysis, the stable knockdowns exhibited no changes to expression of NRF2-ARE pathway proteins (Figure 5.5A).

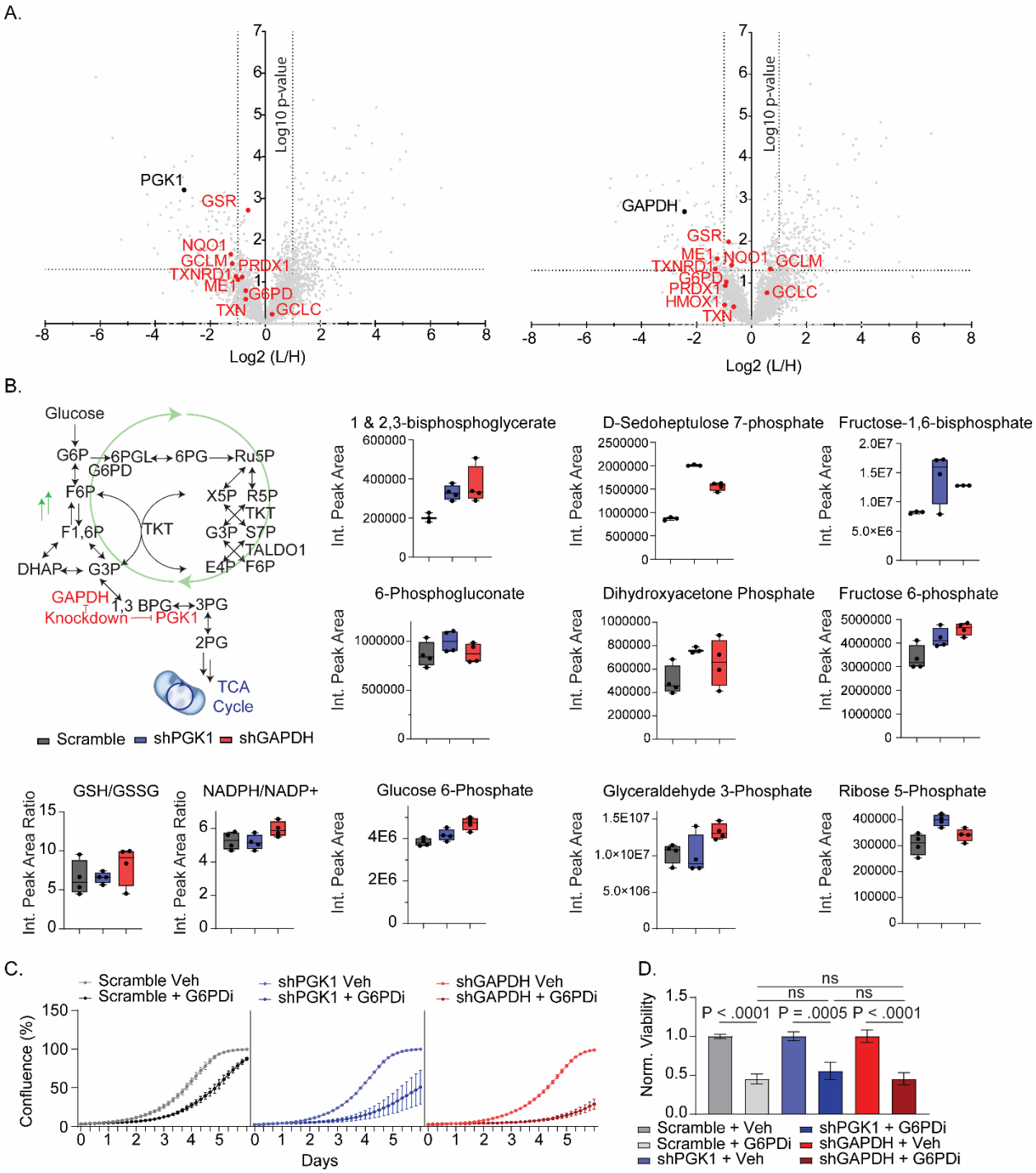

Figure 5.5: Stable Knockdown of Central Glycolysis Upregulates Pentose Phosphate Pathway Metabolism: (A) Relative protein expression of NRF2-ARE signature proteins in light-labeled shPGK1 or shGAPDH cells versus heavy-labeled shScramble control, n = 4 bio-replicates **(B)** Simplified schematic of upregulated central metabolic intermediates in response to central glycolytic knockdown and quantified comparisons of select metabolites in upper glycolysis and the Pentose Phosphate Pathway for shPGK1, shGAPDH, or shScramble HCT116

Figure 5.5 Continued
cells, n = 4 bio-replicates. Metabolites quantified as integrated peak areas. **(C)** Comparative growth rate of shPGK1, shGAPDH, or shScramble HCT116 cells quantified by Incucyte live-cell analysis over 5 days treated with or without pentose phosphate inhibitor G6PDi **(D)** Relative viability comparison of HCT116 stable cell lines in response to ± 40 µM G6PDi for 48 hours. Cell viability quantified by Calcein-AM fluorescent signal, n = 3 bio-replicates. All statistical analysis is by ordinary one-way analysis of variance (ANOVA).

However, the metabolomic profile of the metabolites of glycolysis and the pentose phosphate pathway (Figure 5.5B) revealed an overall increase in upper glycolytic and lower pentose phosphate pathway metabolites in both the knockdown lines relative to controls, consistent with a blockade of central glycolysis.[31, 213] Furthermore, despite deep knockdown of central glycolytic enzymes, the ratio of metabolites associated with redox stress detoxification such as reduced/oxidized glutathione and NADPH/NADP+ in the knockdown lines were found to be similar to controls.

We hypothesized that the increased level of metabolites between upper glycolysis and the pentose phosphate pathway in the knockdowns were a compensatory rewiring mechanism in the knockdown lines to maintain equivalent redox potential as the control cells. To test this, we challenged the stable cell lines with G6PD inhibitor[112, 214, 215] to determine whether the knockdown lines would be more sensitive to disruption of the pentose phosphate pathway. Although knockdown cell lines did not show significant viability differences compared to control cell lines (Figure 5.5D), their growth rates were found to be impaired when challenged with G6PD inhibitor relative to scrambled control cell lines. Moreover, the growth rate of shGAPDH cells, which demonstrated a slight increase in NADPH/NADP+ ratio in comparison to shPGK1 or control cells, was more heavily impaired than shPGK1.

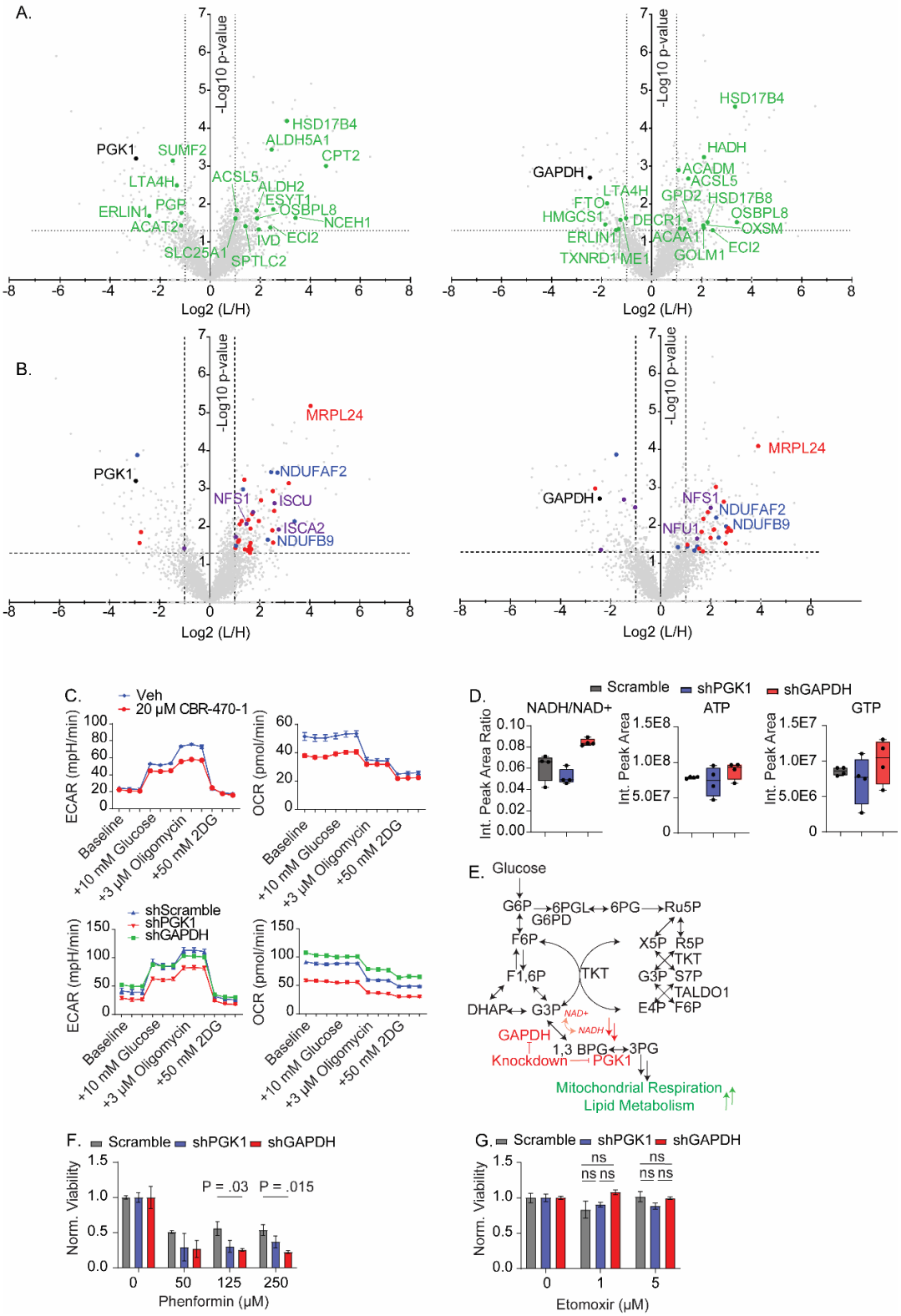

Figure 5.6: Stable Knockdown of Central Glycolysis Differentially Upregulates Mitochondrial Metabolism

Figure 5.6 Continued
(A) Relative protein expression of proteins associated with lipid metabolism and transport (green) and **(B)** proteins associated with iron-sulfur cluster electron transfer (purple), mitochondrial translation (red) and the electron transport chain (blue) in light-labeled shPGK1 or shGAPDH cells versus heavy-labeled shScramble control, n = 4 bio-replicates. **(C)** Representative glycolytic stress test Seahorse profiles of wild-type HCT116 cells challenged with CBR-470-1 for 24 hrs. (top) or stable HCT116 knockdown lines (bottom). OCR and ECAR represent oxygen consumption rate and extracellular acidification rate, respectively. **(D)** Comparative levels of select bioenergetic and redox nucleotides in shPGK1, shGAPDH, or shScramble HCT116 cells, n = 4 bio-replicates. Metabolites quantified as integrated peak areas. **(E)** Simplified schematic of compensatory metabolic adaptation in lower glycolysis and TCA in response to central glycolytic knockdown. **(F-G)** Comparative viability of stable knockdown cell lines after 48 hrs. of treatment with **(F)** phenformin or **(G)** etomoxir at the indicated concentrations. Viability quantification utilized Calcein-AM fluorescent signal. All statistical analysis is by ordinary one-way analysis of variance (ANOVA).

We continued to profile the knockdown lines by profiling the protein expression and metabolism downstream of central glycolysis (Figure 5.6 A-D). Both knockdown lines demonstrated similar proteomics profiles (Figure 5.6 A, B) with expression of proteins associated with lipid metabolism/transport and mitochondria upregulated, consistent with metabolic adaptation to glycolytic blockade. However, when comparing global metabolic profiles via Seahorse assay (Figure 5.6C), we found shPGK1 cell profiles to be more akin to treatment with CBR-470-1, while shGAPDH cell profiles showed elevated basal ECAR and consistently elevated OCR. The comparative NADH/NAD+ ratio as well as other TCA associated metabolites (Figure 5.6D) in shGAPDH cells was more elevated than in control or shPGk1 cells.

We hypothesized that although the adaptive metabolic response of shPGK1 and shGAPDH bore similarities in both proteomic profiles as well as in upper glycolysis, the knockdown of GAPDH induced comparatively greater reprogramming of mitochondrial processes than knockdown of PGK1 (Figure 5.6E). Such processes include mitochondrial respiration and electron transport chain (ETC) activity as well as fatty acid oxidation[212], both of

which are upregulated in the proteomic profiles. To test whether perturbing these pathways resulted in greater sensitivity in shGAPDH cell lines, we challenged the stable cell lines with mitochondrial ETC complex I inhibitor phenformin (Figure 5.6F) and etomoxir (Figure 5.6G), an inhibitor of CPT1 which governs the import of long chain fatty acids into the mitochondria oxidation. We found that while perturbation of the ETC by phenformin resulted in greater viability loss in both knockdown lines compared to control, shGAPDH was comparatively more affected than shPGK1, consistent with previous data (Figure 5.6A-D). In contrast, inhibition of CPT1 showed no significant difference in viability amongst cell lines.

These results may indicate that mitochondrial fatty acid oxidation is not utilized by shGAPDH cells to rebalance NADH/NAD+ ratio. Alternatively, it is known that short and medium chain fatty acids enter the mitochondria directly and may be preferentially used for respiration upon CPT1 blockade.[216, 217] Furthermore, proteins of the peroxisome such as HSD17B4, ECI2, ACSL5 are upregulated in proteomic profiles indicating that oxidation by the peroxisome may also be contributing to CPT1 resistance.

More broadly, knockdown of PGK1 results in the loss of ATP generation, which can be compensated for with increased levels of mitochondrial activity. However, knockdown of GAPDH may heavily perturb the balance of cytosolic ratio of NAD+/NADH. Although shuttling mechanisms between the cytosol and mitochondria are normally used to re-balance this ratio, the malate/aspartate shuttle which replenishes cytosolic NAD+ to create mitochondrial NADH, may not operate efficiently when concentrations of cytosolic NAD+ are high. Moreover, higher levels of DHAP arising from central glycolytic perturbation may also cause the glycerol phosphate

shuttle to favor NAD+ in the cytosol. Thus, the elevated OCR and NADH/NAD+ ratio observed in shGAPDH stable cells may result from a compensatory upregulation to generate NADH.

Discussion

In summary, this study sought to assess the response of cancer cell lines to central glycolytic perturbation. Using acute perturbation of cancer cell lines using inhibitors, we demonstrated that acute central glycolytic perturbation heavily and specifically correlates with glutathione associated stress response. Additionally, using inducible knockdown as another model of central glycolytic redox stress, we find that similar redox stress liabilities remain despite cells being under a longer 'semi-acute' perturbation timeframe. Finally, we find that these redox liabilities no longer remain in chronic knockdown models. Instead, metabolite exchange between upper glycolysis and the pentose phosphate pathway as well as mitochondrial respiration appear to be upregulated. Moreover, despite both being adjacent steps of central glycolysis, there appear to be additional compensatory responses in GAPDH knockdown cells versus PGK1 knockdown cells.

Many steps in metabolism are coupled to parallel processes that produce or consume energy carrier molecules such as ATP/ADP or redox cofactors such as NAD(H) and NADP(H). However, while ATP/ADP are transported in bulk by highly abundant ADP/ATP translocases, redox equivalents are shuttled between the cytosol and the impermeable mitochondrial membrane via interconversion of glycolytic and TCA cycle intermediates to maintain cellular redox homeostasis. The greater mitochondrial compensatory reprogramming in shGAPDH versus shPGK1 cells may reflect the relative difficulty in balancing redox equivalents relative to bioenergetic equivalents between cell compartments while glycolysis is perturbed.

From a biological perspective, one function of the Glycolysis-NRF2-ARE pathway is to coordinate influxes of glucose, signaling the production of reductive antioxidant molecules that are scaled to the anticipated redox stress (and potential damage) that results from reactive glycolytic byproducts such as MGO and from mitochondrial reactive oxygen species byproducts. However, whereas regular metabolism can bolster redox stress response by leveraging ROS scavenging systems made up of superoxide dismutases, catalases, peroxidases, and thioredoxins, acute blockade of central glycolysis seems to allocate much of the redox stress burden solely onto glutathione. This highlights both the importance of glutathione in resolving stress arising from glycolytic reactive organic species and demonstrates the damage specificity of different cellular detoxification mechanisms.

In more heterogeneous environments such as the lactate rich tumor microenvironment, lactate may provide an alternative source of metabolites for cells to supplement and rebalance NADPH/NADP+ and NADH/NAD+ ratios, limiting redox stress, mitochondrial reprogramming, and sensitivity to central glycolytic perturbation. In contrast cell sensitivity may be exacerbated under hypoxic environments where glycolysis and oxidative stress are upregulated and NRF2 activation supports cell survival.

Future studies profiling central glycolytic perturbation in these metabolically complex environments will help connect the Glycolysis-NRF2 signaling axis to more clinically relevant conditions and may prove to be advantageous in enhancing the effects of GSH depletion and/or sensitizing cell types previously more resistant to ROS stress.

Future Directions

The dynamics of the lipidome, the state of the mitochondria, and the role of peroxisomes in response to redox stress are all direct future directions to this study of central glycolytic perturbation responses. With respect to the lipidome, it is well-annotated[218] that lipids have critical roles in cell structure, signaling and bioenergetics. Under redox stress conditions, lipids regulate a diverse host of key functions including homeostasis, energy storage, inflammation, and maintenance of electrochemical subcellular gradients. Under oxidative stress, dysregulation of lipid peroxide clearance and iron metabolism lead to ferroptosis and cell death.[105, 219] Although acute assays did not find correlation between sensitivity between central glycolytic perturbation and ferroptosis regulatory genes such as GPX4, further work testing whether acute glycolytic perturbation relates to this lipid based redox stress pathway in a non-GPX4 related manner are still needed via cell assays measuring downstream secondary products of ferroptosis (4-HNE and MDA) via immunoblot, challenging cells with CBR-470-1 in combination with inducers of ferroptosis (erastin) or inhibitors from ferroptosis (iron chelators) as some examples.

With respect to the mitochondria under chronic perturbation, many of the upregulated proteins were iron-sulfur cluster metalloproteins best known for their role in redox reactions within the electron transport chain. In connection to ferroptosis mentioned above, upregulated mitogenesis may be a compensatory adaptation in which ferroptosis is inhibited via ‘chelation’ of excess iron by mitochondria into additional electron transport chain proteins. Understanding whether the proteomic data showing upregulated mitochondrial proteins directly results in increased number of mitochondrial and/or the increased turnover of mitochondria in chronically perturbed cells may hint at how cells adapt to prolonged glycolytic perturbation and redox stress.

Related to mitochondrial dysregulation, the metabolomic data noted relatively little disruption of NAD/NADH balance within chronically reprogrammed cells despite deep knockdown and presumed perturbation of cytosolic processes that are needed to balance NAD/NADH ratio such as GAPDH mediated conversion of G3AP to 1,3 BPG. One possible explanation is that compensatory responses by the peroxisome have emerged as a means by which lipid metabolism and redox stress response[216, 217] is regulated. Indeed, the co-upregulation of many proteins in both the peroxisome and the mitochondria in Chapter 5 proteomic datasets (see Table 5.2, uploaded as a separate supplementary file) may be a sign that mitochondrial dysregulation is stimulating a compensatory increase in peroxisome expression and an increase in exchange of NAD/NADH between cytosol, peroxisome, and mitochondria. activity to respond to metabolic dysregulation. Mapping the exchange of fatty acid lipid metabolism between the three compartments using deuterium labeled fatty acids may be a way in which peroxisomal and/or mitochondrial compensatory upregulation can be mapped and whether they are responsible for rebalancing cellular NAD/NADH redox ratio.

Additional Figures

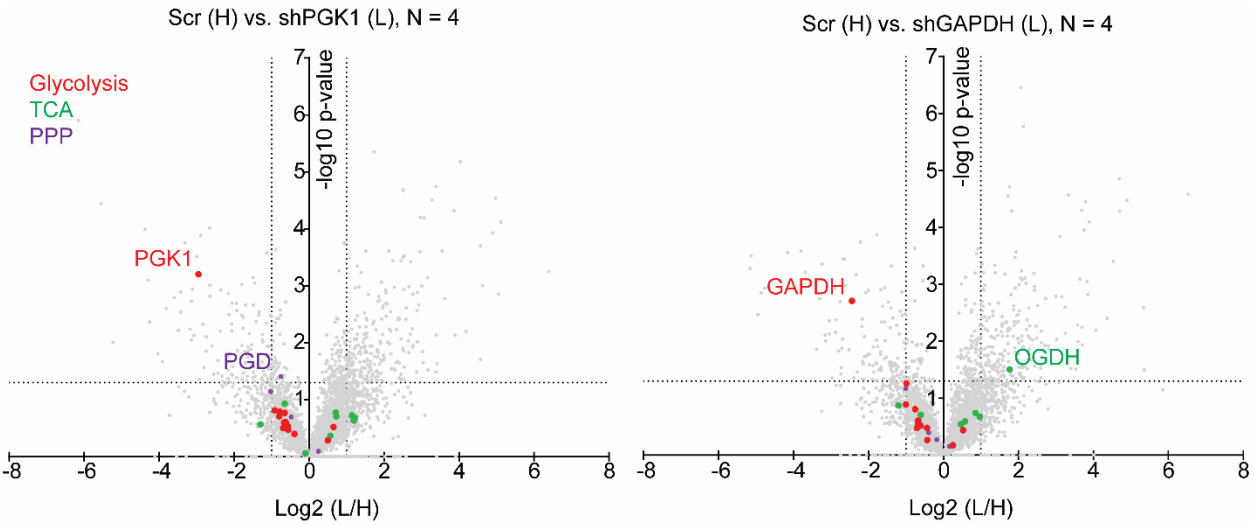

Figure 5.7 Relative protein expression of metabolic proteins: in glycolysis (red), TCA (green), and the pentose phosphate pathway (purple) in light-labeled shPGK1 or shGAPDH HCT116 cells versus heavy-labeled shScramble control, n = 4 bio-replicates. Statistically significant enzymes are labeled.

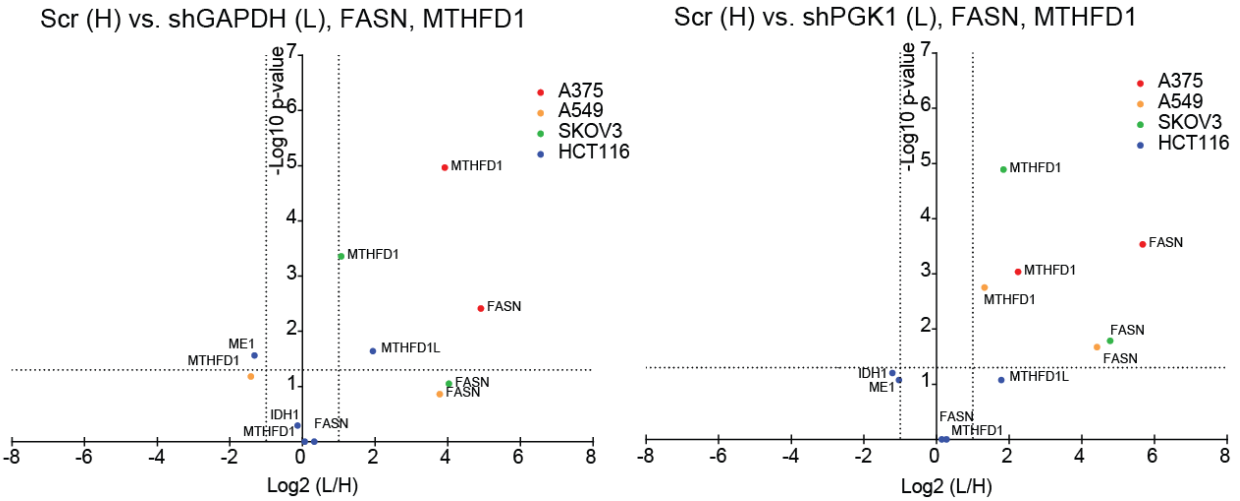

Figure 5.8 Relative protein expression of NADPH generating redox proteins across different cancer stable lines: in light-labeled shPGK1 or shGAPDH stable cell lines versus heavy-labeled shScramble controls, n = 4 bio-replicates for HCT116 lines, n = 3 for all other lines.

Tables

Table 5.1 Average Integrated Peak Area of Central Metabolites in HCT116 stable knockdown lines, UChicago CCC Metabolomics Platform

Metabolite	Integrated Peak Area Scramble	STD	Integrated Peak Area shPGK1	STD	Integrated Peak Area shGAPDH	STD
1,3-bisphosphoglycerate/2,3-bisphosphoglycerate	202323.6667	18922.53546	329714.75	32965.6983	366285	83936.80405
2-phosphoglycerate/3-phosphoglycerate	8449597.75	797132.4981	6713229.667	136805.6581	8789234.75	262309.2312
6-Phosphogluconate	863348	111210.4327	1000534.5	96539.62174	880410.75	86060.91094
D-Sedoheptulose 7-phosphate	865607	27904.48216	2008830	13170.60738	1555203.5	76224.07071
Dihydroxyacetone Phosphate(DHAP)	498279	110287.5307	761851.6667	21014.65289	654520.75	175033.4365
Fructose-1,6-bisphosphate	8189503.333	163026.7137	14269765.25	3812500.996	12800662	29426.50888
Glucose	207553196	27963071.55	187271366	58666548.26	215207456	16505752.65
Glucose 1-Phosphate/Galactose 1-Phosphate/ Fructose 6-phosphate	3367644.75	451367.3097	4214452.25	352403.5364	4605031	234073.5098
Glucose 6-Phosphate	3827314	160384.4726	4160874.25	233633.1351	4695944.25	259998.189
Glyceraldehyde 3-Phosphate	10351985	1194774.457	10030090.5	2367268.667	13272682.25	958542.9935
Glycerol 3-Phosphate/Glycerol 1-Phosphate	4730941	943513.8398	3861034.667	109967.9735	4219224	343901.7959
Lactate	5045245632	538177834	5187120896	597372656.9	5682577024	548308609.3
Pyruvate	296625032	4958667.182	314723884	31398651.92	372092960	29109832.09
Ribose 5-Phosphate	305058.25	35619.83866	397156.75	19686.70328	340442.75	21406.33498
Ribulose 5-phosphate/Xylulose 5-phosphate	264977.25	83075.4704	320550.25	52452.12644	304659.25	51058.04683
Phosphoenolpyruvate	1565703	272792.6	1412832.8	317744.9	1561654.3	222089.9
ATP	78531422	1146786	7.3E+07	1.8E+07	9E+07	1E+07
ADP	18449652	209001.7	1.8E+07	2776388	2E+07	1E+06
AMP	3127783	67716.11	3109675	476798	3E+06	328821
CTP	5201770.75	341764.5	4938119	1318828	6E+06	1E+06
CDP	215593.5	32801.93	206338	46982.9	214677	36558
CMP	192488	23120.08	168803	29279.6	176727	18579
GTP	8557457.5	496512.8	7279716	2982347	1E+07	3E+06
GDP	1483839	16504.34	1343233	390735	2E+06	280337
GMP	500323.75	14093.81	499754	86889.3	534731	52397
UTP	15394143.5	1226731	1.5E+07	3361311	2E+07	2E+06
UDP	671609.25	88981.46	665074	130960	615059	86522
UMP	595796.25	51202.45	633920	61766.3	597137	28320
Glutathione Oxidized	94684740	18071639	8.7E+07	1.8E+07	8E+07	3E+07
Glutathione Reduced	581825368	56660499	5.6E+08	6.9E+07	6E+08	4E+07
NAD+	57566117	1553637	5.7E+07	8076309	6E+07	5E+06
NADH	3536573.5	641653.2	2939086	640524	5E+06	497212
NADP+	627288.5	48415.46	579237	163240	604437	87519
NADPH	3282129	66665.89	3013519	880022	4E+06	568256
NADH/NAD+	0.06150445	0.011361	0.05168	0.00645	0.0845	0.0029
NADPH/NADP+	5.266609	0.454978	5.1749	0.38708	5.9645	0.3993
ATP	78531422	1146786	7.3E+07	1.8E+07	9E+07	1E+07

Table 5.2 Chronic Proteomic Perturbations, Significant Hits: Dataset of significantly (log2 Light/Heavy ratio > 1 or < -1, -log10 p-value > 1.3, up or downregulated protein expression in light-labeled shPGK1 (‘P’) or shGAPDH (‘G’) stable cell lines versus heavy-labeled shScramble control (‘S’) cell lines. **Uploaded separately as a supplemental file**, n = 4 bio-replicates for HCT116 lines and n = 3 for all other cell lines (A549, A375, SKOV3).

SUMMARY, BIGGER PICTURE FUTURE DIRECTIONS, AND CONCLUDING REMARKS

This dissertation spans five chapters, each delving into aspects of how cellular metabolism resulting reactive metabolite modifications dynamically modulate biology from both a fundamental as well as disease perspective.

Chapter 3 discusses the prevalence and dynamic regulatory role of 3-phosphoglyceryl-lysine (pgK) modifications in cyanobacteria, indicating their evolutionary conservation and fundamental importance in cellular regulation. The study shows pgK's key role in managing carbon flux and its oscillatory behavior akin to phosphorylation, especially in the switching between light/dark metabolic pathways, emphasizing its critical role in carbon allocation between bioenergetic and biosynthetic processes. Moreover, this research serves as an example of how intrinsically coupled rmPTM mediated regulation is to fundamental pathways like glycolysis across all organisms. Given the conservation of active site lysines across prokaryotes[141], studying rmPTM regulation within the context of gut microbiota is a way to link rmPTM signaling between simple prokaryotes and complex eukaryotes. Though it has been long understood that metabolite signaling regulates host-microbiome interactions,[220] the biological regulation of microbiota at the PTM level is only beginning to be mapped and understood starting with phosphorylation and acetylation.[221] Investigating how metabolite precursors of rmPTMs are exchanged between host and microbiome, how nutrition and diet can program microbiome metabolism at the enzyme and pathway levels may lend insight into how the microbiome supports human health and conversely, how dysregulated signaling via rmPTMs induces the microbiome to support the onset and development of numerous diseases.

Chapter 4 examines the detoxification mechanism of DJ-1 against methylglyoxal (MGO). The study unambiguously confirms DJ-1's role in MGO detoxification as a glyoxalase while providing a plausible explanation of why various groups observed varying ratios of L to D-lactate production from DJ-1 mediated detoxification. The research also highlights the non-enzymatic conversion of MGO to lactate, a factor crucial in accounting for cellular responses to oxidative stress and implications in diseases like Parkinson's in both the presence and absence of detoxification mechanisms. Beyond disease biology in humans and in connection to Chapter 3, the non-glutathione dependent and/or non-enzymatic conversion of MGO to lactate may lend insight as to how life was able to survive, develop, and evolve means of defending against reactive glycolytic byproducts between the evolution of glycolysis ~3.5 billion years ago[3, 151] and the Great Oxygenation Event[222, 223] ~2.1 billion years ago which is thought to have stimulated the evolution of glutathione biosynthesis in organisms.[224] Moreover, the roles that MGO regulation by tissue specific isozymes of glyoxalases are increasingly being mapped outside mammalian contexts and have been associated with diverse plant based functions including but not limited to aging, intercellular signaling, seed germination, and pollination.[74] These studies ultimately highlight the universality of rmPTM based signaling regulation across life and the intrinsic importance in mapping rmPTMs in the proteome.

The appendix to Chapter 4 focuses on the unique role of HDAC3 in removing glyceryl modifications from lysines, indicating a two-step removal process for pgK modifications. This finding underscores HDAC3's potential role in regulating pgK across various proteins, which could have significant implications in understanding neurodegenerative diseases like Parkinson's. While the work is far from finished, it highlights how HDACs may have exciting, yet

undiscovered roles in regulating protein function directly as a PTM eraser in addition to its more indirect regulatory functions at the epigenetic level.

Chapter 5 explores the response of cancer cell lines to central glycolytic perturbations and maps differences in acute, intermediate, and chronic responses. The findings reveal that acute perturbation correlates with glutathione-associated stress response and highlights that this differs chronically perturbed in GAPDH and PGK1 knockdown cells. The study suggests that acute glycolytic blockades burden glutathione with redox stress, emphasizing its role in detoxifying glycolytic byproducts and maintaining redox balance in varying environmental conditions. Connecting to a bigger picture, interesting correlations exist connecting lower glycolytic metabolites like lactate and central metabolites such as 1,3 BPG, MGO, lactyol-glutathione,[66] and triose-phosphates in diseases.[225] As glycolytic flux can be modulated via central glycolytic metabolites, they can affect the downstream flux of lactate. In turn, lactate levels can be increased via detoxification in response to increased central metabolite flux. This increase can result in altered bioenergetics, including increased lipid biosynthesis via citrate and cholesterol biosynthesis via Acetyl-CoA from lactate pyruvate interconversion. These phenomena in turn can be counteracted by central reactive metabolites like MGO via modulation of cholesterol metabolism[179] or possibly via redox stress signaling to the mitochondria as per Chapter 5. Both Lactate and 1,3 BPG PTMs are in turn, installed[46, 60, 226] via metabolic flux, but are also uninstalled and regulated by HDAC proteins. Intracellularly, the balance in levels of these metabolites may act to regulate internal metabolic flux for an individual cell. Beyond the individual cell, lactate's role as an intercellular shuttling metabolite, and may act alongside

central glycolytic metabolites to balance bioenergetics, biosynthesis, redox state, lipid metabolism, and energy storage systemically between cells and tissues.

Collectively, these chapters contribute insights into the growing body of knowledge pertaining to molecular mechanisms of central glycolytic reactive metabolite modifications and their implications in cellular metabolism, stress responses, and disease pathology.

ADDENDUM

Supplementary data tables

Supplementary Table 3.1: Cyanobacteria Metabolites UChicago CCC Metabolomics Platform

Metabolite	Annot. DeltaMass [ppm]	Calc. MW	m/z	RT [min]	Reference Ion	Annotation Source
Xanthosine	0.59	284.0759	283.0686	5.771	[M-H]-1	RT
Xanthosine - Monophosphate	2.13	364.0428	365.0501	10.202	[M+H]+1	RT+MS/MS
N6-(Delta2-Isopentenyl)-Adenine	-0.35	203.117	202.1098	2.025	[M-H]-1	RT+MS/MS
2'-Deoxyadenosine	1.56	251.1022	252.1095	3.107	[M+H]+1	RT+MS/MS
5'-Deoxyadenosine	1.62	251.1023	252.1095	2.759	[M+H]+1	RT+MS/MS
Adenosine	1.04	267.097	268.1043	3.647	[M+H]+1	RT+MS/MS
Deoxyguanosine	0.68	267.0969	266.0897	5.234	[M-H]-1	RT;Skyline
Guanosine	0.69	283.0919	282.0846	6.135	[M-H]-1	RT;Skyline
Thymidine	0.98	242.0905	241.0832	2.566	[M-H]-1	RT
Adenosine monophosphate/Deoxyguanosine monophosphate	0.18	347.0632	346.0559	7.44	[M-H]-1	RT+MS/MS
Guanosine Monophosphate	0.14	363.0581	362.0508	9.268	[M-H]-1	RT+MS/MS
Thymidine - Monophosphate	0.57	322.0568	321.0495	6.695	[M-H]-1	RT+MS/MS

Supplementary Table 3.1 continues

Metabolite	Annot. DeltaMass [ppm]	Calc. MW	m/z	RT [min]	Reference Ion	Annotation Source
Adenosine 5'-Diphosphate	0.22	427.0295	426.0222	8.751	[M-H]-1	RT+MS/MS
Anserine	1.81	240.1227	241.13	6.574	[M+H]+1	RT;Skyline
Adenosine Triphosphate	0.46	506.996	505.9887	9.514	[M-H]-1	RT+MS/MS
Decanoate	0.15	172.1464	171.1391	1.499	[M-H]-1	RT
Tryptophan	1.1	204.0901	205.0974	5.532	[M+H]+1	RT+MS/MS;Skyline
Nicotinamide Mononucleotide	2.89	334.0576	335.0648	8.279	[M+H]+1	RT
Methylthioadenosine	1.89	297.0901	298.0974	2.46	[M+H]+1	RT+MS/MS
1-Methyladenosine	1.94	281.113	282.1202	3.091	[M+H]+1	RT
Ophthalmate	0.51	289.1275	288.1203	6.925	[M-H]-1	RT+MS/MS
Lumichrome	-0.73	242.0802	241.0729	2.122	[M-H]-1	RT
Cellobiose/Maltose/Lactose/Trehalose_02	0.16	342.1163	341.109	8.368	[M-H]-1	RT+MS/MS
Treahalose/Maltose/Cellobiose/Lactose_01	0.58	342.1164	341.1091	7.757	[M-H]-1	RT+MS/MS
Laurate	-0.36	200.1776	199.1703	1.567	[M-H]-1	RT+MS/MS;Skyline

Supplementary Table 3.1 continues

Metabolite	Annot. DeltaMass [ppm]	Calc. MW	m/z	RT [min]	Reference Ion	Annotation Source
L-Cysteine-glutathione disulfide	0.22	426.088	425.0807	9.205	[M-H]-1	RT
S-Adenosylhomocysteine	2.28	384.1225	385.1297	6.993	[M+H]+1	RT+MS/MS
Myristate	-0.27	228.2089	227.2016	1.522	[M-H]-1	RT+MS/MS
S-Adenosylmethionine	2.05	398.1381	399.1453	8.831	[M+H]+1	RT+MS/MS
Uridine Diphosphate Glucose/Uridine Diphosphategalactose	0.19	566.0551	565.0479	9.078	[M-H]-1	RT+MS/MS
ADP-Glucose	0.15	589.0823	588.0751	8.293	[M-H]-1	RT
Palmitoleate	-0.15	254.2245	253.2173	1.501	[M-H]-1	RT+MS/MS
Palmitate	-0.65	256.2401	255.2328	1.512	[M-H]-1	RT
Uridine Diphosphate-N-Acetylglucosamine/Uridine Diphosphate-N-Acetylgalactosamine	-0.14	607.0815	606.0742	8.341	[M-H]-1	RT
Heptadecanoate	-0.58	270.2557	269.2485	1.511	[M-H]-1	RT
Raffinose	0.39	504.1692	503.162	9.05	[M-H]-1	RT

Supplementary Table 3.1 continues

Metabolite	Annot. DeltaMass [ppm]	Calc. MW	m/z	RT [min]	Reference Ion	Annotation Source
Petroselinate/Elaidate/Oleate	-0.18	282.2558	281.2486	1.506	[M-H]-1	RT
Stearate	-0.56	284.2714	283.2641	1.505	[M-H]-1	RT
Glutathione oxidized	0.77	612.1524	611.1451	9.865	[M-H]-1	RT+MS/MS
Arachidate	-0.25	312.3028	311.2955	1.502	[M-H]-1	RT
NAD+	0.98	663.1098	662.1025	7.703	[M-H]-1	RT
NADP	0.98	743.0762	742.0689	9.6	[M-H]-1	RT+MS/MS
Acetyl-CoA	0.55	809.1262	808.1189	6.988	[M-H]-1	RT
Stachyose	0.49	666.2222	665.2149	9.47	[M-H]-1	RT;Skyline
FAD	0.23	785.1573	784.15	6.143	[M-H]-1	RT;Skyline
Glyoxylate	0.49	74.00043	72.99315	2.599	[M-H]-1	RT;Skyline
Glycine	0.35	75.03205	74.02478	7.988	[M-H]-1	RT;Skyline
Pyruvate	0.63	88.0161	87.00882	2.571	[M-H]-1	RT;Skyline
N-Formylglycine	0.14	103.027	102.0197	4.845	[M-H]-1	RT;Skyline
Phosphoenolpyruvate (PEP)	0.68	167.9825	166.9752	9.911	[M-H]-1	RT+MS/MS
Lactate/Glyceraldehyde	0.99	90.03178	89.02451	3.586	[M-H]-1	RT+MS/MS
Glycerate	1.17	106.0267	105.0195	5.169	[M-H]-1	RT+MS/MS;Skyline
Alanine	0.89	89.04776	90.05503	7.375	[M+H]+1	RT+MS/MS;Skyline
Beta-Alanine	0.89	89.04776	90.05503	7.843	[M+H]+1	RT+MS/MS;Skyline
Serine	0.79	105.0427	106.05	7.916	[M+H]+1	RT
Cysteate	0.71	169.0046	167.9973	8.023	[M-H]-1	RT
2-phosphoglycerate/3-phosphoglycerate	0.56	185.993	184.9858	9.61	[M-H]-1	RT+MS/MS

Supplementary Table 3.1 continues

Metabolite	Annot. DeltaMass [ppm]	Calc. MW	m/z	RT [min]	Reference Ion	Annotation Source
Glycerol 3-Phosphate/ Glycerol 1-Phosphate	0.49	172.0138	171.0065	8.116	[M-H]-1	RT
Threitol/Erythritol	1.07	122.058	121.0508	5.054	[M-H]-1	RT+MS/MS;Skyline
Fumarate	NA	116.011	115.0037	9.03	[M-H]-1	Skyline
Succinate	NA	118.0266	117.0193	8.53	[M-H]-1	Skyline
Malate	0.72	134.0216	133.0143	8.675	[M-H]-1	RT+MS/MS
Aspartate	1.12	133.0377	134.0449	7.889	[M+H]+1	RT+MS/MS
Isobutyrate /Butyrate/ Acetoin	-0.09	88.05242	87.04515	2.133	[M-H]-1	RT;Skyline
Glycolaldehyde Dimer	1.18	120.0424	119.0351	3.69	[M-H]-1	RT;Skyline
Creatine	1.03	131.0696	132.0769	7.432	[M+H]+1	RT
Allothreonine/Threonine	0.97	119.0584	120.0656	6.997	[M+H]+1	RT+MS/MS
Homoserine	1.06	119.0584	120.0657	7.548	[M+H]+1	RT+MS/MS
Glutamine	0.07	146.0692	145.0619	8.184	[M-H]-1	RT+MS/MS;Skyline
Betaine	0.73	117.0791	118.0863	5.068	[M+H]+1	RT+MS/MS
Norvaline/ Valine	0.75	117.0791	118.0863	5.878	[M+H]+1	RT+MS/MS
Methionine	0.75	149.0512	150.0584	5.295	[M+H]+1	RT+MS/MS
Methionine Sulfoxide	1.12	165.0462	166.0534	6.481	[M+H]+1	RT
Xylitol/Ribitol/Arabitol	0.35	152.0685	151.0613	5.892	[M-H]-1	RT;Skyline
Choline	NA	103.0997	104.107	10.06	[M+H]+1	Skyline
Phosphoryl	1.63	183.0663	184.0736	8.036	[M+H]+1	RT

Supplementary Table 3.1 continues

Metabolite	Annot. DeltaMass [ppm]	Calc. MW	m/z	RT [min]	Reference Ion	Annotation Source
choline						
Orotate	0.35	156.0172	155.0099	4.063	[M-H]-1	RT+MS/MS;Skyline
Xanthine	0.4	152.0335	151.0262	5.125	[M-H]-1	RT
Adenine	0.06	135.0545	136.0618	3.8	[M+H]+1	RT+MS/MS
Guanine	1.14	151.0496	152.0569	5.72	[M+H]+1	RT+MS/MS;Skyline
4-Imidazoleacetate	0.91	126.043	125.0358	5.747	[M-H]-1	RT;Skyline
2-Methylmaleate	0.95	130.0267	129.0195	2.886	[M-H]-1	RT+MS/MS;Skyline
Oxoglutarate (alpha-Ketoglutarate)	0.37	146.0216	145.0143	8.263	[M-H]-1	RT+MS/MS
Ureidosuccinic acid(Carbamoyl aspartate)	0	176.0433	175.0361	9.115	[M-H]-1	RT
2-hydroxyglutarate		148.0373	147.03	8.2	[M-H]-1	RT;Skyline
Citramalate	0.76	148.0373	147.03	7.848	[M-H]-1	RT+MS/MS
Proline	1.53	115.0635	114.0562	6.117	[M-H]-1	RT+MS/MS;Skyline
Hydroxyproline	1.08	131.0584	132.0657	7.268	[M+H]+1	RT+MS/MS;Skyline
Glutamate	0.7	147.0533	148.0605	7.62	[M+H]+1	RT+MS/MS;Skyline
S-Carboxymethylcysteine	0.64	179.0253	178.0181	7.245	[M-H]-1	RT
N-Acetylaspa	1.36	174.0643	175.0716	5.219	[M+H]+1	RT

Supplementary Table 3.1 continues

Metabolite	Annot. DeltaMass [ppm]	Calc. MW	m/z	RT [min]	Reference Ion	Annotation Source
ragine						
2-Keto-3-Deoxy-D-Gluconic Acid/Gluconolactone	0.5	178.0478	177.0406	5.195	[M-H]-1	RT;Skyline
Ethyl 3-Ureidopropionate	1.16	160.085	161.0923	2.798	[M+H]+1	RT;Skyline
Trans-1,2-Cyclohexanediol/Hexanoate	1.14	116.0839	115.0766	1.687	[M-H]-1	RT;Skyline
Gluconate	0.41	196.0584	195.0511	6.883	[M-H]-1	RT
Hexonate	0.54	196.0584	195.0511	7.248	[M-H]-1	RT
Citrulline	1.64	175.096	176.1032	8.219	[M+H]+1	RT+MS/MS
Isoleucine	0.51	131.0947	132.102	5.521	[M+H]+1	RT+MS/MS;Skyline
Leucine	0.61	131.0947	132.102	5.255	[M+H]+1	RT+MS/MS;Skyline
Glucose 1-Phosphate/ Fructose 6-phosphate	0.22	260.0298	259.0225	8.837	[M-H]-1	RT+MS/MS;Skyline
Glucose 6-Phosphate	0.2	260.0298	259.0225	9.395	[M-H]-1	RT+MS/MS
Hexose phosphate_01	0.03	260.0297	259.0225	9.004	[M-H]-1	RT
Arginine	-0.6	174.1116	173.1043	12.994	[M-H]-1	RT+MS/MS
Mannitol/Galactitol/Hexitol	0.73	182.0792	181.0719	6.626	[M-H]-1	RT+MS/MS
Pterin	0.61	163.0495	164.0568	4.813	[M+H]+1	RT+MS/MS
Nicotinamide	0.89	122.0481	123.0554	2.445	[M+H]+1	RT+MS/MS
Urocanate	1.05	138.0431	139.0504	5.038	[M+H]+1	RT+MS/M

Supplementary Table 3.1 continues

Metabolite	Annot. DeltaMass [ppm]	Calc. MW	m/z	RT [min]	Reference Ion	Annotation Source
						S
Aconitate	0.55	174.0165	173.0093	9.783	[M-H]-1	RT
Sorbate	1.19	112.0526	111.0453	1.833	[M-H]-1	RT;Skyline
Citrate	0.37	192.0271	191.0198	9.912	[M-H]-1	RT+MS/MS;Skyline
Isocitrate	0.3	192.0271	191.0198	10.437	[M-H]-1	RT+MS/MS;Skyline
Histidine	1.37	155.0697	156.077	7.979	[M+H]+1	RT+MS/MS;Skyline
N-Acetylaspartate	0.55	175.0482	174.0409	7.812	[M-H]-1	RT
N-Acetylproline	1.22	157.0741	158.0814	2.897	[M+H]+1	RT;Skyline
N-Acetylglutamate	0.11	189.0637	188.0565	7.522	[M-H]-1	RT+MS/MS
Quinate	0.66	192.0635	191.0562	5.85	[M-H]-1	RT
Homocitrulline	1.32	189.1116	190.1189	7.816	[M+H]+1	RT
Carnitine	1.25	161.1054	162.1127	6.549	[M+H]+1	RT
D-Sedoheptulose 7-phosphate	0.29	290.0404	289.0331	9.021	[M-H]-1	RT
Hydroxybenzaldehyde/Benzoate	0.48	122.0368	121.0296	2.013	[M-H]-1	RT
Salicylamide	0.57	137.0478	136.0405	1.743	[M-H]-1	RT;Skyline
Trigonelline	1.34	137.0479	216.0691	6.057	[M+DMSO+H]+1	RT
Suberate	0.34	174.0893	173.082	6.126	[M-H]-1	RT;Skyline
N-Acetylleucine	0.77	173.1053	172.0981	1.809	[M-H]-1	RT
N-Acetylgluc	0.36	301.0564	300.0491	8.16	[M-H]-1	RT

Supplementary Table 3.1 continues

Metabolite	Annot. DeltaMass [ppm]	Calc. MW	m/z	RT [min]	Reference Ion	Annotation Source
osamine - phosphate						
N,N-Dimethylarginine	1.7	202.1433	203.1506	10.977	[M+H]+1	RT+MS/MS
Glycero-3-Phosphocholine	1.27	257.1032	258.1104	7.468	[M+H]+1	RT;Skyline
Pyridoxal	1.29	167.0585	168.0657	2.586	[M+H]+1	RT+MS/MS;Skyline
3-(2-Hydroxyphenyl)Propanoate	0.32	166.0631	165.0558	1.668	[M-H]-1	RT
Tyrosine	0.79	181.074	182.0813	6.323	[M+H]+1	RT+MS/MS
Uridine	0.02	244.0695	243.0623	4.1	[M-H]-1	RT+MS/MS
Uridine Monophosphate	0.22	324.0359	323.0287	8.205	[M-H]-1	RT+MS/MS
Cytidine	1.46	243.0859	244.0932	5.596	[M+H]+1	RT;Skyline
uridine 5′-diphosphate	2.11	404.0031	405.0104	9.432	[M+H]+1	RT
Uridine 5'-diphosphate (UDP)	0.54	404.0024	402.9951	9.426	[M-H]-1	RT+MS/MS
Cytidine 5' monophosphate(5'-CMP)	0.14	323.0519	322.0446	8.742	[M-H]-1	RT+MS/MS
Cytidine monophosphate(CMP)	1.1	323.0522	324.0595	8.737	[M+H]+1	RT+MS/MS
Cytidine Diphosphate	2.32	403.0191	404.0264	9.784	[M+H]+1	RT+MS/MS
Azelate	0.26	188.1049	187.0976	5.363	[M-H]-1	RT+MS/M

Supplementary Table 3.1 continues

Metabolite	Annot. DeltaMass [ppm]	Calc. MW	m/z	RT [min]	Reference Ion	Annotation Source
						S;Skyline
O-Acetylcarnitine	1.55	203.1161	204.1234	5.136	[M+H]+1	RT
Nonanoate	-0.41	158.1306	157.1233	1.496	[M-H]-1	RT
N,N,N-Trimethyllysine	0.87	188.1526	189.1599	11.442	[M+H]+1	RT+MS/MS
Indole-3-carboxaldehyde (Indole-3-carbaldehyde)_01	-0.72	145.0527	144.0456	1.846	[M-H]-1	RT;Skyline

Supplementary Table 3.2: Cyanobacteria QQQ Targeted Metabolomics MRM: Acquisition parameters used for targeted metabolomic measurements on a triple quadrupole mass spectrometer. Glyceraldehyde-3-phosphate, GAP; Ribose-5-phosphate, R5P

Metabolites	Precursor mass	MSl Resolution	Product ion	MS2 Resolution	Dwell	Fragmentor	Collision Energy	Polarity
GAP	l69	Wide	96.9	Unit	l00	l00	5	Neg
R5P	228.7	Wide	78.8	Unit	l00	l00	35	Neg

Supplementary Table 4.1 Primers for cloning HDAC3 CRISPR KO plasmids

Gene Target	**Primer Forward**	**Primer Reverse**
HDAC3 KO1	CACCGGTTGGTAGAAGTCCACTACC	AAACGGTAGTGGACTTCTACCAACC
HDAC3 KO2	CACCGGGAGCACAATGCACGTGGGT	AAACACCCACGTGCATTGTGCTCCC
KO control	CACCGGGAGTAGTTGCAAGGTAG	AAACCTACCTTGCAACTACTCCC
HDAC3 sh1	CCGGTCCTTCCACAAATACGGAAATTCTCGAGAATTTCCGTATTTGTGGAAGGTTTTTG	AATTCAAAAACCTTCCACAAATACGGAAATTCTCGAGAATTTCCGTATTTGTGGAAGGA
HDAC3 sh2	CCGGTCAAGAGTCTTAATGCCTTCAACTCGAGTTGAAGGCATTAAGACTCTTGTTTTTG	AATTCAAAAACAAGAGTCTTAATGCCTTCAACTCGAGTTGAAGGCATTAAGACTCTTGA

Supplementary Table 5.1: Metabolites Index UChicago CCC Metabolomics Platform

Metabolite	Calc. MW	m/z	RT [min]	Reference Ion	Annotation source
2-hydroxyglutarate Neg			8.32	[M-H]-1	RT
3-Phosphoglycerate/2-Phosphoglycerate Neg	185.9925	184.9852	9.638	[M-H]-1	MS/MS+RT
5'-Phosphoribosyl-N-formylglycinamide Neg	314.0507	313.0435	8.397	[M-H]-1	RT
6-phosphogluconate Neg			10.13	[M-H]-1	RT
Alanine Neg	89.04743	88.04015	7.32	[M-H]-1	RT
alpha-Ketoglutarate Neg	146.0211	145.0138	8.397	[M-H]-1	RT
Arginine Neg	174.1112	173.1039	12.605	[M-H]-1	RT
Asparagine Neg	132.0531	131.0458	7.554	[M-H]-1	RT
Aspartate Neg	133.0372	132.0299	7.975	[M-H]-1	RT
Beta-alanine Neg	89.04745	88.04017	7.971	[M-H]-1	RT
Citrate Neg	192.0265	191.0192	10.088	[M-H]-1	RT
Coenzyme A Neg	767.1127	766.1054	7.966	[M-H]-1	RT
Creatine Neg	131.0691	130.0618	7.332	[M-H]-1	RT
Fructose-1,6-bisphosphate Neg	339.9952	338.9879	10.534	[M-H]-1	RT
Fumarate Neg			8.81	[M-H]-1	RT
g-Glutamylcysteine Neg	250.0617	249.0544	7.391	[M-H]-1	RT
Glucose Neg	180.0629	179.0557	7.149	[M-H]-1	RT
Glucose-1-phosphate/Fructose-6-phosphate Neg	260.0291	259.0218	8.87	[M-H]-1	RT
Glucose-6-phosphate Neg	260.029	259.0218	9.429	[M-H]-1	RT
Glutamate Neg	147.0527	146.0454	7.694	[M-H]-1	RT
Glutamine Neg	146.0687	145.0615	7.526	[M-H]-1	RT
Glutathione oxidized Neg	612.1501	611.1428	9.906	[M-H]-1	MS/MS+RT
Glutathione reduced Neg	307.0827	306.0754	7.603	[M-H]-1	RT
Glyceraldehyde 3-Phosphate/DHAP Neg	169.9976	168.9903	8.359	[M-H]-1	RT
Glycerol 3-phosphate/Glycerol-2-phosphate Neg	172.0132	171.0059	8.19	[M-H]-1	RT
Glycine Neg	75.03182	74.02454	7.842	[M-H]-1	RT
Isoleucine Neg	131.0943	130.087	5.144	[M-H]-1	RT
Lactate Neg	90.03135	89.02407	3.299	[M-H]-1	RT

Supplementary Table 5.1 continued

Metabolite	Calc. MW	m/z	RT [min]	Reference Ion	Annotation source
Lactoyl glutathione Neg	379.104	378.0967	7.008	[M-H]-1	RT
L-alpha-Glycerylphosphorylcholine Neg	257.1021	256.0949	7.375	[M-H]-1	RT
Leucine Neg	131.0943	130.087	4.904	[M-H]-1	RT
Lysine Neg	146.1051	145.0978	12.219	[M-H]-1	RT
Malate Neg	134.0212	133.014	8.78	[M-H]-1	RT
Methionine Neg	149.0506	148.0434	5.233	[M-H]-1	RT
N-Acetyl-glutamate Neg	189.0632	188.0559	7.66	[M-H]-1	MS/MS
N-Acetyl-L-cysteine Neg	163.0298	162.0225	2.568	[M-H]-1	RT
N-Acetylneuraminic acid Neg	309.1052	308.0979	6.699	[M-H]-1	RT
Nicotinamide Neg			2.31	[M+H]+1	RT
Pantothenic acid Neg	219.1101	218.1028	3.095	[M-H]-1	MS/MS
Phenylalanine Neg	165.0785	164.0712	4.364	[M-H]-1	RT
Phosphocreatine Neg	211.0352	210.0279	8.463	[M-H]-1	RT
Phosphoenolpyruvic acid Neg	167.9819	166.9746	9.966	[M-H]-1	RT
Phosphoserine Neg	185.0085	184.0012	7.718	[M-H]-1	RT
Proline Neg	115.063	114.0558	6.108	[M-H]-1	RT
Pyruvate Neg	88.01579	87.00852	2.582	[M-H]-1	RT
Ribose-5-phosphate Neg	230.0186	229.0114	8.587	[M-H]-1	RT
Sedoheptulose 7-phosphate Neg	290.0396	289.0323	9.044	[M-H]-1	RT
Serine Neg	105.0423	104.0351	7.812	[M-H]-1	RT
Succinate Neg			8.34	[M-H]-1	RT
Threonine Neg	119.058	118.0507	6.93	[M-H]-1	RT
Tryptophan Neg	204.0893	203.082	5.421	[M-H]-1	RT
Tyrosine Neg	181.0734	180.0661	6.28	[M-H]-1	RT
UDP-N-acetylglucosamine/UDP-N-acetylgalactosamine Neg	607.0797	606.0724	8.437	[M-H]-1	RT
Uracil Neg	112.027	111.0198	3	[M-H]-1	RT
Uridine 5'-diphosphogalactose/Uridine-5'-diphosphoglucose Neg	566.0533	565.046	9.149	[M-H]-1	MS/MS+RT
Xanthine Neg	152.033	151.0257	5.115	[M-H]-1	RT

Supplementary Table 5.1 continued

Metabolite	Formula	Calc. MW	m/z	RT [min]	Reference Ion	Annotation source
Glutathione reduced Pos	C10 H17 N3 O6 S	307.08319	308.09047	7.599	[M+H]+1	MS/MS+RT
Proline Pos	C5 H9 N O2	115.06309	116.07036	6.071	[M+H]+1	MS/MS+RT
Glutamate Pos	C5 H9 N O4	147.05285	148.06012	7.691	[M+H]+1	MS/MS+RT
Betaine Pos	C5 H11 N O2	117.07873	118.08601	5.003	[M+H]+1	MS/MS+RT
Leucine Pos	C6 H13 N O2	131.09435	132.10163	4.877	[M+H]+1	MS/MS+RT
Phenylalanine Pos	C9 H11 N O2	165.07869	166.08597	4.345	[M+H]+1	MS/MS+RT
Isoleucine Pos	C6 H13 N O2	131.09437	132.10165	5.131	[M+H]+1	MS/MS+RT
5-aminoimidazole ribotide Pos	C8 H14 N3 O7 P	295.05827	296.06555	7.369	[M+H]+1	MS
N-Acetylputrescine Pos	C6 H14 N2 O	130.11035	131.11763	9.932	[M+H]+1	MS/MS
L-Glutathione oxidized Pos	C20 H32 N6 O12 S2	612.15093	613.15821	9.9	[M+H]+1	MS/MS+RT
Tyrosine Pos	C9 H11 N O3	181.07357	182.08085	6.274	[M+H]+1	MS/MS+RT
Arginine Pos	C6 H14 N4 O2	174.11136	175.11864	12.601	[M+H]+1	RT
Glutamine Pos	C5 H10 N2 O3	146.06885	147.07613	7.544	[M+H]+1	MS/MS+RT
Valine Pos	C5 H11 N O2	117.07872	118.086	5.869	[M+H]+1	MS/MS+RT
Tryptophan Pos	C11 H12 N2 O2	204.08952	205.0968	5.465	[M+H]+1	MS/MS+RT
Glutathione Reduced Pos	C10 H17 N3 O6 S	307.08333	308.09061	8.623	[M+H]+1	MS/MS+RT
Methionine Pos	C5 H11 N O2 S	149.05074	150.05802	5.234	[M+H]+1	MS/MS+RT

Supplementary Table 5.1 continued

Metabolite	Formula	Calc. MW	m/z	RT [min]	Reference Ion	Annotation source
Carnitine Pos	C7 H15 N O3	161.10488	162.11216	6.476	[M+H]+1	MS/MS+RT
UDP-N-acetylglucosamine/UDP-N-acetylgalactosamine Pos	C17 H27 N3 O17 P2	607.0805	608.08777	8.42	[M+H]+1	RT
Phosphocreatine Pos	C4 H10 N3 O5 P	211.03548	212.04276	8.461	[M+H]+1	RT
Alanine Pos	C3 H7 N O2	89.04747	90.05475	7.328	[M+H]+1	RT
Asparagine Pos	C4 H8 N2 O3	132.05321	133.06049	7.561	[M+H]+1	RT
Propionylcarnitine Pos	C10 H19 N O4	217.13103	218.1383	4.377	[M+H]+1	RT
Lysine Pos	C6 H14 N2 O2	146.10524	147.11252	12.223	[M+H]+1	RT
N,N-dimethylarginine Pos	C8 H18 N4 O2	202.14256	203.14984	10.7	[M+H]+1	RT

REFERENCES

1. Hanahan D, Weinberg RA. Hallmarks of cancer: the next generation. *Cell*. 2011;144(5):646-74.

2. DeBerardinis RJ, Chandel NS. Fundamentals of cancer metabolism. *Sci Adv*. 2016;2(5):e1600200.

3. Chandel NS. Glycolysis. *Cold Spring Harb Perspect Biol*. 2021;13(5).

4. Lunt SY, Vander Heiden MG. Aerobic glycolysis: meeting the metabolic requirements of cell proliferation. *Annu Rev Cell Dev Biol*. 2011;27:441-64.

5. Vander Heiden MG. Targeting cancer metabolism: a therapeutic window opens. *Nat Rev Drug Discov*. 2011;10(9):671-84.

6. Vazquez A, Tedeschi PM, Bertino JR. Overexpression of the mitochondrial folate and glycine-serine pathway: a new determinant of methotrexate selectivity in tumors. *Cancer Res*. 2013;73(2):478-82.

7. Stine ZE, Walton ZE, Altman BJ, Hsieh AL, Dang CV. MYC, Metabolism, and Cancer. *Cancer Discov*. 2015;5(10):1024-39.

8. Speltz TE, Qiao Z, Swenson CS, Shangguan X, Coukos JS, Lee CW, et al. Targeting MYC with modular synthetic transcriptional repressors derived from bHLH DNA-binding domains. *Nat Biotechnol*. 2023;41(4):541-51.

9. Dong Y, Tu R, Liu H, Qing G. Regulation of cancer cell metabolism: oncogenic MYC in the driver's seat. *Signal Transduct Target Ther*. 2020;5(1):124.

10. Dhanasekaran R, Deutzmann A, Mahauad-Fernandez WD, Hansen AS, Gouw AM, Felsher DW. The MYC oncogene - the grand orchestrator of cancer growth and immune evasion. *Nat Rev Clin Oncol*. 2022;19(1):23-36.

11. Cairns RA, Harris IS, Mak TW. Regulation of cancer cell metabolism. *Nat Rev Cancer*. 2011;11(2):85-95.

12. Stratton MR, Campbell PJ, Futreal PA. The cancer genome. *Nature*. 2009;458(7239):719-24.

13. Jones PA, Baylin SB. The fundamental role of epigenetic events in cancer. *Nat Rev Genet*. 2002;3(6):415-28.

14. Hay N. Reprogramming glucose metabolism in cancer: can it be exploited for cancer therapy? *Nat Rev Cancer*. 2016;16(10):635-49.

15. Kresge N, Simoni RD, Hill RL. Otto Fritz Meyerhof and the elucidation of the glycolytic pathway. *J Biol Chem*. 2005;280(4):e3.

16. Baker SA, Rutter J. Metabolites as signalling molecules. *Nat Rev Mol Cell Biol*. 2023;24(5):355-74.

17. Vander Heiden MG, Cantley LC, Thompson CB. Understanding the Warburg effect: the metabolic requirements of cell proliferation. *Science*. 2009;324(5930):1029-33.

18. Petersen MC, Vatner DF, Shulman GI. Regulation of hepatic glucose metabolism in health and disease. *Nat Rev Endocrinol*. 2017;13(10):572-87.

19. Rines AK, Sharabi K, Tavares CD, Puigserver P. Targeting hepatic glucose metabolism in the treatment of type 2 diabetes. *Nat Rev Drug Discov*. 2016;15(11):786-804.

20. Ravera S, Podesta M, Sabatini F, Dagnino M, Cilloni D, Fiorini S, et al. Discrete Changes in Glucose Metabolism Define Aging. *Sci Rep*. 2019;9(1):10347.

21. Wiley CD, Campisi J. The metabolic roots of senescence: mechanisms and opportunities for intervention. *Nat Metab*. 2021;3(10):1290-301.

22. Vlassara H, Uribarri J. Advanced glycation end products (AGE) and diabetes: cause, effect, or both? *Curr Diab Rep*. 2014;14(1):453.

23. Goldin A, Beckman JA, Schmidt AM, Creager MA. Advanced glycation end products: sparking the development of diabetic vascular injury. *Circulation*. 2006;114(6):597-605.

24. Chaudhuri J, Bains Y, Guha S, Kahn A, Hall D, Bose N, et al. The Role of Advanced Glycation End Products in Aging and Metabolic Diseases: Bridging Association and Causality. *Cell Metab*. 2018;28(3):337-52.

25. Schroter D, Hohn A. Role of Advanced Glycation End Products in Carcinogenesis and their Therapeutic Implications. *Curr Pharm Des*. 2018;24(44):5245-51.

26. Geicu OI, Stanca L, Voicu SN, Dinischiotu A, Bilteanu L, Serban AI, Calu V. Dietary AGEs involvement in colonic inflammation and cancer: insights from an in vitro enterocyte model. *Sci Rep*. 2020;10(1):2754.

27. Chen Z, Yuan Z, Yang S, Zhu Y, Xue M, Zhang J, Leng L. Brain Energy Metabolism: Astrocytes in Neurodegenerative Diseases. *CNS Neurosci Ther*. 2023;29(1):24-36.

28. Haque E, Kamil M, Hasan A, Irfan S, Sheikh S, Khatoon A, et al. Advanced glycation end products (AGEs), protein aggregation and their cross talk: new insight in tumorigenesis. *Glycobiology*. 2019;30(1):49-57.

29. Naftaly A, Izgilov R, Omari E, Benayahu D. Revealing Advanced Glycation End Products Associated Structural Changes in Serum Albumin. *ACS Biomater Sci Eng*. 2021;7(7):3179-89.

30. Chen X, Liu Y, Kong L, Wen Z, Wang W, Wang C. Quantitative Chemoproteomic Profiling of Protein Cross-Links Induced by Methylglyoxal. *ACS Chem Biol*. 2022;17(8):2010-7.

31. Bollong MJ, Lee G, Coukos JS, Yun H, Zambaldo C, Chang JW, et al. A metabolite-derived protein modification integrates glycolysis with KEAP1-NRF2 signalling. *Nature*. 2018;562(7728):600-4.

32. Kulkarni RA, Bak DW, Wei D, Bergholtz SE, Briney CA, Shrimp JH, et al. A chemoproteomic portrait of the oncometabolite fumarate. *Nat Chem Biol*. 2019;15(4):391-400.

33. Wang Q, Zhang Y, Yang C, Xiong H, Lin Y, Yao J, et al. Acetylation of metabolic enzymes coordinates carbon source utilization and metabolic flux. *Science*. 2010;327(5968):1004-7.

34. Choudhary C, Kumar C, Gnad F, Nielsen ML, Rehman M, Walther TC, et al. Lysine acetylation targets protein complexes and co-regulates major cellular functions. *Science*. 2009;325(5942):834-40.

35. Choudhary C, Weinert BT, Nishida Y, Verdin E, Mann M. The growing landscape of lysine acetylation links metabolism and cell signalling. *Nat Rev Mol Cell Biol*. 2014;15(8):536-50.

36. Wagner GR, Bhatt DP, O'Connell TM, Thompson JW, Dubois LG, Backos DS, et al. A Class of Reactive Acyl-CoA Species Reveals the Non-enzymatic Origins of Protein Acylation. *Cell Metab*. 2017;25(4):823-37 e8.

37. Trefely S, Lovell CD, Snyder NW, Wellen KE. Compartmentalised acyl-CoA metabolism and roles in chromatin regulation. *Mol Metab*. 2020;38:100941.

38. Paik WK, Pearson D, Lee HW, Kim S. Nonenzymatic acetylation of histones with acetyl-CoA. *Biochim Biophys Acta*. 1970;213(2):513-22.

39. Wagner GR, Payne RM. Widespread and enzyme-independent Nepsilon-acetylation and Nepsilon-succinylation of proteins in the chemical conditions of the mitochondrial matrix. *J Biol Chem*. 2013;288(40):29036-45.

40. Wagner GR, Hirschey MD. Nonenzymatic protein acylation as a carbon stress regulated by sirtuin deacylases. *Mol Cell*. 2014;54(1):5-16.

41. Bork NI, Nikolaev VO. cGMP Signaling in the Cardiovascular System-The Role of Compartmentation and Its Live Cell Imaging. *Int J Mol Sci*. 2018;19(3).

42. Li ZN, Luo Y. HSP90 inhibitors and cancer: Prospects for use in targeted therapies (Review). *Oncol Rep*. 2023;49(1).

43. He Y, Zheng CC, Yang J, Li SJ, Xu TY, Wei X, et al. Lysine butyrylation of HSP90 regulated by KAT8 and HDAC11 confers chemoresistance. *Cell Discov*. 2023;9(1):74.

44. Zhang Z, Tan M, Xie Z, Dai L, Chen Y, Zhao Y. Identification of lysine succinylation as a new post-translational modification. *Nat Chem Biol*. 2011;7(1):58-63.

45. Du J, Zhou Y, Su X, Yu JJ, Khan S, Jiang H, et al. Sirt5 is a NAD-dependent protein lysine demalonylase and desuccinylase. *Science*. 2011;334(6057):806-9.

46. Moellering RE, Cravatt BF. Functional Lysine Modification by an Intrinsically Reactive Primary Glycolytic Metabolite. *Science*. 2013;341(6145):549-53.

47. Baldensperger T, Glomb MA. Pathways of Non-enzymatic Lysine Acylation. *Front Cell Dev Biol*. 2021;9:664553.

48. James AM, Hoogewijs K, Logan A, Hall AR, Ding S, Fearnley IM, Murphy MP. Non-enzymatic N-acetylation of Lysine Residues by AcetylCoA Often Occurs via a Proximal S-acetylated Thiol Intermediate Sensitive to Glyoxalase II. *Cell Rep*. 2017;18(9):2105-12.

49. Gruning NM, Du D, Keller MA, Luisi BF, Ralser M. Inhibition of triosephosphate isomerase by phosphoenolpyruvate in the feedback-regulation of glycolysis. *Open Biol*. 2014;4(3):130232.

50. Ho PC, Bihuniak JD, Macintyre AN, Staron M, Liu X, Amezquita R, et al. Phosphoenolpyruvate Is a Metabolic Checkpoint of Anti-tumor T Cell Responses. *Cell*. 2015;162(6):1217-28.

51. Orozco JM, Krawczyk PA, Scaria SM, Cangelosi AL, Chan SH, Kunchok T, et al. Dihydroxyacetone phosphate signals glucose availability to mTORC1. *Nat Metab*. 2020;2(9):893-901.

52. Ge X, Li M, Yin J, Shi Z, Fu Y, Zhao N, et al. Fumarate inhibits PTEN to promote tumorigenesis and therapeutic resistance of type2 papillary renal cell carcinoma. *Mol Cell*. 2022;82(7):1249-60 e7.

53. Li R, Zhang P, Wang Y, Tao K. Itaconate: A Metabolite Regulates Inflammation Response and Oxidative Stress. *Oxid Med Cell Longev*. 2020;2020:5404780.

54. Peace CG, O'Neill LA. The role of itaconate in host defense and inflammation. *J Clin Invest*. 2022;132(2).

55. Qin W, Qin K, Zhang Y, Jia W, Chen Y, Cheng B, et al. S-glycosylation-based cysteine profiling reveals regulation of glycolysis by itaconate. *Nat Chem Biol*. 2019;15(10):983-91.

56. Liao ST, Han C, Xu DQ, Fu XW, Wang JS, Kong LY. 4-Octyl itaconate inhibits aerobic glycolysis by targeting GAPDH to exert anti-inflammatory effects. *Nat Commun*. 2019;10(1):5091.

57. Chang JW, Lee G, Coukos JS, Moellering RE. Profiling Reactive Metabolites via Chemical Trapping and Targeted Mass Spectrometry. *Anal Chem*. 2016;88(13):6658-61.

58. Park SY, Kim JS. A short guide to histone deacetylases including recent progress on class II enzymes. *Exp Mol Med*. 2020;52(2):204-12.

59. Peng L, Seto E. Deacetylation of nonhistone proteins by HDACs and the implications in cancer. *Handb Exp Pharmacol*. 2011;206:39-56.

60. Heremans IP, Caligiore F, Gerin I, Bury M, Lutz M, Graff J, et al. Parkinson's disease protein PARK7 prevents metabolite and protein damage caused by a glycolytic metabolite. *Proc Natl Acad Sci U S A*. 2022;119(4).

61. Farrera DO, Galligan JJ. The Human Glyoxalase Gene Family in Health and Disease. *Chem Res Toxicol*. 2022;35(10):1766-76.

62. Shipanova IN, Glomb MA, Nagaraj RH. Protein modification by methylglyoxal: chemical nature and synthetic mechanism of a major fluorescent adduct. *Arch Biochem Biophys*. 1997;344(1):29-36.

63. Henle T, Walter AW, Klostermeyer H. Detection and identification of the cross-linking amino acids N tau- and N pi-(2'-amino-2'-carboxy-ethyl)-L-histidine ("histidinoalanine", HAL) in heated milk products. *Z Lebensm Unters Forsch*. 1993;197(2):114-7.

64. van Eupen MG, Schram MT, Colhoun HM, Hanssen NM, Niessen HW, Tarnow L, et al. The methylglyoxal-derived AGE tetrahydropyrimidine is increased in plasma of individuals with type 1 diabetes mellitus and in atherosclerotic lesions and is associated with sVCAM-1. *Diabetologia*. 2013;56(8):1845-55.

65. Ahmed MU, Brinkmann Frye E, Degenhardt TP, Thorpe SR, Baynes JW. N-epsilon-(carboxyethyl)lysine, a product of the chemical modification of proteins by methylglyoxal, increases with age in human lens proteins. *Biochem J*. 1997;324 (Pt 2)(Pt 2):565-70.

66. Gaffney DO, Jennings EQ, Anderson CC, Marentette JO, Shi T, Schou Oxvig AM, et al. Non-enzymatic Lysine Lactoylation of Glycolytic Enzymes. *Cell Chem Biol*. 2020;27(2):206-13 e6.

67. Lederer MO, Klaiber RG. Cross-linking of proteins by Maillard processes: characterization and detection of lysine-arginine cross-links derived from glyoxal and methylglyoxal. *Bioorg Med Chem*. 1999;7(11):2499-507.

68. Nagaraj RH, Shipanova IN, Faust FM. Protein cross-linking by the Maillard reaction. Isolation, characterization, and in vivo detection of a lysine-lysine cross-link derived from methylglyoxal. *J Biol Chem*. 1996;271(32):19338-45.

69. Baird L, Yamamoto M. The Molecular Mechanisms Regulating the KEAP1-NRF2 Pathway. *Mol Cell Biol*. 2020;40(13).

70. Luengo A, Abbott KL, Davidson SM, Hosios AM, Faubert B, Chan SH, et al. Reactive metabolite production is a targetable liability of glycolytic metabolism in lung cancer. *Nat Commun*. 2019;10(1):5604.

71. Rounds L, Nagle RB, Muranyi A, Jandova J, Gill S, Vela E, Wondrak GT. Glyoxalase 1 Expression as a Novel Diagnostic Marker of High-Grade Prostatic Intraepithelial Neoplasia in Prostate Cancer. *Cancers (Basel)*. 2021;13(14).

72. Schlotterer A, Pfisterer F, Kukudov G, Heckmann B, Henriquez D, Morath C, et al. Neuronal damage and shortening of lifespan in C. elegans by peritoneal dialysis fluid: Protection by glyoxalase-1. *Biomed Rep*. 2018;8(6):540-6.

73. Chaudhuri J, Bose N, Gong J, Hall D, Rifkind A, Bhaumik D, et al. A Caenorhabditis elegans Model Elucidates a Conserved Role for TRPA1-Nrf Signaling in Reactive alpha-Dicarbonyl Detoxification. *Curr Biol*. 2016;26(22):3014-25.

74. Singla-Pareek SL, Kaur C, Kumar B, Pareek A, Sopory SK. Reassessing plant glyoxalases: large family and expanding functions. *New Phytol*. 2020;227(3):714-21.

75. Ghosh A, Kushwaha HR, Hasan MR, Pareek A, Sopory SK, Singla-Pareek SL. Presence of unique glyoxalase III proteins in plants indicates the existence of shorter route for methylglyoxal detoxification. *Sci Rep*. 2016;6:18358.

76. Sankaranarayanan S, Jamshed M, Kumar A, Skori L, Scandola S, Wang T, et al. Glyoxalase Goes Green: The Expanding Roles of Glyoxalase in Plants. *Int J Mol Sci*. 2017;18(4).

77. Zheng RH, Su S, Xiao H, Tian HQ. Calcium: A Critical Factor in Pollen Germination and Tube Elongation. *Int J Mol Sci*. 2019;20(2).

78. Rogers A, Kumarathunge DP, Lombardozzi DL, Medlyn BE, Serbin SP, Walker AP. Triose phosphate utilization limitation: an unnecessary complexity in terrestrial biosphere model representation of photosynthesis. *New Phytol*. 2021;230(1):17-22.

79. McClain AM, Sharkey TD. Triose phosphate utilization and beyond: from photosynthesis to end product synthesis. *J Exp Bot*. 2019;70(6):1755-66.

80. Fabre D, Yin X, Dingkuhn M, Clement-Vidal A, Roques S, Rouan L, et al. Is triose phosphate utilization involved in the feedback inhibition of photosynthesis in rice under conditions of sink limitation? *J Exp Bot*. 2019;70(20):5773-85.

81. Michelet L, Zaffagnini M, Morisse S, Sparla F, Perez-Perez ME, Francia F, et al. Redox regulation of the Calvin-Benson cycle: something old, something new. *Front Plant Sci*. 2013;4:470.

82. Richarme G, Dairou J. Parkinsonism-associated protein DJ-1 is a bona fide deglycase. *Biochem Biophys Res Commun*. 2017;483(1):387-91.

83. Mazza MC, Shuck SC, Lin J, Moxley MA, Termini J, Cookson MR, Wilson MA. DJ-1 is not a deglycase and makes a modest contribution to cellular defense against methylglyoxal damage in neurons. *J Neurochem*. 2022;162(3):245-61.

84. Matsuda N, Kimura M, Queliconi BB, Kojima W, Mishima M, Takagi K, et al. Parkinson's disease-related DJ-1 functions in thiol quality control against aldehyde attack in vitro. *Sci Rep*. 2017;7(1):12816.

85. Lee JY, Song J, Kwon K, Jang S, Kim C, Baek K, et al. Human DJ-1 and its homologs are novel glyoxalases. *Hum Mol Genet*. 2012;21(14):3215-25.

86. Richarme G, Mihoub M, Dairou J, Bui LC, Leger T, Lamouri A. Parkinsonism-associated protein DJ-1/Park7 is a major protein deglycase that repairs methylglyoxal- and glyoxal-glycated cysteine, arginine, and lysine residues. *J Biol Chem*. 2015;290(3):1885-97.

87. Richarme G, Liu C, Mihoub M, Abdallah J, Leger T, Joly N, et al. Guanine glycation repair by DJ-1/Park7 and its bacterial homologs. *Science*. 2017;357(6347):208-11.

88. Zhang L, Wang J, Wang J, Yang B, He Q, Weng Q. Role of DJ-1 in Immune and Inflammatory Diseases. *Front Immunol*. 2020;11:994.

89. Galligan JJ, Wepy JA, Streeter MD, Kingsley PJ, Mitchener MM, Wauchope OR, et al. Methylglyoxal-derived posttranslational arginine modifications are abundant histone marks. *Proc Natl Acad Sci U S A*. 2018;115(37):9228-33.

90. Zheng Q, Omans ND, Leicher R, Osunsade A, Agustinus AS, Finkin-Groner E, et al. Reversible histone glycation is associated with disease-related changes in chromatin architecture. *Nat Commun*. 2019;10(1):1289.

91. Canet-Avilés RM, Wilson MA, Miller DW, Ahmad R, McLendon C, Bandyopadhyay S, et al. The Parkinson's disease protein DJ-1 is neuroprotective due to cysteine-sulfinic acid-driven mitochondrial localization. *Proc Natl Acad Sci U S A*. 2004;101(24):9103-8.

92. Wang Z, Liu J, Chen S, Wang Y, Cao L, Zhang Y, et al. DJ-1 modulates the expression of Cu/Zn-superoxide dismutase-1 through the Erk1/2-Elk1 pathway in neuroprotection. *Ann Neurol*. 2011;70(4):591-9.

93. Girotto S, Cendron L, Bisaglia M, Tessari I, Mammi S, Zanotti G, Bubacco L. DJ-1 is a copper chaperone acting on SOD1 activation. *J Biol Chem*. 2014;289(15):10887-99.

94. Xu S, Yang X, Qian Y, Xiao Q. Parkinson's disease-related DJ-1 modulates the expression of uncoupling protein 4 against oxidative stress. *J Neurochem*. 2018;145(4):312-22.

95. Gan L, Johnson DA, Johnson JA. Keap1-Nrf2 activation in the presence and absence of DJ-1. *Eur J Neurosci*. 2010;31(6):967-77.

96. Im JY, Lee KW, Woo JM, Junn E, Mouradian MM. DJ-1 induces thioredoxin 1 expression through the Nrf2 pathway. *Hum Mol Genet*. 2012;21(13):3013-24.

97. Clements CM, McNally RS, Conti BJ, Mak TW, Ting JP. DJ-1, a cancer- and Parkinson's disease-associated protein, stabilizes the antioxidant transcriptional master regulator Nrf2. *Proc Natl Acad Sci U S A*. 2006;103(41):15091-6.

98. Dolgacheva LP, Berezhnov AV, Fedotova EI, Zinchenko VP, Abramov AY. Role of DJ-1 in the mechanism of pathogenesis of Parkinson's disease. *J Bioenerg Biomembr*. 2019;51(3):175-88.

99. Zheng Q, Osunsade A, David Y. Protein arginine deiminase 4 antagonizes methylglyoxal-induced histone glycation. *Nat Commun*. 2020;11(1):3241.

100. Schumacher D, Morgenstern J, Oguchi Y, Volk N, Kopf S, Groener JB, et al. Compensatory mechanisms for methylglyoxal detoxification in experimental & clinical diabetes. *Mol Metab*. 2018;18:143-52.

101. Nokin MJ, Durieux F, Bellier J, Peulen O, Uchida K, Spiegel DA, et al. Hormetic potential of methylglyoxal, a side-product of glycolysis, in switching tumours from growth to death. *Sci Rep*. 2017;7(1):11722.

102. Leone A, Nigro C, Nicolo A, Prevenzano I, Formisano P, Beguinot F, Miele C. The Dual-Role of Methylglyoxal in Tumor Progression - Novel Therapeutic Approaches. *Front Oncol*. 2021;11:645686.

103. Xiao W, Loscalzo J. Metabolic Responses to Reductive Stress. *Antioxid Redox Signal*. 2020;32(18):1330-47.

104. Estrela JM, Ortega A, Obrador E. Glutathione in cancer biology and therapy. *Crit Rev Clin Lab Sci*. 2006;43(2):143-81.

105. Jiang X, Stockwell BR, Conrad M. Ferroptosis: mechanisms, biology and role in disease. *Nat Rev Mol Cell Biol*. 2021;22(4):266-82.

106. Harris IS, Endress JE, Coloff JL, Selfors LM, McBrayer SK, Rosenbluth JM, et al. Deubiquitinases Maintain Protein Homeostasis and Survival of Cancer Cells upon Glutathione Depletion. *Cell Metab*. 2019;29(5):1166-81 e6.

107. Huang R, Zhou PK. DNA damage repair: historical perspectives, mechanistic pathways and clinical translation for targeted cancer therapy. *Signal Transduct Target Ther*. 2021;6(1):254.

108. Perillo B, Di Donato M, Pezone A, Di Zazzo E, Giovannelli P, Galasso G, et al. ROS in cancer therapy: the bright side of the moon. *Exp Mol Med*. 2020;52(2):192-203.

109. Coukos JS, Moellering RE. Methylglyoxal Forms Diverse Mercaptomethylimidazole Crosslinks with Thiol and Guanidine Pairs in Endogenous Metabolites and Proteins. *ACS Chem Biol*. 2021;16(11):2453-61.

110. Ju HQ, Lin JF, Tian T, Xie D, Xu RH. NADPH homeostasis in cancer: functions, mechanisms and therapeutic implications. *Signal Transduct Target Ther*. 2020;5(1):231.

111. Ying M, You D, Zhu X, Cai L, Zeng S, Hu X. Lactate and glutamine support NADPH generation in cancer cells under glucose deprived conditions. *Redox Biol*. 2021;46:102065.

112. Chen L, Zhang Z, Hoshino A, Zheng HD, Morley M, Arany Z, Rabinowitz JD. NADPH production by the oxidative pentose-phosphate pathway supports folate metabolism. *Nat Metab*. 2019;1:404-15.

113. Fan J, Ye J, Kamphorst JJ, Shlomi T, Thompson CB, Rabinowitz JD. Quantitative flux analysis reveals folate-dependent NADPH production. *Nature*. 2014;510(7504):298-302.

114. Loeber G, Dworkin MB, Infante A, Ahorn H. Characterization of cytosolic malic enzyme in human tumor cells. *FEBS Lett*. 1994;344(2-3):181-6.

115. L MG, Boulay K, Topisirovic I, Huot ME, Mallette FA. Oncogenic Activities of IDH1/2 Mutations: From Epigenetics to Cellular Signaling. *Trends Cell Biol*. 2017;27(10):738-52.

116. Yoo HC, Yu YC, Sung Y, Han JM. Glutamine reliance in cell metabolism. *Exp Mol Med*. 2020;52(9):1496-516.

117. Xiong J. Fatty Acid Oxidation in Cell Fate Determination. *Trends Biochem Sci*. 2018;43(11):854-7.

118. Ogiwara H, Takahashi K, Sasaki M, Kuroda T, Yoshida H, Watanabe R, et al. Targeting the Vulnerability of Glutathione Metabolism in ARID1A-Deficient Cancers. *Cancer Cell*. 2019;35(2):177-90 e8.

119. Nishizawa S, Araki H, Ishikawa Y, Kitazawa S, Hata A, Soga T, Hara T. Low tumor glutathione level as a sensitivity marker for glutamate-cysteine ligase inhibitors. *Oncol Lett*. 2018;15(6):8735-43.

120. Bustos SA, Golden SS. Expression of the psbDII gene in Synechococcus sp. strain PCC 7942 requires sequences downstream of the transcription start site. *J Bacteriol*. 1991;173(23):7525-33.

121. Hidese R, Ohbayashi R, Kato Y, Matsuda M, Tanaka K, Imamura S, et al. ppGpp accumulation reduces the expression of the global nitrogen homeostasis-modulating NtcA regulon by affecting 2-oxoglutarate levels. *Commun Biol*. 2023;6(1):1285.

122. Zhang S, Sun J, Feng D, Sun H, Cui J, Zeng X, et al. Unlocking the potentials of cyanobacterial photosynthesis for directly converting carbon dioxide into glucose. *Nat Commun*. 2023;14(1):3425.

123. Kanno M, Carroll AL, Atsumi S. Global metabolic rewiring for improved CO(2) fixation and chemical production in cyanobacteria. *Nat Commun*. 2017;8:14724.

124. Marchler-Bauer A, Bo Y, Han L, He J, Lanczycki CJ, Lu S, et al. CDD/SPARCLE: functional classification of proteins via subfamily domain architectures. *Nucleic Acids Res*. 2017;45(D1):D200-D3.

125. Lu S, Wang J, Chitsaz F, Derbyshire MK, Geer RC, Gonzales NR, et al. CDD/SPARCLE: the conserved domain database in 2020. *Nucleic Acids Res*. 2020;48(D1):D265-D8.

126. Wang J, Chitsaz F, Derbyshire MK, Gonzales NR, Gwadz M, Lu S, et al. The conserved domain database in 2023. *Nucleic Acids Res*. 2023;51(D1):D384-D8.

127. Sherman BT, Hao M, Qiu J, Jiao X, Baseler MW, Lane HC, et al. DAVID: a web server for functional enrichment analysis and functional annotation of gene lists (2021 update). *Nucleic Acids Res*. 2022;50(W1):W216-W21.

128. Thornalley PJ, Yurek-George A, Argirov OK. Kinetics and mechanism of the reaction of aminoguanidine with the alpha-oxoaldehydes glyoxal, methylglyoxal, and 3-deoxyglucosone under physiological conditions. *Biochem Pharmacol*. 2000;60(1):55-65.

129. Lo TW, Selwood T, Thornalley PJ. The reaction of methylglyoxal with aminoguanidine under physiological conditions and prevention of methylglyoxal binding to plasma proteins. *Biochem Pharmacol*. 1994;48(10):1865-70.

130. Intlekofer AM, Wang B, Liu H, Shah H, Carmona-Fontaine C, Rustenburg AS, et al. L-2-Hydroxyglutarate production arises from noncanonical enzyme function at acidic pH. *Nat Chem Biol*. 2017;13(5):494-500.

131. Moreno-Yruela C, Olsen CA. High-throughput screening of histone deacetylases and determination of kinetic parameters using fluorogenic assays. *STAR Protoc*. 2021;2(1):100313.

132. Hyun K, Jeon J, Park K, Kim J. Writing, erasing and reading histone lysine methylations. *Exp Mol Med*. 2017;49(4):e324.

133. Zhao A, Zhou H, Yang J, Li M, Niu T. Epigenetic regulation in hematopoiesis and its implications in the targeted therapy of hematologic malignancies. *Signal Transduct Target Ther*. 2023;8(1):71.

134. Kageyama H, Nishiwaki T, Nakajima M, Iwasaki H, Oyama T, Kondo T. Cyanobacterial circadian pacemaker: Kai protein complex dynamics in the KaiC phosphorylation cycle in vitro. *Mol Cell*. 2006;23(2):161-71.

135. Dong G, Golden SS. How a cyanobacterium tells time. *Curr Opin Microbiol*. 2008;11(6):541-6.

136. Welkie DG, Rubin BE, Diamond S, Hood RD, Savage DF, Golden SS. A Hard Day's Night: Cyanobacteria in Diel Cycles. *Trends Microbiol*. 2019;27(3):231-42.

137. Diamond S, Jun D, Rubin BE, Golden SS. The circadian oscillator in Synechococcus elongatus controls metabolite partitioning during diurnal growth. *Proc Natl Acad Sci U S A*. 2015;112(15):E1916-25.

138. Chen X, Schreiber K, Appel J, Makowka A, Fahnrich B, Roettger M, et al. The Entner-Doudoroff pathway is an overlooked glycolytic route in cyanobacteria and plants. *Proc Natl Acad Sci U S A*. 2016;113(19):5441-6.

139. Stein BD, Ferrarone JR, Gardner EE, Chang JW, Wu D, Hollstein PE, et al. LKB1-Dependent Regulation of TPI1 Creates a Divergent Metabolic Liability between Human and Mouse Lung Adenocarcinoma. *Cancer Discov*. 2023;13(4):1002-25.

140. Guerreiro AC, Benevento M, Lehmann R, van Breukelen B, Post H, Giansanti P, et al. Daily rhythms in the cyanobacterium synechococcus elongatus probed by high-resolution mass spectrometry-based proteomics reveals a small defined set of cyclic proteins. *Mol Cell Proteomics*. 2014;13(8):2042-55.

141. Nakayasu ES, Burnet MC, Walukiewicz HE, Wilkins CS, Shukla AK, Brooks S, et al. Ancient Regulatory Role of Lysine Acetylation in Central Metabolism. *mBio*. 2017;8(6).

142. Gonzalez JM, Marti-Arbona R, Chen JCH, Unkefer CJ. The structure of Synechococcus elongatus enolase reveals key aspects of phosphoenolpyruvate binding. *Acta Crystallogr F Struct Biol Commun*. 2022;78(Pt 4):177-84.

143. Ehammer H, Rauch G, Prem A, Kappes B, Macheroux P. Conservation of NADPH utilization by chorismate synthase and its implications for the evolution of the shikimate pathway. *Mol Microbiol*. 2007;65(5):1249-57.

144. Maclean J, Ali S. The structure of chorismate synthase reveals a novel flavin binding site fundamental to a unique chemical reaction. *Structure*. 2003;11(12):1499-511.

145. Kitzing K, Auweter S, Amrhein N, Macheroux P. Mechanism of chorismate synthase. Role of the two invariant histidine residues in the active site. *J Biol Chem*. 2004;279(10):9451-61.

146. Gurrieri L, Fermani S, Zaffagnini M, Sparla F, Trost P. Calvin-Benson cycle regulation is getting complex. *Trends Plant Sci*. 2021;26(9):898-912.

147. Lucius S, Theune M, Arrivault S, Hildebrandt S, Mullineaux CW, Gutekunst K, Hagemann M. CP12 fine-tunes the Calvin-Benson cycle and carbohydrate metabolism in cyanobacteria. *Front Plant Sci*. 2022;13:1028794.

148. Shi Y, Zhang Y, Lin S, Wang C, Zhou J, Peng D, Xue Y. dbPSP 2.0, an updated database of protein phosphorylation sites in prokaryotes. *Sci Data*. 2020;7(1):164.

149. Huang JX, Lee G, Cavanaugh KE, Chang JW, Gardel ML, Moellering RE. High throughput discovery of functional protein modifications by Hotspot Thermal Profiling. *Nat Methods*. 2019;16(9):894-901.

150. Lin S, Wang C, Zhou J, Shi Y, Ruan C, Tu Y, et al. EPSD: a well-annotated data resource of protein phosphorylation sites in eukaryotes. *Brief Bioinform*. 2021;22(1):298-307.

151. Caetano-Anolles G, Yafremava LS, Gee H, Caetano-Anolles D, Kim HS, Mittenthal JE. The origin and evolution of modern metabolism. *Int J Biochem Cell Biol*. 2009;41(2):285-97.

152. Werner A, Broeckling CD, Prasad A, Peebles CAM. A comprehensive time-course metabolite profiling of the model cyanobacterium Synechocystis sp. PCC 6803 under diurnal light:dark cycles. *Plant J*. 2019;99(2):379-88.

153. Jaiswal D, Wangikar PP. Dynamic Inventory of Intermediate Metabolites of Cyanobacteria in a Diurnal Cycle. *iScience*. 2020;23(11):101704.

154. Satagopan S, Huening KA, Tabita FR. Selection of Cyanobacterial (Synechococcus sp. Strain PCC 6301) RubisCO Variants with Improved Functional Properties That Confer

Enhanced CO(2)-Dependent Growth of Rhodobacter capsulatus, a Photosynthetic Bacterium. *mBio*. 2019;10(4).

155. Ahn HJ, Yoon HJ, Lee B, 2nd, Suh SW. Crystal structure of chorismate synthase: a novel FMN-binding protein fold and functional insights. *J Mol Biol*. 2004;336(4):903-15.

156. Pattanayak GK, Lambert G, Bernat K, Rust MJ. Controlling the Cyanobacterial Clock by Synthetically Rewiring Metabolism. *Cell Rep*. 2015;13(11):2362-7.

157. Mehdizadeh Allaf M, Peerhossaini H. Cyanobacteria: Model Microorganisms and Beyond. *Microorganisms*. 2022;10(4).

158. van Duijn CM, Dekker MC, Bonifati V, Galjaard RJ, Houwing-Duistermaat JJ, Snijders PJ, et al. Park7, a novel locus for autosomal recessive early-onset parkinsonism, on chromosome 1p36. *Am J Hum Genet*. 2001;69(3):629-34.

159. Bonifati V, Rizzu P, Squitieri F, Krieger E, Vanacore N, van Swieten JC, et al. DJ-1(PARK7), a novel gene for autosomal recessive, early onset parkinsonism. *Neurol Sci*. 2003;24(3):159-60.

160. Bonifati V, Rizzu P, van Baren MJ, Schaap O, Breedveld GJ, Krieger E, et al. Mutations in the DJ-1 gene associated with autosomal recessive early-onset parkinsonism. *Science*. 2003;299(5604):256-9.

161. Nuytemans K, Theuns J, Cruts M, Van Broeckhoven C. Genetic etiology of Parkinson disease associated with mutations in the SNCA, PARK2, PINK1, PARK7, and LRRK2 genes: a mutation update. *Hum Mutat*. 2010;31(7):763-80.

162. Nagakubo D, Taira T, Kitaura H, Ikeda M, Tamai K, Iguchi-Ariga SM, Ariga H. DJ-1, a novel oncogene which transforms mouse NIH3T3 cells in cooperation with ras. *Biochem Biophys Res Commun*. 1997;231(2):509-13.

163. Canet-Aviles RM, Wilson MA, Miller DW, Ahmad R, McLendon C, Bandyopadhyay S, et al. The Parkinson's disease protein DJ-1 is neuroprotective due to cysteine-sulfinic acid-driven mitochondrial localization. *Proc Natl Acad Sci U S A*. 2004;101(24):9103-8.

164. Kim SJ, Park YJ, Hwang IY, Youdim MB, Park KS, Oh YJ. Nuclear translocation of DJ-1 during oxidative stress-induced neuronal cell death. *Free Radic Biol Med*. 2012;53(4):936-50.

165. Ismail IA, Kang HS, Lee HJ, Kim JK, Hong SH. DJ-1 upregulates breast cancer cell invasion by repressing KLF17 expression. *Br J Cancer*. 2014;110(5):1298-306.

166. Zhou J, Liu H, Zhang L, Liu X, Zhang C, Wang Y, et al. DJ-1 promotes colorectal cancer progression through activating PLAGL2/Wnt/BMP4 axis. *Cell Death Dis*. 2018;9(9):865.

167. Jain D, Jain R, Eberhard D, Eglinger J, Bugliani M, Piemonti L, et al. Age- and diet-dependent requirement of DJ-1 for glucose homeostasis in mice with implications for human type 2 diabetes. *J Mol Cell Biol*. 2012;4(4):221-30.

168. Waanders LF, Chwalek K, Monetti M, Kumar C, Lammert E, Mann M. Quantitative proteomic analysis of single pancreatic islets. *Proc Natl Acad Sci U S A*. 2009;106(45):18902-7.

169. Danileviciute E, Zeng N, Capelle CM, Paczia N, Gillespie MA, Kurniawan H, et al. PARK7/DJ-1 promotes pyruvate dehydrogenase activity and maintains T(reg) homeostasis during ageing. *Nat Metab*. 2022;4(5):589-607.

170. Shendelman S, Jonason A, Martinat C, Leete T, Abeliovich A. DJ-1 is a redox-dependent molecular chaperone that inhibits alpha-synuclein aggregate formation. *PLoS Biol*. 2004;2(11):e362.

171. Xu J, Zhong N, Wang H, Elias JE, Kim CY, Woldman I, et al. The Parkinson's disease-associated DJ-1 protein is a transcriptional co-activator that protects against neuronal apoptosis. *Hum Mol Genet*. 2005;14(9):1231-41.

172. Kim RH, Smith PD, Aleyasin H, Hayley S, Mount MP, Pownall S, et al. Hypersensitivity of DJ-1-deficient mice to 1-methyl-4-phenyl-1,2,3,6-tetrahydropyrindine (MPTP) and oxidative stress. *Proc Natl Acad Sci U S A*. 2005;102(14):5215-20.

173. Hayashi T, Ishimori C, Takahashi-Niki K, Taira T, Kim YC, Maita H, et al. DJ-1 binds to mitochondrial complex I and maintains its activity. *Biochem Biophys Res Commun*. 2009;390(3):667-72.

174. Moellering RE, Cravatt BF. Functional lysine modification by an intrinsically reactive primary glycolytic metabolite. *Science*. 2013;341(6145):549-53.

175. Krymkiewicz N. Reactions of methylglyoxal with nucleic acids. *FEBS Lett*. 1973;29(1):51-4.

176. Lo TW, Westwood ME, McLellan AC, Selwood T, Thornalley PJ. Binding and modification of proteins by methylglyoxal under physiological conditions. A kinetic and mechanistic study with N alpha-acetylarginine, N alpha-acetylcysteine, and N alpha-acetyllysine, and bovine serum albumin. *The Journal of biological chemistry*. 1994;269(51):32299-305.

177. Murata-Kamiya N, Kamiya H. Methylglyoxal, an endogenous aldehyde, crosslinks DNA polymerase and the substrate DNA. *Nucleic Acids Res*. 2001;29(16):3433-8.

178. Ahmed N, Thornalley PJ, Dawczynski J, Franke S, Strobel J, Stein G, Haik GM. Methylglyoxal-derived hydroimidazolone advanced glycation end-products of human lens proteins. *Invest Ophthalmol Vis Sci*. 2003;44(12):5287-92.

179. Coukos JS, Lee CW, Pillai KS, Liu KJ, Moellering RE. Widespread, Reversible Cysteine Modification by Methylglyoxal Regulates Metabolic Enzyme Function. *ACS Chem Biol*. 2023;18(1):91-101.

180. Thornalley PJ. Methylglyoxal, glyoxalases and the development of diabetic complications. *Amino Acids*. 1994;6(1):15-23.

181. Allaman I, Bélanger M, Magistretti PJ. Methylglyoxal, the dark side of glycolysis. *Front Neurosci*. 2015;9:23.

182. Xue M, Rabbani N, Thornalley PJ. Glyoxalase in ageing. *Semin Cell Dev Biol*. 2011;22(3):293-301.

183. Sharma N, Rao SP, Kalivendi SV. The deglycase activity of DJ-1 mitigates α-synuclein glycation and aggregation in dopaminergic cells: Role of oxidative stress mediated downregulation of DJ-1 in Parkinson's disease. *Free Radic Biol Med*. 2019;135:28-37.

184. Atieh TB, Roth J, Yang X, Hoop CL, Baum J. DJ-1 Acts as a Scavenger of α-Synuclein Oligomers and Restores Monomeric Glycated α-Synuclein. *Biomolecules*. 2021;11(10).

185. Thornalley PJ. The glyoxalase system: new developments towards functional characterization of a metabolic pathway fundamental to biological life. *Biochem J*. 1990;269(1):1-11.

186. Rabbani N, Thornalley PJ. Methylglyoxal, glyoxalase 1 and the dicarbonyl proteome. *Amino Acids*. 2012;42(4):1133-42.

187. Sousa Silva M, Gomes RA, Ferreira AE, Ponces Freire A, Cordeiro C. The glyoxalase pathway: the first hundred years... and beyond. *Biochem J*. 2013;453(1):1-15.

188. Thornalley PJ. Glyoxalase I--structure, function and a critical role in the enzymatic defence against glycation. *Biochem Soc Trans*. 2003;31(Pt 6):1343-8.

189. Cameron AD, Ridderström M, Olin B, Mannervik B. Crystal structure of human glyoxalase II and its complex with a glutathione thiolester substrate analogue. *Structure*. 1999;7(9):1067-78.

190. Flick MJ, Konieczny SF. Identification of putative mammalian D-lactate dehydrogenase enzymes. *Biochem Biophys Res Commun*. 2002;295(4):910-6.

191. Tao X, Tong L. Crystal structure of human DJ-1, a protein associated with early onset Parkinson's disease. *J Biol Chem*. 2003;278(33):31372-9.

192. Mihoub M, Abdallah J, Richarme G. Protein Repair from Glycation by Glyoxals by the DJ-1 Family Maillard Deglycases. *Adv Exp Med Biol*. 2017;1037:133-47.

193. Richarme G, Abdallah J, Mathas N, Gautier V, Dairou J. Further characterization of the Maillard deglycase DJ-1 and its prokaryotic homologs, deglycase 1/Hsp31, deglycase 2/YhbO, and deglycase 3/YajL. *Biochem Biophys Res Commun*. 2018;503(2):703-9.

194. Jun YW, Kool ET. Small Substrate or Large? Debate Over the Mechanism of Glycation Adduct Repair by DJ-1. *Cell Chem Biol*. 2020;27(9):1117-23.

195. Pfaff DH, Fleming T, Nawroth P, Teleman AA. Evidence Against a Role for the Parkinsonism-associated Protein DJ-1 in Methylglyoxal Detoxification. *J Biol Chem*. 2017;292(2):685-90.

196. Andreeva A, Bekkhozhin Z, Omertassova N, Baizhumanov T, Yeltay G, Akhmetali M, et al. The apparent deglycase activity of DJ-1 results from the conversion of free methylglyoxal present in fast equilibrium with hemithioacetals and hemiaminals. *J Biol Chem*. 2019;294(49):18863-72.

197. Gao Q, Jacob-Dolan JW, Scheck RA. Parkinsonism-Associated Protein DJ-1 Is an Antagonist, Not an Eraser, for Protein Glycation. *Biochemistry*. 2023;62(6):1181-90.

198. Choi J, Tak S, Jung HM, Cha S, Hwang E, Lee D, et al. Kinetic evidence in favor of glyoxalase III and against deglycase activity of DJ-1. *Protein Sci*. 2023;32(5):e4641.

199. Zhou XZ, N.; Hossain, F.; Kandalai, S.; Tian, H.; Zheng, Q. Biosynthesis of D/L-lactate from methylglyoxal. *Tetrahedron*. 2022;127(19):133087.

200. Sibbersen C, Palmfeldt J, Hansen J, Gregersen N, Jørgensen KA, Johannsen M. Development of a chemical probe for identifying protein targets of α-oxoaldehydes. *Chem Commun (Camb)*. 2013;49(38):4012-4.

201. Sibbersen C, Schou Oxvig AM, Bisgaard Olesen S, Nielsen CB, Galligan JJ, Jørgensen KA, et al. Profiling of Methylglyoxal Blood Metabolism and Advanced Glycation End-Product Proteome Using a Chemical Probe. *ACS Chem Biol*. 2018;13(12):3294-305.

202. Rabbani N, Thornalley PJ. Measurement of methylglyoxal by stable isotopic dilution analysis LC-MS/MS with corroborative prediction in physiological samples. *Nat Protoc*. 2014;9(8):1969-79.

203. Choi D, Kim J, Ha S, Kwon K, Kim EH, Lee HY, et al. Stereospecific mechanism of DJ-1 glyoxalases inferred from their hemithioacetal-containing crystal structures. *FEBS J*. 2014;281(24):5447-62.

204. Jennings EQ, Ray JD, Zerio CJ, Trujillo MN, McDonald DM, Chapman E, et al. Sirtuin 2 Regulates Protein LactoylLys Modifications. *Chembiochem*. 2021;22(12):2102-6.

205. Moreno-Yruela C, Zhang D, Wei W, Baek M, Liu W, Gao J, et al. Class I histone deacetylases (HDAC1-3) are histone lysine delactylases. *Sci Adv*. 2022;8(3):eabi6696.

206. Li Y, Gu Z, Lin S, Chen L, Dzreyan V, Eid M, et al. Histone Deacetylases as Epigenetic Targets for Treating Parkinson's Disease. *Brain Sci*. 2022;12(5).

207. Thomas EA, D'Mello SR. Complex neuroprotective and neurotoxic effects of histone deacetylases. *J Neurochem*. 2018;145(2):96-110.

208. Alenghat T, Meyers K, Mullican SE, Leitner K, Adeniji-Adele A, Avila J, et al. Nuclear receptor corepressor and histone deacetylase 3 govern circadian metabolic physiology. *Nature*. 2008;456(7224):997-1000.

209. Ko Y, Hong M, Lee S, Kumar M, Ibrahim L, Nutsch K, et al. S-lactoyl modification of KEAP1 by a reactive glycolytic metabolite activates NRF2 signaling. *Proc Natl Acad Sci U S A*. 2023;120(20):e2300763120.

210. Ghandi M, Huang FW, Jane-Valbuena J, Kryukov GV, Lo CC, McDonald ER, 3rd, et al. Next-generation characterization of the Cancer Cell Line Encyclopedia. *Nature*. 2019;569(7757):503-8.

211. Canarelli SE, Swalm BM, Larson ET, Morrison MJ, Weerapana E. Monitoring GAPDH activity and inhibition with cysteine-reactive chemical probes. *RSC Chem Biol*. 2022;3(7):972-82.

212. Liberti MV, Allen AE, Ramesh V, Dai Z, Singleton KR, Guo Z, et al. Evolved resistance to partial GAPDH inhibition results in loss of the Warburg effect and in a different state of glycolysis. *J Biol Chem*. 2020;295(1):111-24.

213. Britt EC, Lika J, Giese MA, Schoen TJ, Seim GL, Huang Z, et al. Switching to the cyclic pentose phosphate pathway powers the oxidative burst in activated neutrophils. *Nat Metab*. 2022;4(3):389-403.

214. Ghergurovich JM, Garcia-Canaveras JC, Wang J, Schmidt E, Zhang Z, TeSlaa T, et al. A small molecule G6PD inhibitor reveals immune dependence on pentose phosphate pathway. *Nat Chem Biol*. 2020;16(7):731-9.

215. Ding H, Chen Z, Wu K, Huang SM, Wu WL, LeBoeuf SE, et al. Activation of the NRF2 antioxidant program sensitizes tumors to G6PD inhibition. *Sci Adv*. 2021;7(47):eabk1023.

216. Wanders RJ, Waterham HR, Ferdinandusse S. Metabolic Interplay between Peroxisomes and Other Subcellular Organelles Including Mitochondria and the Endoplasmic Reticulum. *Front Cell Dev Biol*. 2015;3:83.

217. Violante S, Achetib N, van Roermund CWT, Hagen J, Dodatko T, Vaz FM, et al. Peroxisomes can oxidize medium- and long-chain fatty acids through a pathway involving ABCD3 and HSD17B4. *FASEB J*. 2019;33(3):4355-64.

218. Hornburg D, Wu S, Moqri M, Zhou X, Contrepois K, Bararpour N, et al. Dynamic lipidome alterations associated with human health, disease and ageing. *Nat Metab*. 2023;5(9):1578-94.

219. Yu Y, Yan Y, Niu F, Wang Y, Chen X, Su G, et al. Ferroptosis: a cell death connecting oxidative stress, inflammation and cardiovascular diseases. *Cell Death Discov*. 2021;7(1):193.

220. Cani PD. Gut microbiota - at the intersection of everything? *Nat Rev Gastroenterol Hepatol*. 2017;14(6):321-2.

221. Duan H, Zhang X, Figeys D. An emerging field: Post-translational modification in microbiome. *Proteomics*. 2023;23(3-4):e2100389.

222. Olejarz J, Iwasa Y, Knoll AH, Nowak MA. The Great Oxygenation Event as a consequence of ecological dynamics modulated by planetary change. *Nat Commun*. 2021;12(1):3985.

223. Fischer WW, Hemp J, Valentine JS. How did life survive Earth's great oxygenation? *Curr Opin Chem Biol*. 2016;31:166-78.

224. Musgrave WB, Yi H, Kline D, Cameron JC, Wignes J, Dey S, et al. Probing the origins of glutathione biosynthesis through biochemical analysis of glutamate-cysteine ligase and glutathione synthetase from a model photosynthetic prokaryote. *Biochem J*. 2013;450(1):63-72.

225. Ortmayr K, Dubuis S, Zampieri M. Metabolic profiling of cancer cells reveals genome-wide crosstalk between transcriptional regulators and metabolism. *Nat Commun*. 2019;10(1):1841.

226. Zhang D, Tang Z, Huang H, Zhou G, Cui C, Weng Y, et al. Metabolic regulation of gene expression by histone lactylation. *Nature*. 2019;574(7779):575-80.